Mitochondrial dynamics and mitophagy during male germline development

Thesis by

Grigor Varuzhanyan

In Partial Fulfillment of the Requirements for the

degree of

Doctor of Philosophy

CALIFORNIA INSTITUTE OF TECHNOLOGY

Pasadena, California

2020

(Defended Sep, 18, 2020)

Grigor Varuzhanyan
ORCID: 0000-0001-6165-0857

ACKNOWLEDGMENTS

Many people have contributed to the work presented in this thesis and have influenced my academic and personal development. Therefore, the work presented herein reflects not just my own accomplishments, but the hard work, inspiration, and excellence of many people, to whom I would like to extend my appreciation.

First, I express my deepest gratitude to my advisor, Dr. David Chan. His logical approach to science, immense knowledge, and high standards motivated me to improve not only as a budding scientist, but also as a person. David taught me not only a tremendous amount about science, but also the true value of objective and critical thinking. He provided me with the intellectual freedom to explore different project ideas and balanced that with the guidance I needed to remain productive. I will be forever grateful for David's support of my application to Caltech's PhD program, without which I would not have been matriculated into the highly competitive program. I am fortunate to have been David's student and the lessons I learned from him will remain imbedded in my mind for the rest of my career.

I would also like to thank my thesis committee members, Dr. Paul Sternberg, Dr. Marianne Bronner, and Dr. Alexei Aravin for monitoring my PhD progress. It has been a privilege to share and discuss my findings with such an exceptional group of scientists and I am honored to have received their support to graduate.

I am especially grateful to the many members of the Chan lab for their friendship and support. First, I would like to express my deepest gratitude to Dr. Hsiuchen Chen for providing training, for helping with generating and maintaining mice, and for her countless insightful suggestions and critiques. This thesis would not have been possible without

Hsiuchen's hard work and brilliance. I would also like to pay my special regards to Dr. Prashant Mishra for providing training and mentorship, which helped me get up to speed at the beginning of my PhD program. I thank Dr. Anh Pham for training during the initial stages of my undergraduate internship; Dr. Raymond Liu for his cloning expertise, the stimulating science discussions and riddles, and the chess matches in between experiments; Dr. Rebecca Rojansky for her initial characterization of the germline defects in mitochondrial fission-deficient mice; Ruohan Wang for friendship and support; Dr. Anand Vaidya for friendship and encouragement for sustainable living; Dr. Christopher Fioresce for his words of encouragement and cell sorting expertise; Dr. Yogaditya Chakrabarti for technical expertise and many stimulating discussions over lunch; Dr. Chun-Shik Shin for his insightful comments during lab meetings; and Shuxia Meng for her amazing work as lab manager. Building relationships with such an exceptional group of people has been the highlight of my PhD program.

I also wish to acknowledge the following collaborators who are not mentioned in the individual chapter acknowledgments. Their important contributions were crucial for the completion of my doctoral work. I thank Carina Rumaldo and the rest of the OLAR staff for their mouse husbandry and veterinary services; Dr. Rochelle Diamond and Jamie Tijerina for FACS analysis; Dr. Michael Griswold and Dr. Cathryn Hogarth of Washington State University for electron microscopy; Dr. Hélio Chiarini-Garcia and André Caldeira-Brant of the Federal University of Minas Gerais for help with identifying germ cell types in electron micrographs; and Dr. Lilien Voong of Caltech's writing center for the many writing tips and for her suggestions that greatly improved the presentation of the figures in Chapter 1.

I thank the many members of Caltech's table tennis club with whom I was able to unwind between and after experiments. I am especially grateful to Dr. Peter Lee and Art Davis for helping me organize Monday practice sessions.

I would also like to express sincere gratitude to my undergraduate advisor, Dr. Andrew Voss, then at the California State Polytechnic University, Pomona (Cal Poly Pomona). Through many long and exciting discussions, Andy opened my eyes to the world of academia and instilled in me excitement about doing science. I would not be where I am today without Andy's encouragement and support during my undergraduate studies. I am also thankful to Dr. Jill Adler-Moore for directing the California Institute for Regenerative Medicine (CIRM) Bridges to Stem Cell Research program at Cal Poly Pomona. Under Dr. Adler's leadership, this program allowed me to undertake a six-month long undergraduate internship in Dr. David Chan's lab at Caltech, which was crucial for my matriculation into the PhD program at Caltech. Years later, this same program enabled two Cal Poly Pomona undergraduates, Alex Gureghyan and William Morris, to undertake internships in David's lab, where they helped me develop assays for the mitochondrial fusion project. I am very grateful to Alex and Will for their hard work and companionship.

I am forever indebted to my parents for their unconditional love and support, and for exemplifying and instilling in me a strong work ethic. My parents left their homeland of Armenia to start a new life in America, where they worked extremely hard to provide opportunities for a good education. I hope completion of my doctorate makes my parents proud as my success is a reflection of their hard work, love, and nurturing. I am also grateful to my older brother for our camaraderie, the many off-road explorations, and the stimulating,

late-night discussions about science and philosophy. I could not have completed graduate school without the love and support of my family.

Finally, I express my deepest and most heartfelt gratitude to my wife for all the wonderful memories we made together. Anahit's love and unwavering support enabled me to overcome even the most difficult of times. I commend her for the countless sacrifices she made to deal with the long and unpredictable hours that went into this doctoral work. Above all, I thank Anahit for the most precious gift of all—our baby boy, Daniel Varuzhanyan. Becoming a husband and father gave me more courage, strength, and fulfilment than I could have ever imagined, and it fueled my motivation to succeed in graduate school.

I thank the following sources for funding: NSF Graduate Research Fellowship (DGE-1144469); NIH Cell and Molecular Biology Training Grant (GM07616T32); California Institute for Regenerative Medicine (Stem Cell Bridges Program, TB1-01176).

ABSTRACT

Mitochondrial fusion and fission (mitochondrial dynamics) and mitophagy are well-established mitochondrial quality control mechanisms that safeguard cellular homeostasis. However, their role during development remains poorly understood. In this thesis, we establish the role of mitochondrial dynamics and mitophagy during the development of the male germline (spermatogenesis).

Spermatogenesis is one of biology's most complex and lengthy differentiation processes, transforming spermatogonial stem cells into highly specialized sperm cells capable of fertilization. This elaborate differentiation program requires multiple transitions in mitochondrial morphology and extensive degradation of mitochondria, making it an attractive model system for investigating mitochondrial dynamics and mitophagy *in vivo*. Indeed, the field of mitochondrial dynamics has a long history with spermatogenesis. The first mitochondrial dynamics gene, *Fuzzy onions* (*Fzo*), was discovered in 1997 to mediate mitochondrial fusion during *Drosophila* spermatogenesis. However, the role of mitochondrial dynamics during mammalian spermatogenesis remained unknown for nearly two decades after discovery of *Fzo*. To address this gap in knowledge, we investigate mitochondrial dynamics and mitophagy during mammalian spermatogenesis. We uncover essential roles for mitochondrial fusion (Chapter 2), mitochondrial fission (Chapter 3), and mitophagy (Chapter 4) during spermatogenesis and show that each of these mitochondrial quality control mechanisms regulates a distinct stage of germ cell development. Our analyses reveal requirements for mitochondrial fusion, fission, and mitophagy that correspond to the mitochondrial and metabolic needs of the developing germ cells.

We also investigate the role of mitochondrial fusion and fission in regulating subcellular mitochondrial domains upon fusion of a skeletal muscle stem cell with a myofiber (Chapter 5). Thus, the work presented in this thesis characterizes the *in vivo* role of mitochondrial dynamics in two systems: male germline development and skeletal muscle regeneration. However, we focus on the role of mitochondrial dynamics and mitophagy during male germline development.

PUBLISHED CONTENT AND CONTRIBUTIONS

Chapter 1 and parts of Chapter 6

Varuzhanyan, G. and Chan, D.C., 2020. Mitochondrial dynamics during spermatogenesis. *Journal of Cell Science*, 133.https://doi.org/10.1242/jcs.235937

GV participated in the literature review and in writing of the manuscript.

Chapter 2

Varuzhanyan, G., Rojansky, R., Sweredoski, M. J., Graham, R. L., Hess, S., Ladinsky, M. S. and Chan, D. C. (2019). Mitochondrial fusion is required for spermatogonial differentiation and meiosis. *eLife* 8, e51601. https://doi.org/10.7554/eLife.51601

GV participated in the conception of projects, performed all the experiments except the SILAC in Figure 6, analyzed and prepared all the data, and participated in writing of the manuscript.

Chapter 3

Varuzhanyan, G., Chen, H., Rojansky, R., Ladinsky, M., S., McCaffery, M., Chan, D., 2020. Mitochondrial fission is required for organization of the mitochondrial sheath in spermatids. *Biochimica et Biophysica Acta (BBA) - General Subjects* (in press).

GV participated in the conception of projects, performed all the experiments except for those in Figures 5C and 5D, analyzed and prepared the data, and participated in writing of the manuscript.

Chapter 5

Mishra, P.*, **Varuzhanyan, G.***, Pham, A. H. and Chan, D. C. (2015). Mitochondrial dynamics is a distinguishing feature of skeletal muscle fiber types and regulates organellar compartmentalization. *Cell Metabolism*, 22, 1033–1044. doi: https://doi.org/10.1016/j.cmet.2015.09.027. ***Co-first author.**

GV participated in the conception of projects, performed experiments, and analyzed and prepared the data related to Figures 5, 6, 7, S3, and S4.

TABLE OF CONTENTS

LIST OF FIGURES

CHAPTER 1

Introduction

Grigor Varuzhanyan and David C. Chan

Division of Biology and Biological Engineering, California Institute of Technology, Pasadena, CA 91125, USA.

Introduction

Mitochondria are crucial to most eukaryotic cells and their function is maintained by several quality control mechanisms. These include mitochondrial fusion and fission (mitochondrial dynamics) and mitophagy, the degradation of mitochondrial content by selective autophagy (Youle and Narendra, 2011). In addition to controlling organelle morphology, continuous fusion and fission events safeguard mitochondrial function by enabling the hundreds of mitochondria within a cell to mix, promoting homogeneity (Chan, 2012). Without fusion, mitochondrial heterogeneity increases, which compromises mitochondrial physiology and leads to cellular dysfunction. For example, in mice, whole-animal ablation of mitochondrial fusion causes embryonic lethality (Chen et al., 2003), and organ-specific ablation disrupts homeostasis in tissues such as brain (Chen et al., 2007), heart (Chen et al., 2011; Papanicolaou Kyriakos N. et al., 2012), and skeletal muscle (Chen et al., 2010; Mishra et al., 2015). Similarly, whole-animal ablation of mitochondrial fission results in midgestation lethality (Ishihara et al., 2009; Wakabayashi et al., 2009), whereas tissue-specific ablation perturbs homoeostasis in the brain (Wakabayashi et al., 2009), heart (Ikeda Yoshiyuki et al., 2015; Kageyama et al., 2014) and skeletal muscle (Favaro et al., 2019). Thus, dynamics serves as a crucial mitochondrial quality control mechanism to promote cell and tissue homeostasis.

Mitophagy is an additional layer of quality control that utilizes autophagy (Mizushima, 2007; Mizushima et al., 1998; Tsukada and Ohsumi, 1993) to remove excessive mitochondria or damaged mitochondria that are beyond repair (Pickles et al., 2018). During mitophagy, microtubule-associated protein 1A/1B light chain 3 (LC3) is recruited to the autophagosomal membrane and binds to mitochondria that selectively express mitophagy

receptors on their outer membrane. This molecular recognition designates damaged mitochondria as cargo for autophagosomes, and the resulting mitophagosomes subsequently fuse with lysosomes for degradation and recycling of the engulfed organelles. Much of the molecular workings of mitophagy have been parsed in cultured cells, and recently developed mouse models are enabling the analysis of mitophagy *in vivo* (Kuma et al., 2017; McWilliams et al., 2016; Sun et al., 2015).

Although mounting evidence suggests that mitochondrial dynamics and mitophagy maintain basal cellular homeostasis, much less is known about their role during differentiation and developmentally regulated mitochondrial and metabolic transitions. Mammalian spermatogenesis is a rich system in which to address this gap in knowledge because it requires several such transitions. In this chapter, we review key aspects of mitochondrial dynamics and mitophagy, and discuss the cellular and metabolic regulation of spermatogenesis. We then describe the various mouse models of mitochondrial dysfunction that exhibit male infertility and discuss the emerging role of mitochondrial dynamics during spermatogenesis. Our discussion centers on mouse spermatogenesis, but insights from other model organisms and clinical studies are discussed where appropriate.

Mitochondrial dynamics at a glance

Despite their static and autonomous appearance in micrographs, mitochondria continuously fuse and divide, resulting in the circulation of their components throughout the entire organellar pool. Unlike most organelles that undergo fusion, mitochondria contain double membranes—a highly folded inner membrane that harbors the oxidative phosphorylation (OXPHOS) complexes and a semi-permeable outer membrane that encloses

the organelle (Tzagoloff, 1982). Mitochondrial fusion therefore involves two separate fusion events, each requiring a unique machinery featuring large guanosine triphosphatase (GTP)-hydrolyzing enzymes of the dynamin superfamily. Outer membrane fusion, mediated by the mitofusins MFN1 and MFN2, is followed by inner membrane fusion, mediated by the dynamin-like 120 kDa protein (OPA1) (Figure 1.1A). Mutations in mitofusins or *Opa1* prevent fusion, which compromises OXPHOS and leads to cellular dysfunction and disease (Chan, 2020).

Mitochondrial fusion is counter-balanced by fission. This balance maintains proper organellar size and morphology, which facilitates mitochondrial distribution and transport throughout the cell. Early steps in mitochondrial fission involve actin filaments and the endoplasmic reticulum, which mark sites of fission by wrapping around and constricting mitochondria (Friedman et al., 2011; Korobova et al., 2013) (Figure 1.1B). Subsequently, receptors on the mitochondrial outer membrane recruit cytosolic dynamin related protein 1 (DRP1), a mechanochemical enzyme that assembles into ring-like structures to further constrict and sever mitochondrial tubules. In mammals, four receptors recruit cytosolic DRP1 to the mitochondrial outer membrane: mitochondrial fission factor (MFF), mitochondrial dynamics proteins of 49 and 51 kDa (MID49 and MID51, respectively), and mitochondrial fission 1 (FIS1) (Chan, 2012). Dynamin-2 (DNM2) has been proposed to act at a terminal step following DRP1 constriction (Lee et al., 2016), but this idea was recently challenged (Fonseca et al., 2019; Kamerkar et al., 2018; Nagashima et al., 2020). Lysosomes (Wong et al., 2018) and Golgi-derived vesicles (Nagashima et al., 2020) have also been implicated in mitochondrial fission, but how they interact with the fission machinery remains to be resolved.

Mitochondrial quality control by mitophagy

Mitophagy is the selective degradation of mitochondria by autophagy (Figure 1.2A). The best characterized model of mitophagy is the phosphatase and tensin homolog (PTEN) induced kinase I (PINK1)-Parkin pathway. PINK1 is a serine/threonine kinase that is normally kept at low levels due to degradation by proteases upon import into the mitochondrial matrix. Insults that disrupt mitochondrial membrane potential prevent PINK1 import and degradation, leading to its stabilization on the mitochondrial outer membrane (Narendra et al., 2010). PINK1 then phosphorylates ubiquitin at the damaged mitochondrial surface, leading to recruitment of the E3 ubiquitin ligase Parkin, which adds additional ubiquitin molecules onto mitochondrial outer membrane proteins. Further phosphorylation of these ubiquitin chains by PINK1 recruits additional Parkin, generating a positive feedback loop that activates the ubiquitin proteasome system (UPS) (Chan et al., 2011; Rakovic et al., 2019) and recruits autophagosomes for mitophagy (Sekine and Youle, 2018).

Mitophagy utilizes the mitochondrial fission 1 protein (FIS1), which is the only receptor of DRP1 in *Saccharomyces cerevisiae* and required for mitochondrial fission in this species (Jakobs et al., 2003; Mozdy et al., 2000; Tieu et al., 2002). In mammalian cells, however, FIS1 has a minor role in mitochondrial fission (Losón et al., 2013; Otera et al., 2010) and a more prominent role in mitophagy. During Parkin-mediated mitophagy, FIS1 interacts with the mitochondrial Rab GTPase-activating protein (GAP), TBC1D15 (Onoue et al., 2013), to inhibit RAB7A (Yamano et al., 2018, 2014). In its active state, RAB7A promotes growth of double membraned autophagosomes by mediating fusion of ATG9A-containing vesicles (Tan and Tang, 2019). It has been proposed that, without FIS1, RAB7A remains constitutively active at the mitochondrial surface, leading to dysregulated growth of

autophagosomal membranes (Figure 1.2B and 1.2C) (Yamano et al., 2014). This cellular defect is observed by light microscopy as LC3 tubulation and aggregation (Yamano et al., 2014). Similarly, large LC3 aggregates are found in *fis-1*-knockout nematodes treated with mitochondrial toxins (Shen et al., 2014). Consistent with its role in mitophagy, FIS1 is required for degradation of paternal mitochondria shortly after fertilization in mice (Rojansky et al., 2016). FIS1 has also been implicated in PINK1-Parkin independent mitophagy (Yamashita et al., 2016). Thus, mammalian FIS1 plays a role in the clearance of mitochondria via mitophagy. However, a recent study reported that *Fis1* knockout in skeletal muscle increases mitophagy (Zhang et al., 2019), indicating that its role in mitophagy may be tissue specific, warranting the study of FIS1 in multiple cell types.

Spermatogenesis overview

Male germ cell development is a promising system for studying mitochondrial dynamics and mitophagy because it involves drastic changes to mitochondrial shape, number, and distribution (Hermo et al., 2010a). This complex and lengthy differentiation process occurs within the highly convoluted seminiferous tubules of the testes (Figure 1.3A), and can be divided spatiotemporally into three major categories—(1) mitotic amplification of spermatogonia, (2) genome reduction in meiotic spermatocytes, and (3) morphological transformation of haploid spermatids into spermatozoa. Mitotically dividing spermatogonia reside near the basement membrane at the tubule periphery, and their differentiated descendants migrate towards the tubule lumen. This process depends critically on the intimately associated somatic Sertoli cells—nurse cells that provide structural support, metabolites, and differentiation cues for the developing germ cells (Griswold, 1998). As

germ cells divide, incomplete cytokinesis allows their daughter cells to remain connected via stable intercellular bridge structures (Greenbaum et al., 2011), enabling them to share gene products (Braun et al., 1989). Numerous such divisions result in the formation of long "chains" of syncytial cells (Figure 1.3B).

In mice, spermatogenesis begins at birth with mitotic divisions of progenitor cells called Type A-single spermatogonia, which give rise to pairs of interconnected cells called Type A-paired spermatogonia (Figure 1.3B). Further divisions produce chains of 4 to 16 cells called Type A-aligned spermatogonia. These divisions expand the pool of undifferentiated spermatogonia while maintaining a subset with spermatogonial stem cell (SSC) activity. However, the molecular identity of SSCs remains a matter of debate. The prevailing model for decades posited that only A-singles retain SSC activity. However, recent studies have challenged this model, and two additional models of SSC dynamics have emerged. The original and revised models are described in two excellent reviews (De Rooij, 2017; Lord and Oatley, 2017). Briefly, in one revised model, SSC activity is restricted to a small subset of A-singles that express stem markers, such as *ID4* and *Pax7* (Aloisio et al., 2014). In the other model, SSC activity is maintained by a much larger population of undifferentiated spermatogonia that express Glial cell line-derived neurotrophic factor (GDNF) family receptor alpha ***(****GFRα1)* (Hara et al., 2014). Together with RET, GFRα1 binds GDNF (Naughton et al., 2006), which is secreted by Sertoli cells to regulate SSC activity (Hofmann, 2008). Chains of *GFRα1*-expressing spermatogonia are proposed to retain stemness by undergoing syncytial fragmentation to revert to smaller chains or A-singles. In contrast, SSCs in *Drosophila* (Spradling et al., 2001) and *Caenorhabditis elegans* (Kimble and White, 1981)

divide asymmetrically, forming one daughter cell that differentiates and another that retains stemness (Oatley and Brinster, 2012).

Upon receiving cues from the surrounding Sertoli cells, chains of undifferentiated spermatogonia begin to differentiate and irreversibly commit to meiosis (Griswold, 2016). The sixth and final mitotic division of differentiating spermatogonia gives rise to spermatocytes, which traverse the blood-testis barrier (BTB), enter the adluminal compartment, and initiate meiosis, a defining event in spermatogenesis (Cohen et al., 2006). In meiosis, a spermatocyte undergoes DNA duplication and two meiotic divisions to generate four haploid round spermatids.

Initially small and inconspicuous, round spermatids undergo spermiogenesis, a dramatic morphological transformation to become polarized sperm cells with a head, midpiece, and tail (Hermo et al., 2010b). This morphological transformation requires culling of excess cellular components into residual bodies for phagocytic degradation by Sertoli cells. Furthermore, the nuclear genetic material is repackaged by protamines—small, arginine-rich, DNA-binding proteins—into a slender and compacted nucleus (Bao and Bedford, 2016), which is capped by the acrosome, a unique lysosome-related organelle that releases digestive enzymes to enable fertilization.

OXPHOS fuels spermatogenesis

These highly coordinated germ cell differentiation events depend on the surrounding Sertoli cells. In addition to providing metabolites and differentiation cues for the developing germ cells, Sertoli cells form the BTB that divides the seminiferous epithelium into the basal and adluminal compartments, secluding the latter from the interstitial space and vasculature

(Stanton, 2016) (Figure 1.4A). As a result, during their progression from spermatogonial stem cells into sperm, germ cells encounter unique microenvironments with varying availability to glucose and other metabolites. Spermatogonia and SSCs reside in the basal compartment, where they have access to the vasculature and interstitial fluid, whereas the more advanced spermatocytes and spermatids in the adluminal compartment have limited access.

Male germ cells have distinct metabolic requirements depending on their differentiation state (Figure 1.4A). Spermatogonia are generally believed to rely on glucose for energy production by glycolysis (Rato et al., 2012). In contrast, spermatocytes and spermatids require lactate and pyruvate for survival (Bajpai et al., 1998; Grootegoed et al., 1984; Nakamura et al., 1984, 1982). This distinction likely reflects the fact that spermatogonia in the basal compartment have direct access to systemic glucose, whereas spermatocytes and spermatids in the adluminal compartment are separated from the vasculature by the blood-testis-barrier. Thus, spermatocytes and spermatids rely on the surrounding Sertoli cells for secretion of lactate as a carbon source (Boussouar and Benahmed, 2004). This idea is further supported by expression of lactate dehydrogenase (*Ldhc*) selectively in advanced germ cells in the adluminal compartment (Goldberg et al., 2010). Because lactate is converted to pyruvate by LDHC, and pyruvate can be converted to acetyl-coenzyme A to fuel OXPHOS, these data indicate that meiotic and post meiotic cells in the adluminal compartment likely rely more heavily on mitochondrial OXPHOS activity.

The requirement for lactate and pyruvate by meiotic spermatocytes is consistent with the high energy demands associated with meiosis and, in particular, meiotic prophase I (MPI). This lengthy process constitutes about 90% of meiosis and a fourth of the entire

spermatogenic process, and is generally subdivided into four stages—leptotene, zygotene, pachytene, and diplotene (Handel and Schimenti, 2010). The leptotene stage marks the formation of the synaptonemal complex—a proteinaceous structure that enables interaction between the homologous chromosomes—and initiation of genome-wide programmed double stranded breaks (DSBs). In zygotene, the synaptonemal complex grows along the homologous chromosomes, enabling them to synapse. During pachytene, synapsis is completed, and adenosine triphosphate (ATP)-dependent biochemical reactions drive homologous recombination and resolution of DSBs. Finally, in diplotene, the recombined chromosomes detach for segregation into daughter cells.

Classic electron microscopy (EM) analyses of mitochondrial ultrastructure in rodent testes provide support for the increased OXPHOS activity during MPI. Mitochondria in spermatogonia are generally small, spherical, and contain "orthodox" cristae (De Martino et al., 1979; Meinhardt et al., 1999; Seitz et al., 1995), an ultrastructural conformation associated with low OXPHOS activity (Hackenbrock, 1966; C. A. Mannella, 2006; Carmen A. Mannella, 2006). Conversely, mitochondria in pachytene spermatocyte are elongated and contain "condensed" cristae, an ultrastructural conformation associated with high OXPHOS utilization. In post-meiotic spermatids, mitochondria fragment and their cristae return to an intermediate state between orthodox and condensed, suggesting a shift back to glycolysis (Meinhardt et al., 1999).

Several mouse models of mitochondrial dysfunction have corroborated the critical contribution of OXPHOS to spermatogenesis and, in particular, to meiosis. For example, mice with error-prone mtDNA replication, due to a mutation in the proofreading subunit of the mtDNA polymerase gamma (*PolGA*^{D257A}), exhibit male infertility (Kujoth et al., 2005;

Trifunovic et al., 2004). Owing to accumulation of mtDNA point mutations and deletions, these "mtDNA mutator" mice have early degeneration of multiple organ systems—a phenotype interpreted as accelerated aging. The testes of mtDNA mutator mice have severe degeneration of seminiferous tubules and depletion of germ cells by 10 months of age (Kujoth et al., 2005). Increasing or decreasing expression of mitochondrial transcription factor A (*Tfam*), which regulates mtDNA levels, mitigates or exacerbates the infertility phenotype in mtDNA mutator mice, respectively (Jiang et al., 2017). Together, these data suggest that spermatogenesis is highly sensitive to perturbations in OXPHOS.

Mouse models also indicate that MPI is highly susceptible to mitochondrial dysfunction. Mice with a large scale (4,696 bp) pathogenic mtDNA deletion have reduced OXPHOS activity and exhibit meiotic arrest during the zygotene to pachytene transition (Nakada et al., 2006). Similarly, mice with genetic ablation of the testis-specific adenine nucleotide translocator (Ant4) are less efficient at utilizing mitochondrial ATP and exhibit spermatogenic arrest during the leptotene stage of MPI (Brower et al., 2009, 2007). These studies indicate that mitochondrial function is particularly important during MPI.

Clinical studies also suggest a link between mtDNA integrity and male fertility. Male patients with infertility are sometimes found to have mtDNA mutations (Baklouti-Gargouri et al., 2014; Carra et al., 2004; Kao et al., 1995; Lestienne et al., 1997), and some patients with mitochondrial disease caused by mtDNA mutations are infertile (Demain et al., 2017; Folgero et al., 1993; Spiropoulos et al., 2002). Furthermore, mutations in the mitochondrial polymerase gamma (*POLG*) contribute to male infertility (Demain et al., 2017; Luoma et al., 2004; Rovio et al., 2001).

The emerging role of mitochondrial dynamics during spermatogenesis

As detailed above, mitochondrial function is essential for spermatogenesis. Because mitochondrial dynamics safeguards mitochondrial function, perturbations in dynamics could be expected to disrupt spermatogenesis. Indeed, Hales and Fuller discovered the first mitochondrial fusion gene during a D*rosophila* mutagenesis screen for male sterility (Hales and Fuller, 1997). During *Drosophila* spermatid development, mitochondria aggregate and fuse to form the Nebenkern, which resembles an onion slice by EM due to the concentric wrapping of two giant mitochondria around each other (Demarco et al., 2014; Fuller, 1993). Hales and Fuller found that mutations in *Fuzzy onions (Fzo)*, a *Drosophila* homolog of mitofusin, cause fragmentation of the Nebenkern (giving it the appearance of "fuzzy onions") and male sterility (Hales and Fuller, 1997). Since then, emerging evidence indicates that other mitochondrial dynamics factors also promote spermatogenesis in the fly. *Drosophila* mitofusin (Dmfn), the other homolog of mammalian mitofusin, as well as *Opa1* and *Drp1*, maintain male germline stem cells (Demarco et al., 2019; Demarco and Jones, 2019). Thus, in flies, spermatogenesis requires both mitochondrial fusion and fission.

In rodents, dramatic morphological transformation of mitochondria during spermatogenesis (Figure 1.4B) suggests an evolutionarily conserved role for mitochondrial dynamics. Mitochondria in spermatogonia and early MPI are generally small and spherical. They elongate during pachytene and then fragment again in post-meiotic spermatids (De Martino et al., 1979). In maturing spermatids, small mitochondrial spheres line the midpiece in highly coordinated arrays and elongate while wrapping around the midpiece (Ho and Wey, 2007). Thus, spermatogenesis carefully regulates mitochondrial morphology to support the physiological requirements of the developing germ cells. Yet, despite these long-known

mitochondrial transitions, the role of the major mitochondrial dynamics factors during mammalian spermatogenesis remained unknown until recently.

The first mitochondrial dynamics factor examined during mouse spermatogenesis was MFN1. Zhang and colleagues removed *Mfn1* from the male germline using the *Vasa*-Cre driver, which expresses around embryonic day 15 (E15) (Zhang et al., 2016). *Mfn1* mutants were infertile, had reduced testis size, and failed to produce sperm. These defects coincided with a reduction in spermatocytes, suggesting a defect during meiosis. Undifferentiated spermatogonia were not reduced during the first round of spermatogenesis, indicating that *Mfn1* is dispensable for the formation of these progenitor cells (Zhang et al., 2016).

Our recent study expanded on the role of mitochondrial fusion during mouse spermatogenesis (Varuzhanyan et al., 2019). We observed that *Mfn1-Mfn2* double mutants failed to produce any sperm, indicating an absolute requirement for mitochondrial fusion during spermatogenesis. Histological analysis revealed a reduction in post-meiotic spermatids in fusion-deficient mice, indicating a defect during meiosis. Consistent with the known energetic demands of meiosis, the zygotene to pachytene transition in wildtype mice was associated with upregulation of OXPHOS. *Mfn1-Mfn2* double mutants exhibited meiotic arrest during this developmental transition, forming fewer pachytene cells that had reduced OXPHOS activity. These data indicate meiosis as the most susceptible stage to loss of mitochondrial fusion. Furthermore, long-term loss of mitochondrial fusion additionally depleted differentiated spermatogonia (Varuzhanyan et al., 2019), which is consistent with upregulation of OXPHOS during spermatogonial differentiation (Lord and Nixon, 2020).

After meiosis, mitochondria undergo robust fragmentation, representing a developmentally regulated mitochondrial fission event. A role for mitochondrial fission in spermatogenesis was shown using mice with a homozygous gene-trap allele of *Mff* (*Mff*^{gt}), which have reduced sperm count and subfertility (Chen et al., 2015). In addition, we recently found that round spermatids in *Mff*^{gt} mice have elongated mitochondria with constrictions indicative of failed fission events (Varuzhanyan et al., 2020). Near the end of spermiogenesis in wildtype mice, small mitochondrial spheres line the sperm axoneme and wrap around the midpiece to form the mitochondrial sheath. This observation suggests that mitochondrial fission in spermatids may facilitate formation of the mitochondrial sheath. Consistent with this idea, *Mff*^{gt} spermatids have disjointed mitochondrial sheaths with large regions lacking mitochondria, suggesting poor recruitment, or wrapping, of mitochondria around the spermatid midpiece (Varuzhanyan et al., 2020).

The role of mitochondrial dynamics during human spermatogenesis remains largely unknown. A clinical study found that low *MFN2* expression in sperm is associated with asthenozoospermia (reduced sperm motility) and reduced sperm mitochondrial membrane potential (Fang et al., 2018). There is no evidence that MFF or other mitochondrial fission factors are important for male fertility in humans. Fetal and adult testis-expressed 1 (FATE1) is a testis-specific protein with some sequence homology to MFF (Olesen et al., 2001), but its role in human fertility remains inconclusive (Olesen et al., 2003).

Autophagy and mitophagy during spermatogenesis

Recent studies indicate that autophagy is vital for cellular remodeling in post-meiotic spermatids (Shang et al., 2016; Wang et al., 2014). A role for autophagy in spermiogenesis

is not surprising given the culling of excess cellular components during this process (Figure 1.5). Removal of the core autophagy gene *Atg7* (Komatsu et al., 2005) from primordial germ cells diminished autophagic flux in spermatids and blocked acrosome biogenesis (Wang et al., 2014). More recently, *Atg7* was found to be important for spermatid polarization and cytoplasmic removal during spermiogenesis (Shang et al., 2016). In elongating spermatids, autophagy was required for the degradation of PDLIM1, a regulator of cytoskeletal dynamics. Removal of *Atg7* did not affect development of earlier germ cell types indicating that autophagy is less active in these cells (Shang et al., 2016). This notion was corroborated by a more recent report that found the highest abundance of autophagosomes in spermatids (Yang et al., 2017). Taken together, these data indicate that autophagy contributes to acrosome maintenance, spermatid polarization, and degradation of cytoplasmic components during spermiogenesis.

Spermiogenesis also removes excess mitochondria, raising the issue of whether mitophagy is involved. In *Pink1*-mutant flies, spermatids have aberrant mitochondria and defects in individualization (Clark et al., 2006). Furthermore, the UPS, which drives Parkin-mediated mitophagy (Chan et al., 2011; Chan and Chan, 2011; Rakovic et al., 2019), is highly active during mammalian spermiogenesis (Bose et al., 2014; Hermo et al., 2010c). These observations raise the possibility that Parkin-mediated mitophagy is involved in degrading mitochondria during spermiogenesis. Just before spermiation (sperm release), excess mitochondria and other cellular components agglomerate into residual bodies for phagocytic degradation by Sertoli cells (Dietert, 1966) (Figure 1.5). However, it is unknown whether spermiogenesis employs a selective or nonselective method for removing mitochondria.

A key feature of spermatid development is formation of the acrosome (Figure 1.5). The acrosome has classically been characterized as a Golgi-derived, lysosome-related organelle (Khawar et al., 2019). Vesicles budding from the trans-Golgi network fuse to each other to form a large proacrosomal granule that attaches to the spermatid nucleus. With continual fusion of vesicles, the acrosomal granule grows and flattens around the spermatid nucleus, eventually covering most of its surface. Besides the Golgi, other sources of membranes can contribute to acrosome biogenesis (Berruti and Paiardi, 2011; Khawar et al., 2019), indicating an essential role for vesicular trafficking during this process. Recently, it was shown that mitochondrial cardiolipin localizes to the acrosome (Ren et al., 2019), suggesting that mitochondria might also provide membranes to the acrosome. Additional evidence also implicates mitochondria in acrosome biogenesis. As described above for cultured cells, FIS1 facilitates mitophagy by interacting with TBC1D15, a RabGAP for RAB7A. TBC1D15 (Zhang et al., 2005) and other TBC domain-containing proteins are highly expressed in the testis and some of them are implicated in acrosome biogenesis. For example, the testis-specific male germ cells Rab GTPase-activating proteins (MgcRabGap) colocalizes with RAB3A in the acrosome (Lin et al., 2011). Furthermore, spermatocytes express TBC1D9 (Nakamura et al., 2015) and spermatozoa express a whole host of Rab proteins (Bae et al., 2019). Therefore, spermatogenesis is a promising system for studying the function of *Fis1 in vivo*.

Thesis synopsis

As described above, spermatogenesis involves multiple shifts in mitochondrial morphology and distribution. We therefore examined whether mitochondrial fusion and fission are important for male germ cell development. In Chapter 2, we show that mitochondrial fusion promotes OXPHOS to enable two metabolic transitions during spermatogenesis: spermatogonial differentiation and meiosis. In Chapter 3, our analyses reveal that mitochondrial fission mediates acute mitochondrial fragmentation during normal post-meiotic spermatid development, which facilitates the wrapping of mitochondria around the sperm midpiece to form the mitochondrial sheath. Thus, mitochondria undergo fusion during early stages of spermatogenesis before undergoing robust fragmentation post-meiosis.

During normal post-meiotic spermatid development, excess mitochondria and other cellular components are discarded into residual bodies. In Chapter 4, we investigate the role of the putative mitophagy gene, *Fis1* during spermatogenesis. We uncover an essential role for *Fis1* in regulating mitochondrial degradation during spermatid maturation. Thus, mitochondrial fusion, fission, and mitophagy are all essential for spermatogenesis and regulate distinct stages of germ cell development.

Chapter 1 Figure Legends

Figure 1.1. Mitochondrial dynamics at a glance

A) Mitochondrial fusion occurs in two distinct steps, both mediated by large GTP hydrolyzing enzyme of the dynamin superfamily. MFN1 and MFN2 mediate fusion of the mitochondrial outer membrane (OM). Then, OPA1 mediates fusion of the inner membrane (IM), which results in mixing of matrix components. Although OPA1 is present on opposing IMs, it is not required to be present on both membranes.

B) Mitochondrial fission is a multistep process. In the initial phase, actin and the endoplasmic reticulum (ER) associate with the mitochondrial tubule. The ER wraps around and constricts the mitochondrion. Receptors on the mitochondrial outer membrane (not shown) recruit cytosolic DRP1 to this constriction site. Multiple DRP1 molecules oligomerize around the mitochondrion to form a ring-shaped structure that further constricts and severs the mitochondrial tubule.

Figure 1.2. Mitochondrial quality control by mitophagy

A) Overview of mitophagy. An autophagosome engulfs a damaged portion of a mitochondrion to form a mitophagosome that fuses with lysosomes. The mitochondrion is degraded in the resulting mitolysosome.

B) A model of FIS1-mediated mitophagy. FIS1 at the mitochondrial surface interacts with TBC1D15, a mitochondrial Rab GAP that inactivates RAB7A, to regulate mitophagosome formation.

C) In the absence of FIS1, the uncontrolled action of RAB7A disrupts autophagosome membrane dynamics.

Figure 1.3. Spermatogenesis overview

A) (Left panel) Anatomy of the mammalian testis highlighting the convoluted seminiferous tubules in which spermatogenesis takes place. (Right panel) Schematic of the seminiferous epithelium highlighting the intimate association between somatic Sertoli cells and germ cells. For simplicity, only the major germ cell types are shown.

B) Cellular pedigree of a single undifferentiated spermatogonium, highlighting germ cell amplification. The theoretical number of syncytial cells at each stage is shown at the bottom. Note that meiotic spermatocytes and post-meiotic spermatids develop on the adluminal side of the blood-testis barrier (BTB).

SG, spermatogonia; SC, spermatocytes; ST, spermatids; A al, A aligned; 1°, primary spermatocyte; 2°, secondary spermatocyte; MI, meiosis I; MII, meiosis II; BTB, blood-testis barrier.

Figure 1.4. Mitochondrial respiration and dynamics during spermatogenesis

A) Mitochondrial respiration during spermatogenesis. Spermatogonia in the basal compartment have direct access to systemic glucose, which they use for glycolysis. Spermatocytes and spermatids in the adluminal compartment, however, are separated from the vasculature and interstitial space by the blood-testis barrier, and thus rely on Sertoli cells for a carbon source. Sertoli cells take up systemic glucose and glycolytically convert it into pyruvate, which is converted into lactate via pyruvate dehydrogenase (PDH). Lactate is then shuttled, via monocarboxylate transporters (MCT), into spermatocytes, which convert it back into pyruvate via lactate dehydrogenase (LDH). Finally, pyruvate gets imported into

mitochondria by the mitochondrial pyruvate carrier (MPC) for fueling oxidative phosphorylation (OXPHOS).

B) Mitochondrial dynamics during spermatogenesis. Mitochondria are generally small and spherical in spermatogonia, which reside in the basal compartment. Upon traversing the blood-testis barrier (dashed red line) and entering the adluminal compartment, mitochondria elongate and cluster around the nuage, also referred to as intermitochondrial cement (IMC). In post-meiotic spermatids, mitochondria fragment. Finally, near the end of spermiogenesis, mitochondria elongate and tightly pack around the sperm midpiece.

Figure 1.5. Mitochondrial reorganization during spermiogenesis

Schematic of spermiogenesis highlighting the formation of the acrosome and the reorganization of mitochondria. During spermatid elongation, a subset of mitochondria line the sperm midpiece, while the rest are culled into residual bodies for phagocytic degradation in Sertoli cells. It is unknown how the cell determines the fate of these two mitochondrial populations. The acrosome (blue) is another organelle that undergoes drastic reorganization during spermiogenesis.

Chapter 1 Figures

Figure 1.1

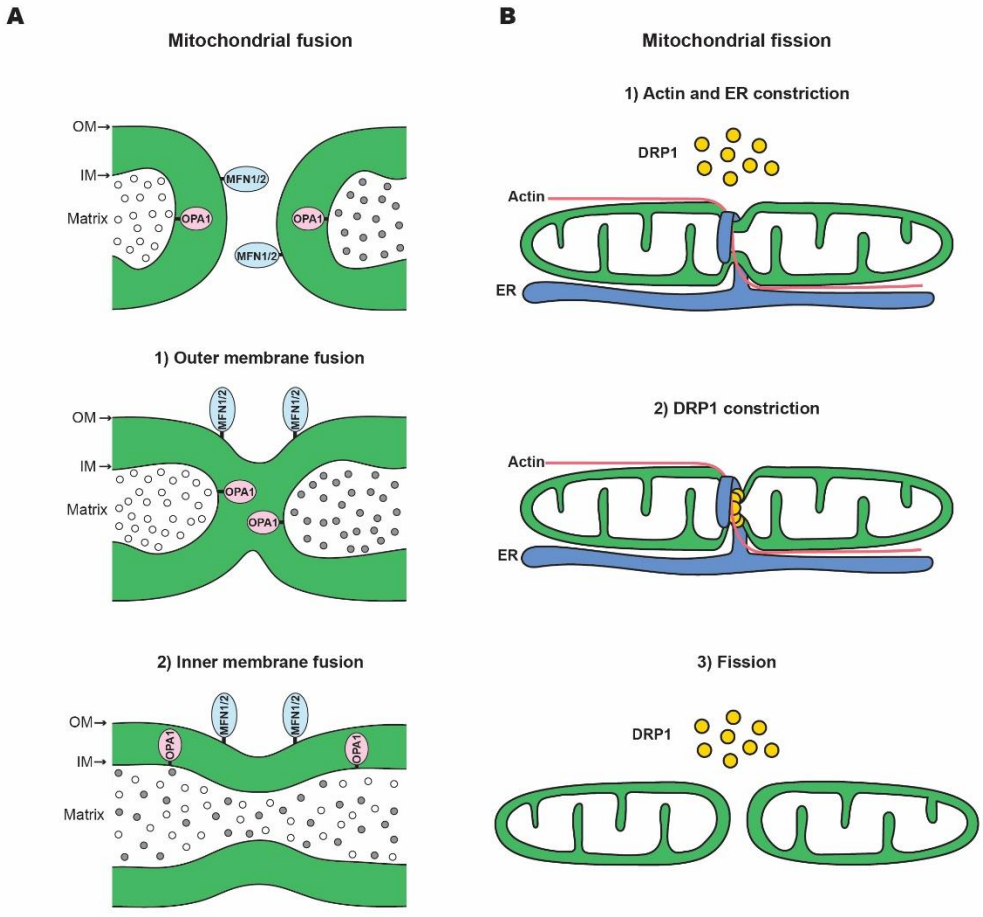

Figure 1.2

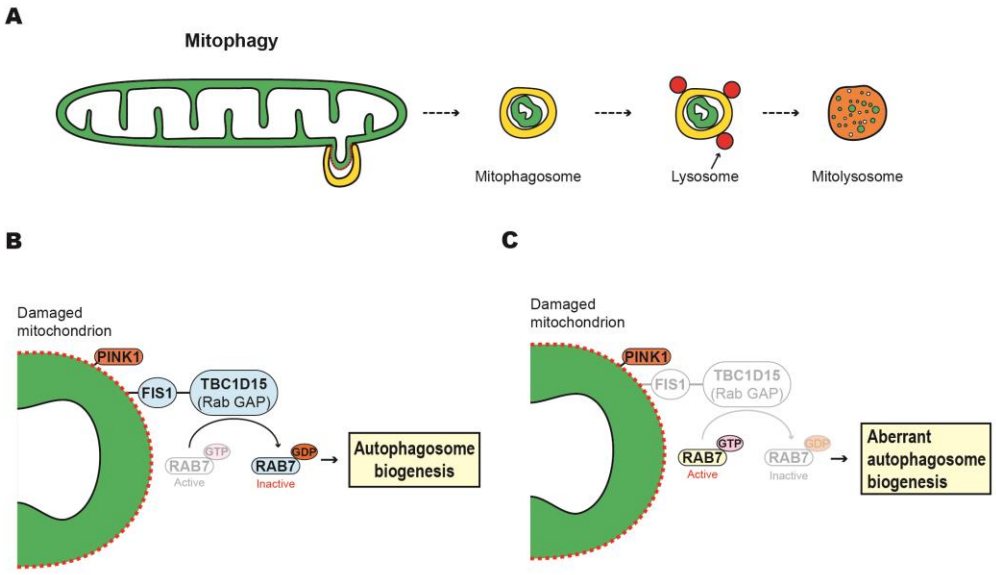
A
Mitophagy
Mitophagosome
Lysosome
Mitolysosome
B
Damaged mitochondrion
PINK1
FIS1
TBC1D15 (Rab GAP)
GTP
RAB7
Active
GDP
RAB7
Inactive
Autophagosome biogenesis
C
Damaged mitochondrion
PINK1
FIS1
TBC1D15 (Rab GAP)
GTP
RAB7
Active
GDP
RAB7
Inactive
Aberrant autophagosome biogenesis

Figure 1.3

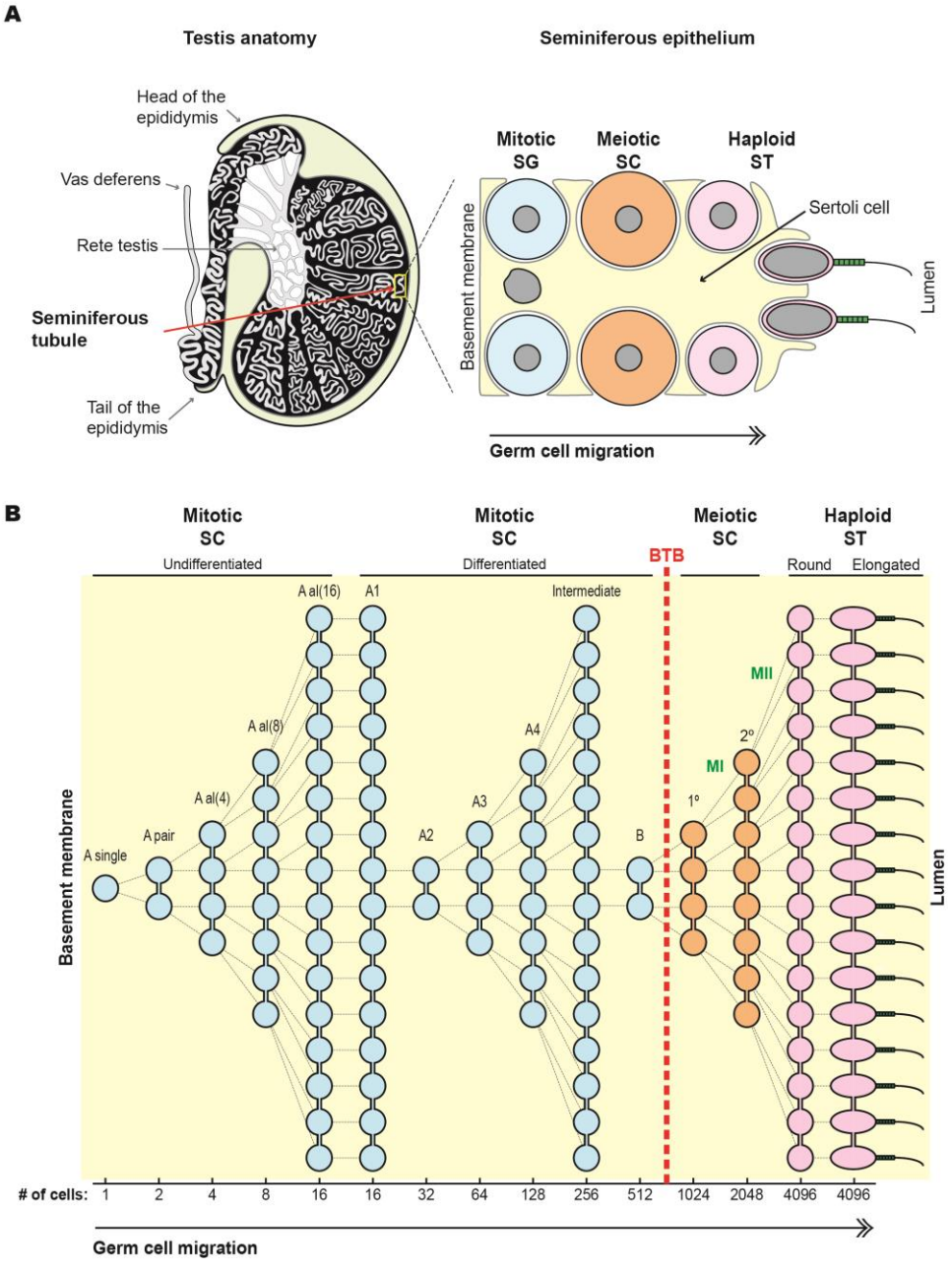
A
Testis anatomy
Seminiferous epithelium
Head of the epididymis
Vas deferens
Rete testis
Seminiferous tubule
Tail of the epididymis
Mitotic SG
Meiotic SC
Haploid ST
Sertoli cell
Basement membrane
Lumen
Germ cell migration
B
Mitotic SC
Undifferentiated
Mitotic SC
Differentiated
BTB
Meiotic SC
Haploid ST
Round
Elongated
A single
A pair
A al(4)
A al(8)
A al(16)
A1
A2
A3
A4
Intermediate
B
1°
MI
2°
MII
Basement membrane
Lumen
# of cells:
1
2
4
8
16
16
32
64
128
256
512
1024
2048
4096
4096
Germ cell migration

Figure 1.4

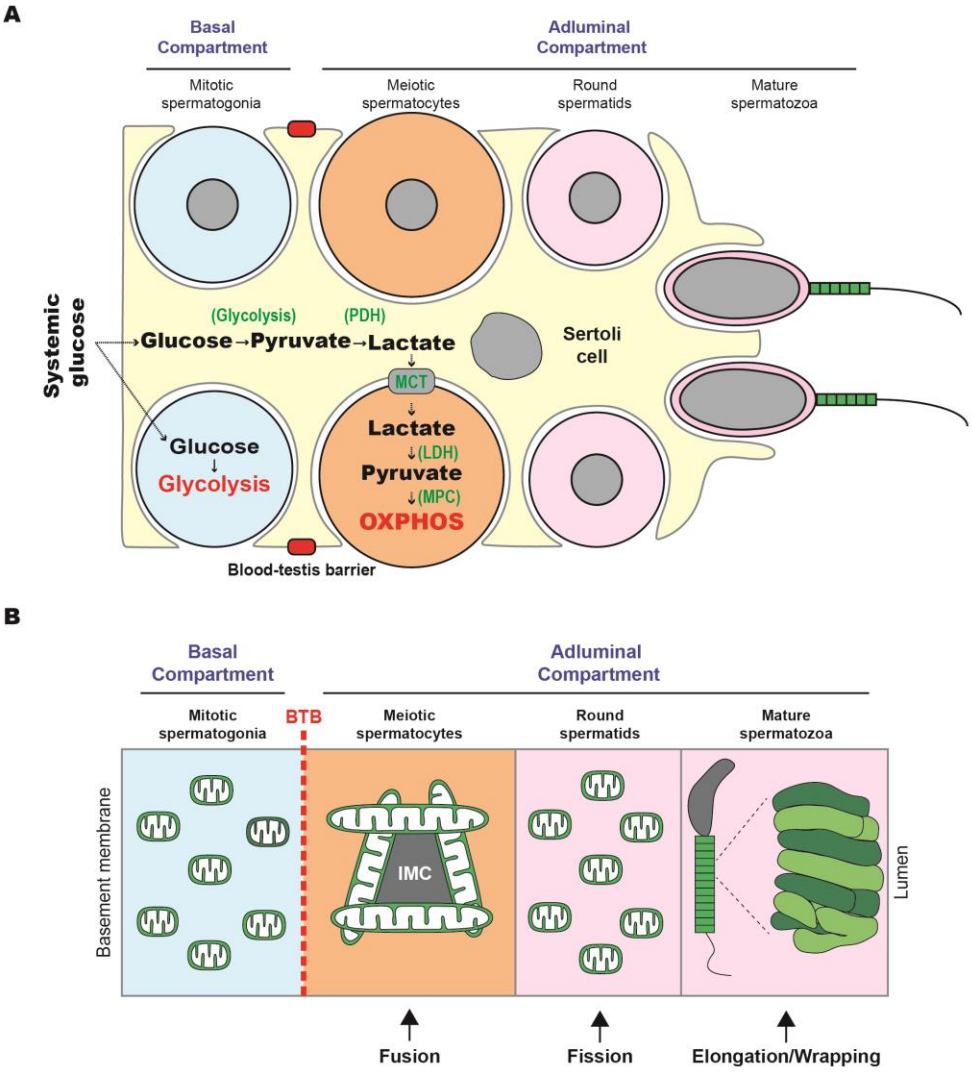
A
Basal Compartment
Adluminal Compartment
Mitotic spermatogonia
Meiotic spermatocytes
Round spermatids
Mature spermatozoa
Systemic glucose
(Glycolysis)
(PDH)
Glucose→Pyruvate→Lactate
MCT
Sertoli cell
Glucose
Glycolysis
Lactate
(LDH)
Pyruvate
(MPC)
OXPHOS
Blood-testis barrier
B
Basal Compartment
Adluminal Compartment
Mitotic spermatogonia
BTB
Meiotic spermatocytes
Round spermatids
Mature spermatozoa
Basement membrane
IMC
Lumen
Fusion
Fission
Elongation/Wrapping

Figure 1.5

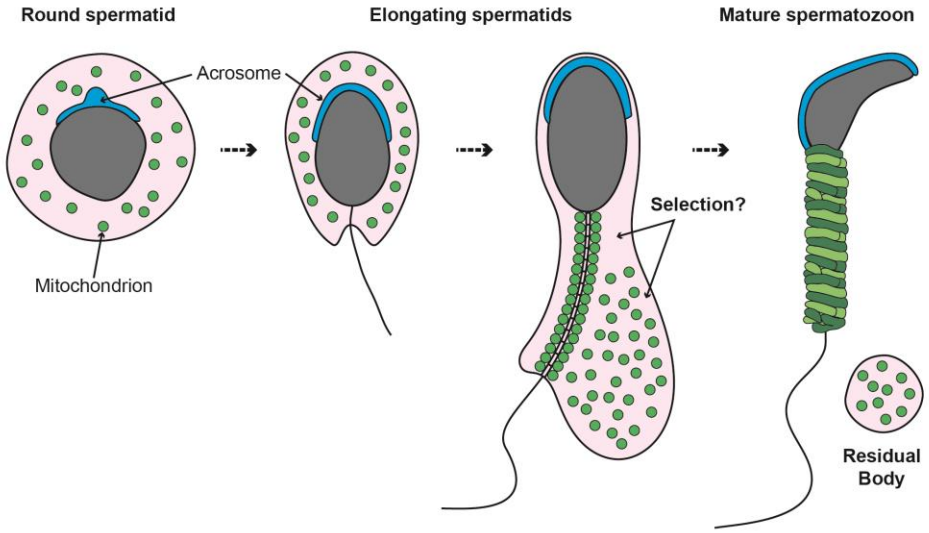
Round spermatid
Elongating spermatids
Mature spermatozoon
Acrosome
Mitochondrion
Selection?
Residual Body

References

Aloisio, G.M., Nakada, Y., Saatcioglu, H.D., Pena, C.G., Baker, M.D., Tarnawa, E.D., Mukherjee, J., Manjunath, H., Bugde, A., Sengupta, A.L., Amatruda, J.F., Cuevas, I., Hamra, F.K., Castrillon, D.H., 2014. PAX7 expression defines germline stem cells in the adult testis. *The Journal of Clinical Investigation* 124, 3929–44. https://doi.org/10.1172/jci75943

Bae, J.-W., Kim, S.-H., Kim, D.-H., Ha, J.J., Yi, J.K., Hwang, S., Ryu, B.-Y., Pang, M.-G., Kwon, W.-S., 2019. Ras-related proteins (Rab) are key proteins related to male fertility following a unique activation mechanism. *Reproductive Biology* 19, 356–362. https://doi.org/10.1016/j.repbio.2019.10.001

Bajpai, M., Gupta, G., Setty, B.S., 1998. Changes in carbohydrate metabolism of testicular germ cells during meiosis in the rat. *European Journal of Endocrinology* 138, 322–7.

Baklouti-Gargouri, S., Ghorbel, M., Ben Mahmoud, A., Mkaouar-Rebai, E., Cherif, M., Chakroun, N., Sellami, A., Fakhfakh, F., Ammar-Keskes, L., 2014. Identification of a novel m.9588G > a missense mutation in the mitochondrial COIII gene in asthenozoospermic Tunisian infertile men. *Journal of Assisted Reproduction and Genetics* 31, 595–600. https://doi.org/10.1007/s10815-014-0187-2

Bao, J., Bedford, M.T., 2016. Epigenetic regulation of the histone-to-protamine transition during spermiogenesis. *Reproduction* 151, R55–R70. https://doi.org/10.1530/REP-15-0562

Berruti, G., Paiardi, C., 2011. Acrosome biogenesis. *Spermatogenesis* 1, 95–98. https://doi.org/10.4161/spmg.1.2.16820

Bose, R., Manku, G., Culty, M., Wing, S.S., 2014. Ubiquitin–Proteasome System in Spermatogenesis, in: Sutovsky, P. (Ed.), Posttranslational Protein Modifications in the Reproductive System, *Advances in Experimental Medicine and Biology*. Springer, New York, NY, pp. 181–213. https://doi.org/10.1007/978-1-4939-0817-2_9

Boussouar, F., Benahmed, M., 2004. Lactate and energy metabolism in male germ cells. *Trends Endocrinol Metab* 15, 345–50. https://doi.org/10.1016/j.tem.2004.07.003

Braun, R.E., Behringer, R.R., Peschon, J.J., Brinster, R.L., Palmiter, R.D., 1989. Genetically haploid spermatids are phenotypically diploid. *Nature* 337, 373–376. https://doi.org/10.1038/337373a0

Brower, J.V., Lim, C.H., Jorgensen, M., Oh, S.P., Terada, N., 2009. Adenine nucleotide translocase 4 deficiency leads to early meiotic arrest of murine male germ cells.

Reproduction (Cambridge, England) 138, 463–70. https://doi.org/10.1530/REP-09-0201

Brower, J.V., Rodic, N., Seki, T., Jorgensen, M., Fliess, N., Yachnis, A.T., McCarrey, J.R., Oh, S.P., Terada, N., 2007. Evolutionarily conserved mammalian adenine nucleotide translocase 4 is essential for spermatogenesis. *J. Biol. Chem.* 282, 29658–29666. https://doi.org/10.1074/jbc.M704386200

Burman, J.L., Pickles, S., Wang, C., Sekine, S., Vargas, J.N.S., Zhang, Z., Youle, A.M., Nezich, C.L., Wu, X., Hammer, J.A., Youle, R.J., 2017. Mitochondrial fission facilitates the selective mitophagy of protein aggregates. *J. Cell Biol.* 216, 3231–3247. https://doi.org/10.1083/jcb.201612106

Carra, E., Sangiorgi, D., Gattuccio, F., Rinaldi, A.M., 2004. Male infertility and mitochondrial DNA. *Biochemical and Biophysical Research Communications* 322, 333–9. https://doi.org/10.1016/j.bbrc.2004.07.112

Chan, D.C., 2020. Mitochondrial dynamics and its involvement in disease. *Annual Review of Pathology: Mechanisms of Disease 15*, null. https://doi.org/10.1146/annurev-pathmechdis-012419-032711

Chan, D.C., 2012. Fusion and fission: interlinked processes critical for mitochondrial health. *Annual Review of Genetics* 46, 265–87. https://doi.org/10.1146/annurev-genet-110410-132529

Chan, N.C., Chan, D.C., 2011. Parkin uses the UPS to ship off dysfunctional mitochondria. *Autophagy* 7, 771–772. https://doi.org/10.4161/auto.7.7.15453

Chan, N.C., Salazar, A.M., Pham, A.H., Sweredoski, M.J., Kolawa, N.J., Graham, R.L.J., Hess, S., Chan, D.C., 2011. Broad activation of the ubiquitin–proteasome system by Parkin is critical for mitophagy. *Hum Mol Genet* 20, 1726–1737. https://doi.org/10.1093/hmg/ddr048

Chen, H., Detmer, S.A., Ewald, A.J., Griffin, E.E., Fraser, S.E., Chan, D.C., 2003. Mitofusins Mfn1 and Mfn2 coordinately regulate mitochondrial fusion and are essential for embryonic development. *The Journal of Cell Biology* 160, 189–200. https://doi.org/10.1083/jcb.200211046

Chen, H., McCaffery, J.M., Chan, D.C., 2007. Mitochondrial fusion protects against neurodegeneration in the cerebellum. *Cell* 130, 548–62. https://doi.org/10.1016/j.cell.2007.06.026

Chen, H., Ren, S., Clish, C., Jain, M., Mootha, V., McCaffery, J.M., Chan, D.C., 2015. Titration of mitochondrial fusion rescues Mff-deficient cardiomyopathy *J Cell Biol* 211, 795–805. https://doi.org/10.1083/jcb.201507035

Chen, H., Vermulst, M., Wang, Y.E., Chomyn, A., Prolla, T.A., McCaffery, J.M., Chan, D.C., 2010. Mitochondrial fusion is required for mtDNA stability in skeletal muscle and tolerance of mtDNA mutations. *Cell* 141, 280–9. https://doi.org/10.1016/j.cell.2010.02.026

Chen, Y., Liu, Y., Dorn, G.W., 2011. Mitochondrial fusion is essential for organelle function and cardiac homeostasis. *Circulation Research* 109, 1327–1331.

Clark, I.E., Dodson, M.W., Jiang, C., Cao, J.H., Huh, J.R., Seol, J.H., Yoo, S.J., Hay, B.A., Guo, M., 2006. Drosophila pink1 is required for mitochondrial function and interacts genetically with parkin. *Nature* 441, 1162.

Cohen, P.E., Pollack, S.E., Pollard, J.W., 2006. Genetic Analysis of Chromosome Pairing, Recombination, and Cell Cycle Control during First Meiotic Prophase in Mammals. *Endocr Rev* 27, 398–426. https://doi.org/10.1210/er.2005-0017

De Martino, C., Floridi, A., Marcante, M.L., Malorni, W., Scorza Barcellona, P., Bellocci, M., Silvestrini, B., 1979. Morphological, histochemical and biochemical studies on germ cell mitochondria of normal rats. *Cell and Tissue Research* 196, 1–22.

De Rooij, D.G., 2017. The nature and dynamics of spermatogonial stem cells. *Development* (Cambridge, England) 144, 3022–3030.

Demain, L.A., Conway, G.S., Newman, W.G., 2017. Genetics of mitochondrial dysfunction and infertility. *Clinical Genetics* 91, 199–207. https://doi.org/10.1111/cge.12896

Demarco, R.S., Eikenes, Å.H., Haglund, K., Jones, D.L., 2014. Investigating spermatogenesis in Drosophila melanogaster. *Methods, Drosophila Developmental Biology Methods* 68, 218–227. https://doi.org/10.1016/j.ymeth.2014.04.020

Demarco, R.S., Jones, D.L., 2019. Mitochondrial fission regulates germ cell differentiation by suppressing ROS-mediated activation of Epidermal Growth Factor Signaling in the Drosophila larval testis. *Sci Rep* 9, 1–10. https://doi.org/10.1038/s41598-019-55728-0

Demarco, R.S., Uyemura, B.S., D'Alterio, C., Jones, D.L., 2019. Mitochondrial fusion regulates lipid homeostasis and stem cell maintenance in the Drosophila testis. *Nature Cell Biology* 21, 710.

Dietert, S.E., 1966. Fine structure of the formation and fate of the residual bodies of mouse spermatozoa with evidence for the participation of lysosomes. *Journal of Morphology* 120, 317–346. https://doi.org/10.1002/jmor.1051200402

du Plessis, S.S., Agarwal, A., Mohanty, G., Van der Linde, M., 2015. Oxidative phosphorylation versus glycolysis: what fuel do spermatozoa use? *Asian Journal of Andrology* 17, 230.

Fang, F., Ni, K., Shang, J., Zhang, X., Xiong, C., Meng, T., 2018. Expression of mitofusin 2 in human sperm and its relationship to sperm motility and cryoprotective potentials. *Experimental Biology and Medicine* (Maywood, N.J.) 1535370218790919. https://doi.org/10.1177/1535370218790919

Favaro, G., Romanello, V., Varanita, T., Desbats, M.A., Morbidoni, V., Tezze, C., Albiero, M., Canato, M., Gherardi, G., Stefani, D.D., Mammucari, C., Blaauw, B., Boncompagni, S., Protasi, F., Reggiani, C., Scorrano, L., Salviati, L., Sandri, M., 2019. DRP1-mediated mitochondrial shape controls calcium homeostasis and muscle mass. *Nat Commun* 10, 1–17. https://doi.org/10.1038/s41467-019-10226-9

Folgero, T., Bertheussen, K., Lindal, S., Torbergsen, T., Oian, P., 1993. Mitochondrial disease and reduced sperm motility. *Human reproduction* (Oxford, England) 8, 1863–8.

Fonseca, T.B., Sánchez-Guerrero, Á., Milosevic, I., Raimundo, N., 2019. Mitochondrial fission requires DRP1 but not dynamins. *Nature* 570, E34–E42. https://doi.org/10.1038/s41586-019-1296-y

Friedman, J.R., Lackner, L.L., West, M., DiBenedetto, J.R., Nunnari, J., Voeltz, G.K., 2011. ER Tubules Mark Sites of Mitochondrial Division. *Science* 334, 358–362. https://doi.org/10.1126/science.1207385

Fuller, M.T., 1993. Spermatogenesis, in: The Development of Drosophila Melanogater. Cold Spring Harbor, New York, pp. 71–147.

Goldberg, E., Eddy, E.M., Duan, C., Odet, F., 2010. LDHC: the ultimate testis-specific gene. *J. Androl.* 31, 86–94. https://doi.org/10.2164/jandrol.109.008367

Greenbaum, M.P., Iwamori, T., Buchold, G.M., Matzuk, M.M., 2011. Germ Cell Intercellular Bridges. *Cold Spring Harb Perspect Biol 3*. https://doi.org/10.1101/cshperspect.a005850

Griswold, M.D., 2016. Spermatogenesis: The Commitment to Meiosis. *Physiological reviews* 96, 1–17. https://doi.org/10.1152/physrev.00013.2015

Griswold, M.D., 1998. The central role of Sertoli cells in spermatogenesis. *Seminars in Cell & Developmental Biology* 9, 411–416. https://doi.org/10.1006/scdb.1998.0203

Grootegoed, J.A., Jansen, R., Van der Molen, H.J., 1984. The role of glucose, pyruvate and lactate in ATP production by rat spermatocytes and spermatids. *Biochimica et biophysica acta* 767, 248–56.

Hackenbrock, C.R., 1966. Ultrustructural bases for metabolically linked mechanical activity in mitochondria I. Reversible Ultrastructural Changes with Change in Metabolic Steady State in Isolated Liver Mitochondria. *J Cell Biol* 30, 269–297. https://doi.org/10.1083/jcb.30.2.269

Hales, K.G., Fuller, M.T., 1997. Developmentally regulated mitochondrial fusion mediated by a conserved, novel, predicted GTPase. *Cell* 90, 121–129.

Handel, M.A., Schimenti, J.C., 2010. Genetics of mammalian meiosis: regulation, dynamics and impact on fertility. *Nature Reviews Genetics* 11, 124–136.

Hara, K., Nakagawa, T., Enomoto, H., Suzuki, M., Yamamoto, M., Simons, B.D., Yoshida, S., 2014. Mouse spermatogenic stem cells continually interconvert between equipotent singly isolated and syncytial states. *Cell stem cell* 14, 658–672.

Hermo, L., Pelletier, R.-M., Cyr, D.G., Smith, C.E., 2010a. Surfing the wave, cycle, life history, and genes/proteins expressed by testicular germ cells. Part 1: Background to spermatogenesis, spermatogonia, and spermatocytes. *Microscopy Research and Technique* 73, 241–278. https://doi.org/10.1002/jemt.20783

Hermo, L., Pelletier, R.-M., Cyr, D.G., Smith, C.E., 2010b. Surfing the wave, cycle, life history, and genes/proteins expressed by testicular germ cells. Part 2: changes in spermatid organelles associated with development of spermatozoa. *Microsc. Res. Tech.* 73, 279–319. https://doi.org/10.1002/jemt.20787

Hermo, L., Pelletier, R.-M., Cyr, D.G., Smith, C.E., 2010c. Surfing the wave, cycle, life history, and genes/proteins expressed by testicular germ cells. Part 4: intercellular bridges, mitochondria, nuclear envelope, apoptosis, ubiquitination, membrane/voltage-gated channels, methylation/acetylation, and transcription factors. *Microsc. Res. Tech.* 73, 364–408. https://doi.org/10.1002/jemt.20785

Ho, H.-C., Wey, S., 2007. Three dimensional rendering of the mitochondrial sheath morphogenesis during mouse spermiogenesis. *Microscopy research and technique* 70, 719–723.

Hofmann, M.-C., 2008. Gdnf signaling pathways within the mammalian spermatogonial stem cell niche. Molecular and Cellular Endocrinology, Special Issue: Stem cells and progenitors in organ maintenance, regeneration and replacement: the role of hormones and growth factors in health and disease 288, 95–103. https://doi.org/10.1016/j.mce.2008.04.012

Hoppins, S., 2014. The regulation of mitochondrial dynamics. Current Opinion in Cell Biology, *Cell organelles* 29, 46–52. https://doi.org/10.1016/j.ceb.2014.03.005

Ikeda Yoshiyuki, Shirakabe Akihiro, Maejima Yasuhiro, Zhai Peiyong, Sciarretta Sebastiano, Toli Jessica, Nomura Masatoshi, Mihara Katsuyoshi, Egashira Kensuke, Ohishi Mitsuru, Abdellatif Maha, Sadoshima Junichi, 2015. Endogenous Drp1 Mediates Mitochondrial Autophagy and Protects the Heart Against Energy Stress. *Circulation Research* 116, 264–278. https://doi.org/10.1161/CIRCRESAHA.116.303356

Ishihara, N., Nomura, M., Jofuku, A., Kato, H., Suzuki, S.O., Masuda, K., Otera, H., Nakanishi, Y., Nonaka, I., Goto, Y.-I., Taguchi, N., Morinaga, H., Maeda, M., Takayanagi, R., Yokota, S., Mihara, K., 2009. Mitochondrial fission factor Drp1 is essential for embryonic development and synapse formation in mice. *Nat. Cell Biol.* 11, 958–966. https://doi.org/10.1038/ncb1907

Jakobs, S., Martini, N., Schauss, A.C., Egner, A., Westermann, B., Hell, S.W., 2003. Spatial and temporal dynamics of budding yeast mitochondria lacking the division component Fis1p. *J. Cell. Sci.* 116, 2005–2014. https://doi.org/10.1242/jcs.00423

Jiang, M., Kauppila, T.E.S., Motori, E., Li, X., Atanassov, I., Folz-Donahue, K., Bonekamp, N.A., Albarran-Gutierrez, S., Stewart, J.B., Larsson, N.G., 2017. Increased Total mtDNA Copy Number Cures Male Infertility Despite Unaltered mtDNA Mutation Load. *Cell metabolism* 26, 429-436.e4. https://doi.org/10.1016/j.cmet.2017.07.003

Kageyama, Y., Hoshijima, M., Seo, K., Bedja, D., Sysa-Shah, P., Andrabi, S.A., Chen, W., Höke, A., Dawson, V.L., Dawson, T.M., Gabrielson, K., Kass, D.A., Iijima, M., Sesaki, H., 2014. Parkin-independent mitophagy requires Drp1 and maintains the integrity of mammalian heart and brain. *The EMBO Journal* 33, 2798–2813. https://doi.org/10.15252/embj.201488658

Kamerkar, S.C., Kraus, F., Sharpe, A.J., Pucadyil, T.J., Ryan, M.T., 2018. Dynamin-related protein 1 has membrane constricting and severing abilities sufficient for mitochondrial and peroxisomal fission. *Nat Commun* 9, 1–15. https://doi.org/10.1038/s41467-018-07543-w

Kao, S., Chao, H.T., Wei, Y.H., 1995. Mitochondrial deoxyribonucleic acid 4977-bp deletion is associated with diminished fertility and motility of human sperm. *Biology of reproduction* 52, 729–36.

Khawar, M.B., Gao, H., Li, W., 2019. Mechanism of Acrosome Biogenesis in Mammals. *Front. Cell Dev. Biol. 7*. https://doi.org/10.3389/fcell.2019.00195

Kimble, J.E., White, J.G., 1981. On the control of germ cell development in Caenorhabditis elegans. *Developmental Biology* 81, 208–219. https://doi.org/10.1016/0012-1606(81)90284-0

Komatsu, M., Waguri, S., Ueno, T., Iwata, J., Murata, S., Tanida, I., Ezaki, J., Mizushima, N., Ohsumi, Y., Uchiyama, Y., Kominami, E., Tanaka, K., Chiba, T., 2005. Impairment of starvation-induced and constitutive autophagy in Atg7-deficient mice. *J Cell Biol* 169, 425–434. https://doi.org/10.1083/jcb.200412022

Korobova, F., Ramabhadran, V., Higgs, H.N., 2013. An actin-dependent step in mitochondrial fission mediated by the ER-associated formin INF2. *Science* 339, 464–467.

Kujoth, G.C., Hiona, A., Pugh, T.D., Someya, S., Panzer, K., Wohlgemuth, S.E., Hofer, T., Seo, A.Y., Sullivan, R., Jobling, W.A., Morrow, J.D., Van Remmen, H., Sedivy, J.M., Yamasoba, T., Tanokura, M., Weindruch, R., Leeuwenburgh, C., Prolla, T.A., 2005. Mitochondrial DNA mutations, oxidative stress, and apoptosis in mammalian aging. *Science* (New York, N.Y.) 309, 481–4. https://doi.org/10.1126/science.1112125

Kuma, A., Komatsu, M., Mizushima, N., 2017. Autophagy-monitoring and autophagy-deficient mice. *Autophagy* 13, 1619–1628. https://doi.org/10.1080/15548627.2017.1343770

Lee, J.E., Westrate, L.M., Wu, H., Page, C., Voeltz, G.K., 2016. Multiple dynamin family members collaborate to drive mitochondrial division. *Nature* 540, 139–143. https://doi.org/10.1038/nature20555

Lestienne, P., Reynier, P., Chretien, M.F., Penisson-Besnier, I., Malthiery, Y., Rohmer, V., 1997. Oligoasthenospermia associated with multiple mitochondrial DNA rearrangements. *Molecular human reproduction 3,* 811–4.

Lin, Y.-H., Lin, Y.-M., Kuo, Y.-C., Wang, Y.-Y., Kuo, P.-L., 2011. Identification and characterization of a novel Rab GTPase-activating protein in spermatids. *Int. J. Androl.* 34, e358-367. https://doi.org/10.1111/j.1365-2605.2010.01126.x

Lord, T., Nixon, B., 2020. Metabolic Changes Accompanying Spermatogonial Stem Cell Differentiation. *Developmental Cell* 52, 399–411. https://doi.org/10.1016/j.devcel.2020.01.014

Lord, T., Oatley, J.M., 2017. A revised Asingle model to explain stem cell dynamics in the mouse male germline. *Reproduction* (Cambridge, England) 154, R55-r64. https://doi.org/10.1530/rep-17-0034

Losón, O.C., Song, Z., Chen, H., Chan, D.C., 2013. Fis1, Mff, MiD49, and MiD51 mediate Drp1 recruitment in mitochondrial fission. *Mol. Biol. Cell* 24, 659–667. https://doi.org/10.1091/mbc.E12-10-0721

Luoma, P., Melberg, A., Rinne, J.O., Kaukonen, J.A., Nupponen, N.N., Chalmers, R.M., Oldfors, A., Rautakorpi, I., Peltonen, L., Majamaa, K., Somer, H., Suomalainen, A., 2004. Parkinsonism, premature menopause, and mitochondrial DNA polymerase γ mutations: clinical and molecular genetic study. *The Lancet* 364, 875–882. https://doi.org/10.1016/S0140-6736(04)16983-3

Mannella, C. A., 2006. The relevance of mitochondrial membrane topology to mitochondrial function. *Biochimica et biophysica acta* 1762, 140–7. https://doi.org/10.1016/j.bbadis.2005.07.001

Mannella, Carmen A., 2006. Structure and dynamics of the mitochondrial inner membrane cristae. Biochimica et Biophysica Acta (BBA) - Molecular Cell Research, M*itochondrial Dynamics in Cell Life and Death* 1763, 542–548. https://doi.org/10.1016/j.bbamcr.2006.04.006

McWilliams, T.G., Prescott, A.R., Allen, G.F.G., Tamjar, J., Munson, M.J., Thomson, C., Muqit, M.M.K., Ganley, I.G., 2016. mito-QC illuminates mitophagy and mitochondrial architecture in vivo. *J. Cell Biol.* 214, 333–345. https://doi.org/10.1083/jcb.201603039

Meinhardt, A., Wilhelm, B., Seitz, J., 1999. Mini symposium. New aspects of spermatogenesis. Expression of mitochondrial marker proteins during spermatogenesis. *Human reproduction update* 5, 108–119. https://doi.org/10.1093/humupd/5.2.108

Mishra, P., Chan, D.C., 2016. Metabolic regulation of mitochondrial dynamics. *J. Cell Biol.* 212, 379–387. https://doi.org/10.1083/jcb.201511036

Mishra, P., Varuzhanyan, G., Pham, A.H., Chan, D.C., 2015. Mitochondrial Dynamics is a Distinguishing Feature of Skeletal Muscle Fiber Types and Regulates Organellar Compartmentalization. *Cell Metab.* 22, 1033–1044. https://doi.org/10.1016/j.cmet.2015.09.027

Mizushima, N., 2007. Autophagy: process and function. *Genes Dev.* 21, 2861–2873. https://doi.org/10.1101/gad.1599207

Mizushima, N., Sugita, H., Yoshimori, T., Ohsumi, Y., 1998. A New Protein Conjugation System in Human the counterpart of the yeast Apg12p conjugation system essential for autophagy. *J. Biol. Chem.* 273, 33889–33892. https://doi.org/10.1074/jbc.273.51.33889

Mozdy, A.D., McCaffery, J.M., Shaw, J.M., 2000. Dnm1p GTPase-mediated mitochondrial fission is a multi-step process requiring the novel integral membrane component Fis1p. *J. Cell Biol.* 151, 367–380. https://doi.org/10.1083/jcb.151.2.367

Nagashima, S., Tábara, L.-C., Tilokani, L., Paupe, V., Anand, H., Pogson, J.H., Zunino, R., McBride, H.M., Prudent, J., 2020. Golgi-derived PI(4)P-containing vesicles drive late steps of mitochondrial division. *Science* 367, 1366–1371. https://doi.org/10.1126/science.aax6089

Nakada, K., Sato, A., Yoshida, K., Morita, T., Tanaka, H., Inoue, S., Yonekawa, H., Hayashi, J., 2006. Mitochondria-related male infertility. *Proceedings of the National Academy of Sciences of the United States of America* 103, 15148–53. https://doi.org/10.1073/pnas.0604641103

Nakamura, M., Fujiwara, A., Yasumasu, I., Okinaga, S., Arai, K., 1982. Regulation of glucose metabolism by adenine nucleotides in round spermatids from rat testes. *The Journal of biological chemistry* 257, 13945–50.

Nakamura, M., Okinaga, S., Arai, K., 1984. Metabolism of pachytene primary spermatocytes from rat testes: pyruvate maintenance of adenosine triphosphate level. *Biology of reproduction* 30, 1187–97.

Nakamura, Y., Asano, A., Hosaka, Y., Takeuchi, T., Iwanaga, T., Yamano, Y., 2015. Expression and intracellular localization of TBC1D9, a Rab GTPase-accelerating protein, in mouse testes. *Exp. Anim.* 64, 415–424. https://doi.org/10.1538/expanim.15-0016

Narendra, D.P., Jin, S.M., Tanaka, A., Suen, D.-F., Gautier, C.A., Shen, J., Cookson, M.R., Youle, R.J., 2010. PINK1 is selectively stabilized on impaired mitochondria to activate Parkin. *PLoS Biol.* 8, e1000298. https://doi.org/10.1371/journal.pbio.1000298

Naughton, C.K., Jain, S., Strickland, A.M., Gupta, A., Milbrandt, J., 2006. Glial Cell-Line Derived Neurotrophic Factor-Mediated RET Signaling Regulates Spermatogonial Stem Cell Fate. *Biol Reprod* 74, 314–321. https://doi.org/10.1095/biolreprod.105.047365

Oatley, J.M., Brinster, R.L., 2012. The germline stem cell niche unit in mammalian testes. *Physiol Rev* 92, 577–595. https://doi.org/10.1152/physrev.00025.2011

Olesen, C., Larsen, N.J., Byskov, A.G., Harboe, T.L., Tommerup, N., 2001. Human FATE is a novel X-linked gene expressed in fetal and adult testis. *Molecular and Cellular Endocrinology* 184, 25–32. https://doi.org/10.1016/S0303-7207(01)00666-9

Olesen, C., Silber, J., Eiberg, H., Ernst, E., Petersen, K., Lindenberg, S., Tommerup, N., 2003. Mutational analysis of the human FATE gene in 144 infertile men. Human genetics 113, 195–201.

Onoue, K., Jofuku, A., Ban-Ishihara, R., Ishihara, T., Maeda, M., Koshiba, T., Itoh, T., Fukuda, M., Otera, H., Oka, T., Takano, H., Mizushima, N., Mihara, K., Ishihara, N., 2013. Fis1 acts as a mitochondrial recruitment factor for TBC1D15 that is involved in regulation of mitochondrial morphology. *J. Cell. Sci.* 126, 176–185. https://doi.org/10.1242/jcs.111211

Otera, H., Wang, C., Cleland, M.M., Setoguchi, K., Yokota, S., Youle, R.J., Mihara, K., 2010. Mff is an essential factor for mitochondrial recruitment of Drp1 during mitochondrial fission in mammalian cellsMff is essential for mitochondrial recruitment of Drp1. *J Cell Biol* 191, 1141–1158. https://doi.org/10.1083/jcb.201007152

Papanicolaou Kyriakos N., Kikuchi Ryosuke, Ngoh Gladys A., Coughlan Kimberly A., Dominguez Isabel, Stanley William C., Walsh Kenneth, 2012. Mitofusins 1 and 2 Are Essential for Postnatal Metabolic Remodeling in Heart. *Circulation Research* 111, 1012–1026. https://doi.org/10.1161/CIRCRESAHA.112.274142

Pickles, S., Vigié, P., Youle, R.J., 2018. Mitophagy and Quality Control Mechanisms in Mitochondrial Maintenance. *Current Biology* 28, R170–R185. https://doi.org/10.1016/j.cub.2018.01.004

Rakovic, A., Ziegler, J., Mårtensson, C.U., Prasuhn, J., Shurkewitsch, K., König, P., Paulson, H.L., Klein, C., 2019. PINK1-dependent mitophagy is driven by the UPS and can occur independently of LC3 conversion. *Cell Death Differ* 26, 1428–1441. https://doi.org/10.1038/s41418-018-0219-z

Rato, L., Alves, M.G., Socorro, S., Duarte, A.I., Cavaco, J.E., Oliveira, P.F., 2012. Metabolic regulation is important for spermatogenesis. *Nature reviews*. Urology 9, 330–8. https://doi.org/10.1038/nrurol.2012.77

Ren, M., Xu, Y., Erdjument-Bromage, H., Donelian, A., Phoon, C.K., Terada, N., Strathdee, D., Neubert, T.A., Schlame, M., 2019. Extramitochondrial cardiolipin suggests a novel function of mitochondria in spermatogenesis. *The Journal of cell biology* 218, 1491–1502.

Rojansky, R., Cha, M.-Y., Chan, D.C., 2016. Elimination of paternal mitochondria in mouse embryos occurs through autophagic degradation dependent on PARKIN and MUL1. *eLife* 5, e17896.

Rovio, A.T., Marchington, D.R., Donat, S., Schuppe, H.-C., Abel, J., Fritsche, E., Elliott, D.J., Laippala, P., Ahola, A.L., McNay, D., Harrison, R.F., Hughes, B., Barrett, T.,

Bailey, D.M.D., Mehmet, D., Jequier, A.M., Hargreave, T.B., Kao, S.-H., Cummins, J.M., Barton, D.E., Cooke, H.J., Wei, Y.-H., Wichmann, L., Poulton, J., Jacobs, H.T., 2001. Mutations at the mitochondrial DNA polymerase (POLG) locus associated with male infertility. *Nature Genetics* 29, 261–262. https://doi.org/10.1038/ng759

Seitz, J., Möbius, J., Bergmann, M., Meinhardt, A., 1995. Mitochondrial differentiation during meiosis of male germ cells. *Int. J. Androl.* 18 Suppl 2, 7–11.

Sekine, S., Youle, R.J., 2018. PINK1 import regulation; a fine system to convey mitochondrial stress to the cytosol. *BMC Biology* 16, 2. https://doi.org/10.1186/s12915-017-0470-7

Serohijos, A.W.R., Chen, Y., Ding, F., Elston, T.C., Dokholyan, N.V., 2006. A structural model reveals energy transduction in dynein. *PNAS* 103, 18540–18545. https://doi.org/10.1073/pnas.0602867103

Shang, Y., Wang, H., Jia, P., Zhao, H., Liu, C., Liu, W., Song, Z., Xu, Z., Yang, L., Wang, Y., 2016. Autophagy regulates spermatid differentiation via degradation of PDLIM1. *Autophagy* 12, 1575–1592.

Shen, Q., Yamano, K., Head, B.P., Kawajiri, S., Cheung, J.T.M., Wang, C., Cho, J.-H., Hattori, N., Youle, R.J., van der Bliek, A.M., 2014. Mutations in Fis1 disrupt orderly disposal of defective mitochondria. *Mol. Biol. Cell* 25, 145–159. https://doi.org/10.1091/mbc.E13-09-0525

Spiropoulos, J., Turnbull, D.M., Chinnery, P.F., 2002. Can mitochondrial DNA mutations cause sperm dysfunction? *Mol Hum Reprod* 8, 719–721. https://doi.org/10.1093/molehr/8.8.719

Spradling, A., Drummond-Barbosa, D., Kai, T., 2001. Stem cells find their niche. *Nature* 414, 98–104. https://doi.org/10.1038/35102160

Stanton, P.G., 2016. Regulation of the blood-testis barrier. *Seminars in cell & developmental biology* 59, 166–173. https://doi.org/10.1016/j.semcdb.2016.06.018

Storey, B.T., 2004. Mammalian sperm metabolism: oxygen and sugar, friend and foe. *Int. J. Dev. Biol.* 52, 427–437. https://doi.org/10.1387/ijdb.072522bs

Sun, N., Yun, J., Liu, J., Malide, D., Liu, C., Rovira, I.I., Holmström, K.M., Fergusson, M.M., Yoo, Y.H., Combs, C.A., Finkel, T., 2015. Measuring In Vivo Mitophagy. *Mol. Cell* 60, 685–696. https://doi.org/10.1016/j.molcel.2015.10.009

Tan, E.H.N., Tang, B.L., 2019. Rab7a and Mitophagosome Formation. *Cells* 8. https://doi.org/10.3390/cells8030224

Tanaka, A., Cleland, M.M., Xu, S., Narendra, D.P., Suen, D.-F., Karbowski, M., Youle, R.J., 2010. Proteasome and p97 mediate mitophagy and degradation of mitofusins induced by Parkin. *J. Cell Biol.* 191, 1367–1380. https://doi.org/10.1083/jcb.201007013

Tieu, Q., Okreglak, V., Naylor, K., Nunnari, J., 2002. The WD repeat protein, Mdv1p, functions as a molecular adaptor by interacting with Dnm1p and Fis1p during mitochondrial fission. *J. Cell Biol.* 158, 445–452. https://doi.org/10.1083/jcb.200205031

Tourmente, M., Villar-Moya, P., Rial, E., Roldan, E.R.S., 2015. Differences in ATP Generation Via Glycolysis and Oxidative Phosphorylation and Relationships with Sperm Motility in Mouse Species. *J Biol Chem* 290, 20613–20626. https://doi.org/10.1074/jbc.M115.664813

Trifunovic, A., Wredenberg, A., Falkenberg, M., Spelbrink, J.N., Rovio, A.T., Bruder, C.E., Bohlooly, Y.M., Gidlof, S., Oldfors, A., Wibom, R., Tornell, J., Jacobs, H.T., Larsson, N.G., 2004. Premature ageing in mice expressing defective mitochondrial DNA polymerase. *Nature* 429, 417–23. https://doi.org/10.1038/nature02517

Tsukada, M., Ohsumi, Y., 1993. Isolation and characterization of autophagy-defective mutants of Saccharomyces cerevisiae. *FEBS Letters* 333, 169–174. https://doi.org/10.1016/0014-5793(93)80398-E

Tzagoloff, A., 1982. Mitochondrial Structure and Compartmentalization, in: Tzagoloff, A. (Ed.), Mitochondria. Springer US, Boston, MA, pp. 15–38. https://doi.org/10.1007/978-1-4613-3294-7_2

Varuzhanyan, G., Chen, H., Rojansky, R., Ladinsky, M., S., McCaffery, M., Chan, D., 2020. Mitochondrial fission is required for organization of the mitochondrial sheath in spermatids. *Biochimica et Biophysica Acta (BBA) - General Subjects* (in press).

Varuzhanyan, G., Rojansky, R., Sweredoski, M.J., Graham, R.L., Hess, S., Ladinsky, M.S., Chan, D.C., 2019. Mitochondrial fusion is required for spermatogonial differentiation and meiosis. eLife 8, p. e51601. doi: 10.7554/eLife.51601.

Wakabayashi, J., Zhang, Z., Wakabayashi, N., Tamura, Y., Fukaya, M., Kensler, T.W., Iijima, M., Sesaki, H., 2009. The dynamin-related GTPase Drp1 is required for embryonic and brain development in mice. *J. Cell Biol.* 186, 805–816. https://doi.org/10.1083/jcb.200903065

Wang, H., Wan, H., Li, X., Liu, W., Chen, Q., Wang, Y., Yang, L., Tang, H., Zhang, X., Duan, E., 2014. Atg7 is required for acrosome biogenesis during spermatogenesis in mice. *Cell research* 24, 852.

Wong, Y.C., Ysselstein, D., Krainc, D., 2018. Mitochondria-lysosome contacts regulate mitochondrial fission via RAB7 GTP hydrolysis. *Nature* 554, 382–386. https://doi.org/10.1038/nature25486

Yamano, K., Fogel, A.I., Wang, C., van der Bliek, A.M., Youle, R.J., 2014. Mitochondrial Rab GAPs govern autophagosome biogenesis during mitophagy. *eLife* 3, e01612. https://doi.org/10.7554/eLife.01612

Yamano, K., Wang, C., Sarraf, S.A., Münch, C., Kikuchi, R., Noda, N.N., Hizukuri, Y., Kanemaki, M.T., Harper, W., Tanaka, K., Matsuda, N., Youle, R.J., 2018. Endosomal Rab cycles regulate Parkin-mediated mitophagy. *eLife* 7. https://doi.org/10.7554/eLife.31326

Yamashita, S., Jin, X., Furukawa, K., Hamasaki, M., Nezu, A., Otera, H., Saigusa, T., Yoshimori, T., Sakai, Y., Mihara, K., Kanki, T., 2016. Mitochondrial division occurs concurrently with autophagosome formation but independently of Drp1 during mitophagy. *J Cell Biol* 215, 649–665. https://doi.org/10.1083/jcb.201605093

Yang, P., Ahmed, N., Wang, L., Chen, H., Waqas, Y., Liu, T., Haseeb, A., Bangulzai, N., Huang, Y., Chen, Q., 2017. In vivo autophagy and biogenesis of autophagosomes within male haploid cells during spermiogenesis. *Oncotarget* 8, 56791–56801. https://doi.org/10.18632/oncotarget.18221

Youle, R.J., Narendra, D.P., 2011. Mechanisms of mitophagy. Nat Rev Mol Cell Biol 12, 9–14. https://doi.org/10.1038/nrm3028

Zhang, J., Wang, Q., Wang, M., Jiang, M., Wang, Y., Sun, Y., Wang, J., Xie, T., Tang, C., Tang, N., Song, H., Cui, D., Chao, R., Ding, S., Ni, B., Chen, X., Wang, Y., 2016. GASZ and mitofusin-mediated mitochondrial functions are crucial for spermatogenesis. *EMBO reports* 17, 220–34. https://doi.org/10.15252/embr.201540846

Zhang, X.-M., Walsh, B., Mitchell, C.A., Rowe, T., 2005. TBC domain family, member 15 is a novel mammalian Rab GTPase-activating protein with substrate preference for Rab7. *Biochemical and Biophysical Research Communications* 335, 154–161. https://doi.org/10.1016/j.bbrc.2005.07.070

Zhang, Z., Sliter, D.A., Bleck, C.K.E., Ding, S., 2019. Fis1 deficiencies differentially affect mitochondrial quality in skeletal muscle. *Mitochondrion* 49, 217–226. https://doi.org/10.1016/j.mito.2019.09.005

CHAPTER 2

Mitochondrial fusion is required for spermatogonial differentiation and meiosis

Grigor Varuzhanyan[1], Rebecca Rojansky[1], Michael J. Sweredoski[2], Robert L.J. Graham[2,3], Sonja Hess[2,4], Mark S. Ladinsky[1], and David C. Chan[1*]

[1]Division of Biology and Biological Engineering, California Institute of Technology, Pasadena, CA 91125, USA.

[2]Proteome Exploration Laboratory of the Beckman Institute, California Institute of Technology, Pasadena, CA 91125, USA.

[3]Current address: School of Biological Sciences, Queens University Belfast, Medical Biology Centre, Belfast BT9 7BL, UK.

[4]Current address: MedImmune, Antibody Discovery and Protein Engineering, Gaithersburg, MD 20878, USA.

Abstract

Differentiating cells tailor their metabolism to fulfill their specialized functions. We examined whether mitochondrial fusion is important for metabolic tailoring during spermatogenesis. Acutely after depletion of mitofusins *Mfn1* and *Mfn2*, spermatogenesis arrests due to failure to accomplish a metabolic shift during meiosis. This metabolic shift includes increased mitochondrial content, mitochondrial elongation, and upregulation of oxidative phosphorylation (OXPHOS). With long-term mitofusin loss, all differentiating germ cell types are depleted, but proliferation of stem-like undifferentiated spermatogonia remains unaffected. Thus, compared with undifferentiated spermatogonia, differentiating spermatogonia and meiotic spermatocytes have cell physiologies that require high levels of mitochondrial fusion. Proteomics in fibroblasts reveals that mitofusin-null cells downregulate respiratory chain complexes and mitochondrial ribosomal subunits. Similarly, mitofusin depletion in immortalized spermatocytes or germ cells *in vivo* results in reduced OXPHOS subunits and activity. We reveal that by promoting OXPHOS, mitofusins enable spermatogonial differentiation and a metabolic shift during meiosis.

Introduction

The first mitochondrial fusion gene, *fuzzy onions (fzo)*, was discovered in 1997 in a *Drosophila melanogaster* mutant exhibiting male sterility (Hales & Fuller, 1997). During early spermatid development in flies, mitochondria aggregate and fuse to become two giant organelles that wrap around each other to form the Nebenkern (Fuller, 1993). Mutations in *fzo* abolish mitochondrial fusion in spermatids, resulting in a morphologically aberrant Nebenkern and sterility. The reason for this stage-specific fusion event and how mitochondrial fusion promotes male fertility in *Drosophila* are unknown.

Fzo is the founding member of an evolutionarily conserved family of mitochondrial fusion proteins known as the mitofusins (Mfns). In humans, there are two homologs known as *MFN1* and *MFN2* (Santel & Fuller, 2001). Fusion acts as a major quality control mechanism for mitochondria by enabling mixing of matrix components and promoting their homogenization (Chan, 2012). In the absence of fusion, mitochondria diverge, become functionally heterogenous, and mitochondrial DNA (mtDNA) and oxidative phosphorylation (OXPHOS) are diminished (Chen, Chomyn, & Chan, 2005; Chen et al., 2003; Chen, McCaffery, & Chan, 2007; Chen et al., 2010; Weaver et al., 2014). Mitochondrial fusion also affects mitochondrial transport and degradation (Chen et al., 2003; Gomes, Di Benedetto, & Scorrano, 2011; Kandul, Zhang, Hay, & Guo, 2016; Misko, Jiang, Wegorzewska, Milbrandt, & Baloh, 2010; Rambold, Kostelecky, Elia, & Lippincott-Schwartz, 2011).

In mammals, spermatogenesis is a cyclical process that involves differentiation of spermatogonia into spermatocytes, which undergo meiosis to form haploid spermatids and

ultimately spermatozoa (Griswold, 2016). Throughout this process, germ cells differentiate in intimate association with nursing Sertoli cells. In addition to providing differentiation cues and metabolites for the developing germ cells, Sertoli cells form the blood-testis barrier (BTB) that separates the seminiferous epithelium into the basal (towards the periphery) and apical (towards the lumen) compartments (Stanton, 2016). Spermatogonia reside within the basal compartment and are comprised of both undifferentiated and differentiating cells. Undifferentiated spermatogonia constitute a dynamic and heterogeneous population that includes the self-renewing stem cell pool (De Rooij, 2017; Lord & Oatley, 2017). Differentiating spermatogonia give rise to spermatocytes that cross the BTB and complete meiosis. After two meiotic divisions, each spermatocyte produces four haploid spermatids that transform into the specialized sperm cells capable of fertilization.

Several observations in humans and mice illustrate the importance of mitochondrial function during spermatogenesis. Some patients with mtDNA disease have sperm defects (Demain, Conway, & Newman, 2017; Folgero, Bertheussen, Lindal, Torbergsen, & Oian, 1993), and sperm from some infertile males harbor mtDNA mutations (Baklouti-Gargouri et al., 2014; Carra, Sangiorgi, Gattuccio, & Rinaldi, 2004; Kao, Chao, & Wei, 1995; Lestienne et al., 1997). Mouse models with a pathogenic mtDNA deletion exhibit spermatogenic arrest during the zygotene stage of Meiotic Prophase I (MPI) (Nakada et al., 2006). Furthermore, a mouse model that is unable to utilize mitochondrial ATP exhibits spermatogenic arrest during the leptotene stage of MPI (Brower, Lim, Jorgensen, Oh, & Terada, 2009). Finally, mouse models that accumulate mtDNA mutations exhibit male

infertility (Jiang et al., 2017; Kujoth et al., 2005; Trifunovic et al., 2004). Much less is known about the role of mitochondrial dynamics in male fertility. The *Drosophila* homologue of mitofusin (*dMfn*) was recently shown to regulate lipid homeostasis and maintenance of germline stem cells in the testis (Demarco, Uyemura, D'Alterio, & Jones, 2019), A clinical study found that low Mfn2 expression in sperm is associated with asthenozoospermia (reduced sperm motility) and reduced sperm mitochondrial membrane potential (Fang et al., 2018). Finally, Mfn1 is required for spermatogenesis in the mouse (Zhang et al., 2016), but the precise stage of the defect as well as the role of Mfn2 remain unknown. To clarify the role of mitochondrial fusion during male germ cell development, we deleted *Mfn1*, *Mfn2*, or both *Mfn1* and *Mfn2* from the male germline and examined all stages of spermatogenesis. Our results show that mitochondrial fusion is required for spermatogonial differentiation and a metabolic shift during meiosis.

Results

Mitofusins are essential for mouse spermatogenesis

To investigate the role of mitofusins during male germ cell development, we removed *Mfn1*, *Mfn2*, or both *Mfn1* and *Mfn2* from the male germline by combining the previously described conditional alleles of *Mfn1* and *Mfn2* with the male germline-specific *Stra8-Cre* driver (Chen et al., 2003; Chen et al., 2007; Sadate-Ngatchou, Payne, Dearth, & Braun, 2008). We designate these mice as S8::Mfn1, S8::Mfn2, and S8::Dm (*double mutant*), respectively, and compared them with age-matched, wild-type (WT) littermates. Our mating scheme also incorporated the conditional *Rosa26*^{PhAM} allele, which encodes a

mitochondrially-targeted, photo-activatable fluorescent protein, mito-Dendra2 (Pham, McCaffery, & Chan, 2012). mito-Dendra2 served as a *Cre* reporter to label the mitochondrial matrix selectively in germ cells. With histological analysis of testis sections, we verified that mito-Dendra2 is restricted to the male germline and absent from the intimately associated Sertoli and interstitial cells (Figure 2S.1A). *Stra8-Cre* expression is reported to begin at post-natal day 3 (P3) in undifferentiated spermatogonia (Sadate-Ngatchou et al., 2008), including the majority of early stem-like GFRα1-positive spermatogonia (Hobbs et al., 2015). Consistent with this, our examination of the mito-Dendra2 Cre reporter clearly demonstrated excision in all germ cell types, including the vast majority of GFRα1-expressing spermatogonia (Figure 2S.1B-C).

All three mitofusin-deficient mouse lines were healthy and showed no changes in weight (Figure 2S.1D). However, they had obviously smaller testes compared with controls (Figures 2.1A, and 2.1B), suggesting an essential role for mitochondrial fusion during spermatogenesis. Indeed, there is significant reduction of spermatozoa in the epididymides of S8::Mfn1 and S8::Mfn2 mice, with the defect more severe with loss of *Mfn1* (Figures 2.1C and 1D). The residual spermatozoa in both mutant lines often display mitochondrial fragmentation and reduced mitochondrial content (Figures 2.1E and 2.1F). Mutant spermatozoa also exhibit morphological defects, particularly kinking near or in the midpiece (Figures 2.1E and 2.1G), and almost a complete loss of motility (Figure 2.1H; Videos 2.1-3). S8::Dm mice have the smallest testes (Figures 2.1A and 2.1B) and strikingly, a complete absence of epididymal spermatozoa (Figures 2.1C and 2.1D). These results indicate an essential role for mitofusins in mammalian spermatogenesis.

Mitofusins are essential for meiosis

To identify the specific stage(s) of the spermatogenic defect in mitofusin-deficient mice, we first analyzed juvenile mice at P24, before the completion of the first round of spermatogenesis. Even at this early time point, mutant mice have substantially smaller testes compared with control (Figure 2.2A). We performed Periodic Acid-Schiff (PAS) staining in testis sections and found that mutant seminiferous tubules are narrower in diameter, sparsely populated, and contain numerous Sertoli cell vacuolizations (Figure 2.2B). Whereas most control seminiferous tubules are packed with round spermatids, S8::Dm tubules have almost a complete absence of post-meiotic spermatids, indicative of an inability to complete meiosis.

To confirm this meiotic defect, we categorized all germ cell types using molecular markers in PFA-fixed, frozen sections (Figures 2.2C-2E and Figure 2S.2A). Haploid spermatids were identified with an antibody against SP-10 (Osuru et al., 2014), which marks the spermatid acrosome (Figure 2.2C). Spermatocytes in Meiotic Prophase I (MPI) were identified using an antibody against histone γH2AX (Hamer et al., 2003), which distinctively labels the various substages of MPI. Differentiated and undifferentiated spermatogonia were labeled using antibodies against c-Kit (Rossi, 2013) and PLZF (Buaas et al., 2004; Costoya et al., 2004), respectively. First, we scored seminiferous tubules based on the most differentiated cell type they contained (Figures 2.2D and 2.S2A). As expected for the P24 time point, the majority of control seminiferous tubules (87 ± 6%) contained germ cells differentiated up to the spermatid stage, and the remaining tubules (13 ± 6%)

contained cells differentiated up to pachytene/diplotene. In contrast, the majority of seminiferous tubules from P24 S8::Dm mice contained cells differentiated only up to the leptotene/zygotene stage (55 ± 2%), indicating a meiotic defect during early MPI. While some mutant seminiferous tubules contained cells differentiated up to the pachytene (22 ± 3%) and spermatid (14 ± 14%) stages (Figure 2.2D), these cell types were depleted to less than 20% compared with control (Figure 2.2E).

To better characterize the meiotic defect, we performed chromosomal spreading of isolated germ cells and scored with γH2AX and SCP3, which mark double stranded breaks (DSBs) and the synaptonemal complex that forms between homologous chromosomes, respectively. Using this assay, we could visualize individual chromosomes and thus distinguish between all substages of MPI: leptotene, zygotene, pachytene, and diplotene (Figures 2.2F). Consistent with data from testis sections, we found that S8::Dm mice have a reduction of pachytene and diplotene spermatocytes and an abundance of both leptotene and zygotene cells, pinpointing the meiotic defect to the zygotene-to-pachytene transition (Figure 2.2G). There were no obvious chromosomal abnormalities in S8::Dm mice. To check whether loss of either mitofusin alone was sufficient to block meiosis, we performed histology and chromosomal spreading in S8::Mfn1 and S8::Mfn2 mice (Figure 2S.2B). We found that loss of *Mfn1* alone was sufficient to cause a similar defect in meiosis, resulting in accumulation of spermatocytes in the leptotene and zygotene stages, and reduced production of spermatids. In contrast, S8::Mfn2 mice had normal progression through MPI at P24. Because *Stra8-Cre*-mediated excision occurs in all germ cell types, including spermatogonia that give rise to meiotic spermatocytes, our results demonstrate that MPI is

the most sensitive stage of spermatogenesis to disruption of mitochondrial fusion (Figure 2.2H).

Mitofusins are required for a metabolic shift during meiosis

Given the MPI abnormality in fusion-deficient mice, we wondered whether mitochondria show any special features during this stage of spermatogenesis. We quantified mitochondrial content in meiotic spermatocytes by measuring mito-Dendra2 fluorescence in immunolabeled testis sections. In P24 WT mice, we found that pachytene/diplotene cells contained over 3 times more mitochondrial signal compared with leptotene/zygotene spermatocytes (Figures 2.3A and 2.3B). Pachytene/diplotene spermatocytes are much sparser in S8::Dm mutant animals, but when present, these cells have less than half the mitochondrial content found in WT animals (Figure 2.3B). To better visualize mitochondrial morphology during MPI, we performed meiotic spreading and immunostained against the outer mitochondrial membrane marker Tom20. We found that WT pachytene/diplotene spermatocytes, compared with leptotene/zygotene spermatocytes, contain elongated and highly clustered mitochondria (Figures 2.3C and 2.3D). Thus, spermatocytes in P24 S8::Dm mice arrest in spermatogenesis just before the increased mitochondrial biogenesis, elongation, and clustering that occurs in pachytene/diplotene. Furthermore, S8::Dm spermatocytes that do make it to the pachytene/diplotene stage have less mitochondrial content and their mitochondria are more fragmented (Figures 2.3C and 2.3D).

As spermatocytes initiate meiosis, they cross the blood-testis-barrier (BTB) and become dependent on lactate secreted by Sertoli cells for energy production (Boussouar & Benahmed, 2004). Lactate is oxidized to pyruvate and transported into mitochondria to fuel OXPHOS (Vanderperre et al., 2016). We therefore examined whether meiotic spermatocytes, relative to spermatogonia, have higher expression of the mitochondrial pyruvate carrier, MPC1. Indeed, we find that while pachytene/diplotene spermatocytes have strong expression of MPC1, spermatogonia have little to no MPC1 protein (Figure 2.3E).

The increased mitochondrial mass and upregulation of MPC1 in pachytene/diplotene spermatocytes suggest that spermatocytes have high OXPHOS utilization compared with pre-meiotic spermatogonia. To test this directly, we used established flow cytometry methods (Bastos et al., 2005) to isolate diploid spermatogonia and tetraploid MPI spermatocytes from WT dissociated seminiferous tubules, confirmed their identities by immunostaining (Figure 2S.3A), and measured their OXPHOS activities using a Seahorse extracellular flux analyzer (Figure 2.3F). Indeed, compared with diploid spermatogonia, tetraploid spermatocytes have substantially greater maximal respiration and spare respiratory capacity, and a modest increase in basal respiration and ATP production (Figure 2.3F and Figure 2.S3B). Taken together, our findings indicate that mitochondrial fusion is required for a metabolic shift during meiosis.

Long-term mitofusin loss results in depletion of all differentiated germ cell types

To examine the long-term effects of mitofusin loss, we analyzed adult mice at P56. By this time, the testes have undergone repeated rounds of spermatogenesis and should have

more complete depletion of mitofusins. PAS-stained testis sections from P56 S8::Dm mice showed greater germ cell depletion and more widespread Sertoli cell vacuolization (Figure 2.4A) compared with P24 mutants. This severe depletion of germ cells was confirmed by flow cytometry, which showed an 80% loss of mito-Dendra2-positive cells from dissociated S8::Dm testes compared with control (Figures 2.4B and 2.4C). To identify the stage of the arrest in P56 mice, we quantified all germ cell types using molecular markers and found a depletion of all differentiating germ cell types in S8::Dm mice (Figures 2.4D-F and 2S.4A). Whereas WT seminiferous tubules invariably contain spermatids at this age, nearly half of the P56 mutant tubules (48 ± 7%) contain only spermatogonia (Figures 2.4D, 2.4E, and Figure 2.S4A). This histological phenotype is quite distinct from P24 mutants, which contain many tubules arrested in meiosis (Figures 2.2B-E). Consistent with the flow cytometry data, quantification using molecular markers showed that S8::Dm tubules, compared with WT, had greater than 80% depletion of all differentiating germ cell types (Figures 2.4F).

Despite this severe depletion of germ cells, mutant seminiferous tubules retained an outer rim of mito-Dendra2-positive germ cells that stained with PLZF, a marker of undifferentiated spermatogonia (Figures 2.4A, 2.4D rightmost panel, and 2.4F). Because undifferentiated spermatogonia are a heterogeneous population that include stem and progenitor spermatogonia (De Rooij, 2017; Lord & Oatley, 2017), we sought to better define the identity of spermatogonia retained at the tubule periphery of S8::Dm mice. To this end, we co-labeled testis sections with the pan-undifferentiated spermatogonial marker, PLZF, and the well-established stem-like spermatogonial marker, GFRα1 (Hara et al., 2014)

(Figures 2.4F and 2.4G). Not only were GFRα1-positive spermatogonia present in S8::Dm mice, but their numbers were also increased over 50%. Because endogenous Stra8 is expressed in late undifferentiated spermatogonia (Endo, Freinkman, de Rooij, & Page, 2017; Hara et al., 2014; Teletin et al., 2019), we characterized expression of the *Stra8-Cre* driver, which utilizes a 1.4 Kb Stra8 promoter fragment (Oulad-Abdelghani et al., 1996; Zhou et al., 2008) (Figures 2.S1A and 2.S1B). Quantification from testis sections in WT and S8::Dm mice shows that the vast majority of GFRα1-positive spermatogonia express *Stra8-Cre/Dn* (Figure 2.4G and Figure 2.S4B). Furthermore, over 40% of these GFRα1-expressing spermatogonia are positive for the proliferation marker Ki-67, similar to that in WT animals (Figures 2.4H and 2.4I). Thus, mitochondrial fusion is required for maintenance of all differentiated germ cell types, but dispensable for self-renewal of stem-like undifferentiated spermatogonia (Figure 2.4J).

To examine whether undifferentiated spermatogonia deplete with age, we examined mice at 4 months of age (P116). Even in these older mice, mutant seminiferous tubules retain an outer rim of undifferentiated spermatogonia that stain with Ki-67 (Figure 2.S4C). To determine whether removal of either mitofusin alone is sufficient to cause depletion of differentiating spermatogonia, we performed histology in S8::Mfn1 and S8::Mfn2 mice (Figure 2.S4D). As in S8::Dm mice, loss of either *Mfn1* or *Mfn2* alone causes severe depletion of germ cells. Quantification of c-Kit-expressing spermatogonia showed that both mutants have severe depletion of differentiating spermatogonia, close to the level observed in S8::Dm mice (Figure 2.S4E). Thus, both *Mfn1* and *Mfn2* are required for maintenance of differentiating spermatogonia. Taken together, our data indicate that long-term mitofusin

loss impairs maintenance of all differentiated germ cell types, but not self-renewal of stem-like spermatogonia.

Mitofusin-deficient germ cells have aberrant cristae ultrastructure and increased apoptosis

We next visualized mitochondrial ultrastructure in testis sections via 3D EM tomography (Figures 2.5A-D, and Figure 2.S5). Mutant mitochondria had aberrant cristae morphology characterized by a fourfold reduction in the number of linear cristae elements and a fourfold increase in swollen, vesiculated cristae (Figures 2.5A and 2.5B). Despite their isolated appearance, all vesiculated cristae in S8::Dm mitochondria could be traced back to the inner mitochondrial membrane using 3D EM tomography (Video 2.4). Furthermore, many cristae junctions (CJs) in mutant mitochondria are significantly widened in diameter (Figures 2.5C, 2.5D, and 2.S5). While most of the CJs in control spermatocytes are narrower than 22.5 nm (64%), the majority in S8::Dm are wider (78%) (Figure 2.S5). In fact, 50% of mutant CJs, compared to 13% in WT, are wider than 27.5 nm. The aberrant cristae morphology and increased CJ diameter are suggestive of increased mitochondrial apoptosis in S8::Dm mice. To verify this, we performed terminal deoxynucleotidyl transferase dUTP nick end labeling (TUNEL) in testis sections. Indeed, S8::Dm sections show increased TUNEL-positive cells, indicative of cell death by apoptosis (Figures 2.5E and 2.5F).

Mitofusin-deficient MEFs have reduced OXPHOS subunits and mitochondrial ribosomes

To understand the cellular mechanism for the spermatogenic and mitochondrial defects, we sought for clues in mitofusin-null mouse embryonic fibroblasts (MEFs), where we could readily obtain sufficient material to do proteomic analysis. We used stable isotope labeling of amino acids in cell culture (SILAC) to quantitatively compare the mitochondrial proteome of *Mfn1/Mfn2*-null MEFs with WT controls (Figure 2.6 and Figure 2.S6). Gene Ontology (GO) analysis revealed two general categories of proteins that are significantly reduced in mitochondria from *Mfn1/Mfn2*-null MEFs: the mitochondrial respiratory chain and the mitochondrial ribosome (Figure 2.6A and Table 2.1). Indeed, 31 out of 34 (91%) identified complex I subunits, all 12 (100%) complex IV subunits, and 74 out of 80 (93%) mitochondrial ribosomal subunits were reduced in *Mfn1/Mfn2*-null MEFs (Table 2.2). Of the proteins that reached statistical significance ($p<0.05$), all 14 complex I subunits, all 4 complex IV subunits, and all 18 mitochondrial ribosomal subunits were reduced (Figure 2.6B). Consistent with reduced OXPHOS activity, *Mfn1/Mfn2*-null MEFs had significantly lower levels of the mitochondrial pyruvate carrier, MPC2 (Bricker et al., 2012; Vanderperre et al., 2016). Additionally, TFAM, a mitochondrial transcriptional activator and mtDNA packaging protein, was significantly reduced. Intriguingly, 14 out of 18 (78%) complex I and IV assembly factors were increased in *Mfn1/Mfn2*-null MEFs and of the 7 that reached statistical significance, all were increased (Figure 2.6B). Our GO analysis also revealed an upregulation of mitochondrial import proteins in *Mfn1/Mfn2*-null MEFs (Figure 2.6A). 17 out of 21 (81%) detected mitochondrial import proteins were increased, and of the 10 that

reached statistical significance, all were increased in *Mfn1/Mfn2*-null MEFs (Figure 2.6B). Taken together, these data suggest that the reduced OXPHOS activity in *Mfn1/Mfn2*-null MEFs (Chen et al., 2005) is caused by downregulation of OXPHOS components and mitochondrial ribosomal subunits.

Mitofusin knockdown in immortalized spermatocytes causes reduced OXPHOS subunits and activity

With the proteomic insights from MEFs, we examined whether OXPHOS deficiency also occurs in germ cells upon loss of mitofusins. To this end, we utilized the widely used spermatocyte cell line, GC-2spd(ts), referred to herein as GC (Figure 2.7 and 2.S7A-D) (M.-C. Hofmann, Hess, Goldberg, & Millan, 1994; M. C. Hofmann, Abramian, & Millán, 1995; Rahman & Huhtaniemi, 2004). To block mitochondrial fusion in GCs, we constructed an shRNA vector for dual Mfn1 and Mfn2 knockdown (shMfn1;Mfn2). Effective mitofusin knockdown was verified by western blotting (Figure 2.S7A and 2.S7B) and by quantifying mitochondrial morphology (Figures 2.7A and 2.7B). Strikingly, mitofusin knockdown in GCs causes widespread mitochondrial fragmentation and reduction in all OXPHOS subunits tested by western blotting: complex I subunit (NdufB8), complex II subunit SDHB, complex III subunit UQRC2, complex IV subunit MTCOI, and complex V subunit ATP5A (Figures 2.7C and 2.7D). To measure OXPHOS activity directly, we measured oxygen consumption in GCs using a Seahorse extracellular flux analyzer. Mitofusin knockdown caused a severe reduction in basal and maximal respiration, ATP production, and spare capacity (Figures 2.7E and 2.7F), but not glycolysis (Figure

2.7G). Interestingly, mitofusin knockdown in MEFs caused mitochondrial fragmentation (Figure 2.S7C), but not OXPHOS deficiency (Figure 2.S7D). Our knockdown procedure, while effective, was not efficient enough to reproduce the OXPHOS deficiency that characterizes mitofusin-null MEFs (Chen et al., 2005). Taken together, these data indicate that GCs are particularly sensitive to loss of mitofusins.

Mitofusin-deficient spermatocytes have reduced OXPHOS components and activity.

To test these findings in germ cells *in vivo*, we performed immunofluorescence against various OXPHOS components in spermatocytes in testis sections (Figures 2.8A and 2.8B). In WT mice, spermatocytes have strong and homogeneous expression of OXPHOS components that uniformly overlaps with mito-Dendra2-labeled mitochondria. In contrast, most spermatocytes in S8::Dm mice show a heterogeneous staining pattern in which a substantial subset of mito-Dendra2-positive mitochondria clearly lack OXPHOS components. Consistent with the proteomics in cultured cells, S8::Dm spermatocytes have reduced and heterogeneous expression of the complex I subunit NdufB6, the complex IV subunit MTCOI, and the mitochondrial pyruvate carrier MPC1 (an obligate binding partner of MPC2). We noted that the mtDNA-encoded MTCOI has the most heterogeneous expression. Similarly, many shMfn1;Mfn2 GCs display reduced or heterogeneous MTCOI expression, with a substantial subset of mitochondria lacking MTCOI (Figure 2.S8A).

In agreement with the progressive loss of differentiated spermatogonia in S8::Dm mice, there is also mitochondrial heterogeneity in this cell type (Figure 2.S8B and 2.S8C). Surprisingly, we also find mitochondrial heterogeneity in undifferentiated spermatogonia,

which are not depleted in S8::Dm mice. Thus, loss of mitofusins leads to heterogeneous mitochondria in all germ cell types. However, the undifferentiated spermatogonia can apparently tolerate this defect, suggesting that these cells are physiologically different.

To test for functional changes in mitochondrial activity, we performed COX/SDH enzyme histochemistry on spermatozoa isolated from S8::Mfn1 and S8::Mfn2 mice and found reduction of both COX and SDH activities (Figure 2.S8D and 2.S8E). Because S8::Dm mice do not produce sperm, we performed COX/SDH enzyme histochemistry in fresh-frozen testis sections and found a severe reduction of COX and SDH activities in S8::Dm germ cells (Figure 2.8C). Thus, mitofusin depletion in germ cells *in vivo* causes ultrastructural defects, heterogeneity in OXPHOS expression, and reduced OXPHOS subunits and activity (Figure 2.9).

Discussion

Mfn1 is known to be required in spermatocytes in mice (Zhang et al., 2016), but it was unclear whether this requirement simply reflected the need for basal mitochondrial dynamics as a housekeeping function. Our study reveals that spermatocytes require mitochondrial fusion as they undergo an acute upregulation of OXPHOS during MPI (Figure 2.9). Analysis of the single mutant mice showed that *Mfn1* but not *Mfn2* is essential for this transition. We show that this transition coincides with increased mitochondrial density, mitochondrial elongation, and upregulation of OXPHOS activity, which are all blocked in fusion-deficient spermatocytes. The increased OXPHOS in pachytene spermatocytes is likely required to fuel ATP-consuming biochemical reactions involved in

homologous recombination and DSB repair. Consistent with this idea, the metabolic environment of spermatocytes changes as they initiate MPI and traverse the blood-testis barrier. In this isolated compartment, spermatocytes are segregated from the vasculature and interstitial fluid and thus rely on metabolites secreted by the nursing Sertoli cells (Boussouar & Benahmed, 2004; Stanton, 2016). As a result, spermatocytes switch their energy dependence from glucose to lactate and pyruvate, which are preferred substrates for OXPHOS (Bajpai, Gupta, & Setty, 1998; Grootegoed, Jansen, & Van der Molen, 1984; Nakamura, Okinaga, & Arai, 1984; Rato et al., 2012). In agreement with upregulation of OXPHOS during pachytene, others and we have found high expression of the mtDNA-encoded COXI protein (Figure 2.8A, middle panel) (Jiang et al., 2017) and mRNA (Saunders, Millar, West, & Sharpe, 1993) in pachytene spermatocytes. Furthermore, we find that spermatocytes, compared with pre-meiotic spermatogonia, switch on expression of the mitochondrial pyruvate carrier, MPC1, presumably to accommodate the greater flux of pyruvate into the OXPHOS pathway. Changes in pyruvate metabolism, driven by MPC expression, have been shown to regulate differentiation of stem cells in other systems (Flores et al., 2017; Schell et al., 2017).

Our findings are in agreement with previous indications that mitochondrial morphology, cristae structure, and OXPHOS activity change during MPI. Round spherical mitochondria with orthodox cristae in early MPI convert in pachytene to more elongated mitochondria with condensed cristae (De Martino et al., 1979; Meinhardt, Wilhelm, & Seitz, 1999; Seitz, Mobius, Bergmann, & Meinhardt, 1995), an ultrastructure associated with active OXPHOS (Hackenbrock, 1966; Mannella, 2006). Furthermore, mitochondrial

function has been shown to be important for this particular developmental stage. Arrest in early MPI occurs in mouse models with a pathogenic mtDNA deletion (Nakada et al., 2006) or inability to utilize mitochondrial ATP (Brower et al., 2009). In addition, mouse models that accumulate mtDNA mutations exhibit male infertility (Jiang et al., 2017; Kujoth et al., 2005; Trifunovic et al., 2004).

In contrast to the Mfn1 study (Zhang et al., 2016), we show that mitofusins are required not only in spermatocytes, but also in differentiating spermatogonia (Figure 2.9). S8::Mfn1, S8::Mfn2, and S8::Dm mice exhibit a progressive loss of all differentiated germ cell types, including the differentiating spermatogonia that give rise to spermatocytes. The age-dependent loss is likely caused by the progressive depletion of mitofusin gene products due to the iterative nature of spermatogenesis. At P24, during the first round of spermatogenesis, germ cells may contain residual levels of mitofusin activity sufficient to mitigate effects on spermatogonia. As a result, the major defect is found during MPI, which is more sensitive to ATP depletion because of the metabolic shift described above. With long-term mitofusin loss in adult mice, even the less sensitive differentiating spermatogonia are affected. Mitochondrial fusion, however, is dispensable for self-renewal of undifferentiated spermatogonia, even though these cells display mitochondrial heterogeneity with loss of mitofusins. Undifferentiated spermatogonia, differentiating spermatogonia, and spermatocytes therefore show progressively increasing requirements for mitochondrial fusion. These results are consistent with a paradigm in various (but not all) stem cell systems, wherein stem cells compared with differentiated cells are less dependent on mitochondrial OXPHOS (Chen & Chan, 2017).

The two major phenotypes of S8::Dm mice—meiotic failure and spermatogonial differentiation—are also observed with loss of *Mfn1* alone. This observation suggests that these defects should be attributed to loss of mitochondrial fusion, rather than non-fusion functions, like ER-mitochondria tethering, that have been attributed to Mfn2 (De Brito & Scorrano, 2008). To further test that our spermatogenesis defects are due to loss of mitochondrial fusion, it will be helpful to analyze mice lacking other mitochondrial dynamics factors, particularly *Opa1*.

To elucidate the cellular mechanism for the spermatogenic arrest we performed proteomics in MEFs and found downregulation of respiratory chain complex I and IV subunits, mitochondrial translation proteins, and the mitochondrial pyruvate carrier, MPC2. A previous proteomic study found that *Mfn2*-null MEFs have a defect in the coenzyme Q pathway, but no change in the levels of respiratory chain complexes (Arnaud Mourier et al., 2015; A. Mourier et al., 2015). In our study, full inhibition of mitochondrial fusion by deletion of both mitofusins uncovers their role in maintaining the respiratory chain and mitochondrial translation. Finally, we find an increase in the respiratory chain complex I and IV assembly factors as well as mitochondrial import proteins in *Mfn1/Mfn2*-null MEFs. These increases may be indicative of a compensatory stress response to the cellular dysfunction caused by mitochondrial fusion deficiency. Importantly, the metabolic derangements revealed by proteomics in MEFs extend to a spermatocyte cell line and to spermatocytes *in vivo*. Thus, our findings provide a rationale for how mitochondrial fusion safeguards mitochondrial function and male fertility.

Materials and methods

Generation of S8::Dm *mice and characterization of Stra8-Cre expression*

All mouse experiments were approved by the California Institute of Technology (Caltech) Institutional Animal Care and Use Committee. S8::Control (Stra8-Cre$^{+/tg}$; *Mfn1*$^{+/lox}$; *Mfn2* $^{+/lox}$; PhAM$^{+/lox}$), S8::Mfn1 (Stra8-Cre$^{+/tg}$; *Mfn1*$^{\Delta/lox}$; *Mfn2*$^{+/lox}$; PhAM$^{+/lox}$), S8::Mfn2 (Stra8-Cre$^{+/tg}$; *Mfn1*$^{+/lox}$; *Mfn* $^{\Delta/lox}$; PhAM$^{+/lox}$), and S8::Dm (Stra8-Cre$^{+/tg}$; *Mfn1*$^{\Delta/lox}$; *Mfn2*$^{\Delta/lox}$; PhAM$^{+/lox}$) mice were generated by crossing Stra8-Cre; *Mfn1*$^{+/\Delta}$; *Mfn2*$^{+/\Delta}$ mice to *Mfn1*$^{loxP/loxP}$; *Mfn2*$^{loxP/loxP}$; PhAM$^{loxP/loxP}$ mice. The delta alleles *Mfn1*$^{\Delta}$ and *Mfn2*$^{\Delta}$ *(Chen et al., 2003),* the conditional alleles *Mfn1*^{loxP} and *Mfn2*^{loxP} (Chen et al., 2007), the Stra8-Cre driver (Jackson Laboratory #017490) (Sadate-Ngatchou et al., 2008), and the mito-Dendra2 allele (Pham et al., 2012) were all described previously. All mice were maintained on a C57B6 background except for *Mfn1*$^{loxP/loxP}$; *Mfn2*$^{loxP/loxP}$; PhAM$^{loxP/loxP}$ mice, which were maintained on a C57B6/129S mixed genetic background.

Epididymal sperm counting and analysis of morphology and motility

Mice were euthanized at P56, and epididymides were dissected and thoroughly minced in 1.7 ml microcentrifuge tubes containing 1 ml PBS. Samples were incubated at 37°C for 20 minutes to allow sperm to swim out. 900 µl of the supernatant was transferred into a fresh microcentrifuge tube. For sperm counting and morphology analysis, samples were allowed to settle for several hours for sperm to stop swimming before counting on a hemocytometer. Sperm counts were normalized to the weight of the epididymides of each mouse. For motility quantification, freshly isolated sperm were transferred to a

hemocytometer, and the proportion of motile sperm was quantified. For motility movies, freshly isolated sperm were transferred to glass-bottom FluoroDish Cell Culture Plates (FD35-100) and imaged at one frame per second for 10 seconds using a confocal microscope as described below.

Periodic acid-Schiff staining

After dissection, testes were fixed in Bouin's fixative overnight at 4ºC, dehydrated in a 30-90% ethanol gradient, cleared in Xylenes, and embedded in paraffin. Tissue blocks were sectioned at 7 µm, deparaffinized, and rehydrated before staining. Briefly, slides were incubated with 1% periodic acid (Electron Microscopy Sciences (EMS); 19324-10) for 30 minutes at RT, washed in running water for 5 minutes, then rinsed in deionized water. Slides were incubated with Schiff's reagent (EMS; 260582-05) for 30 minutes at RT and washed as described above before counterstaining with Hematoxylin Gill 2 for 30 seconds at RT. Slides were washed in running water for 1 minute, dehydrated with ethanol, cleared with xylene, then mounted using Cytoseal XYL mounting media (Thermo Fisher Scientific; 22-050-262).

Immunofluorescence

For immunostaining of tissue sections, testes were cut at the poles, fixed in 4% PFA for 4 hours at 4°C, incubated with 30% sucrose in PBS overnight at 4°C (or until tissues sank), incubated in a 1:1 solution of 30% sucrose in PBS and optimal cutting temperature (OCT) embedding medium (Thermo Fisher Scientific; NC9636948) for 15-30 minutes, then

embedded in OCT medium and frozen in dry ice. Tissue blocks were sectioned at 10 µm onto glass slides, dried overnight, and stored at -80°C until ready for immunostaining. Frozen slides were briefly thawed at room temperature, rehydrated in PBS, permeabilized with 0.15% TX-100 for 15 minutes, and blocked for 1 hour using Blocking Buffer (10% FBS, 3% BSA, 0.05% TX-100 in PBS). Slides were incubated with primary antibodies in a humidified chamber overnight at 4°C, washed three times in PBS for 15 minutes each, then incubated with secondary antibodies in a humidified chamber for 2.5 hours at RT. Slides were counterstained with DAPI, washed as described above, mounted with Fluorogel (EMS; 17985-10), coverslipped, sealed with nail polish, and stored at 4ºC before imaging.

For immunostaining of FACS sorted germ cells, cells were plated onto 8-chamber glass slides (VWR, 62407-296) pre-coated with Cell-Tak (Corning; 354240). After cell adhesion, cells were washed with PBS, fixed in 10% Neutral Buffered Formalin (Sigma Aldrich, HT501128-), and immunostained as described above.

Western blotting

Cells were grown to confluency in 6-well plates and lysed in 200 µL of Lysis Buffer (20 mM Tris-Cl, 150 mM NaCl, 2mM EDTA, 1% Triton X-100, pH 7.5 with Halt Protease Inhibitor added to 1X). Proteins (5 µg) were separated by SDS-PAGE and transferred to Polyvinylidene difluoride membranes using semi-dry electrophoresis. Membranes were blocked with 5% non-fat dry milk for 1 hr at RT, followed by primary antibody incubation overnight at 4°C. HRP-conjugated secondary antibodies were applied for 2 hr at RT. Immobilon Western chemiluminescent HRP substrate (Millipore 90720) was added

according to the manufacturer's instructions and the protein bands were visualized on X-ray film (Amersham Hyperfilm MP). For analysis, densitometry was performed in ImageJ and protein levels were normalized to that of tubulin.

Antibodies

The following antibodies were used for immunofluorescence. rabbit anti-γH2AX (ab11174, Abcam); mouse anti-γH2AX (ab26350, Abcam); rabbit anti-c-Kit (3074S, Cell Signaling Technology); rabbit anti-GFRα1; (AF560-SP, R&D Systems); rabbit anti-Ki67 (ab15580, Abcam); rabbit anti-MPC1 (HPA045119, Millipore Sigma); mouse anti-MTCOI (ab14705, Abcam); mouse anti-Ndufb6 (ab110244, Abcam); rabbit anti-PLZF (SC-22831, Santa Cruz Biotech); mouse anti-PLZF (SC-28319, Santa Cruz Biotech); rabbit anti-SCP3; (ab15093, Abcam); mouse anti-SCP3 (ab97672, Abcam); mouse anti-SDHA (ab14715, Abcam); guinea pig anti-SP-10 (gift from Prabhakara P. Reddi); rabbit anti-Tom20 (SC-11415, Santa Cruz, Biotech); mouse anti-Total OXPHOS (ab110413, Abcam). The following antibodies were used for western blotting. Chicken anti-Mfn1 (Chen et al., 2003); rabbit anti-Mfn2 (D2D10S #9482, Cell Signaling Technology); mouse anti-tubulin (T6199, Sigma).

Chromosome spreading of meiotic spermatocytes

Chromosome spreading was performed as described previously (Gaysinskaya, Soh, van der Heijden, & Bortvin, 2014; Peters, Plug, van Vugt, & de Boer, 1997). Briefly, testes were decapsulated and placed into 10 cm petri dishes containing 3 ml MEM-α. Seminiferous

tubules were loosened under a dissecting microscope with forceps, and the interstitial cells were washed away. The seminiferous tubules were transferred to a fresh 10 cm petri dish containing 300 µl MEM-α and the tubules were torn between two fine forceps for 3-5 minutes. A cell suspension was made with an additional 1 ml MEM-α using a P1000 pipette and the large tubular remnants were removed by centrifugation at 500 rpm (27 RCF) for 1 min. The cells were concentrated by centrifugation for 7 minutes at 1000 rpm (106 RCF), and 500 µl of the supernatant was discarded. Upon re-suspending cells, 600 µl of Hypotonic Buffer was added to 600 µl of the cell suspension and incubated for 7 minutes at RT. The suspension was spun at 1000 rpm (106 RCF) for 7 minutes and 1100 µl of the supernatant was discarded. The cells were re-suspended in residual hypotonic buffer (this is an essential step to prevent cell clumping) before adding 1 ml of 100 mM working sucrose solution. 100-200 µl of cell suspension was added to glass slides pre-coated with Fixation Buffer (1% PFA, 0.15% TX-100) and incubated for 1 to 1.5 h at RT in a humidified chamber. Slides were stored at -80ºC until they were ready for immunostaining. Slides were immunostained as described above. For immunostaining mitochondria, TX-100 was omitted from the Fixation Buffer.

Electron microscopy and dual-axis tomography

Mouse testes were dissected and immediately fixed with cold 3% glutaraldehyde, 1% paraformaldehyde, 5% sucrose in 0.1 M sodium cacodylate trihydrate. Pre-fixed pieces of tissue were rinsed with fresh cacodylate buffer and placed into brass planchettes (Type A; Ted Pella, Inc., Redding, CA) prefilled with 10% Ficoll in cacodylate buffer. Samples

were covered with the flat side of a Type-B brass planchette and rapidly frozen with a HPM-010 high-pressure freezing machine (Leica Microsystems, Vienna Austria). The frozen samples were transferred under liquid nitrogen to cryotubes (Nunc) containing a frozen solution of 2.5% osmium tetroxide, 0.05% uranyl acetate in acetone. Tubes were loaded into an AFS-2 freeze-substitution machine (Leica Microsystems) and processed at -90°C for 72 h, warmed over 12 h to -20°C, held at that temperature for 8 h, then warmed to 4°C for 2 h. The fixative was removed, and the samples were rinsed 4x with cold acetone, and then were infiltrated with Epon-Araldite resin (Electron Microscopy Sciences, Port Washington PA) over 48 h. Samples were flat-embedded between two Teflon-coated glass microscope slides, and the resin polymerized at 60°C for 24-48 hr.

Flat-embedded testis samples were observed with a stereo dissecting microscope, and appropriate regions were extracted with a microsurgical scalpel and glued to the tips of plastic sectioning stubs. Semi-thick (400 nm) serial sections were cut with a UC6 ultramicrotome (Leica Microsystems) using a diamond knife (Diatome, Ltd. Switzerland). Sections were placed on Formvar-coated copper-rhodium slot grids (Electron Microscopy Sciences) and stained with 3% uranyl acetate and lead citrate. Gold beads (10 nm) were placed on both surfaces of the grid to serve as fiducial markers for subsequent image alignment. Grids were placed in a dual-axis tomography holder (Model 2040, E.A. Fischione Instruments, Export PA) and imaged with a Tecnai TF30ST-FEG transmission electron microscope (300 KeV) equipped with a 2k x 2k CCD camera (XP1000; Gatan, Inc. Pleasanton CA). Tomographic tilt-series and large-area montaged overviews were acquired automatically using the SerialEM software package (Mastronarde, 2005). For tomography,

samples were tilted +/- 64° and images collected at 1° intervals. The grid was then rotated 90° and a similar series taken about the orthogonal axis. Tomographic data was calculated, analyzed and modeled using the IMOD software package (Kremer, Mastronarde, & McIntosh, 1996; Mastronarde, 2008) on MacPro computers (Apple, Inc., Cupertino, CA).

Apoptotic cell labeling

To label apoptotic nuclei, the TUNEL assay was performed in PFA-fixed, OCT-embedded testis sections using the ApopTag® Red In Situ Apoptosis Detection Kit (Millipore; S7165) according to the manufacturer's protocol. Nuclei were counterstained with DAPI.

Imaging and image processing

Confocal fluorescence images and videos were acquired using an inverted Zeiss LSM 710 confocal microscope with a 60X Plan-Apochromat objective. Epifluorescence and bright-field images were acquired using an upright Nikon Eclipse Ni-E fluorescence microscope equipped with a Ds-Ri2 camera and CFI Plan Apochromat Lambda objectives. For PAS histology images, Z stacks were acquired and all-in-focus images were created using the NIS Elements Extended Depth of Focus plugin. All images were processed using ImageJ. All image modifications were performed on entire images (no masking was used) and were performed identically between genotypes.

Germ cell quantification from testis sections

Germ cells were counted from 10 µm testis sections using the germ cell markers described in the main text. Quantification was restricted to germ cells within round transverse sections of seminiferous tubules and is reported as either the mean number of germ cells per seminiferous tubule cross section or the most differentiated cell type per seminiferous tubule cross section. Only germ cells expressing Dendra2 were included in the quantification to exclude cells without *Stra8-Cre* expression. For each genotype, at least 50 transverse sectioned seminiferous tubules were quantified from at least 4 mice.

COX/SDH enzyme histochemistry

COX/SDH double-labeling was performed as described previously (Ross, 2011) with minor modifications. Briefly, testes were embedded in OCT medium, frozen in liquid nitrogen and cryosectioned at 10 µm. Slides were stained with COX buffer for 25 minutes at RT in the dark. Slides were washed twice with dH20 for 5 minutes then stained with SDH buffer at 37C for 45 minutes in the dark. Slides were washed twice with dH20 and destained using a 30%-90%-30% acetone gradient. After two additional washes in dH20, slides were counterstained with DAPI and mounted using Fluorogel. For COX/SDH double labeling of sperm, cells were isolated as described above. 20-50 µl of isolated sperm were smeared onto glass slides and allowed to air dry for 1 hr at RT prior to performing the enzymatic assay as described above.

Fluorescence-activated cell sorting (FACS)

Cells were sorted at Caltech's Flow Cytometry Facility using a Sony SY3200 analyzer. Testes were dissociated from adult males (2-3 months old) as described previously (Gaysinskaya & Bortvin, 2015; Gaysinskaya et al., 2014). The cell suspension was passed through a 100 µm nylon cell strainer, pelleted at 150 *g* for 5 minutes, and stained for 1 hour with 5 µg/ml Hoechst 33342 in Flow Cytometry Buffer (HBSS with 2.5 mg/ml fraction V BSA, 10 Mm HEPES buffer, 6.6 mM sodium pyruvate, 0.05% sodium lactate, DNase and 1 mM MgCl2, pH 7.2). The nuclear dye was washed away with Flow Cytometry Buffer, and the cells were filtered through a 40 µm mesh. 7-AAD was added for exclusion of dead cells. Diploid, tetraploid, and haploid cells were isolated as described before (Bastos et al., 2005), and verified using germ cell-specific markers (Figure 2.S3A).

Respiration measurements

For respiration measurements in dissociated germ cells, testicular cells were sorted using FACS as described above into germ cell collection media (DMEM 11995 supplemented with 10% FBS, 1% Pen/Strep, 6.6 mM sodium pyruvate, 0.05% sodium lactate). The cells were pelleted at 150 g for 5 minutes and incubated in Seahorse media (Sigma-Aldrich; #D5030 supplemented with 5% FBS, 1% Pen/Strep, 2mM glutamine, 6.6 mM sodium pyruvate, 3 mM sodium lactate, and 10 mM glucose) before plating onto 96-well plates pre-coated with Cell-Tak (Corning; 354240) per manufacturer's instructions. The plated cells were spun for 1000 rpm for 5 minutes to promote cell-adhesion. The Mitochondrial Stress Test was performed using a Seahorse Biosciences Extracellular Flux

Analyzer (model XF96). 5 µM oligomycin was added to inhibit complex V; 10 µM CCCP was added to uncouple the proton gradient; and 5 µM Antimycin A was added to inhibit complex III. For respiration measurements in immortalized spermatocytes (GC2spd(ts)), a non-targeting cell line and two separate shMfn1;Mfn2 cell lines were used: shMfn1;Mfn2 (A) and shMfn1;Mfn2 (B). 20,000 cells were plated onto 96-well plates 16 hours before the Seahorse experiment in complete media (DMEM 11995 supplemented with 10% FBS, 1% Pen/Strep). One hour before the experiment, cells were washed into Seahorse media (Sigma-Aldrich; #D5030 supplemented with glutamine, sodium pyruvate, Pen/Strep, and 25 mM glucose). The Mitochondrial Stress Test was performed as described above. Values were normalized to the total number of cells remaining per well after the Seahorse experiment. For counting, cells were trypsinized, resuspended in complete medium, and counted using a tally counter. Normalization was performed using Agilent's Seahorse Wave Desktop Software.

shRNA knockdown in immortalized spermatocytes

GC-2spd(ts) immortalized spermatocytes (CRL-2196^{TM}) were purchased from ATCC®. For dual Mfn1 and Mfn2 knockdown in immortalized spermatocytes, shRNAs against Mfn1 and Mfn2 were cloned into the FUChW-H1H1 vector containing dual H1 promoters (Rojansky, Cha, & Chan, 2016) and transferred to pRetroX. The shRNA target sequences are below.

Non-Targeting: CGTTAATCGCGTATAATACGC

Mfn1: CGGTATCTCCACTGAAGCA

Mfn2-1: GGATTGGTCATACCACCAATT

Mfn2-2: GCCTGGATGCTGATGTGTTTG

Retroviral vectors were cotransfected into 293T cells with pCL-Eco (Adgene #12371) using calcium phosphate precipitation. Virus was collected, filtered, and added to GC-2spd(ts) immortalized spermatocytes in the presence of Polybrene. Cells were spun at 2,400 rpm for 30 minutes and incubated for 8 hr before replacing with complete medium (DMEM 11995, 10% fetal bovine serum, 1% Pen/Strep). To achieve efficient Mfn2 KD, spermatocytes were first dually knocked down for Mfn1 and Mfn2 using shMfn1;Mfn2-1, followed by Mfn2 knockdown using shMfn2-2.

Stable isotope labeling of amino acids in cell culture (SILAC)

DMEM lacking arginine and lysine was used, along with 10% dialyzed fetal bovine serum. For heavy labeling, Arg6 (U-$^{13}C_6$) and Lys8 (U-$^{13}C_6$, U-$^{15}N_2$) (Cambridge Isotopes) were supplemented at the same concentration as in the standard DMEM formulation. For light labeling, regular DMEM was used.

Isolation of mitochondria

Mitochondria were isolated from a 1:1 mixture of heavy and light SILAC-labeled, WT and *Mfn1/Mfn2*-null MEFs. Cells were lysed using a nitrogen bomb (Parr) at 200 psi for 10 min. Lysates were centrifuged at 600 *g* for 5 minutes to remove nuclei and intact

cells. The supernatant was resuspended in 15 ml Isolation Buffer (IB) (220 mM Mannitol, 70 mM sucrose, 10 mM HEPES-KOH pH 7.4, 1 mM EGTA, and protease inhibitors) and homogenized with a glass–glass Dounce homogenizer. Lysates were centrifuged for 600 *g* for 5 min and the supernatants containing the crude mitochondrial fraction were centrifuged at 10,000 *g* for 10 min. Crude mitochondria were further purified by a discontinuous Percoll gradient consisting of 80, 52, and 21% Percoll. Following centrifugation at 23,200 rpm for 90 min, mitochondria were collected at the 21%/52% interface, washed with IB, and pelleted by centrifugation at 13,000 rpm for 10 min.

Mass spectrometry

Samples were analyzed on a hybrid LTQ-Orbitrap mass spectrometer with a nanoelectrospray ion source (Thermo Scientific) coupled to an EASY-nLC HPLC (Proxeon Biosystems, Waltham, MA). Peptides were separated online using a 75 μm ID by 15 cm silica analytical column packed in-house with reversed phase ReproSil-Pur C18AQ 3 μm resin (Dr. Maisch GmbH, Ammerbuch-Entringen, Germany). The analytical gradient was 2-30% solvent B in 150 minutes at 350 nl/min where solvent B was acetonitrile in 0.2% formic acid. The mass spectrometer collected spectra in data-dependent mode, with a survey spectrum collected from 300-1700 m/z at 60k resolution followed by 10 MS/MS spectra from the most intense precursors. Precursors were fragmented using CID with 35% normalized collision energy and activation Q of 0.25. Only precursors with charge states 2+ and 3+ were selected for fragmentation and dynamic exclusion was enabled with duration of 90 s and an exclusion window of 10 ppm.

Bioinformatical analysis

Thermo raw files were searched using MaxQuant (v. 1.6.1.0) (Cox & Mann, 2008; Cox et al., 2011) against the UniProt mouse database (61,681 entries) and a contaminant database (245 entries). Arg6 and Lys8 SILAC labels were specified with re-quantify and match between runs enabled. Trypsin was specified as the digestion enzyme with up to two missed cleavages allowed. Oxidation of methionine and protein N-terminal acetylation were specified as variable modifications and carbamidomethylation of cysteine was specified as a fixed modification. Precursor mass tolerance was 4.5 ppm after recalibration and fragment ion mass tolerance was 0.5 Da.

Following the database search, proteins not annotated in MitoCarta (Calvo, Clauser, & Mootha, 2016) were removed. Protein replicate ratios were averaged together and these ratios were then normalized so that the global mean ratio was 1:1. Limma was used to assess individual protein fold change significance and confidence intervals (Ritchie et al., 2015; Smyth, 2004). One-sample t-tests were used to identify GO terms with annotated protein mean ratios statistically different from 1:1. All *p*-values were adjusted using the Benjamini and Hochberg method (Benjamini & Hochberg, 1995).

Replicates and statistical reporting

Pairwise comparisons were made using the Student's t-test. When multiple pairwise comparisons were made from the same dataset, *p*-values were adjusted using the Bonferroni correction. For comparisons of more than two means, one-way ANOVA was used, followed by Tukey's post hoc test. Number of mice and replicates are indicated in figure legends. All

outliers were included in the analysis. All data are represented as mean ± SEM. **** indicates $p \leq 0.0001$; *** indicates $p \leq 0.001$; ** indicates $p \leq 0.01$; * indicates $p \leq 0.05$.

Acknowledgments

We thank Hsiuchen Chen for her initial characterization of S8::Mfn1 and S8::Mfn2 mice, for help with maintaining mouse colonies, and for overall guidance throughout the project. We thank Safia Malki and Alex Bortvin for providing a detailed protocol for chromosomal spreading and with help identifying germ cell-specific markers; Prabhakara P. Reddi for providing the SP-10 antibody; and Jared Rutter for advice on studying MPC1. We thank all members of the Chan Lab for helpful discussions and for comments on the manuscript. Grigor Varuzhanyan was supported by a National Science Foundation Graduate Research Fellowship (DGE-1144469) and a National Institutes of Health Cell and Molecular Biology Training Grant (GM07616T32). Sonja Hess and Robert L.J. Graham were supported by grants from the Gordon and Betty Moore Foundation through GBMF775 and the Beckman Institute. This work was supported by NIH grants GM119388 and GM127147. MSL was supported by the National Institute of Allergy and Infectious Diseases (NIAID) (2 P50 AI150464) (awarded to Pamela J, Bjorkman, Caltech). We thank the Caltech Kavli Nanoscience Institute for maintenance of the TF-30 electron microscope.

Chapter 2 Figure legends

Figure 2.1: Mitofusins are essential for mammalian spermatogenesis.

(A) Comparison of testicular size in mice of the indicated genotype. Tissues have been fixed with Bouin's solution, which gives them the yellow appearance. Scale bar, 0.5 cm.

(B) Testes weight measurements from adult P56 mice. Both organs were used. N≥7.

(C) Epididymal sperm count. Note that S8::Dm mice do not produce any sperm. N≥6.

(D) Histological analysis of sperm in cauda epididymis sections. Mature sperm are identified by the rod-like mito-Dendra2 (Dn) signal (green) in the midpiece. Nuclei are labeled with DAPI (blue). Scale bars, 50 μm.

(E) Morphological comparison of isolated caudal spermatozoa. Mitochondria are labeled with mito-Dendra2. Note that mutant sperm have patchy, fragmented mitochondria and sharp kinking near or in the midpiece. Scale bar, 5 μm.

(F-H) Quantification of mitochondrial morphology (F), sperm morphology (G), and motility (H). N≥3.

For more information on motility, see Videos 2.1-3. All data are from adult P56 mice. Data are represented as mean ± SEM. ****$p \leq 0.0001$; ***$p \leq 0.001$; **$p \leq 0.01$; *$p \leq 0.05$. For statistical tests used, see Material and Methods section. See also Figure 1.S1 and Videos 2.1-3.

Figure 2.2: Mitofusins are required for meiosis.

(A) Testes weight measurements from juvenile P24 mice. N≥3.

(B) Periodic Acid-Schiff (PAS) histology testis sections. Note the absence of post-meiotic spermatids in S8::Dm tubules. Scale bars, 50 μm. On the right are stylized depictions of the 100X panels. SG, spermatogonium; SC, spermatocyte; ST, spermatid; Lum, lumen; Ser, Sertoli cell cytoplasm.

(C) Analysis of the major germ cell types in WT and mutant testis sections. For clarity, the borders of mutant seminiferous tubules are outlined by dashed lines. The markers used are indicated. Scale bar, 20 μm. Dn, mito-Dendra2

(D) Doughnut graphs tabulating the most differentiated cell type found in seminiferous tubule cross sections. For *p*-values, see Figure 2.S2A, which shows the same data displayed as bar charts. N=4.

(E) Quantification of germ cells in seminiferous tubule cross sections. Mutant values are plotted relative to control, which is set at 100% and indicated by the gray bar. There is an upward trend from differentiated spermatogonia to the leptotene/zygotene stage, but this difference was not statistically significant. N=4.

(F) Representative images of chromosomal spreads from WT spermatocytes in meiotic prophase I (MPI). Mutant meiotic spreads had no obvious chromosomal abnormalities. Scale bar, 20 μm.

(G) Quantification of MPI substages from chromosomal spreads. In the mutant, note the bottleneck at the zygotene-to-pachytene transition. N=4.

(H) Schematic of normal spermatogenesis (left), and the meiotic defect in mutants (right). ST, spermatid; MPI, Meiotic Prophase I; SC, spermatocyte; P/D, pachytene/diplotene; L/Z, leptotene/zygotene; SG, spermatogonium.

All data are from P24 juvenile mice. Data are represented as mean ± SEM. ****$p \leq 0.0001$; ***$p \leq 0.001$; **$p \leq 0.01$; *$p \leq 0.05$. For statistical tests used, see the Materials and Methods section. See also Figure 2.S2.

Figure 2.3: Spermatocytes undergo a metabolic shift during meiosis.

(A) Analysis of mitochondrial content in MPI spermatocytes from testis sections. Mitochondria were visualized by mito-Dendra2 (Dn). γH2AX staining was used to distinguish pachytene/diplotene spermatocytes from leptotene/zygotene spermatocytes, as in Figure 2C. For clarity, the border of the mutant seminiferous tubule is outlined by a dashed line. Scale bar, 20 μm.

(B) Quantification of mito-Dendra2 fluorescence in spermatocytes in testis sections. N=4.

(C) Analysis of mitochondrial morphology from meiotic spreads in WT spermatocytes. Mitochondria were visualized with the outer mitochondrial membrane marker, Tom20, and the stages of meiosis were distinguished by γH2AX staining. Note the clustering and elongation in Pachytene/Diplotene spermatocytes. Scale bar, 10 μm.

(D) Analysis of mitochondrial morphology in S8::Dm spermatocytes. Note the fragmented mitochondrial morphology in Pachytene/Diplotene. Scale bar, 10 μm.

(E) Selective expression of the mitochondrial pyruvate carrier, MPC1, in WT spermatocytes. The basement membrane at the tubule periphery is indicated by the yellow dashed line. The fluorescence of mitochondria within the boxed region were analyzed by line scanning (right). Arbitrary units, au. Scale bar, 10 μm.

(F) Comparison of oxygen consumption rates (OCR) from diploid versus tetraploid germ cells from WT adult testes (2-3 months). Germ cells were isolated by FACS and oxygen consumption analyzed with a Seahorse extracellular flux analyzer. 2N, diploid; 4N, tetraploid; Oligo, Oligomycin; CCCP, Carbonyl cyanide m-chlorophenyl hydrazine; Ant A, Antimycin A. The average values from 3 separate experiments are plotted.

SC, spermatocyte; P/D, pachytene/diplotene; L/Z, leptotene/zygotene; SG, spermatogonium. All data are from P24 mice unless otherwise noted. All data are from P24 mice. Data are represented as mean ± SEM. ***$p \leq 0.001$; *$p \leq 0.05$. For statistical tests used, see Material and Methods section. See also Figure 2.S3.

Figure 2.4: Long-term mitofusin loss results in depletion of all differentiated germ cell types.

(A) PAS histology in P56 testis sections. Scale bar, 50 μm. On the right are stylized depictions of the 100X panels. SG, spermatogonium; SC, spermatocyte; ST, spermatid; Lum, lumen; Ser, Sertoli cell cytoplasm.

(B) FACS analysis of germ cells in WT and mutant testes. Testes were dissociated and FACS was used to quantify the number of mito-Dendra2-positive germ cells. Dendra fluorescence (x-axis) is shown in arbitrary units (au). The histograms were normalized by plotting the same number of somatic (mito-Dendra2-negative) cells between S8::Control and S8::Dm samples.

(C) Quantification of the results from (B). N=5.

(D) Immunolabeling of the major germ cell types in WT and mutant animals. Scale bar, 20 µm.

(E) Doughnut graphs indicating germ cell types in seminiferous tubule cross sections. Each seminiferous tubule cross section was scored for its most advanced germ cell type. Note that in WT tubules, all seminiferous tubules contain spermatids. For *p*-values, see Figure 2.S4A. N=4.

(F) Quantification of germ cell types per tubule cross section. Mutant values are plotted relative to control, which is set to 100% and indicated by the gray bar. N=4.

(G) Immunolabeling of stem-like spermatogonia. PLZF marks all undifferentiated spermatogonia and GFRα1 marks stem-like spermatogonia. Note that all GFRα1 spermatogonia express PLZF, but not vice versa. Scale bar, 20 µm.

(H) Immunolabeling of the proliferation marker Ki-67 in GFRα1-expressing spermatogonia in testis section. Scale bar, 20 µm.

(I) Percent of GFRα1-expressing spermatogonia that are positive for the proliferation marker Ki67. N=4.

(J) Schematic of normal spermatogenesis (left) and the defect in P56 S8::Dm mice (right). SPZ, spermatozoon; ST, spermatid; MPI; Meiotic Prophase I; SC, spermatocyte; P/D, pachytene/diplotene; L/Z, leptotene/zygotene; SG, spermatogonium. Ac, acrosome, XY, sex body; PM, plasma membrane; Nuc, nucleus. N≥4, unless otherwise indicated. Data are represented as mean ± SEM. ****$p \leq 0.0001$; ***$p \leq 0.001$. For statistical tests used, see the Materials and Methods section. See also Figure 2.S4.

Figure 2.5: Mitofusin-deficient germ cells have increased apoptosis.

(A) EM tomograms from adult P56 testis sections highlighting mitochondrial cristae morphology. The following pseudocolors are used: mitochondrial matrix, blue; cristae lumen, pink; nucleus, green. Nuc, nucleus.

(B) Quantification of mitochondrial cristae morphology from EM tomograms. At least 70 cristae junctions were quantified from at least 4 different EM tomograms from a single mouse from each genotype.

(C) EM tomograms from testis sections highlighting cristae junctions. Mitochondrial matrices are colored blue, and mitochondrial intermembrane spaces and cristae are colored pink.

(D) Quantification of cristae junction diameters from EM tomograms.

(E) TUNEL staining of PFA-fixed testis sections. Cells were labeled for TUNEL, mito-Dendra2 (Dn), and nuclei (DAPI). Scale bars, 20 μm.

(F) Quantification showing the percentage of seminiferous tubule cross-sections containing TUNEL-positive cells. N=3.

Data are represented as mean ± SEM. ****$p \leq 0.0001$; ***$p \leq 0.001$; **$p \leq 0.01$; *$p \leq 0.05$. For statistical tests used, see the Materials and Methods section. See also Figure 2.S5.

Figure 2.6: Mitofusin-deficient MEFs have reduced OXPHOS subunits and mitochondrial ribosomes.

(A) Volcano plot showing enriched Gene Ontology terms from SILAC experiments in MEFs. SILAC was performed on isolated mitochondria from WT and *Mfn1/Mfn2*-null MEFs. See also Table 2.1.

(B) Comparison of individual mitochondrial proteins from SILAC analysis of MEFs. Bar charts show the protein ratios in *Mfn1/Mfn2-null* versus WT. Only proteins with ratios that reached statistical significance ($p \leq 0.05$) are plotted. For a complete list of proteins, see Table 2.1. The black dashed line indicates a mutant to WT ratio of 1:1. Magenta bars indicate proteins that are reduced and green bars indicate proteins that are increased. See also Table 2.2. Two biological replicates were used. Assembly factor, AF. For statistical tests used, see the Materials and Methods section.

Figure 2.7: Mitofusin-deficient immortalized spermatocytes have reduced OXPHOS subunits and activity.

(A) Immunostaining against the mitochondrial outer membrane marker, Tom20 in an immortalized spermatocyte cell line, GC-2Spd(ts) (GC). Note the mitochondrial fragmentation in shMfn1;Mfn2 treated cells compared to the non-targeting control. Scale bar, 20 μm.

(B) Quantification of mitochondrial morphology in GCs. Mean values from 3 replicates are plotted.

(C) Western blots showing various respiratory chain complexes in GCs. NT, non-targeting.

(D) Densitometry analysis of western blots. Mean values from 4 replicates are plotted.

(E) Oxygen Consumption Rate (OCR) measurements in GCs.

(F) Quantification from E.

(G) Extracellular Acidification Rate (ECAR) measurements in GCs.

Oligo, oligomycin; CCCP, carbonyl cyanide m-chlorophenyl hydrazine; Ant A, antimycin A. Data are represented as mean ± SEM. ****$p \leq 0.0001$; ***$p \leq 0.001$; **$p \leq 0.01$. For statistical tests used, see the Materials and Methods section. See also Figure 2.S7.

Figure 2.8: *In vivo* spermatocytes have heterogeneous mitochondria and reduced OXPHOS activity.

(A) Immunolabeling of NDUFB6, MTCOI, and MPC1 in spermatocytes in testis sections. Line scans are shown as arbitrary units (au) to the right. Scale bars, 20 μm.

(B) Quantification showing the percentage of spermatocytes with reduced or heterogeneous staining. L/Z, leptotene/zygotene; P/D, pachytene/diplotene. N=4.

(C) COX/SDH enzyme histochemistry in adult testis sections. Note that mutant sections have much reduced OXPHOS activity. Scale bars, 50 μm. ST, spermatid; SC, spermatocyte; SG, spermatogonium.

Data are represented as mean ± SEM. ****$p \leq 0.0001$; ***$p \leq 0.001$; **$p \leq 0.01$. For statistical tests used, see the Materials and Methods section. See also Figure 2.S8.

Figure 2.9: Model.

Top panel. Two key transitions during normal spermatogenesis are indicated: spermatogonial differentiation and the metabolic shift during meiosis. The metabolic shift includes increased mitochondrial biogenesis, fusion, and OXPHOS. Bottom panel. In juvenile mitochondrial fusion-deficient mice, spermatocytes have functionally heterogeneous mitochondria that are unable to accomplish this metabolic shift, resulting in meiotic arrest. Adult mutant mice have an earlier defect, wherein all differentiating germ cell types are lost, but self-renewal of stem-like undifferentiated spermatogonia remains intact.

Chapter 2 Figures

Figure 2.1

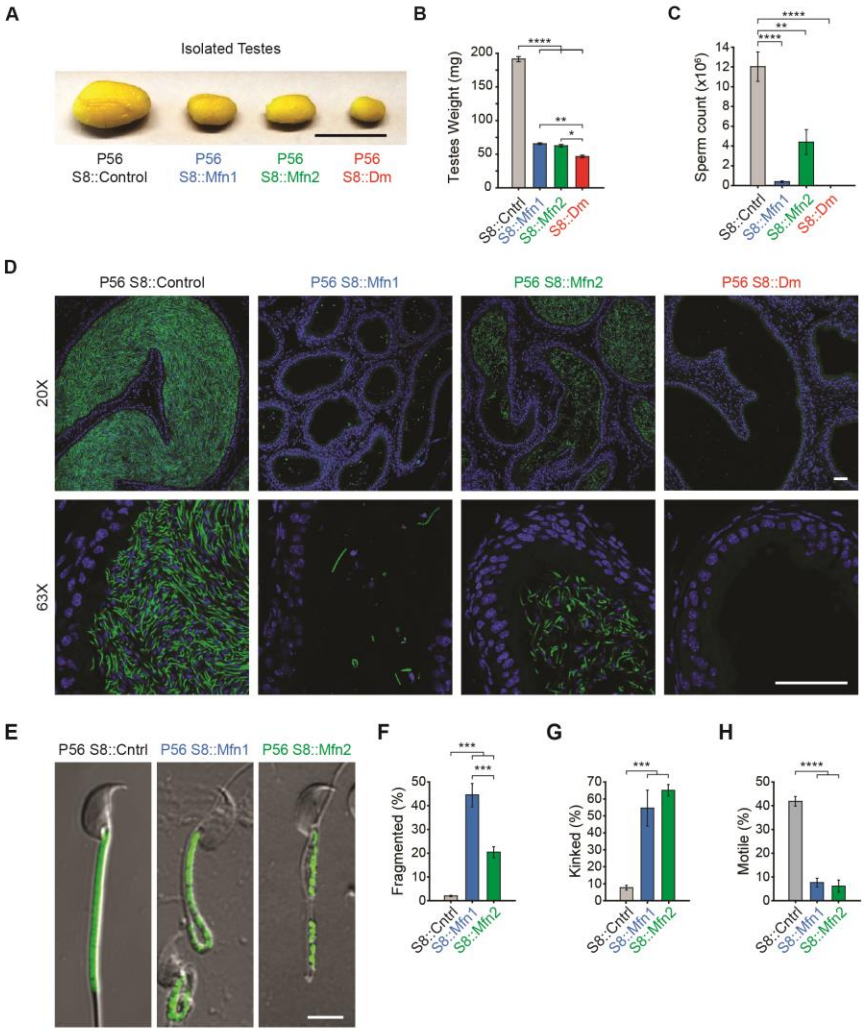

Figure 2.2

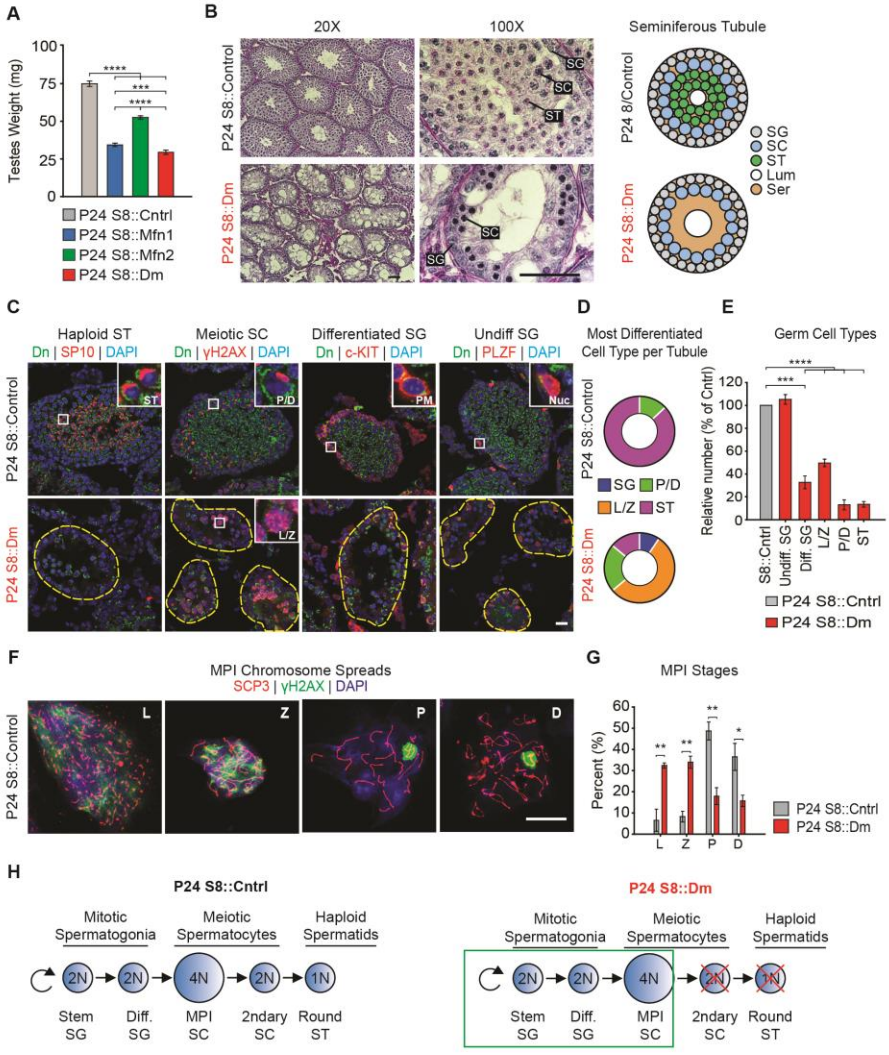
A
Testes Weight (mg)
100
75
50
25
0
****
***
****
P24 S8::Cntrl
P24 S8::Mfn1
P24 S8::Mfn2
P24 S8::Dm
B
20X
100X
Seminiferous Tubule
P24 S8::Control
P24 S8::Dm
SG
SC
ST
P24 8/Control
P24 S8::Dm
SG
SC
ST
Lum
Ser
C
Haploid ST
Dn | SP10 | DAPI
Meiotic SC
Dn | γH2AX | DAPI
Differentiated SG
Dn | c-KIT | DAPI
Undiff SG
Dn | PLZF | DAPI
P24 S8::Control
P24 S8::Dm
ST
P/D
PM
Nuc
L/Z
D
Most Differentiated
Cell Type per Tubule
P24 S8::Control
P24 S8::Dm
SG
P/D
L/Z
ST
E
Germ Cell Types
Relative number (% of Cntrl)
120
100
80
60
40
20
0
****
***
S8::Cntrl
Undiff. SG
Diff. SG
L/Z
P/D
ST
P24 S8::Cntrl
P24 S8::Dm
F
MPI Chromosome Spreads
SCP3 | γH2AX | DAPI
P24 S8::Control
L
Z
P
D
G
MPI Stages
Percent (%)
60
50
40
30
20
10
0
**
**
**
*
L
Z
P
D
P24 S8::Cntrl
P24 S8::Dm
H
P24 S8::Cntrl
Mitotic Spermatogonia
Meiotic Spermatocytes
Haploid Spermatids
2N
2N
4N
2N
1N
Stem SG
Diff. SG
MPI SC
2ndary SC
Round ST
P24 S8::Dm
Mitotic Spermatogonia
Meiotic Spermatocytes
Haploid Spermatids
2N
2N
4N
2N
1N
Stem SG
Diff. SG
MPI SC
2ndary SC
Round ST

Figure 2.3

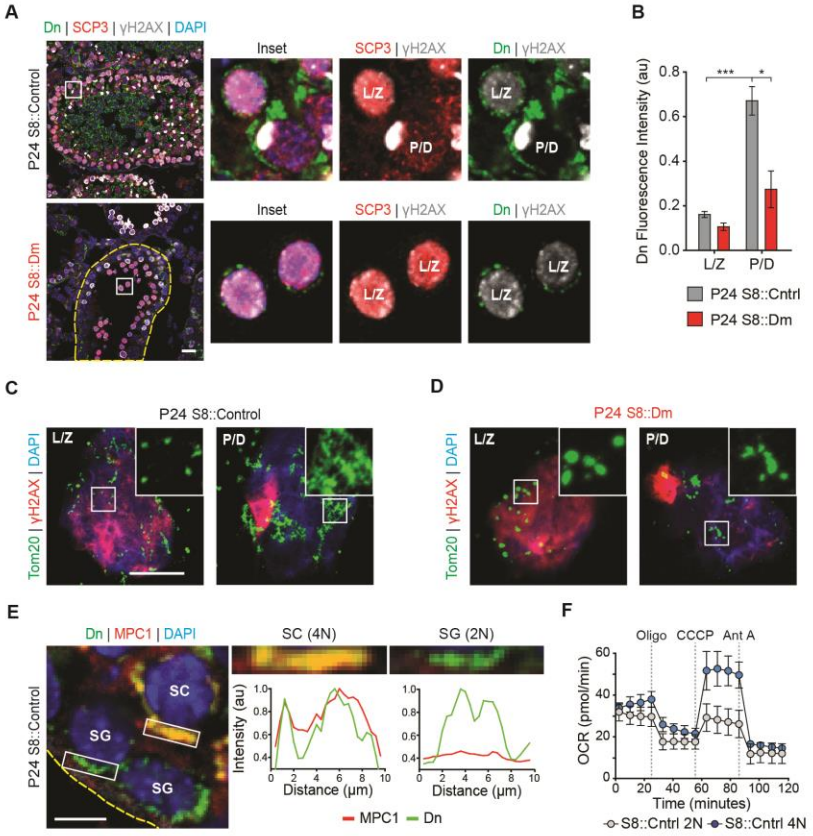
A
Dn | SCP3 | γH2AX | DAPI
P24 S8::Control
P24 S8::Dm
Inset
SCP3 | γH2AX
Dn | γH2AX
L/Z
P/D
B
Dn Fluorescence Intensity (au)
***
*
L/Z
P/D
P24 S8::Cntrl
P24 S8::Dm
C
P24 S8::Control
Tom20 | γH2AX | DAPI
D
P24 S8::Dm
E
Dn | MPC1 | DAPI
SC
SG
SC (4N)
SG (2N)
Intensity (au)
Distance (μm)
MPC1
Dn
F
Oligo
CCCP
Ant A
OCR (pmol/min)
Time (minutes)
S8::Cntrl 2N
S8::Cntrl 4N

Figure 2.4

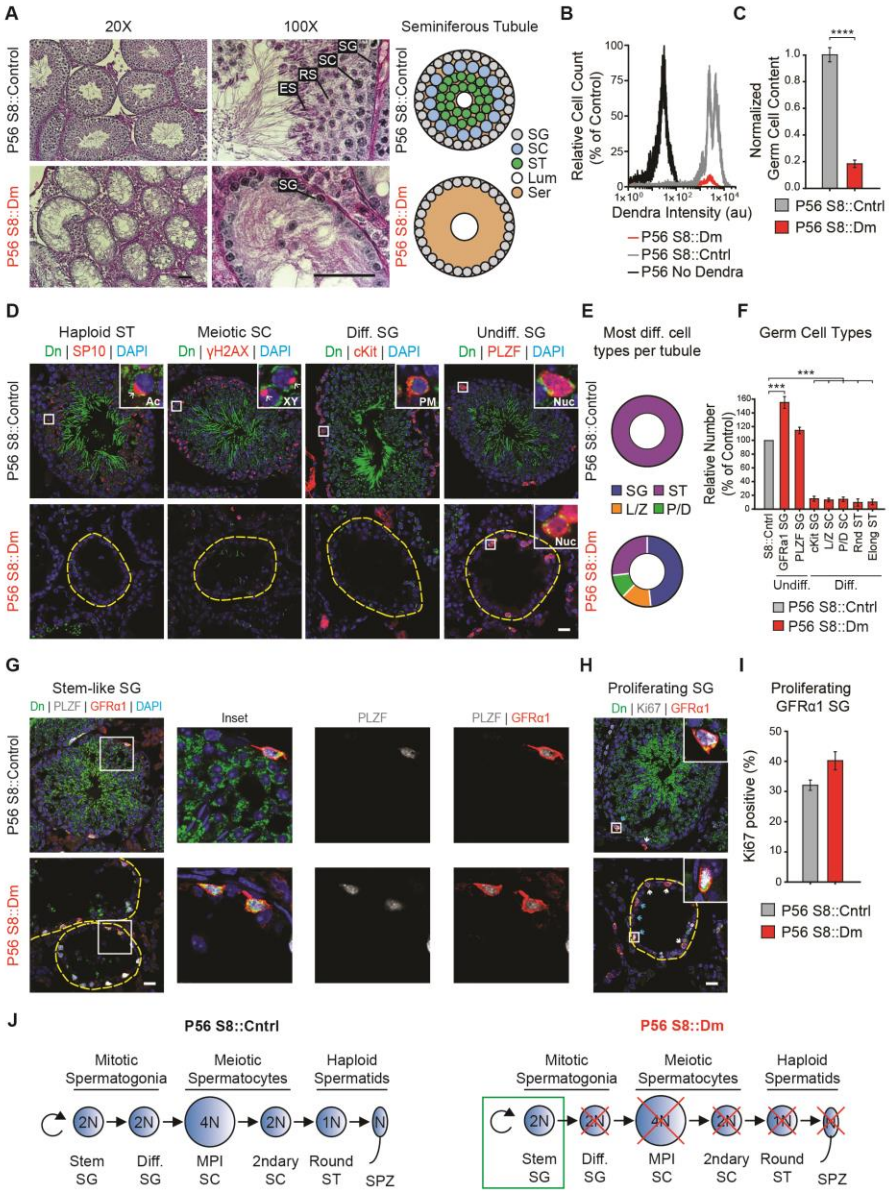
A
20X
100X
Seminiferous Tubule
P56 S8::Control
P56 S8::Dm
SG
SC
RS
ES
ST
Lum
Ser
B
Relative Cell Count (% of Control)
Dendra Intensity (au)
P56 S8::Dm
P56 S8::Cntrl
P56 No Dendra
C
Normalized Germ Cell Content
P56 S8::Cntrl
P56 S8::Dm
D
Haploid ST
Dn | SP10 | DAPI
Meiotic SC
Dn | γH2AX | DAPI
Diff. SG
Dn | cKit | DAPI
Undiff. SG
Dn | PLZF | DAPI
Ac
XY
PM
Nuc
E
Most diff. cell types per tubule
SG
ST
L/Z
P/D
F
Germ Cell Types
Relative Number (% of Control)
S8::Cntrl
GFRa1 SG
PLZF SG
cKit SG
L/Z SC
P/D SC
Rnd ST
Elong ST
Undiff.
Diff.
P56 S8::Cntrl
P56 S8::Dm
G
Stem-like SG
Dn | PLZF | GFRα1 | DAPI
Inset
PLZF
PLZF | GFRα1
H
Proliferating SG
Dn | Ki67 | GFRα1
I
Proliferating GFRα1 SG
Ki67 positive (%)
P56 S8::Cntrl
P56 S8::Dm
J
P56 S8::Cntrl
P56 S8::Dm
Mitotic Spermatogonia
Meiotic Spermatocytes
Haploid Spermatids
2N
4N
1N
N
Stem SG
Diff. SG
MPI SC
2ndary SC
Round ST
SPZ

Figure 2.5

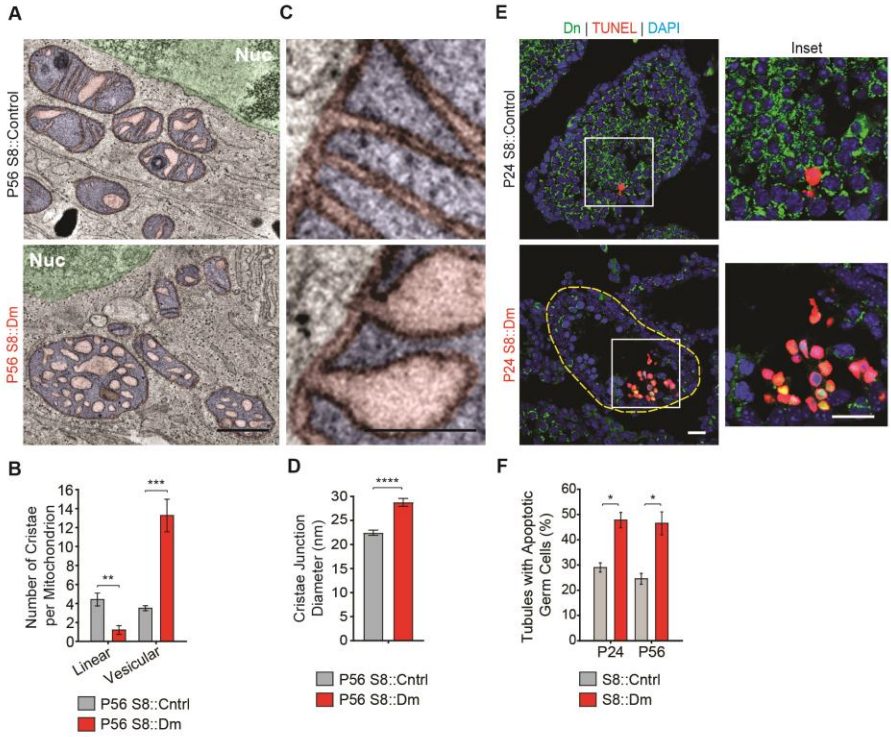
A
C
E
Dn | TUNEL | DAPI
Inset
P56 S8::Control
P56 S8::Dm
P24 S8::Control
P24 S8::Dm
Nuc
Nuc
B
Number of Cristae per Mitochondrion
Linear
Vesicular
P56 S8::Cntrl
P56 S8::Dm
D
Cristae Junction Diameter (nm)
P56 S8::Cntrl
P56 S8::Dm
F
Tubules with Apoptotic Germ Cells (%)
P24
P56
S8::Cntrl
S8::Dm

Figure 2.6

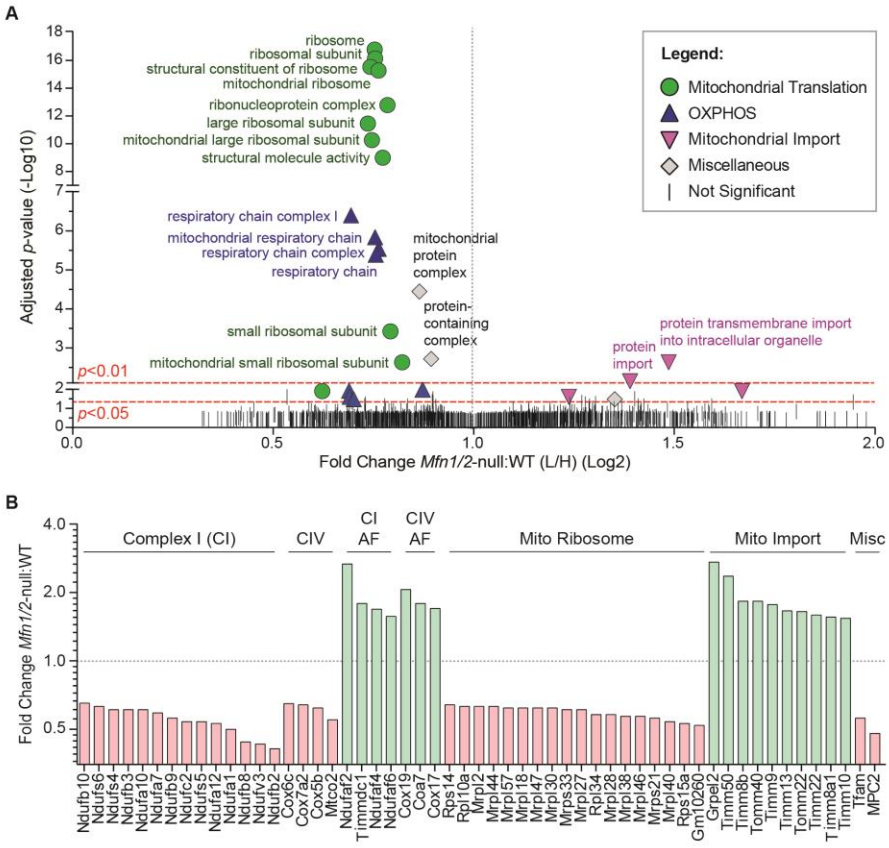
A
Adjusted p-value (-Log10)
Fold Change Mfn1/2-null:WT (L/H) (Log2)
Legend:
Mitochondrial Translation
OXPHOS
Mitochondrial Import
Miscellaneous
Not Significant
ribosome
ribosomal subunit
structural constituent of ribosome
mitochondrial ribosome
ribonucleoprotein complex
large ribosomal subunit
mitochondrial large ribosomal subunit
structural molecule activity
respiratory chain complex I
mitochondrial respiratory chain
respiratory chain complex
respiratory chain
mitochondrial protein complex
protein-containing complex
small ribosomal subunit
mitochondrial small ribosomal subunit
protein transmembrane import into intracellular organelle
protein import
p<0.01
p<0.05
B
Fold Change Mfn1/2-null:WT
Complex I (CI)
CIV
CI AF
CIV AF
Mito Ribosome
Mito Import
Misc
Ndufb10
Ndufs6
Ndufs4
Ndufb3
Ndufa10
Ndufa7
Ndufb9
Ndufc2
Ndufs5
Ndufa12
Ndufa1
Ndufb8
Ndufv3
Ndufb2
Cox6c
Cox7a2
Cox5b
Mtco2
Ndufaf2
Timmdc1
Ndufaf4
Ndufaf6
Cox19
Coa7
Cox17
Rps14
Rpl10a
Mrpl2
Mrpl44
Mrpl57
Mrpl18
Mrpl47
Mrpl30
Mrps33
Mrpl27
Rpl34
Mrpl28
Mrpl38
Mrpl46
Mrps21
Mrpl40
Rps15a
Gm10260
Grpel2
Timm50
Timm8b
Tomm40
Timm9
Timm13
Tomm22
Timm8a1
Timm10
Ttam
MPC2

Figure 2.7

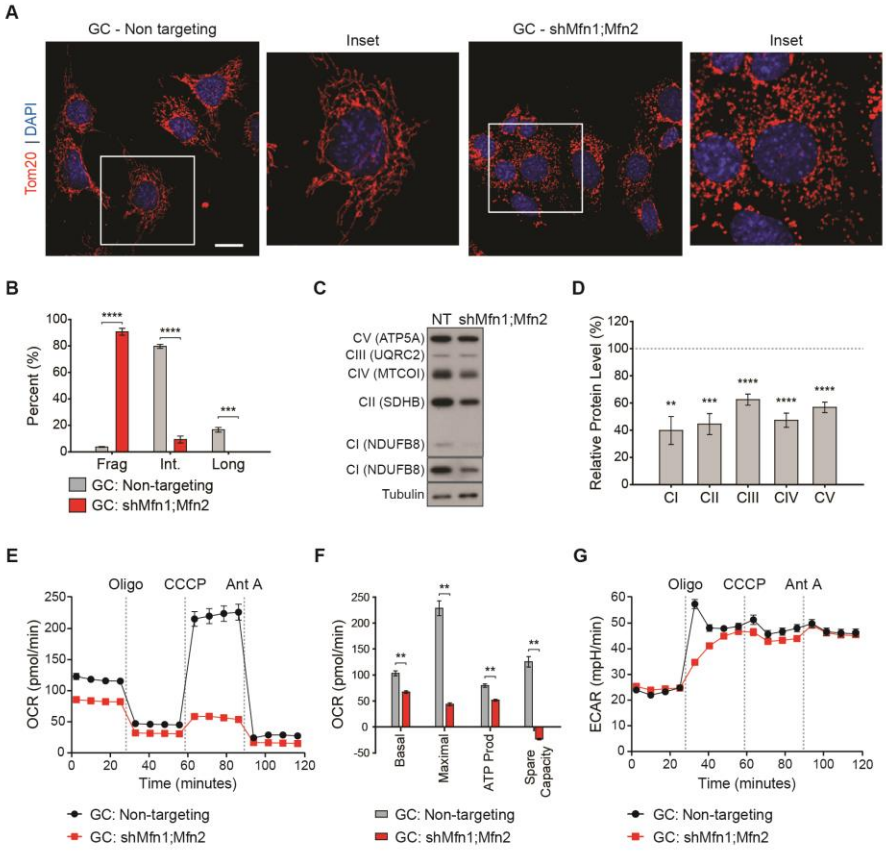
A
GC - Non targeting
Inset
GC - shMfn1;Mfn2
Inset
Tom20 | DAPI
B
Percent (%)
Frag
Int.
Long
GC: Non-targeting
GC: shMfn1;Mfn2
C
NT shMfn1;Mfn2
CV (ATP5A)
CIII (UQRC2)
CIV (MTCOI)
CII (SDHB)
CI (NDUFB8)
CI (NDUFB8)
Tubulin
D
Relative Protein Level (%)
CI
CII
CIII
CIV
CV
E
Oligo
CCCP
Ant A
OCR (pmol/min)
Time (minutes)
GC: Non-targeting
GC: shMfn1;Mfn2
F
OCR (pmol/min)
Basal
Maximal
ATP Prod
Spare Capacity
GC: Non-targeting
GC: shMfn1;Mfn2
G
Oligo
CCCP
Ant A
ECAR (mpH/min)
Time (minutes)
GC: Non-targeting
GC: shMfn1;Mfn2

Figure 2.8

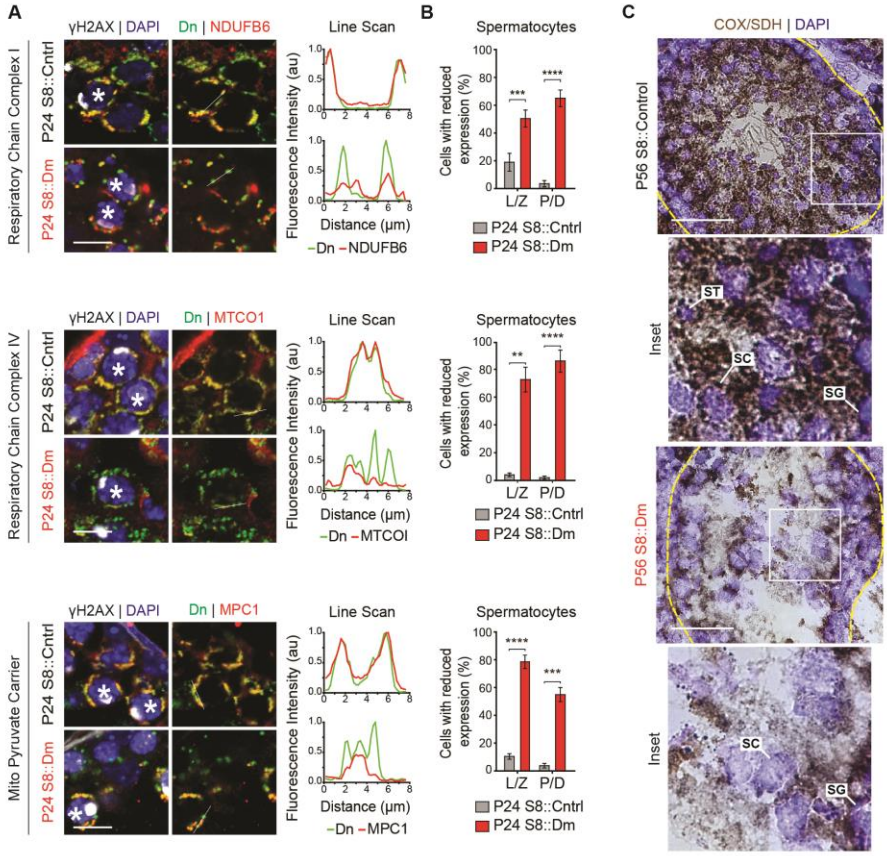
A
γH2AX | DAPI
Dn | NDUFB6
Line Scan
Respiratory Chain Complex I
P24 S8::Cntrl
P24 S8::Dm
Fluorescence Intensity (au)
Distance (μm)
Dn
NDUFB6
γH2AX | DAPI
Dn | MTCO1
Line Scan
Respiratory Chain Complex IV
P24 S8::Cntrl
P24 S8::Dm
Fluorescence Intensity (au)
Distance (μm)
Dn
MTCOI
γH2AX | DAPI
Dn | MPC1
Line Scan
Mito Pyruvate Carrier
P24 S8::Cntrl
P24 S8::Dm
Fluorescence Intensity (au)
Distance (μm)
Dn
MPC1
B
Spermatocytes
Cells with reduced expression (%)
L/Z
P/D
P24 S8::Cntrl
P24 S8::Dm
Spermatocytes
Cells with reduced expression (%)
L/Z
P/D
P24 S8::Cntrl
P24 S8::Dm
Spermatocytes
Cells with reduced expression (%)
L/Z
P/D
P24 S8::Cntrl
P24 S8::Dm
C
COX/SDH | DAPI
P56 S8::Control
Inset
ST
SC
SG
P56 S8::Dm
Inset
SC
SG

Figure 2.9

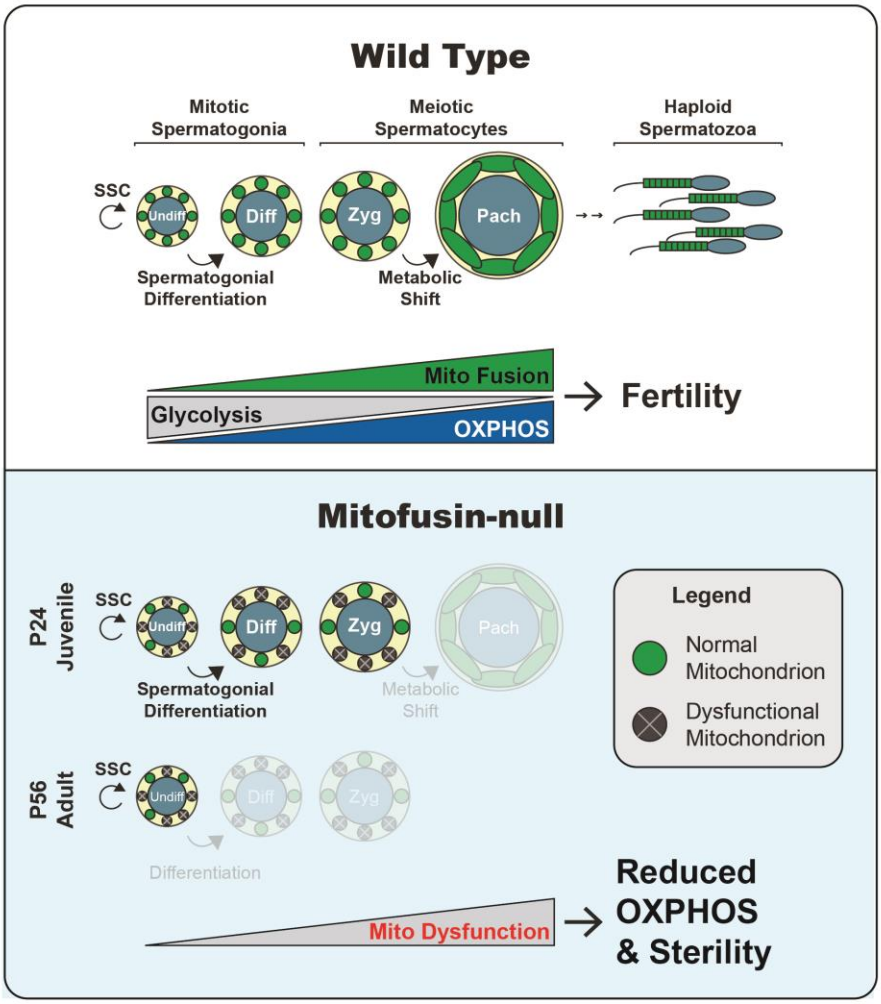
Wild Type
Mitotic Spermatogonia
Meiotic Spermatocytes
Haploid Spermatozoa
SSC
Undiff
Diff
Zyg
Pach
Spermatogonial Differentiation
Metabolic Shift
Mito Fusion
Glycolysis
OXPHOS
Fertility
Mitofusin-null
P24 Juvenile
SSC
Undiff
Diff
Zyg
Pach
Spermatogonial Differentiation
Metabolic Shift
Legend
Normal Mitochondrion
Dysfunctional Mitochondrion
P56 Adult
SSC
Undiff
Diff
Zyg
Differentiation
Mito Dysfunction
Reduced OXPHOS & Sterility

Chapter 2 Supplemental figure legends

Figure 2.S1

(A) mito-Dendra2 (Dn) expression in testis sections. Note that the classical Sertoli cell projections contain Tom20 (a marker of the mitochondrial outer membrane), but not the germ cell-specific mito-Dendra2. Some of these projections are underlined in yellow. Scale bar, 20 μm.

(B) Cre activity in undifferentiated spermatogonia. Mitochondria are labeled with mito-Dendra2 (Dn) (green); total undifferentiated spermatogonia are labeled with an antibody against PLZF (white); stem-like spermatogonia are labeled with an antibody against GFRα1 (red); and nuclei are labeled with DAPI (blue). The mito-Dendra2 allele requires *Stra8-Cre*-mediated excision for expression. Scale bar, 20 μm.

(C) Quantitation of *Stra8-Cre/Dn* expression in GFRα1 stem-like spermatogonia from testis sections. N=3. A total of 150 cells were counted. Data are represented as mean ± SEM. For statistical tests used, see the Materials and Methods section.

(D) Quantification of animal weight from the indicated mouse lines. N≥7. All data are from P56 mice. Data are represented as mean ± SEM. For statistical tests used, see the Materials and Methods section.

Figure 2.S2

(A) Same data as in Figure 2.2D, but displayed as bar charts to indicate statistical significance. ST, spermatid; P/D, pachytene/diplotene; L/Z, leptotene/zygotene; SG,

spermatogonium. N=4. Data are represented as mean ± SEM. ****$p \leq 0.0001$; ***$p \leq 0.001$; *$p \leq 0.05$. For statistical tests used, see the Materials and Methods section.

(B) PAS-stained testis sections from the indicated genotypes. Note the absence of spermatids in S8::Mfn1 tubules. Scale bar, 50 µm.

(C) Chromosome spread analysis in the indicated genotypes. Note the meiotic block in S8::Mfn1, but not S8::Mfn2 mice. N=6. Data are represented as mean ± SEM. **$p \leq 0.01$; *$p \leq 0.05$. For statistical tests used, see the Materials and Methods section.

Figure 2.S3

(A) Analysis of sorted germ cells by immunostaining with specific markers. Scale bars, 20 µm.

(B) Quantification of OXPHOS parameters from Figure 2.3F. The average values from 3 independent experiments are plotted. Data are represented as mean ± SEM. *$p \leq 0.05$. For statistical tests used, see the Materials and Methods section.

Figure 2.S4

(A) Plot of the most differentiated cell type found in seminiferous tubules. Same data as in Figure 2.4E, but displayed as bar charts to indicate statistical significance. N=4. Data are represented as mean ± SEM. ****$p \leq 0.0001$; **$p \leq 0.01$; *$p \leq 0.05$. For statistical tests used, see the Materials and Methods section.

(B) Quantification of *Stra8-Cre/Dn* expression in stem-like GFRα1-expressing spermatogonia. N=3. 150 cells were counted from each genotype. For statistical tests used, see the Materials and Methods section.

(C) Testis sections from 4-months-old S8::Dm mice stained with PLZF or Ki-67. Scale bar, 20 µm.

(D) PAS-stained testis histology of the indicated genotypes. Note the loss of germ cells from the center of the tubules in both S8::Mfn1 and S8::Mfn2 mice. Scale bars, 50 µm.

(E) Quantification of c-Kit expressing spermatogonia in the indicated genotypes. N=4.

Data are represented as mean ± SEM. ***$p \leq 0.001$. For statistical tests used, see the Materials and Methods section.

Figure 2.S5

Size distribution of cristae junction diameters in spermatocytes from Figures 2.5C and 2.5D. 99 CJs were measured from control and 118 from mutant.

Figure 2.S6

Schematic of SILAC experiment in MEFs.

Figure 2.S7

(A)Western blots showing Mfn1 and Mfn2 levels in the GC-2spd(ts) cell line after knockdown. NT, non-targeting.

(B) Densitometry analysis of western blots, plotted relative to control, which was set at 100%. Tubulin was used a loading control. Mean values from four replicates are plotted. Data are represented as mean ± SEM. ****$p \leq 0.0001$. For statistical tests used, see the Materials and Methods section.

(C) Quantification of mitochondrial morphology in MEFs. Mean values from three replicates are plotted. Data are represented as mean ± SEM. **$p \leq 0.01$. For statistical tests used, see the Materials and Methods section.

(D) Oxygen Consumption Rate (OCR) measurements in MEFs. Oligo, Oligomycin; CCCP, Carbonyl cyanide m-chlorophenyl hydrazine; Ant A, Antimycin A. Data are represented as mean ± SEM. For statistical tests used, see the Materials and Methods section.

Figure 2.S8

(A) Immunolabeling of the mtDNA-encoded respiratory chain complex IV subunit MTCOI (green). Mitochondria are labeled with the outer mitochondrial membrane marker Tom20 (red). Scale bar, 20 μm.

(B) Analysis of mitochondrial heterogeneity in differentiated and undifferentiated spermatogonia. MTCOXI protein was examined in c-Kit-positive cells (differentiated spermatogonia) and PLZF-positive cells (undifferentiated spermatogonia). Line scans are shown as arbitrary units (au) to the right. SG, spermatogonia. Scale bar, 20 μm.

(C) Quantification showing the percentage of differentiated and undifferentiated spermatogonia with heterogeneous MTCOXI protein. N=4. Data are represented as mean ± SEM. *$p \leq 0.05$. For statistical tests used, see the Materials and Methods section.

(D) COX/SDH enzyme histochemistry in isolated spermatozoa from S8::Mfn1 and S8::Mfn2 mice. S8::Dm mice do not produce any sperm. Scale bars, 10 µm.

(E) Quantification of COX and SDH pixel intensity from midpieces of isolated spermatozoa. N=3. Data are represented as mean ± SEM. ***$p \leq 0.001$; **$p \leq 0.01$. For statistical tests used, see the Materials and Methods section.

Supplementary Video 2.1

Supplementary file 2.1, Related to Figure 2.6A

Table showing enriched Gene Ontology terms from SILAC experiments in MEFs. SILAC was performed on mitochondria isolated from WT or *Mfn1/Mfn2*-null MEFs.

Supplementary file 2.2, Related to Figure 2.6B

Table showing the SILAC ratios for individual mitochondrial proteins.

Please download the supplementary table files using the following link: Supplementary files - Chapter 2

Chapter 2 Supplemental figures

Figure 2S.1

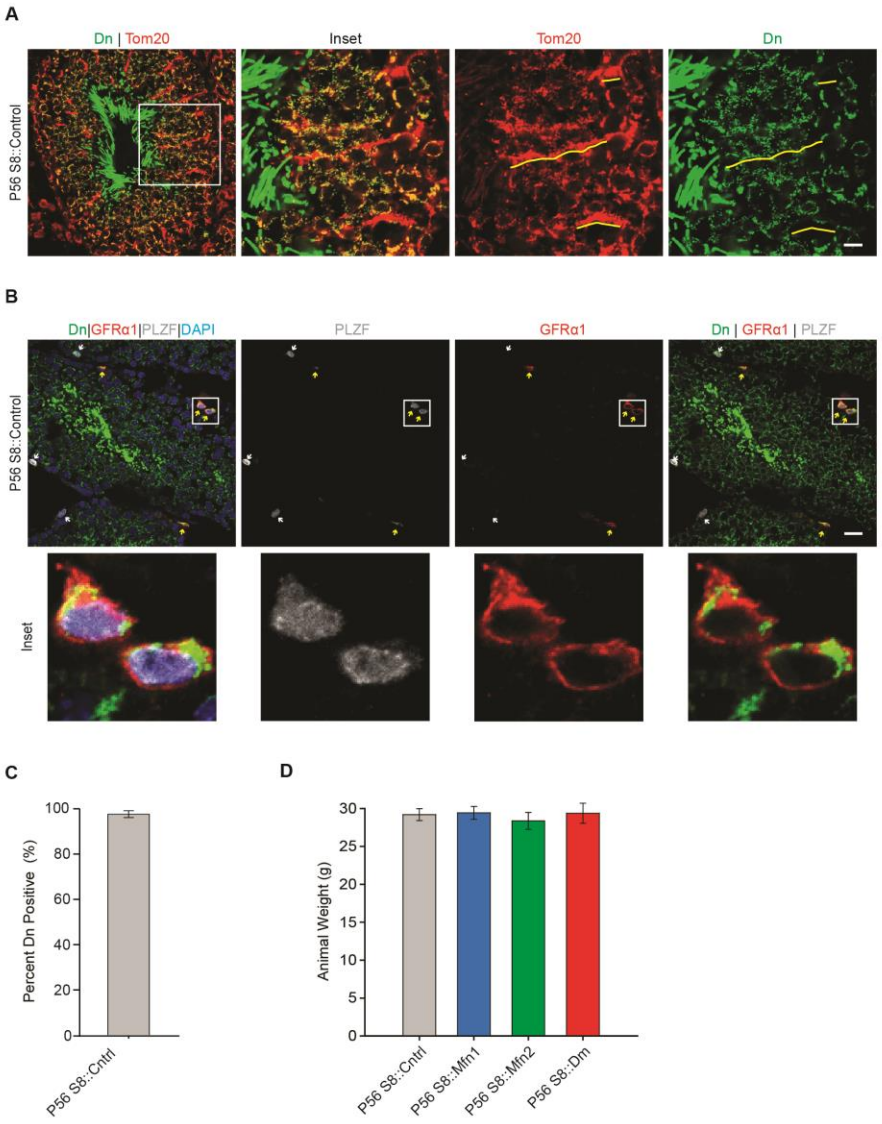

Figure 2S.2

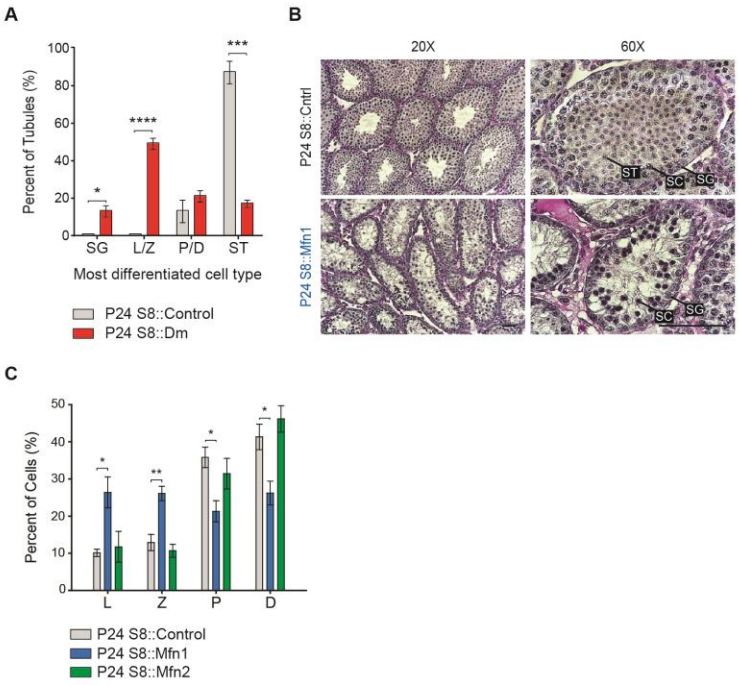
A
Percent of Tubules (%)
100
80
60
40
20
0
*
****
***
SG
L/Z
P/D
ST
Most differentiated cell type
P24 S8::Control
P24 S8::Dm
B
20X
60X
P24 S8::Cntrl
P24 S8::Mfn1
ST
SC
SG
SC
SG
C
Percent of Cells (%)
50
40
30
20
10
0
*
**
*
*
L
Z
P
D
P24 S8::Control
P24 S8::Mfn1
P24 S8::Mfn2

Figure 2S.3

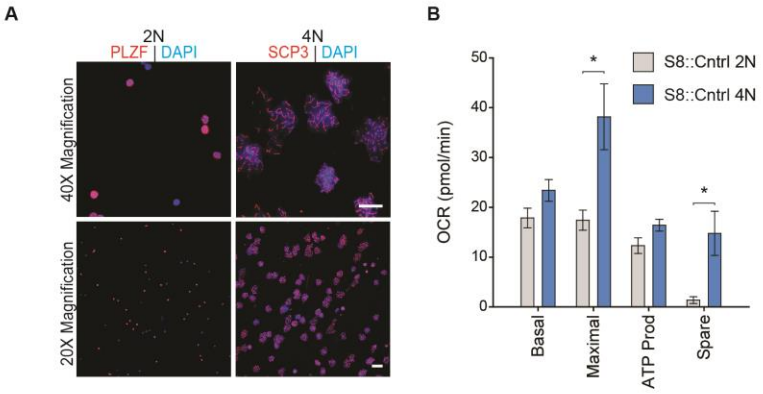
A
2N
PLZF | DAPI
4N
SCP3 | DAPI
40X Magnification
20X Magnification
B
OCR (pmol/min)
50
40
30
20
10
0
S8::Cntrl 2N
S8::Cntrl 4N
*
*
Basal
Maximal
ATP Prod
Spare

Figure 2S.4

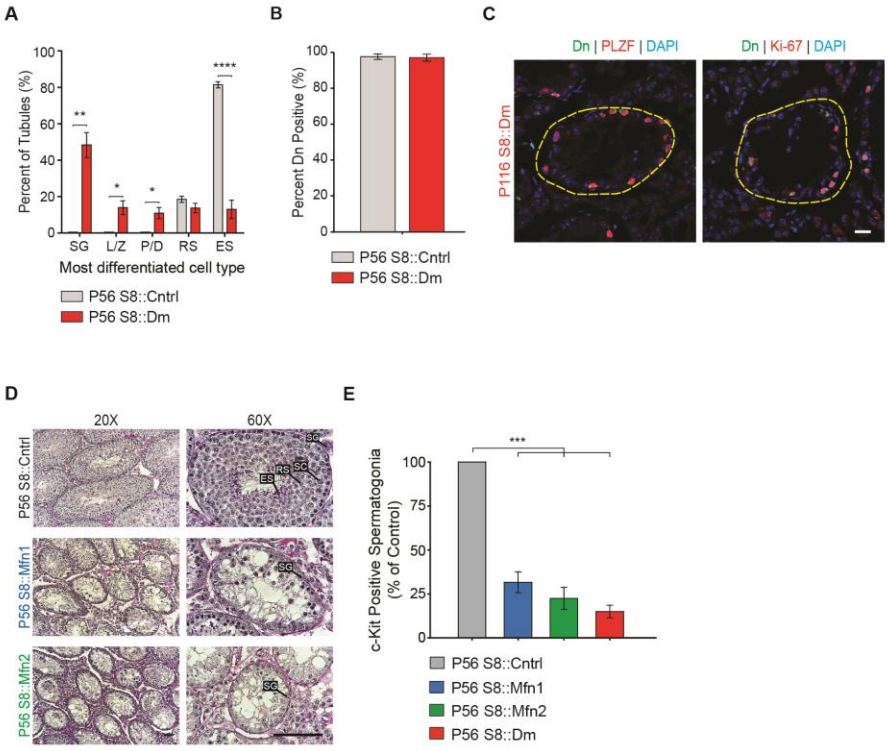
A
Percent of Tubules (%)
100
80
60
40
20
0
**
*
*
****
SG
L/Z
P/D
RS
ES
Most differentiated cell type
P56 S8::Cntrl
P56 S8::Dm
B
Percent Dn Positive (%)
100
80
60
40
20
0
P56 S8::Cntrl
P56 S8::Dm
C
Dn | PLZF | DAPI
Dn | Ki-67 | DAPI
P116 S8::Dm
D
20X
60X
P56 S8::Cntrl
P56 S8::Mfn1
P56 S8::Mfn2
SG
RS
ES
E
***
c-Kit Positive Spermatogonia (% of Control)
100
75
50
25
0
P56 S8::Cntrl
P56 S8::Mfn1
P56 S8::Mfn2
P56 S8::Dm

Figure 2S.5

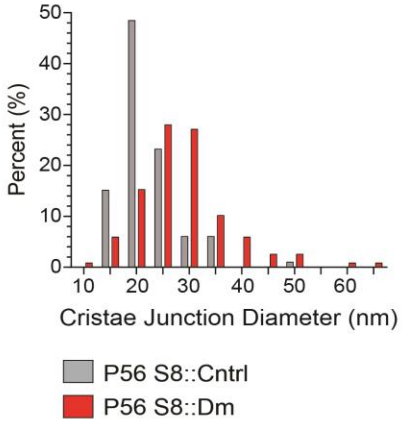
50
40
30
20
10
0
Percent (%)
10
20
30
40
50
60
Cristae Junction Diameter (nm)
P56 S8::Cntrl
P56 S8::Dm

Figure 2S.6

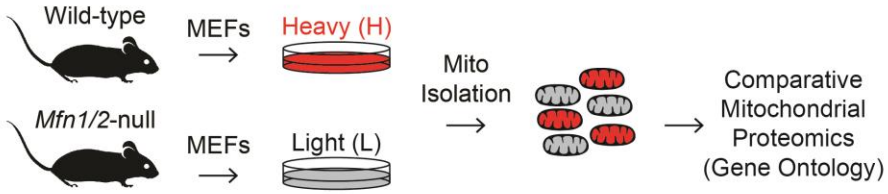
Wild-type
MEFs
Heavy (H)
Mfn1/2-null
MEFs
Light (L)
Mito
Isolation
Comparative
Mitochondrial
Proteomics
(Gene Ontology)

Figure 2S.7

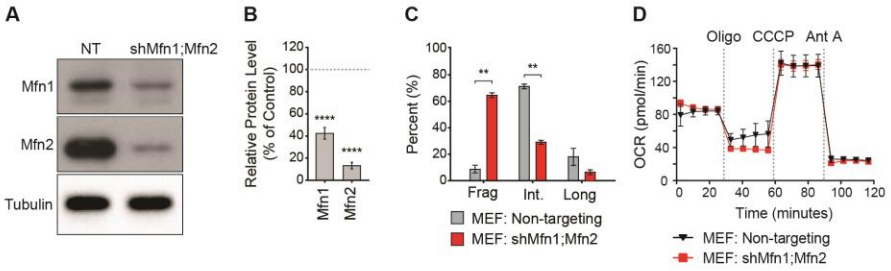
A
NT
shMfn1;Mfn2
Mfn1
Mfn2
Tubulin
B
Relative Protein Level (% of Control)
Mfn1
Mfn2
C
Percent (%)
Frag
Int.
Long
MEF: Non-targeting
MEF: shMfn1;Mfn2
D
Oligo
CCCP
Ant A
OCR (pmol/min)
Time (minutes)
MEF: Non-targeting
MEF: shMfn1;Mfn2

Figure 2S.8

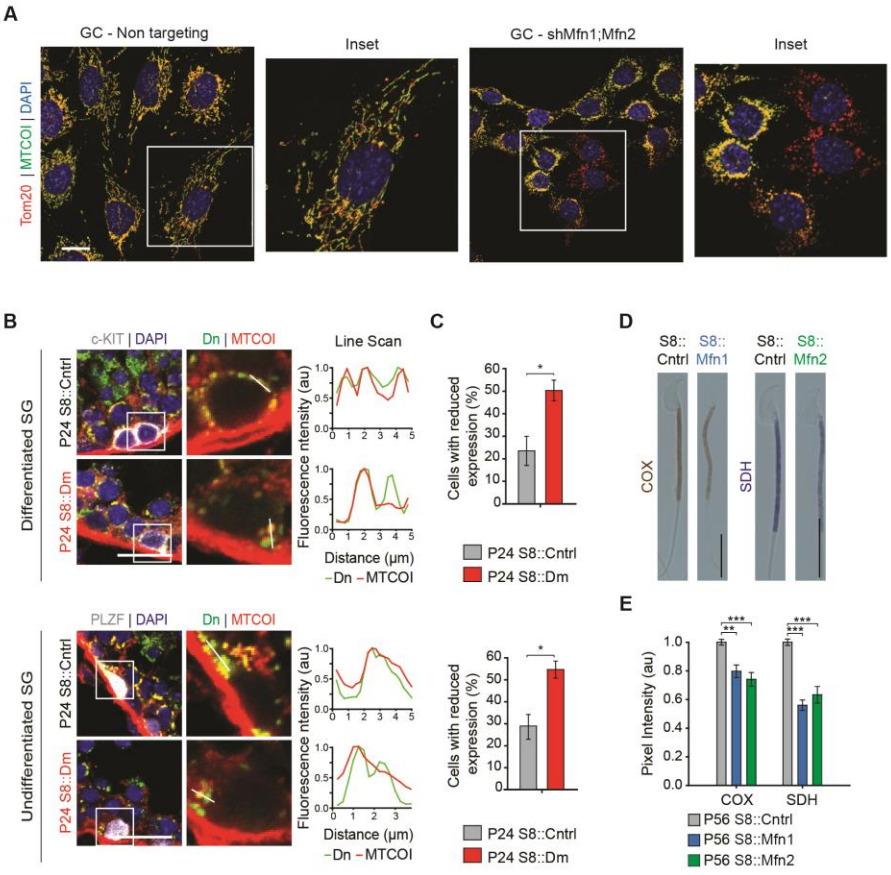
A
GC - Non targeting
Inset
GC - shMfn1;Mfn2
Inset
Tom20 | MTCOI | DAPI
B
c-KIT | DAPI
Dn | MTCOI
Line Scan
Differentiated SG
P24 S8::Cntrl
P24 S8::Dm
Fluorescence ntensity (au)
Distance (μm)
Dn
MTCOI
PLZF | DAPI
Undifferentiated SG
C
Cells with reduced expression (%)
P24 S8::Cntrl
P24 S8::Dm
D
S8:: Cntrl
S8:: Mfn1
S8:: Cntrl
S8:: Mfn2
COX
SDH
E
Pixel Intensity (au)
COX
SDH
P56 S8::Cntrl
P56 S8::Mfn1
P56 S8::Mfn2

Video legends

Video 2.1:

Movie of sperm isolated from P56 S8::Control mice.

Video 2.2:

Movie of sperm isolated from P56 S8::Mfn1 mice.

Video 2.3:

Movie of sperm isolated from P56 S8::Mfn2 mice.

Video 2.4:

EM tomogram of mitochondrion from P56 S8::Dm testis section showing that all cristae in the 400 nm testis section that can be traced back to the mitochondrial inner membrane are connected via cristae junctions. Scale bar, 200 nm.

Video files

Please download video files using the following link: Video files - Chapter 2

References

Bajpai, M., Gupta, G., & Setty, B. S. (1998). Changes in carbohydrate metabolism of testicular germ cells during meiosis in the rat. *Eur J Endocrinol, 138*(3), 322-327.

Baklouti-Gargouri, S., Ghorbel, M., Ben Mahmoud, A., Mkaouar-Rebai, E., Cherif, M., Chakroun, N., . . . Ammar-Keskes, L. (2014). Identification of a novel m.9588G > a missense mutation in the mitochondrial COIII gene in asthenozoospermic Tunisian infertile men. *J Assist Reprod Genet, 31*(5), 595-600. doi:10.1007/s10815-014-0187-2

Bastos, H., Lassalle, B., Chicheportiche, A., Riou, L., Testart, J., Allemand, I., & Fouchet, P. (2005). Flow cytometric characterization of viable meiotic and postmeiotic cells by Hoechst 33342 in mouse spermatogenesis. *Cytometry A, 65*(1), 40-49. doi:10.1002/cyto.a.20129

Benjamini, Y., & Hochberg, Y. (1995). Controlling the False Discovery Rate - a Practical and Powerful Approach to Multiple Testing. *Journal of the Royal Statistical Society Series B-Methodological, 57*(1), 289-300.

Boussouar, F., & Benahmed, M. (2004). Lactate and energy metabolism in male germ cells. *Trends Endocrinol Metab, 15*(7), 345-350. doi:10.1016/j.tem.2004.07.003

Bricker, D. K., Taylor, E. B., Schell, J. C., Orsak, T., Boutron, A., Chen, Y. C., Rutter, J. (2012). A mitochondrial pyruvate carrier required for pyruvate uptake in yeast, Drosophila, and humans. *Science, 337*(6090), 96-100. doi:10.1126/science.1218099

Brower, J. V., Lim, C. H., Jorgensen, M., Oh, S. P., & Terada, N. (2009). Adenine nucleotide translocase 4 deficiency leads to early meiotic arrest of murine male germ cells. *Reproduction, 138*(3), 463-470. doi:10.1530/REP-09-0201

Buaas, F. W., Kirsh, A. L., Sharma, M., McLean, D. J., Morris, J. L., Griswold, M. D., Braun, R. E. (2004). Plzf is required in adult male germ cells for stem cell self-renewal. *Nat Genet, 36*(6), 647-652. doi:10.1038/ng1366

Calvo, S. E., Clauser, K. R., & Mootha, V. K. (2016). MitoCarta2.0: an updated inventory of mammalian mitochondrial proteins. *Nucleic Acids Res, 44*(D1), D1251-1257. doi:10.1093/nar/gkv1003

Carra, E., Sangiorgi, D., Gattuccio, F., & Rinaldi, A. M. (2004). Male infertility and mitochondrial DNA. *Biochem Biophys Res Commun, 322*(1), 333-339. doi:10.1016/j.bbrc.2004.07.112

Chan, D. C. (2012). Fusion and fission: interlinked processes critical for mitochondrial health. *Annu Rev Genet, 46*, 265-287. doi:10.1146/annurev-genet-110410-132529

Chen, H., & Chan, D. C. (2017). Mitochondrial Dynamics in Regulating the Unique Phenotypes of Cancer and Stem Cells. *Cell Metab, 26*(1), 39-48. doi:10.1016/j.cmet.2017.05.016

Chen, H., Chomyn, A., & Chan, D. C. (2005). Disruption of fusion results in mitochondrial heterogeneity and dysfunction. *J Biol Chem, 280*(28), 26185-26192. doi:10.1074/jbc.M503062200

Chen, H., Detmer, S. A., Ewald, A. J., Griffin, E. E., Fraser, S. E., & Chan, D. C. (2003). Mitofusins Mfn1 and Mfn2 coordinately regulate mitochondrial fusion and are essential for embryonic development. *J Cell Biol, 160*(2), 189-200. doi:10.1083/jcb.200211046

Chen, H., McCaffery, J. M., & Chan, D. C. (2007). Mitochondrial fusion protects against neurodegeneration in the cerebellum. *Cell, 130*(3), 548-562. doi:10.1016/j.cell.2007.06.026

Chen, H., Vermulst, M., Wang, Y. E., Chomyn, A., Prolla, T. A., McCaffery, J. M., & Chan, D. C. (2010). Mitochondrial fusion is required for mtDNA stability in skeletal muscle and tolerance of mtDNA mutations. *Cell, 141*(2), 280-289. doi:10.1016/j.cell.2010.02.026

Costoya, J. A., Hobbs, R. M., Barna, M., Cattoretti, G., Manova, K., Sukhwani, M., . . . Pandolfi, P. P. (2004). Essential role of Plzf in maintenance of spermatogonial stem cells. *Nat Genet, 36*(6), 653-659. doi:10.1038/ng1367

Cox, J., & Mann, M. (2008). MaxQuant enables high peptide identification rates, individualized p.p.b.-range mass accuracies and proteome-wide protein quantification. *Nat Biotechnol, 26*(12), 1367-1372. doi:10.1038/nbt.1511

Cox, J., Neuhauser, N., Michalski, A., Scheltema, R. A., Olsen, J. V., & Mann, M. (2011). Andromeda: A Peptide Search Engine Integrated into the MaxQuant

Environment. *Journal of Proteome Research, 10*(4), 1794-1805. doi: 10.1021/Pr101065j

De Brito, O. M., & Scorrano, L. (2008). Mitofusin 2 tethers endoplasmic reticulum to mitochondria. *Nature, 456*(7222), 605.

De Martino, C., Floridi, A., Marcante, M. L., Malorni, W., Scorza Barcellona, P., Bellocci, M., & Silvestrini, B. (1979). Morphological, histochemical and biochemical studies on germ cell mitochondria of normal rats. *Cell Tissue Res, 196*(1), 1-22.

De Rooij, D. G. (2017). The nature and dynamics of spermatogonial stem cells. *Development, 144*(17), 3022-3030.

Demain, L. A., Conway, G. S., & Newman, W. G. (2017). Genetics of mitochondrial dysfunction and infertility. *Clin Genet, 91*(2), 199-207. doi:10.1111/cge.12896

Demarco, R. S., Uyemura, B. S., D'Alterio, C., & Jones, D. L. (2019). Mitochondrial fusion regulates lipid homeostasis and stem cell maintenance in the Drosophila testis. *Nature cell biology, 21*(6), 710.

Endo, T., Freinkman, E., de Rooij, D. G., & Page, D. C. (2017). Periodic production of retinoic acid by meiotic and somatic cells coordinates four transitions in mouse spermatogenesis. *Proceedings of the National Academy of Sciences*, 201710837.

Fang, F., Ni, K., Shang, J., Zhang, X., Xiong, C., & Meng, T. (2018). Expression of mitofusin 2 in human sperm and its relationship to sperm motility and cryoprotective potentials. *Exp Biol Med (Maywood)*, 1535370218790919. doi:10.1177/1535370218790919

Flores, A., Schell, J., Krall, A. S., Jelinek, D., Miranda, M., Grigorian, M., Lowry, W. E. (2017). Lactate dehydrogenase activity drives hair follicle stem cell activation. *Nat Cell Biol, 19*(9), 1017-1026. doi:10.1038/ncb3575

Folgero, T., Bertheussen, K., Lindal, S., Torbergsen, T., & Oian, P. (1993). Mitochondrial disease and reduced sperm motility. *Hum Reprod, 8*(11), 1863-1868.

Fuller, M. T. (1993). Spermatogenesis. In *The development of drosophila melanogater* (pp. 71-147). Cold Spring Harbor, New York.

Gaysinskaya, V., & Bortvin, A. (2015). Flow cytometry of murine spermatocytes. *Curr Protoc Cytom, 72*, 7.44.41-24. doi:10.1002/0471142956.cy0744s72

Gaysinskaya, V., Soh, I. Y., van der Heijden, G. W., & Bortvin, A. (2014). Optimized flow cytometry isolation of murine spermatocytes. *Cytometry A, 85*(6), 556-565. doi:10.1002/cyto.a.22463

Gomes, L. C., Di Benedetto, G., & Scorrano, L. (2011). During autophagy mitochondria elongate, are spared from degradation and sustain cell viability. *Nat Cell Biol, 13*(5), 589-598. doi: 10.1038/ncb2220

Griswold, M. D. (2016). Spermatogenesis: The Commitment to Meiosis. *Physiol Rev, 96*(1), 1-17. doi:10.1152/physrev.00013.2015

Grootegoed, J. A., Jansen, R., & Van der Molen, H. J. (1984). The role of glucose, pyruvate and lactate in ATP production by rat spermatocytes and spermatids. *Biochim Biophys Acta, 767*(2), 248-256.

Hackenbrock, C. R. (1966). Ultrastructural bases for metabolically linked mechanical activity in mitochondria. I. Reversible ultrastructural changes with change in metabolic steady state in isolated liver mitochondria. *J Cell Biol, 30*(2), 269-297.

Hales, K. G., & Fuller, M. T. (1997). Developmentally regulated mitochondrial fusion mediated by a conserved, novel, predicted GTPase. *Cell, 90*(1), 121-129.

Hamer, G., Roepers-Gajadien, H. L., van Duyn-Goedhart, A., Gademan, I. S., Kal, H. B., van Buul, P. P., & de Rooij, D. G. (2003). DNA double-strand breaks and gamma-H2AX signaling in the testis. *Biol Reprod, 68*(2), 628-634.

Hara, K., Nakagawa, T., Enomoto, H., Suzuki, M., Yamamoto, M., Simons, B. D., & Yoshida, S. (2014). Mouse spermatogenic stem cells continually interconvert between equipotent singly isolated and syncytial states. *Cell stem cell, 14*(5), 658-672.

Hobbs, R. M., La, H. M., Mäkelä, J. A., Kobayashi, T., Noda, T., & Pandolfi, P. P. (2015). Distinct germline progenitor subsets defined through Tsc2–mTORC1 signaling. *EMBO Rep, 16*(4), 467-480.

Hofmann, M.-C., Hess, R. A., Goldberg, E., & Millan, J. L. (1994). Immortalized germ cells undergo meiosis in vitro. *Proceedings of the National Academy of Sciences, 91*(12), 5533-5537.

Hofmann, M. C., Abramian, D., & Millán, J. L. (1995). A haploid and a diploid cell cycle coexist in an in vitro immortalized spermatogenic cell line. *Developmental genetics, 16*(2), 119-127.

Jiang, M., Kauppila, T. E. S., Motori, E., Li, X., Atanassov, I., Folz-Donahue, K., Larsson, N. G. (2017). Increased Total mtDNA Copy Number Cures Male Infertility Despite Unaltered mtDNA Mutation Load. *Cell Metab, 26*(2), 429-436.e424. doi:10.1016/j.cmet.2017.07.003

Kandul, N. P., Zhang, T., Hay, B. A., & Guo, M. (2016). Selective removal of deletion-bearing mitochondrial DNA in heteroplasmic Drosophila. *Nat Commun, 7*, 13100. doi:10.1038/ncomms13100

Kao, S., Chao, H. T., & Wei, Y. H. (1995). Mitochondrial deoxyribonucleic acid 4977-bp deletion is associated with diminished fertility and motility of human sperm. *Biol Reprod, 52*(4), 729-736.

Kremer, J. R., Mastronarde, D. N., & McIntosh, J. R. (1996). Computer visualization of three-dimensional image data using IMOD. *J Struct Biol, 116*(1), 71-76. doi:10.1006/jsbi.1996.0013

Kujoth, G. C., Hiona, A., Pugh, T. D., Someya, S., Panzer, K., Wohlgemuth, S. E., Prolla, T. A. (2005). Mitochondrial DNA mutations, oxidative stress, and apoptosis in mammalian aging. *Science, 309*(5733), 481-484. doi:10.1126/science.1112125

Lestienne, P., Reynier, P., Chretien, M. F., Penisson-Besnier, I., Malthiery, Y., & Rohmer, V. (1997). Oligoasthenospermia associated with multiple mitochondrial DNA rearrangements. *Mol Hum Reprod, 3*(9), 811-814.

Lord, T., & Oatley, J. M. (2017). A revised Asingle model to explain stem cell dynamics in the mouse male germline. *Reproduction, 154*(2), R55-R64.

Mannella, C. A. (2006). Structure and dynamics of the mitochondrial inner membrane cristae. *Biochim Biophys Acta, 1763*(5-6), 542-548. doi:10.1016/j.bbamcr.2006.04.006

Mastronarde, D. N. (2005). Automated electron microscope tomography using robust prediction of specimen movements. *J Struct Biol, 152*(1), 36-51. doi:10.1016/j.jsb.2005.07.007

Mastronarde, D. N. (2008). Correction for non-perpendicularity of beam and tilt axis in tomographic reconstructions with the IMOD package. *J Microsc, 230*(Pt 2), 212-217. doi:10.1111/j.1365-2818.2008.01977.x

Meinhardt, A., Wilhelm, B., & Seitz, J. (1999). Mini symposium. New aspects of spermatogenesis. Expression of mitochondrial marker proteins during spermatogenesis. *Human Reproduction Update, 5*(2), 108-119. doi:10.1093/humupd/5.2.108

Misko, A., Jiang, S., Wegorzewska, I., Milbrandt, J., & Baloh, R. H. (2010). Mitofusin 2 is necessary for transport of axonal mitochondria and interacts with the Miro/Milton complex. *J Neurosci, 30*(12), 4232-4240. doi:10.1523/jneurosci.6248-09.2010

Mourier, A., Motori, E., Brandt, T., Lagouge, M., Atanassov, I., Galinier, A., Dieterich, C. (2015). Mitofusin 2 is required to maintain mitochondrial coenzyme Q levels. *J Cell Biol, 208*(4), 429-442.

Mourier, A., Motori, E., Brandt, T., Lagouge, M., Atanassov, I., Galinier, A., Larsson, N. G. (2015). Mitofusin 2 is required to maintain mitochondrial coenzyme Q levels. *J Cell Biol, 208*(4), 429-442. doi:10.1083/jcb.201411100

Nakada, K., Sato, A., Yoshida, K., Morita, T., Tanaka, H., Inoue, S., Hayashi, J. (2006). Mitochondria-related male infertility. *Proc Natl Acad Sci U S A, 103*(41), 15148-15153. doi:10.1073/pnas.0604641103

Nakamura, M., Okinaga, S., & Arai, K. (1984). Metabolism of pachytene primary spermatocytes from rat testes: pyruvate maintenance of adenosine triphosphate level. *Biol Reprod, 30*(5), 1187-1197.

Osuru, H. P., Monroe, J. E., Chebolu, A. P., Akamune, J., Pramoonjago, P., Ranpura, S. A., & Reddi, P. P. (2014). The acrosomal protein SP-10 (Acrv1) is an ideal marker for staging of the cycle of seminiferous epithelium in the mouse. *Mol Reprod Dev, 81*(10), 896-907. doi:10.1002/mrd.22358

Oulad-Abdelghani, M., Bouillet, P., Decimo, D., Gansmuller, A., Heyberger, S., Dolle, P., Chambon, P. (1996). Characterization of a premeiotic germ cell-specific cytoplasmic protein encoded by Stra8, a novel retinoic acid-responsive gene. *J Cell Biol, 135*(2), 469-477.

Peters, A. H., Plug, A. W., van Vugt, M. J., & de Boer, P. (1997). A drying-down technique for the spreading of mammalian meiocytes from the male and female germline. *Chromosome Res, 5*(1), 66-68.

Pham, A. H., McCaffery, J. M., & Chan, D. C. (2012). Mouse lines with photo-activatable mitochondria to study mitochondrial dynamics. *Genesis, 50*(11), 833-843. doi:10.1002/dvg.22050

Rahman, N. A., & Huhtaniemi, I. T. (2004). Testicular cell lines. *Molecular and cellular endocrinology, 228*(1-2), 53-65.

Rambold, A. S., Kostelecky, B., Elia, N., & Lippincott-Schwartz, J. (2011). Tubular network formation protects mitochondria from autophagosomal degradation during nutrient starvation. *Proc Natl Acad Sci U S A, 108*(25), 10190-10195. doi:10.1073/pnas.1107402108

Rato, L., Alves, M. G., Socorro, S., Duarte, A. I., Cavaco, J. E., & Oliveira, P. F. (2012). Metabolic regulation is important for spermatogenesis. *Nat Rev Urol, 9*(6), 330-338. doi:10.1038/nrurol.2012.77

Ritchie, M. E., Phipson, B., Wu, D., Hu, Y., Law, C. W., Shi, W., & Smyth, G. K. (2015). limma powers differential expression analyses for RNA-sequencing and microarray studies. *Nucleic Acids Res, 43*(7), e47. doi:10.1093/nar/gkv007

Rojansky, R., Cha, M.-Y., & Chan, D. C. (2016). Elimination of paternal mitochondria in mouse embryos occurs through autophagic degradation dependent on PARKIN and MUL1. *eLife, 5*, e17896.

Ross, J. M. (2011). Visualization of mitochondrial respiratory function using cytochrome c oxidase/succinate dehydrogenase (COX/SDH) double-labeling histochemistry. *J Vis Exp* (57), e3266. doi:10.3791/3266

Rossi, P. (2013). Transcriptional control of KIT gene expression during germ cell development. *Int J Dev Biol, 57* (2-4), 179-184. doi:10.1387/ijdb.130014pr

Sadate-Ngatchou, P. I., Payne, C. J., Dearth, A. T., & Braun, R. E. (2008). Cre recombinase activity specific to postnatal, premeiotic male germ cells in transgenic mice. *Genesis, 46*(12), 738-742. doi:10.1002/dvg.20437

Santel, A., & Fuller, M. T. (2001). Control of mitochondrial morphology by a human mitofusin. *J Cell Sci, 114*(Pt 5), 867-874.

Saunders, P. T., Millar, M. R., West, A. P., & Sharpe, R. M. (1993). Mitochondrial cytochrome C oxidase II messenger ribonucleic acid is expressed in pachytene spermatocytes at high levels and in a stage-dependent manner during spermatogenesis in the rat. *Biol Reprod, 48*(1), 57-67.

Schell, J. C., Wisidagama, D. R., Bensard, C., Zhao, H., Wei, P., Tanner, J., Rutter, J. (2017). Control of intestinal stem cell function and proliferation by mitochondrial pyruvate metabolism. *Nat Cell Biol, 19*(9), 1027-1036. doi:10.1038/ncb3593

Seitz, J., Mobius, J., Bergmann, M., & Meinhardt, A. (1995). Mitochondrial differentiation during meiosis of male germ cells. *Int J Androl, 18 Suppl 2*, 7-11.

Smyth, G. K. (2004). Linear models and empirical bayes methods for assessing differential expression in microarray experiments. *Stat Appl Genet Mol Biol, 3*, Article3. doi:10.2202/1544-6115.1027

Stanton, P. G. (2016). Regulation of the blood-testis barrier. *Semin Cell Dev Biol, 59*, 166-173. doi:10.1016/j.semcdb.2016.06.018

Teletin, M., Vernet, N., Yu, J., Klopfenstein, M., Jones, J. W., Féret, B., Mark, M. (2019). Two functionally redundant sources of retinoic acid secure spermatogonia differentiation in the seminiferous epithelium. *Development, 146*(1), dev170225.

Trifunovic, A., Wredenberg, A., Falkenberg, M., Spelbrink, J. N., Rovio, A. T., Bruder, C. E., . . . Larsson, N. G. (2004). Premature ageing in mice expressing defective mitochondrial DNA polymerase. *Nature, 429*(6990), 417-423. doi:10.1038/nature02517

Vanderperre, B., Cermakova, K., Escoffier, J., Kaba, M., Bender, T., Nef, S., & Martinou, J. C. (2016). MPC1-like Is a Placental Mammal-specific

Mitochondrial Pyruvate Carrier Subunit Expressed in Postmeiotic Male Germ Cells. *J Biol Chem, 291*(32), 16448-16461. doi:10.1074/jbc.M116.733840

Weaver, D., Eisner, V., Liu, X., Varnai, P., Hunyady, L., Gross, A., & Hajnoczky, G. (2014). Distribution and apoptotic function of outer membrane proteins depend on mitochondrial fusion. *Mol Cell, 54*(5), 870-878. doi:10.1016/j.molcel.2014.03.048

Zhang, J., Wang, Q., Wang, M., Jiang, M., Wang, Y., Sun, Y., Wang, Y. (2016). GASZ and mitofusin-mediated mitochondrial functions are crucial for spermatogenesis. *EMBO Rep, 17*(2), 220-234. doi:10.15252/embr.201540846

Zhou, Q., Nie, R., Li, Y., Friel, P., Mitchell, D., Hess, R. A., Griswold, M. D. (2008). Expression of stimulated by retinoic acid gene 8 (Stra8) in spermatogenic cells induced by retinoic acid: an in vivo study in vitamin A-sufficient postnatal murine testes. *Biol Reprod, 79*(1), 35-42. doi:10.1095/biolreprod.107.066795

CHAPTER 3

Mitochondrial fission is required for organization of the mitochondrial sheath in spermatids

Grigor Varuzhanyan[1], Hsiuchen Chen[1], Rebecca Rojansky[1], Mark S Ladinsky[1], J. Michael McCaffery[2], and David C. Chan[1*]

[1]Division of Biology and Biological Engineering, California Institute of Technology, Pasadena, CA 91125, USA.

[2]Integrated Imaging Center, Department of Biology, Johns Hopkins University, Baltimore, MD 21218.

Abstract

Mitochondrial fission counterbalances fusion to maintain organelle morphology. Here, we investigate the role of mitochondrial fission during mammalian spermatogenesis, a complex developmental process involving several drastic changes to mitochondrial shape and organization. Mitochondria are generally small and spherical in spermatogonia, elongate during meiosis, and fragment in haploid round spermatids. Near the end of spermatid maturation, small mitochondrial spheres line the axoneme, elongate, and tightly wrap around the midpiece to form the mitochondrial sheath, which is critical for fueling flagellar movements. Using genetic ablation in mice, we find that Mitochondrial fission factor (*Mff*) is required for mitochondrial fragmentation in haploid round spermatids and for organizing mitochondria in the midpiece in elongating spermatids. In *Mff* mutant mice, round spermatids have aberrantly elongated mitochondria that often show central constrictions, suggestive of failed fission events. In elongating spermatids and spermatozoa, mitochondrial sheaths are disjointed, containing fewer and swollen mitochondria. These mitochondrial abnormalities in *Mff* mutant sperm are associated with reduced respiratory chain Complex IV activity, aberrant sperm morphology and motility, and reduced fertility.

Introduction

The balance between mitochondrial fusion and fission regulates mitochondrial morphology and cell metabolism (Chan, 2020b; Mishra and Chan, 2016). For some cells, this balance has been shown to maintain mitochondrial size, shape, and number in accordance with cell physiology. In the long processes of neurons, for example,

mitochondria are maintained at a small size compatible with efficient transport along the long distances from the cell body to the nerve terminal (Schwarz, 2013). However, the role of mitochondrial dynamics in regulating mitochondrial organization and distribution in other cell types is less well understood.

Mitochondrial fission is a multistep process involving several cellular factors. In the initial phase, the endoplasmic reticulum (ER) constricts the mitochondrion with help from actin filaments (Friedman et al., 2011; Korobova et al., 2013). Next, receptors on the mitochondrial outer membrane recruit DRP1 (Dynamin-related protein 1), which oligomerizes into a ring-like structure on the mitochondrial surface to further constrict and sever the mitochondrion. In mammals, DRP1 can be recruited by four different receptors: MFF (Mitochondrial fission factor), MID49 (Mitochondrial dynamics protein of 49 kDa), MID51 (Mitochondrial dynamics protein of 51 kDa), and FIS1 (Mitochondrial fission 1 protein), with the latter having only a minor role (Chan, 2012b; Losón et al., 2013; Otera et al., 2010). DNM2 was reported to mediate the final step in fission following DRP1 constriction (Lee et al., 2016b), but this notion has been challenged (Fonseca et al., 2019b; Kamerkar et al., 2018). Here we investigate the role of *Mff*-mediated mitochondrial fission during mammalian spermatogenesis, which requires drastic changes to mitochondrial morphology and distribution.

Spermatogenesis is a highly complex differentiation process associated with several mitochondrial transformations. This lengthy process can be divided into three major developmental programs: 1) mitotic amplification of spermatogonia, 2) meiotic division of spermatocytes to form haploid spermatids, and 3) morphological transformation of round

spermatids into mature sperm, a process termed spermiogenesis. During these developmental transitions, mitochondria undergo dramatic changes in morphology, distribution, and number (De Martino et al., 1979b). Mitochondria are generally small and fragmented in spermatogonia, elongate and cluster around the nuage during meiosis, and fragment again in post-meiotic spermatids. Near the end of spermatid maturation, small spherical mitochondria line up longitudinally on the axoneme of the midpiece. These mitochondria elongate and tightly wrap around the axoneme in a coordinated manner to organize into a compact mitochondrial sheath that fuels sperm motility (Ho and Wey, 2007b). The molecular factors that drive these coordinated mitochondrial rearrangements are unknown.

Because mammalian spermatogenesis involves drastic changes to mitochondrial morphology and organization, it is a promising model for studying the role of developmentally regulated alterations to mitochondrial dynamics. Indeed, mitochondrial fusion has been shown to be important for maintaining OXPHOS activity in meiotic spermatocytes (Varuzhanyan et al., 2019b; Zhang et al., 2016b). Furthermore, we previously reported that mice homozygous for a gene-trap allele of *Mff* (*Mff*^{gt}) have reduced fertility and sperm count (Chen et al., 2015b), but the underlying reasons were unclear. To this end, we analyzed the mitochondrial defects present in the male germ cells of *Mff*^{gt} mice. Our results suggest that spermiogenesis is highly dependent on mitochondrial fission.

Results

Mff^{gt} sperm have disjointed mitochondrial sheaths.

To visualize male germ cells within the seminiferous epithelium, we performed Periodic–acid Schiff staining in wild type (WT) and *Mff*^{gt} testis sections (Figure 3.1). *Mff*^{gt} testes do not exhibit any obvious degeneration of seminiferous tubules, and all major germ cell types—spermatogonia (SG), spermatocytes (SC), spermatids (ST), and spermatozoa (SZ)—are present, indicating that loss of *Mff* does not impair generation of any one cell type. To examine the ultrastructure of *Mff*^{gt} sperm, we isolated sperm from caudal epididymides and subjected them to scanning electron microscopy (SEM). *Mff*^{gt} sperm often had morphological abnormalities in the midpiece (Figure 3.2A, white arrows) and kinking in or near the midpiece (Figure 3.2A, yellow arrow). Because the mitochondrial sheath is a major component of the midpiece, we utilized a mitochondrially targeted Dendra2 (Dn) fluorescent protein (Pham et al., 2012) to examine mitochondrial structure in sperm (Figures 3.2B and 3.2C). WT sperm have abundant mitochondria tightly packed in the sperm midpiece with little or no gaps between adjacent organelles. In contrast, *Mff*^{gt} sperm have notably fewer mitochondria, resulting in disjointed mitochondrial sheaths with large gaps between adjacent organelles. Quantification of total Dn fluorescence in sperm midpieces confirmed that *Mff*^{gt} mutant sperm have substantially reduced mitochondrial content (Figure 3.2C). In addition, imaging of sperm by differential interference microscopy (DIC) showed prominent defects in overall sperm morphology (Figures 3.2D and 3.2E). Over 60% of *Mff*^{gt} sperm contain kinks, which are found in the midpiece (>15%), the principal piece (>40%), or the neck (>5%).

Mitochondria in *Mff^{gt}* sperm are sparse and swollen.

To visualize the ultrastructure of sperm mitochondria, we performed electron tomography of epididymal sections to generate three-dimensional renderings of mitochondrial sheaths (Figures 3.3A and 3.3B, and Videos 3.1-4). When mitochondrial sheaths are visualized in longitudinal sections of WT sperm, thin, rod-like mitochondria can be seen tightly and uniformly wrapping around the sperm axoneme (Figure 3.3A and Videos 2.1-2). In contrast, mutant sperm have disjointed mitochondrial sheaths with great variation in mitochondrial morphology. Mutant mitochondria appear highly swollen, have increased transverse diameters, and are too sparse to pack into a uniform sheath. In transverse sections of sperm midpieces, mutant mitochondria are also slightly elongated compared to control (Figure 3.3B and Videos 3.3-4). These data suggest that in the absence of fission, aberrantly enlarged mitochondria are poorly recruited to the sperm midpiece, resulting in disjointed mitochondrial sheaths. TEM analysis of spermatozoa in testis sections showed similar defects (Figure 3.S1), indicating that spermatozoa contain defective mitochondria prior to their release into the epididymides.

***Mff^{gt}* is required for developmentally regulated mitochondrial fragmentation in spermatids.**

We next visualized mitochondrial morphology in early stage spermatids before they form mitochondrial sheaths (Figure 3.4). Whereas round and elongating spermatids of WT mice almost invariably contain fragmented mitochondria, the vast majority of mutant round and elongating spermatids contain tubular mitochondria (Figures 3.4A-4C). To visualize

mitochondrial ultrastructure, we performed transmission electron microscopy (TEM) of testis sections in WT and *Mff*^{gt} mice (Figure 3.4D-4F). Consistent with observations made using light microscopy, we find that most round spermatid mitochondria are small and fragmented. In contrast, more than 20% of mutant mitochondria exhibit an elongated and highly constricted morphology, suggestive of a fission defect. Almost 80% of round spermatids (31 out of 39) contained one or more constricted mitochondria (Figure 3.4F).

Mff^{gt} sperm have reduced respiratory chain Complex IV activity, motility, and fertility.

To examine sperm mitochondrial function, we examined respiratory chain activity in isolated sperm by histochemical analysis of respiratory chain Complex IV (cytochrome c oxidase; COX) and succinate dehydrogenase (SDH) enzyme activity (Figures 3.5A and 3.5B). COX activity is visualized by oxidation of 3,3'-Diaminobenzidine (DAB) by cytochrome *c* into a brown product that can be visualized by light microscopy. SDH activity is visualized by oxidation of succinate by SDH followed by reduction of Nitro blue tetrazolium chloride (NBT), which forms a dark blue precipitate. In WT sperm midpieces, strong and uniform COX and SDH staining indicated normal OXPHOS activity (Figure 3.5A; top and middle panels). When COX and SDH stains are done simultaneously, only COX activity can be seen because the DAB reaction product saturates the cell (Figure 3.5A; bottom panel). Midpiece mitochondria in mutant sperm have a greater than 20% reduction in COX staining and an almost 20% increase in NBT staining (Figures 3.5A and 3.5B). When COX and SDH are monitored simultaneously in mutant sperm, blue coloring was

evident due to decreased COX staining and increased SDH staining. These results indicate reduced Complex IV activity in *Mff*^{gt} sperm. In other cell types with low COX/high SDH activity, such as mtDNA-deficient skeletal muscle, increased SDH activity is correlated with increased mitochondrial mass. However, *Mff*^{gt} sperm have reduced mitochondria mass (Figures 3.2B and 3.2C). Thus, the cause of the increased NBT staining in *Mff*^{gt} sperm is unclear, but previous studies have correlated increased NBT staining in spermatozoa with increased reactive oxygen species (ROS) (Baehner et al., 1976; Tunc et al., 2010).

Because reduced respiratory chain activity has been associated with reduced sperm motility (Ruiz-Pesini et al., 1998), we examined sperm motility by time-lapse microscopy (Videos 3.5-6). Mutant sperm were significantly less motile compared to WT controls. Because *Mff*^{gt} mice are runted and exhibit severe cardiomyopathy (Chen et al., 2015b), it is important to distinguish whether their reduced fertility is due to an inherent defect in sperm function or secondary to other health problems. To this end, we performed *in vitro* fertilization using sperm from WT/Dn and *Mff*^{gt}/Dn males with oocytes from WT females and tracked fertilization success by progression to the 2-cell stage (Figures 3.5C and 3.5D). WT sperm successfully fertilized 64.1% (21.5 out of 33.5) of WT oocytes. In contrast, mutant sperm failed to fertilize any oocytes (0 out of 35.75).

Discussion

Recent studies have uncovered the importance of mitochondrial dynamics for male fertility (Chen et al., 2015b; Varuzhanyan et al., 2019b; Zhang et al., 2016b). Mitochondria

in stem and progenitor spermatogonia are sparse, small, and spherical. However, as germ cells enter meiosis, mitochondria increase their numbers, cluster, and undergo fusion, which promotes OXPHOS. The increase in OXPHOS at this time is likely necessary to drive the ATP-dependent processes associated with Meiotic Prophase I. Following meiosis, mitochondria return to a fragmented state, presumably to facilitate transport and reorganization onto the sperm midpiece during spermatid maturation. In mature spermatids, small mitochondrial spheres are arranged around the sperm axoneme, elongate, and tightly wrap around the axoneme to form the mitochondrial sheath, which fuels sperm motility.

The data presented here indicate that mitochondrial fission is acutely activated in post-meiotic round spermatids, which have much more fragmented mitochondria compared to earlier meiotic spermatocytes. However, in Mff^{gt} round spermatids, mitochondria fail to fragment, forming long tubular mitochondria with striking constrictions that may represent trapped fission intermediates. Based on the reduced mitochondrial content in Mff^{gt} midpieces, we suggest that fission is important for generating small mitochondrial fragments that can more easily be recruited to the sperm midpiece to form the mitochondrial sheath. In Mff^{gt} mutants, it is likely that the low density of mitochondria associated with the midpiece, along with reduced Complex IV activity, contribute to their reduced fertility.

Materials and methods

Generation of mice

All mouse experiments were approved by the California Institute of Technology Institutional Animal Care and Use Committee. WT/Dn ($Mff^{+/+}$; $Rosa26^{PhAM(+/excised)}$) and

Mff^{gt}/Dn mice (*Mff*^{gt}; *Rosa26*$^{PhAM(+/excised)}$) were generating by crossing *Mff*$^{+/+}$ and *Mff*^{gt} mice with *Rosa26*$^{PhAM(excised/excised)}$ mice. *Mff*^{gt} mice, described previously (Chen et al., 2015b), were maintained on a 129P2/OlaHsd and C57Bl/6J background and are available at the Mutant Mouse Resource & Research Center (RRID: MMRRC_066700-UCD). *Rosa26*$^{PhAM(excised/excised)}$ mice were described previously (Pham et al., 2012) and are available at the Jackson Laboratory (#018397).

Periodic–acid Schiff (PAS) staining

Testes were fixed in Bouin's fixative overnight at 4°C, dehydrated in a 30–90% ethanol series, cleared in Xylenes, and embedded in paraffin. Tissue blocks were sectioned at 7 µm, deparaffinized, and rehydrated before staining. Slides were incubated with 1% periodic acid (Electron Microscopy Sciences (EMS); 19324–10) for 30 min at RT, washed in running water for 5 min, then rinsed in deionized water. Slides were incubated with Schiff's reagent (EMS; 260582–05) for 30 min at RT and washed as described above before counterstaining with Gill 2 Hematoxylin for 30 s at RT. Slides were washed in running water for 1 min, dehydrated with ethanol, cleared with xylene, then mounted using Cytoseal XYL mounting media (Thermo Fisher Scientific; 22-050-262).

Scanning electron microscopy (SEM)

Epididymides were minced in PBS and incubated at 37˚C for 15 minutes for sperm to swim out. Sperm cells were pelleted with gentle centrifugation at 400 *g* for 10 min at RT and washed once in PBS. The samples were resuspended in sodium cacodylate and fixed

with 3.0% formaldehyde and 1.5% glutaraldehyde in sodium cacodylate buffer (0.1M sodium cacodylate containing 5 mM Ca^{2+} and 2.5% Sucrose at pH 7.4). Samples were washed 3X in sodium cacodylate buffer before proceeding to SEM. Cellulose-nitrate filter circles were overlaid/activated with 2% glutaraldehyde for 30' and subsequently washed three times with ddH_2O. Sperm were overlaid onto the cellulose-nitrate activated filters for 20'. Filters were washed gently 1X in 100 mM cacodylate buffer and fixed in Palade's OsO4 for 1 hr at 4°C by immersion in the fixative. Filters were then washed in ddH_2O and dehydrated through a graded series of ethanol to 100%, followed by 3X washes of 100% ethanol. Filters were then critical point dried in a Tousimis 795 critical point dryer, or washed 2X with hexamethyldisilazane and allowed to dry slowly at room temp under the hood. Filters were mounted onto aluminum specimen stubs using carbon transfer tabs, grounded to the stub with silver paste, and sputtered with Pt for one minute in an Anatech Hummer 6.2 sputter coater. Stubs were then observed in an FEI Quanta 200 ESEM at a 10KeV under high vacuum.

Light microscopy and image processing

Confocal fluorescence images, videos, and differential interference contrast (DIC) images were acquired using an inverted Zeiss LSM 710 confocal microscope with a 60X Plan-Apochromat objective. For live-cell motility videos, cells were maintained at 37°C and 5% CO_2. Bright-field images for histology were acquired using an upright Nikon Eclipse Ni-E fluorescence microscope equipped with a Ds-Ri2 camera and CFI Plan Apochromat Lambda objectives. Z stacks were acquired, and all-in-focus images were created using the

NIS Elements Extended Depth of Focus plugin. All images were processed using ImageJ. All image modifications were performed on entire images (no masking was used) and were performed identically between genotypes.

Transmission electron microscopy (TEM) of testis sections

Testes were dissected, cut at the poles and fixed for one hour at RT with 3% formaldehyde and 1.5% glutaraldehyde in sodium cacodylate buffer (0.1M sodium cacodylate containing 5 mM Ca^{2+} and 2.5% Sucrose at pH 7.4). Samples were washed 3X in sodium cacodylate buffer. Samples were then postfixed in Palade's OsO4, stained in Kellenberger uranyl acetate, dehydrated through a graded series of EtOH, and flat embedded in EMBED 812 (EMS). 80-nm testis sections were prepared on an ultramicrotome (UCT; Leica), collected onto 400 mesh high-transmission nickel grids, and poststained with lead citrate and uranyl acetate. Images were collected with a transmission electron microscope (Tecnai 12; FEI) operating at 100 kV and equipped with an Olympus Soft Imaging System (OSIS) digital camera (Megaview III; Olympus).

3D Electron tomography of epididymal sperm

Caudal epididymides were dissected and immediately fixed with cold 3% glutaraldehyde, 1% paraformaldehyde, 5% sucrose in 0.1 M sodium cacodylate trihydrate. Pre-fixed pieces of tissue were rinsed with fresh cacodylate buffer and placed into brass planchettes (Type A; Ted Pella, Inc, Redding, CA) prefilled with 10% Ficoll in cacodylate buffer. Samples were covered with the flat side of a Type-B brass planchette and rapidly

frozen with a HPM-010 high-pressure freezing machine (Leica Microsystems, Vienna Austria). The frozen samples were transferred under liquid nitrogen to cryotubes (Nunc) containing a frozen solution of 2.5% osmium tetroxide, 0.05% uranyl acetate in acetone. Tubes were loaded into an AFS-2 freeze-substitution machine (Leica Microsystems) and processed at −90°C for 72 hr, warmed over 12 hr to −20°C, held at that temperature for 8 hr, then warmed to 4°C for 2 hr. The fixative was removed, and the samples were rinsed 4x with cold acetone, and then were infiltrated with Epon-Araldite resin (Electron Microscopy Sciences, Port Washington PA) over 48 hr. Samples were flat-embedded between two Teflon-coated glass microscope slides, and the resin polymerized at 60°C for 24–48 hr.

Flat-embedded epididymis samples were observed with a stereo dissecting microscope, and appropriate regions were extracted with a microsurgical scalpel and glued to the tips of plastic sectioning stubs. Semi-thick (400 nm) serial sections were cut with a UC6 ultramicrotome (Leica Microsystems) using a diamond knife (Diatome, Ltd. Switzerland). Sections were placed on Formvar-coated copper-rhodium slot grids (Electron Microscopy Sciences) and stained with 3% uranyl acetate and lead citrate. Gold beads (10 nm) were placed on both surfaces of the grid to serve as fiducial markers for subsequent image alignment. Grids were placed in a dual-axis tomography holder (Model 2040, E.A. Fischione Instruments, Export PA) and imaged with a Tecnai TF30ST-FEG transmission electron microscope (300 KeV) equipped with a 2k × 2 k CCD camera (XP1000; Gatan, Inc Pleasanton CA). Tomographic tilt-series and large-area montaged overviews were acquired automatically using the SerialEM software package (Mastronarde, 2005). For tomography, samples were tilted + /- 64° and images collected at 1° intervals. The grid was then rotated

90° and a similar series taken about the orthogonal axis. Tomographic data was calculated, analyzed and modeled using the IMOD software package (Kremer et al., 1996; Mastronarde, 2008) on MacPro computers (Apple, Inc, Cupertino, CA).

COX/SDH Enzyme Histochemistry

COX/SDH labeling was performed as described previously (Ross, 2011), with minor modifications. Briefly, sperm cells were isolated from the caudal epididymis as described above, placed onto glass slides, and dried under a ventilated hood. Slides were stained with COX buffer for 25 min at RT in the dark, washed twice with dH_20 for 5 min, then stained with SDH buffer at 37ºC for 45 min in the dark. Slides were washed two more times with dH_20 and destained using a 30%–90%–30% acetone gradient. After two additional washes in dH_20, slides were mounted using Fluorogel.

Sperm motility

Cauda epididymides of *Mff*^{gt} and WT male littermates were dissected into 0.5 mL modified Tris-buffered medium (mTBM) pre-warmed to 37°C and 5% CO_2. mTBM was composed of 113.1 mM NaCl, 3 mM KCl, 7.5 mM $CaCl_2$, 5 mM sodium pyruvate, 11 mM glucose, 1 mM caffeine, and 20 mM Tris., as described before (Park and Niwa, 2009). Sperm were released by mincing the tissue with a 26-gauge needle and incubated at 37°C and 5% CO_2 for 15 minutes to allow for swim out. After incubation, the tissue was removed, and the fluid was mixed gently and collected into 1 mL Eppendorf tubes. Sperm were washed twice by gentle centrifugation at 833 *g* for 5 minutes, resuspended in 0.5 mL

mTBM, then incubated at 37°C and 5% CO_2 for 30 minutes for capacitation. Sperm were plated at $5x10^5$ sperm/mL in Nunc Lab-Tek II Chambered Coverglass slides (154852, Thermo), and videos were acquired as described above.

In vitro fertilization

For oocyte and sperm collection and fertilization all media was pre-warmed to 37˚C at 95% humidity, 5% CO_2, 5% O_2, and 90% N_2. Ovarian stimulation was performed as described previously (Baltimore et al., 2016). Briefly, female C57BL/6J mice between 21 and 25 days of age were injected intraperitoneally with 25 I.U. of PMSG (G-4877 Sigma) on day -2, followed by 5 I.U. of HCG (C-1063, Sigma) 48 hours later on day 0. Sperm were collected from the cauda epididymides of WT/Dn or *Mff*^{gt}/Dn mice into 0.5 mL of Fertiup medium (KYD-002-05-EX, Cosmo Bio USA) at 37˚C, counted with a hemocytometer, and capacitated at a concentration of 2-4 x 10^6 cells/mL for 1.5-2 hr at 37˚C, 95% humidity, 5% CO_2, 5% O_2, 90% N_2.

Primed females were anesthetized with Ketamine-Xylazine and oviducts were dissected into 0.5 mL of Cook's IVF medium (K-RVFE-50, Cooks) to wash, then transferred to 0.15 mL of Cook's IVF medium overlaid with mineral oil (M-8410, Sigma) into which the cumulus mass was released. Capacitated sperm were diluted to a final concentration of 1-2 x 10^5 sperm/mL in 0.2 mL CARD medium (KYD-003-EX, Cosmo Bio USA) overlaid with mineral oil, into which the cumulus mass was then transferred. The sperm and ova were co-incubated for 4-6 hours at 37˚C, 95% humidity, 5% CO_2, 5% O_2, and 90% N_2, transferred through four 0.15 mL washes of Cook's IVF medium overlaid with

mineral oil, then cultured in 0.5 mL Cook's IVF medium at 37˚C, 95% humidity, 5% CO_2, 5% O_2, 90% N_2 for 16-18 hr, at which point presumptive embryos were examined for progression to 2-cell stage.

Quantification

Quantification of total Dn fluorescence in sperm midpieces was performed on confocal images in which the sperm midpiece had been cropped and straightened using ImageJ. Integrated density (mean times area) values were plotted. Dn intensity plots in Figure 3.2B are "column average plots" generated from entire midpieces that were straightened using ImageJ. Quantification of sperm morphology was performed under the 100X objective of an upright Nikon Eclipse Ni-E fluorescence microscope. Quantification of mitochondrial morphology in round and elongating spermatids from WT/Dn and *Mff*^{gt}/Dn mice was done by scoring seminiferous tubule transverse sections that were circular and had an obvious lumen. Seminiferous tubules in which the majority of round or elongating spermatids contained tubular mitochondria were scored as "tubular." All others were scored as "fragmented."

Replicates and statistical reporting

Pairwise comparisons were made using the Student's *t*-test. When multiple pairwise comparisons were made from the same dataset, *p*-values were adjusted using the Bonferroni correction. Number of mice and replicates are indicated in figure legends. All outliers were

included in the analysis. All data are represented as mean ± SEM. **** indicates $p \leq 0.0001$; *** indicates $p \leq 0.001$; ** indicates $p \leq 0.01$; * indicates $p \leq 0.05$.

Acknowledgments

We thank all members of the Chan Lab for helpful discussions. This work was supported by the National Institutes of Health [grant R35 GM127147]. Grigor Varuzhanyan was supported by a National Science Foundation Graduate Research Fellowship (DGE-1144469) and a National Institutes of Health Cell and Molecular Biology Training Grant (GM07616T32). Mark Ladinsky was supported by the National Institute of Allergy and Infectious Diseases (NIAID) (2 P50 AI150464) (awarded to Pamela J. Bjorkman, Caltech).

Chapter 3 Figure Legends

Figure 3.1. Histological analysis of seminiferous epithelium of *Mff*^{gt} mice.

Periodic-acid Schiff staining of Bouin's-fixed testis sections. Note that all major germ cell types are present in *Mff*^{gt} mice. SG, spermatogonium; SC, spermatocyte; ST, spermatid; SZ, spermatozoa. Scale bars, 50 µm.

Figure 3.2. Visualization of mitochondrial sheaths in *Mff*^{gt}.

A) Scanning electron micrographs (SEM) of sperm isolated from the caudal epididymides. Note that the *Mff*^{gt} sperm cell has indentations in the midpiece and kinking at the distal end of the midpiece. Scale bar, 20 µm.

B) Top panel, DIC (direct interference contrast) and fluorescence micrographs of epididymal sperm. Green fluorescence comes from Dn (mito-Dendra2). Bottom panel, column average plot of Dn intensity along the length of the midpieces. Scale bars, 10 µm.

C) Quantification of total Dn fluorescence from sperm midpieces. At least 10 cells from each of four WT and four *Mff*^{gt} animals were quantified.

D) Representative examples of *Mff*^{gt} sperm exhibiting kinking in the midpiece, principal piece, and neck.

E) Quantification of sperm morphology. At least 100 cells from each of four WT and four *Mff*^{gt} were quantified. Data are represented as mean ± SEM. **$p \leq 0.01$. For statistical tests used, see the Materials and methods section.

Figure 3.3. Ultrastructural analysis of *Mff*^{gt} mitochondrial sheaths.

A) 3D electron tomography of longitudinal section of epididymal sperm. Note that *Mff*^{gt} sperm have wider mitochondria, and large empty spaces where mitochondria should be present. For more information about the 3D renderings, see Videos 3.1-2.

B) 3D electron tomography of transverse section of epididymal sperm. For more information about the 3D renderings, see Videos 3.3-4.

Scale bars, 20 µm. For more information, see also Figure 3.S1.

Figure 3.4. Mitochondrial morphology in *Mff*^{gt} round spermatids.

A) Mitochondrial morphology in round spermatids. Scale bar, 20 µm.

B) Mitochondrial morphology in elongating spermatids. Scale bar, 20 µm.

C) Quantification of mitochondrial morphology in round and elongating spermatids. At least 20 seminiferous tubule cross sections from each of two WT and three *Mff*^{gt} mice were scored.

D) TEM of round spermatids in testis sections. The following pseudocolors are used: nuclei, blue; mitochondria, red; ER, yellow. Low magnification panel scale bar, 5 µm. High magnification panel scale bars, 200 nm.

E) Quantification of mitochondrial morphology from TEM micrographs of round spermatids. A total of 36 cells from two WT mice and 39 cells from one *Mff*^{gt} mouse were quantified.

F) Frequency distribution of round spermatid mitochondria with aberrant constrictions. A total of 36 cells from two WT mice and 39 cells from one *Mff*^{gt} mouse were quantified.

Data are represented as mean ± SEM. ***p≤0.001; **** p≤0.0001. For statistical tests used, see the Materials and methods section.

Figure 3.5. *Mff*^{gt} sperm have reduced Complex IV activity and reduced fertility.

A) COX and SDH staining of WT and *Mff*^{gt} sperm. Scale bar, 10 μm.

B) Quantification of COX and SDH staining. At least 10 cells from each of four WT and four *Mff*^{gt} mice were quantified.

C) Schematic of IVF experiment.

D) Quantification of IVF outcomes.

Data are represented as mean ± SEM. ***p≤0.001; **** p≤0.0001. For statistical tests used, see the Materials and methods section.

Chapter 3 Figures

Figure 3.1

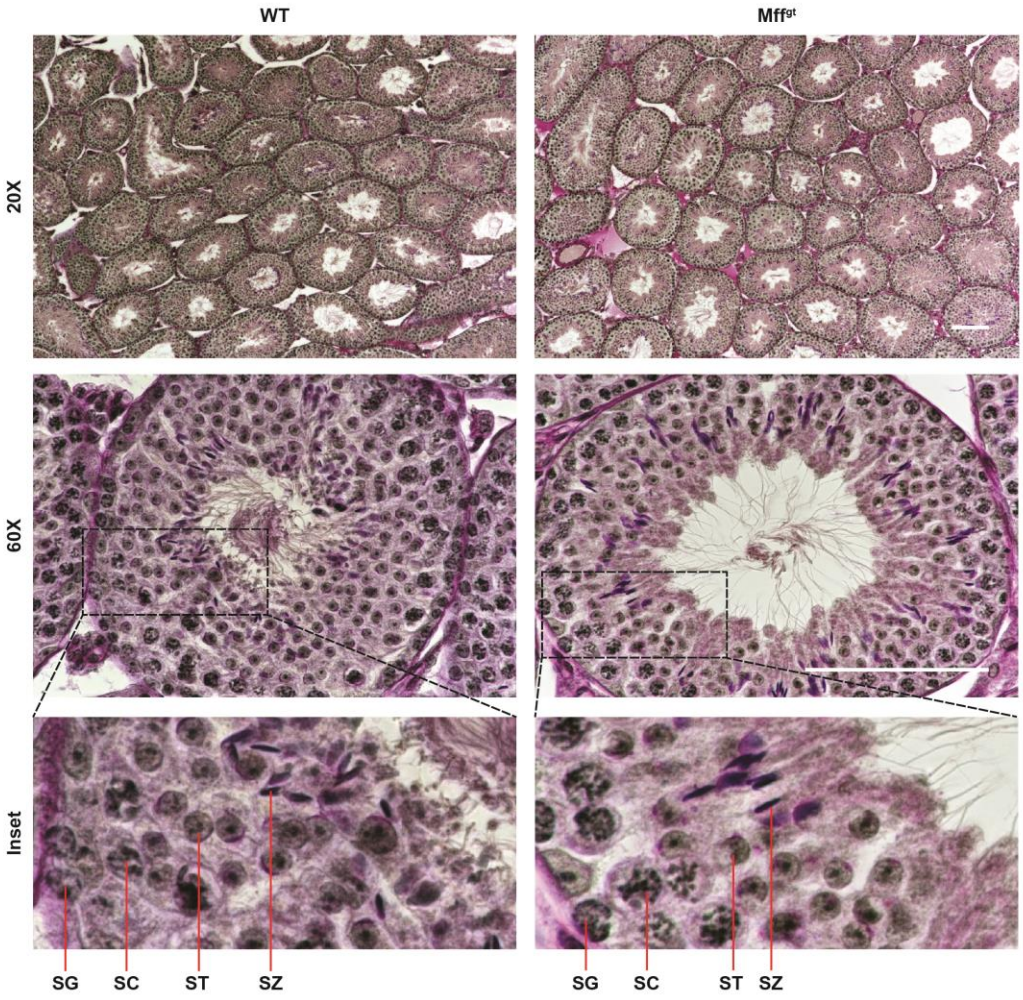

Figure 3.2

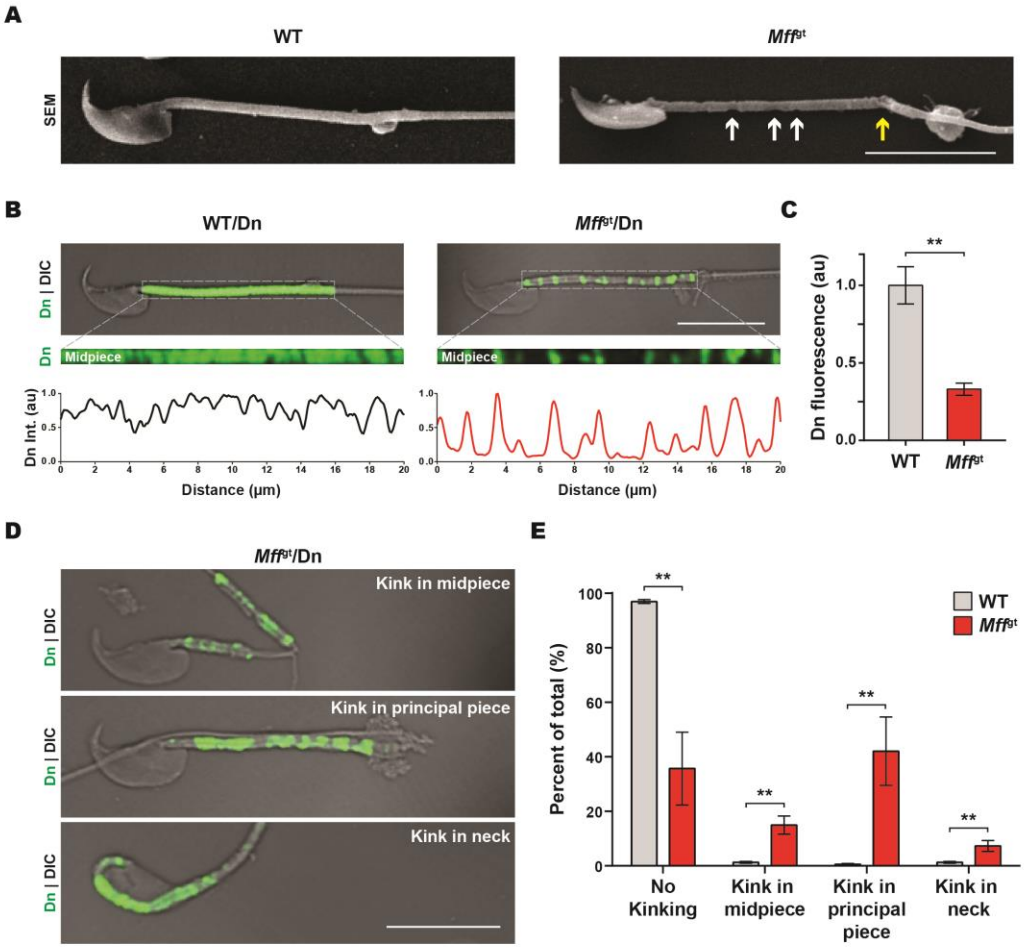
A
WT
Mff^gt
SEM
B
WT/Dn
Mff^gt/Dn
Dn | DIC
Dn
Midpiece
Dn Int. (au)
Distance (μm)
C
Dn fluorescence (au)
WT
Mff^gt
D
Mff^gt/Dn
Kink in midpiece
Kink in principal piece
Kink in neck
E
Percent of total (%)
WT
Mff^gt
No Kinking
Kink in midpiece
Kink in principal piece
Kink in neck

Figure 3.3

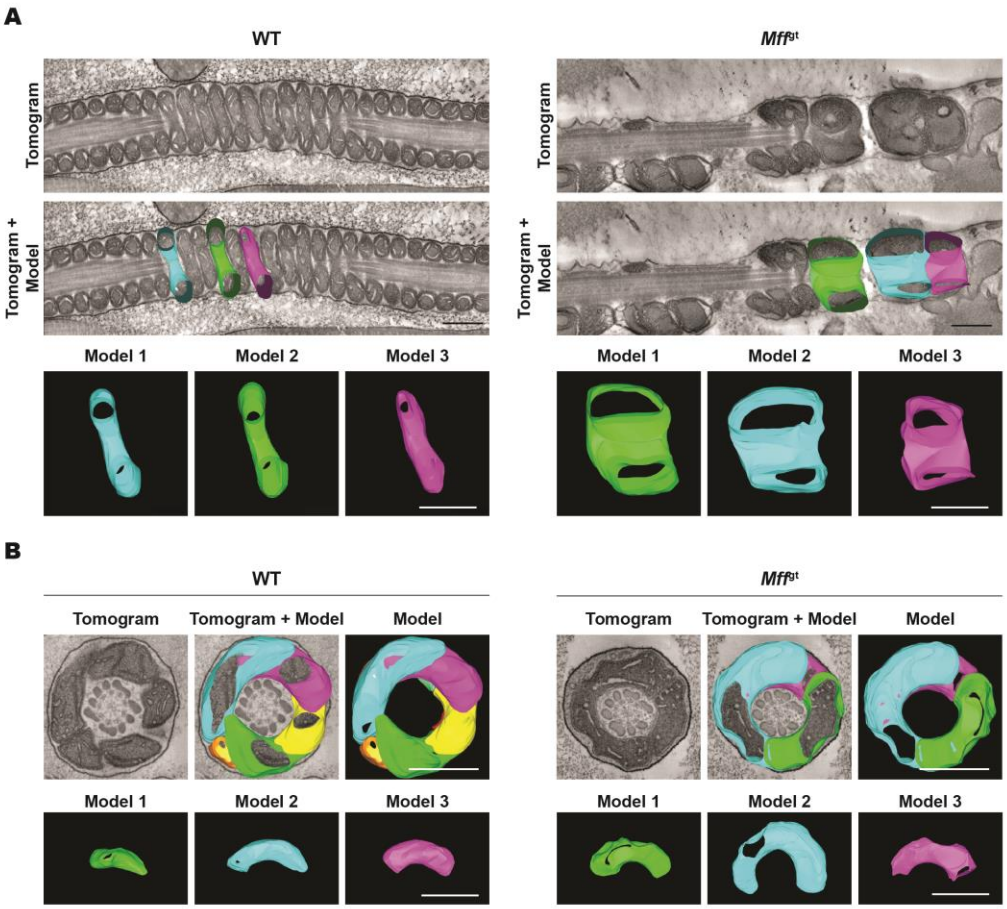
A
WT
Mff^gt
Tomogram
Tomogram + Model
Model 1
Model 2
Model 3
B
WT
Mff^gt
Tomogram
Tomogram + Model
Model
Model 1
Model 2
Model 3

Figure 3.4

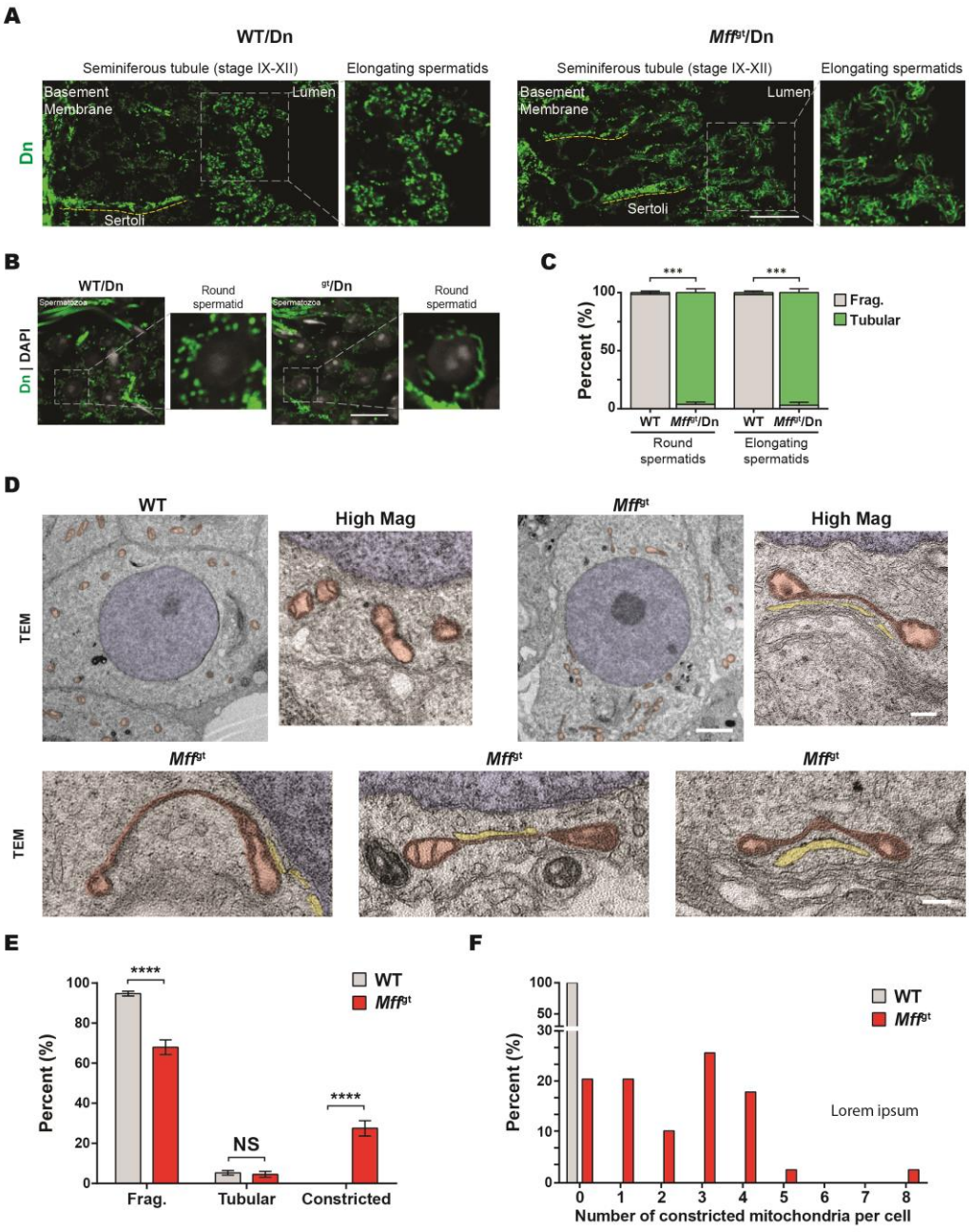
A
WT/Dn
Mff^gt/Dn
Seminiferous tubule (stage IX-XII)
Elongating spermatids
Basement Membrane
Lumen
Sertoli
Dn
B
WT/Dn
gt/Dn
Round spermatid
Spermatozoa
Dn | DAPI
C
Percent (%)
Frag.
Tubular
WT
Mff^gt/Dn
Round spermatids
Elongating spermatids
D
WT
Mff^gt
High Mag
TEM
E
Percent (%)
WT
Mff^gt
Frag.
Tubular
Constricted
NS
****
F
Percent (%)
Lorem ipsum
Number of constricted mitochondria per cell

Figure 3.5

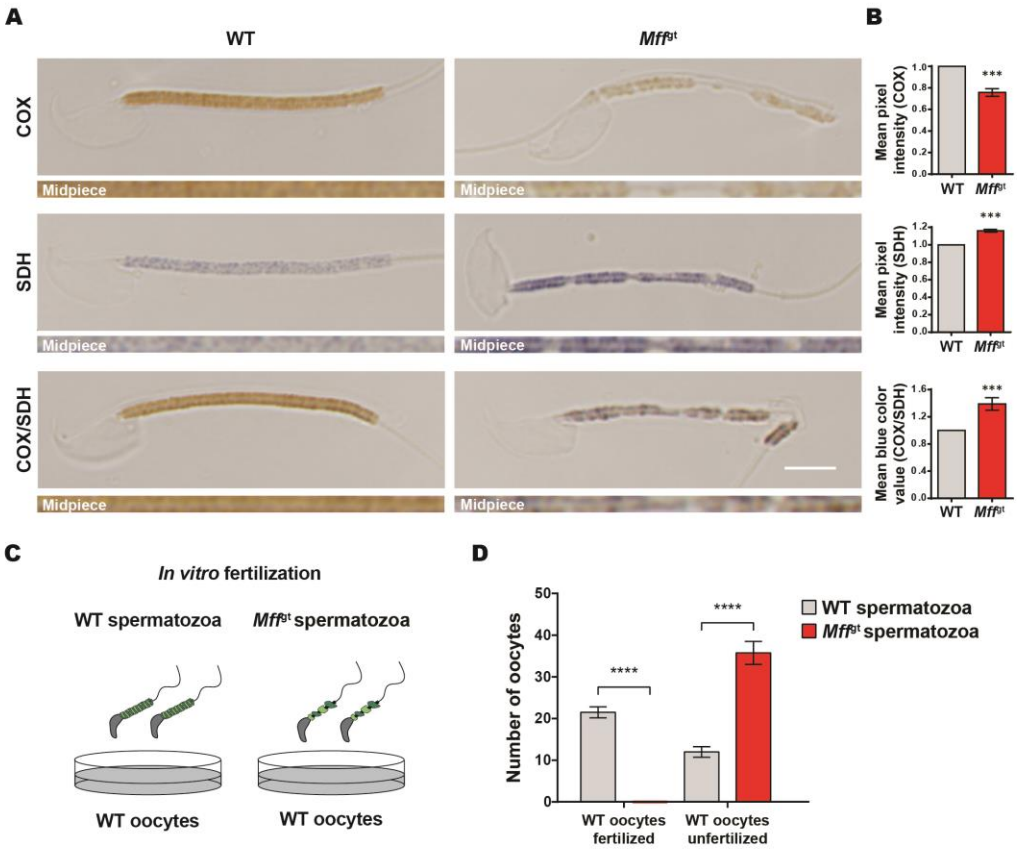
A
WT
Mff^gt
COX
SDH
COX/SDH
Midpiece
B
Mean pixel intensity (COX)
Mean pixel intensity (SDH)
Mean blue color value (COX/SDH)
***
WT
Mff^gt
C
In vitro fertilization
WT spermatozoa
Mff^gt spermatozoa
WT oocytes
WT oocytes
D
Number of oocytes
****
****
WT spermatozoa
Mff^gt spermatozoa
WT oocytes fertilized
WT oocytes unfertilized

Chapter 3 Supplementary figure legend

Figure 3.S1—related to Figure 3.3.

TEM in *Mff*^{gt} testis sections showing mitochondrial sheath morphology. Scale bar, 1 µm.

Chapter 3 Supplementary figure

Figure 3S.1

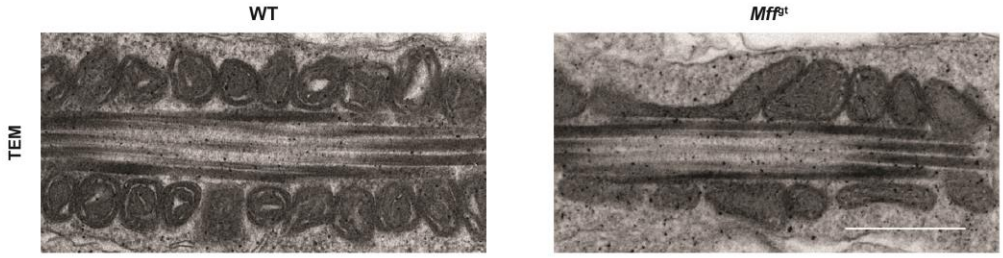

Video legends

Video 3.1:

EM tomogram and 3D rendering of longitudinal section of sperm from WT epididymis.

Video 3.2:

EM tomogram and 3D rendering of longitudinal section of sperm from *Mff*^{gt} epididymis.

Video 3.3:

EM tomogram and 3D rendering of transverse section of sperm from WT epididymis

Video 3.4:

EM tomogram and 3D rendering of transverse section of sperm from *Mff*^{gt} epididymis

Video 3.5:

Movie of sperm isolated from epididymides of a WT mouse.

Video 3.6:

Movie of sperm isolated from epididymides of a *Mff*^{gt} mouse.

Video files

Please download video files using the following link: Video Files - Chapter 3

References

Baehner, R. L., Boxer, L. A. and Davis, J. (1976). The biochemical basis of nitroblue tetrazolium reduction in normal human and chronic granulomatous disease polymorphonuclear leukocytes.

Baltimore, D., Hong, E. J., Lois-Caballe, C. and Pease, S. (2016). Method for producing transgenic animals.

Chan, D. C. (2012). Fusion and Fission: Interlinked Processes Critical for Mitochondrial Health. *Annual Review of Genetics* 46, 265–287.

Chan, D. C. (2020). Mitochondrial Dynamics and Its Involvement in Disease. *Annual Review of Pathology: Mechanisms of Disease* 15, null.

Chen, H., Ren, S., Clish, C., Jain, M., Mootha, V., McCaffery, J. M. and Chan, D. C. (2015). Titration of mitochondrial fusion rescues Mff-deficient cardiomyopathy. *J Cell Biol* 211, 795–805.

De Martino, C., Floridi, A., Marcante, M. L., Malorni, W., Scorza Barcellona, P., Bellocci, M. and Silvestrini, B. (1979). Morphological, histochemical and biochemical studies on germ cell mitochondria of normal rats. *Cell and tissue research* 196, 1–22.

Fonseca, T. B., Sánchez-Guerrero, Á., Milosevic, I. and Raimundo, N. (2019). Mitochondrial fission requires DRP1 but not dynamins. *Nature* 570, E34–E42.

Friedman, J. R., Lackner, L. L., West, M., DiBenedetto, J. R., Nunnari, J. and Voeltz, G. K. (2011). ER Tubules Mark Sites of Mitochondrial Division. *Science* 334, 358–362.

Ho, H.-C. and Wey, S. (2007). Three dimensional rendering of the mitochondrial sheath morphogenesis during mouse spermiogenesis. *Microscopy research and technique* 70, 719–723.

Kamerkar, S. C., Kraus, F., Sharpe, A. J., Pucadyil, T. J. and Ryan, M. T. (2018). Dynamin-related protein 1 has membrane constricting and severing abilities sufficient for mitochondrial and peroxisomal fission. *Nat Commun* 9, 1–15.

Korobova, F., Ramabhadran, V. and Higgs, H. N. (2013). An actin-dependent step in mitochondrial fission mediated by the ER-associated formin INF2. *Science* 339, 464–467.

Lee, J. E., Westrate, L. M., Wu, H., Page, C. and Voeltz, G. K. (2016). Multiple dynamin family members collaborate to drive mitochondrial division. *Nature* 540, 139–143.

Losón, O. C., Song, Z., Chen, H. and Chan, D. C. (2013). Fis1, Mff, MiD49, and MiD51 mediate Drp1 recruitment in mitochondrial fission. *Mol. Biol. Cell* 24, 659–667.

Mishra, P. and Chan, D. C. (2016). Metabolic regulation of mitochondrial dynamics. *J. Cell Biol.* 212, 379–387.

Otera, H., Wang, C., Cleland, M. M., Setoguchi, K., Yokota, S., Youle, R. J. and Mihara, K. (2010). Mff is an essential factor for mitochondrial recruitment of Drp1 during mitochondrial fission in mammalian cellsMff is essential for mitochondrial recruitment of Drp1. *J Cell Biol* 191, 1141–1158.

Park, K.-W. and Niwa, K. (2009). Bovine Oocytes Can Be Penetrated in Modified Tris-buffered Medium. *Asian Australas. J. Anim. Sci* 22, 500–506.

Pham, A. H., McCaffery, J. M. and Chan, D. C. (2012). Mouse lines with photo-activatable mitochondria to study mitochondrial dynamics. *genesis* 50, 833–843.

Ross, J. M. (2011). Visualization of mitochondrial respiratory function using cytochrome c oxidase/succinate dehydrogenase (COX/SDH) double-labeling histochemistry. *Journal of visualized experiments : JoVE* e3266.

Ruiz-Pesini, E., Diez, C., Lapeña, A. C., Pérez-Martos, A., Montoya, J., Alvarez, E., Arenas, J. and López-Pérez, M. J. (1998). Correlation of sperm motility with mitochondrial enzymatic activities. *Clin Chem* 44, 1616–1620.

Schwarz, T. L. (2013). Mitochondrial trafficking in neurons. *Cold Spring Harb Perspect Biol* 5,.

Tunc, O., Thompson, J. and Tremellen, K. (2010). Development of the NBT assay as a marker of sperm oxidative stress. *International Journal of Andrology* 33, 13–21.

Varuzhanyan, G., Rojansky, R., Sweredoski, M. J., Graham, R. L., Hess, S., Ladinsky, M. S. and Chan, D. C. (2019). Mitochondrial fusion is required for spermatogonial differentiation and meiosis. *eLife* 8, e51601.

Zhang, J., Wang, Q., Wang, M., Jiang, M., Wang, Y., Sun, Y., Wang, J., Xie, T., Tang, C., Tang, N., et al. (2016). GASZ and mitofusin-mediated mitochondrial functions are crucial for spermatogenesis. *EMBO reports* 17, 220–34.

CHAPTER 4

Fis1-mediated mitophagy is required for spermatid development

Grigor Varuzhanyan[1], Hsiuchen Chen[1], Shun-ichi Yamashita[2], Tomotake Kanki[2], Tsui-Fen Chen[3], Jeff Jones[3], Brett Lomenick[3], Mark S Ladinsky[1], and David C. Chan[1*]

[1]Division of Biology and Biological Engineering, California Institute of Technology, Pasadena, CA 91125, USA.

[2]Department of Cellular Physiology, Niigata University Graduate School of Medical and Dental Sciences, Niigata 951-8510, Japan.

[3]Proteome Exploration Laboratory of the Beckman Institute, California Institute of Technology, Pasadena, CA 91125, USA.

Abstract

Mitochondrial dynamics and mitophagy are important quality control mechanisms that safeguard mitochondrial function. *Fis1* is implicated in mitochondrial fission and mitophagy, but its role in tissue homeostasis and development remains poorly characterized. We report the generation of a conditional *Fis1* knockout mouse and show that *Fis1* is required for spermatogenesis. In wildtype mice, post-meiotic spermatids generate acrosomes and remove excess mitochondria and other cellular components to form highly compacted sperm cells. Loss of *Fis1* perturbs homeostasis of the acrosome and drives the coalescence of round spermatids into multinucleated giant cells (GCs). Using PhAM mice and novel conditional mitophagy reporter mice, we show that *Fis1*-null mitochondria fail to turn over and accumulate within GCs. These cellular defects are associated with a block in autophagic flux and a buildup of massive autolysosome-like structures. *Fis1*-null GCs have aberrant bowl-shaped mitochondria and display increased respiratory chain activity. We verify these findings by relative protein quantification using isobaric labeling and unexpectedly find an enrichment of proteins involved in the nuclear DNA damage response. We conclude that *Fis1*-mediated mitophagy is required for cellular homeostasis during spermatid development.

Introduction

Mitochondria are important cellular hubs that enable a wide range of physiological processes, such as ATP production via oxidative phosphorylation (OXPHOS), calcium buffering, and apoptosis. To preserve these crucial mitochondrial functions, cells utilize

multiple mitochondrial quality control mechanisms, including mitochondrial dynamics and mitophagy (Chan, 2020). During the last two decades, a tremendous effort has been made to establish and characterize the molecular factors that mediate these important quality control mechanisms. A particularly interesting factor is the Mitochondrial fission protein 1 (FIS1). *Fis1* was first identified as a Dnm1 receptor in the budding yeast, *Saccharomyces cerevisiae* (Fekkes et al., 2000; Mozdy et al., 2000; Tieu and Nunnari, 2000). During mitochondrial fission in yeast, FIS1 recruits DNM1 via the adaptor proteins MDV1 and CAF4, which serve as bridges between FIS1 and DNM1. However, mammalian cells lack orthologs of *Mdv1* and *Caf4* and *Fis1*'s role in mitochondrial fission in mammalian cells has been disputed. *Fis1* was initially reported to have an evolutionarily conserved role in mitochondrial fission, but later studies reported that *Fis1* has little (Loson et al., 2013) or no (Otera et al., 2010) role in mitochondrial fission. A recent structural study of human *Fis1* (Hill et al., 2020) and a study using fungus *Fis1* (Navarro-Espíndola et al., 2020) once again implicated *Fis1* in mitochondrial fission. Thus, the role of *Fis1* in mitochondrial fission remains unclear.

Fis1 is now thought to have a more prominent role in mitophagy. *Fis1* has been implicated in mitophagy in various cell types including cultured cells (Shen et al., 2014; Yamano et al., 2018, 2014), nematodes (Shen et al., 2014), early mouse embryos (Rojansky et al., 2016), and mouse skeletal muscles (Zhang et al., 2019). Recently, *Fis1* was shown to interact with the autophagy factor STX17 (Xian et al., 2019), suggesting that *Fis1* may have a more general function during unselective autophagy. Consistent with this idea, *Fis1* has been shown to mediate mitochondrion-lysosome contacts via the TBC1D15-Rab7 pathway

(Wong et al., 2018), and disruption of *Fis1* perturbs lysosomal function (Joshi et al., 2019; Kim et al., 2016). Thus, *Fis1* is implicated in both mitochondrial fission and degradation, but its precise mechanism of action, especially in mammalian tissues remains unclear.

Spermatogenesis is a promising system to investigate the role of *Fis1 in vivo* because it is highly sensitive to perturbations in mitochondrial dynamics (Varuzhanyan and Chan, 2020) and autophagy (Shang et al., 2016; Wang et al., 2014, p. 7). The role of mitophagy in germ cells remains unknown. To examine the role of *Fis1* in mitophagy during male germline development, we generate and characterize germ cell-specific *Fis1* KO and mitophagy reporter mice.

Results

Fis1 is required for spermatogenesis

To study the role of *Fis1* during male germline development, we generated mice with a conditional *Fis1* allele (Figure 4.S1A). To verify that Cre-mediated recombination results in a knockout, we immortalized MEFs from conditional *Fis1* embryos and transfected with EGFP-Cre. We verified Cre excision by genotyping at the *Fis1* locus (Figure 4.S1B) and checked protein levels by western blotting (Figure 4.S1C) and immunostaining (Figure 4.S1D). To remove *Fis1* from the male germline, we crossed conditional *Fis1* mice to the Stra8-Cre driver (Sadate-Ngatchou et al., 2008). We refer to the mutants as S8/Fis1, and their age-matched wild type (WT) littermate controls as S8/Control. Stra8-Cre expression is reported to begin at postnatal day 3 (P3) (Sadate-

Ngatchou et al., 2008) in the majority of stem-like GFRα1-positive spermatogonia (Hobbs et al., 2015; Varuzhanyan et al., 2019). Therefore, all major germ cell types should be depleted of *Fis1*. To verify knockout in germ cells, we genotyped tail DNA (Figure 4.S1B) and immunostained testis sections using an antibody against FIS1 (Figure 4.S1E). In control mice, *Fis1* is expressed in both germ and Sertoli cells, and in mutant mice, *Fis1* expression is eliminated selectively from germ cells.

S8/Fis1 mice were healthy, displaying no changes in weight compared to controls (Figure 4.1A). However, their testes were significantly smaller than controls (Figure 4.1B) and their epididymides were completely devoid of spermatozoa (Figures 4.1C and 4.1D), indicating an essential role for *Fis1* during spermatogenesis. To examine whether this spermatogenic defect is associated with increased cell death, we performed terminal deoxynucleotidyl transferase dUTP nick end labeling (TUNEL) in testis sections (Figures 4.1E and 4.1F). S8/Fis1 testes had more than four-fold increase in TUNEL positive tubules, indicating increased cell death by apoptosis.

During normal germ cell development, apoptotic germ cells are phagocytosed by Sertoli cells (Braun, 1998; Elliott et al., 2010). We wondered whether apoptotic germ cells in S8/Fis1 mutants were similarly phagocytosed. To address this experimentally, we performed the TUNEL assay and co-stained against Rab7, a small GTPase associated with phagophore maturation and subsequent fusion with lysosomes (Zhang et al., 2009) (Figures 4.1G and 4.1H). In control testes, about one third of TUNEL positive cells were enclosed by ring-like structures decorated with Rab7, suggesting that they are on the pathway to phagocytic degradation. S8/Fis1 cells had a five-fold increase in the number of Rab7

positive phagosomes. Thus, depletion of FIS1 causes apoptotic loss of germ cells, which are then likely eliminated by Sertoli cell phagocytosis.

Germ cell *Fis1* deletion results in multinucleated giant cells

To better understand the spermatogenic defect in S8/Fis1 mice, we performed Periodic Acid-Schiff (PAS) staining of adult testis sections (Figure 4.2A). Control tubules exhibited classical germ cell organization and their lumens were filled with spermatozoa. In stark contrast, S8/Fis1 tubules were devoid of mature spermatozoa and were filled with structures that resemble previously described multinucleated giant cells (GCs) (MacGregor et al., 1990). We verified that these structures are multinucleated by staining testis sections with DAPI and the plasma membrane marker, Na/K-ATPase, to delineate germ cell boundaries (Figure 4.2B). The GCs were strongly positive for the spermatid-specific acrosome marker SP-10 (Osuru et al., 2014) (Figure 4.2C, 4.2D). In WT testis sections, SP-10 expression was restricted to round and elongating spermatids, with the most intense staining highlighting the crescent-shaped acrosome. In contrast, SP-10 staining was diffuse and much more intense in S8/Fis1 GCs. The majority of S8/Fis1 tubules contained spermatid GCs (Figure 4.2E).

***Fis1* is required for acrosome homoeostasis**

To determine the stage of the spermatogenic arrest in S8/Fis1 mice, we performed PAS-staining in juvenile P28 mice, which are undergoing the first round of spermatogenesis. The PAS reaction clearly marks the acrosome in WT spermatids (Osuru

et al., 2014, p. 10) (Figure 4.3A). In *Fis1*-null mutants, round spermatids were present, but the acrosome appeared fragmented. To verify that the aberrant PAS-positive structures in the mutant tubules were indeed fragmented acrosomes, we stained testis sections with the SP-10 acrosome marker described above (Figure 4.3B). Indeed, the SP-10-positive acrosome structures in mutant tubules were fragmented and distributed throughout the cytoplasm (Figure 4.3B).

To visualize acrosome ultrastructure, we performed electron tomography (Figures 4.3C and 4.3D). WT spermatids contained normal acrosomes, which could be seen directly adjacent to the trans Golgi network. Trans Golgi cisternae could be seen fusing with the acrosome, consistent with previous observations that the acrosome is largely a Golgi-derived organelle (Berruti and Paiardi, 2011) (Figure 4.3C and Videos 4.1-2). In contrast, S8/Fis1 GCs generally contained fragmented acrosomes (Figures 4.3C, 4.3D), indicating a defect in acrosome biogenesis or maintenance.

Spermatogenesis is initiated by a pulse of retinoic acid that travels like a wave along the length of a seminiferous tubule. As a result, different regions of a tubule are in distinct developmental phases that display unique cellular associations, referred to as “stages” (Griswold, 2016; Russell et al., 1993). The stage of the seminiferous epithelium is defined by the developmental steps of spermatids. In mice, spermatid development is divided into 16 steps, which are defined by the extent the acrosome covers the nucleus. To determine the stage of the spermatogenic arrest in S8/Fis1 mice, we examined younger (P23) mice whose acrosomes were first forming (Figure 4.3E). We analyzed spermatid steps using the acrosome marker SP-10. Acrosome structures formed normally up to at least Step-5 in

S8/Fis1 mice, indicating *Fis1* is required for maintenance, but not formation of the acrosome. Strikingly, no Step-9 elongating spermatids could be found in juvenile or adult S8/Fis1 testes (Figure 4.3F). Taken together, these data indicate that spermatogenesis in S8/Fis1 mice arrests between Stage V and Stage VIII.

Fis1-null giant cells exhibit mitochondrial accumulation and perturbed mitophagy

To understand the cellular mechanism for these spermatogenic defects, we first examined mitochondria using PhAM mice (Pham et al., 2012). We noticed a marked increase in mitochondrial Dendra2 fluorescence intensity in S8/Fis1 GCs compared to WT spermatids (Figure 4.4A), indicating mitochondrial accumulation. To test whether the increased Dendra2 fluorescence in S8/Fis1 GCs could be due to defective mitophagy, we generated conditional mitophagy reporter mice, which express a mitochondrially targeted mCherry-EGFP fusion protein, preceded by a floxed stop cassette (Figures 4.S4A and 4.S4B). In acidic compartments, mitochondrial EGFP fluorescence is selectively quenched while mCherry fluorescence remains relatively stable. Thus, mitochondria that are undergoing mitophagy exhibit red-only fluorescence. To study mitophagy specifically in germ cells, we crossed conditional mitophagy reporter mice to the Stra8-Cre driver and visualized PFA-fixed testis sections by confocal microscopy. Using this system, we found an increase in red-only signals in S8/Fis1 GCs, which were much larger compared to control (Figures 4.4B and 4.4C). Because *Fis1*-null mitochondria accumulate in GCs, these data suggest that *Fis1*-null mitochondria fail to get recycled, despite being targeted to the autophagy pathway.

Interestingly, red-only mitophagy signals could also be seen outside of germ cells, within the Sertoli cell cytoplasm (Figures 4.4D and 4.4E). Because the mitophagy reporter is driven by Stra8-Cre expression in germ cells, the red-only signals in Sertoli cells should be derived from germ cell mitochondria. Red-only mitophagy signals within the Sertoli cell cytoplasm could reflect a hitherto uncharacterized transcellular degradation of germ cell mitochondria by Sertoli cells (transmitophagy), as occurs in glial cells (Davis et al., 2014). Alternatively, it may reflect phagocytic degradation of apoptotic germ cells (heterophagy), which is known to occur in Sertoli cells. *Fis1* mutant tubules exhibit increased mitophagy signals in Sertoli cells (Figures 4.4D and 4.4E), which may reflect the increased phagocytosis described above (Figures 4.1G and 4.1H).

S8/Fis1 spermatid giant cells exhibit aberrant autophagy

Our results demonstrated that *Fis1*-null GCs form large mitophagic vesicles (Figure 4.4B). We therefore checked whether *Fis1*-null GCs have a block in autophagic flux. We first examined the expression of ATG9A (Figure 4.5A), an integral membrane protein on vesicles that generate autophagosomes (Imai et al., 2016). Interestingly, in WT mice, ATG9A localizes to the acrosome, suggesting that the acrosome may serve as a phagophore assembly site. In contrast, ATG9A accumulates throughout the cytoplasm in S8/Fis1 GCs. We next looked at the expression patterns of LC3B and LAMP1, which mark autophagosomes and lysosomes, respectively (Figures 4.5B and 4.5C). Compared to control, *Fis1* mutants exhibited an accumulation of large LC3B and LAMP1 aggregates, consistent with a block in autophagic flux. To visualize the ultrastructure of the autophagic

structures described above, we performed electron tomography in testis section. Consistent with the immunostaining data, our EM analysis identified massive autophagic structures that resemble autolysosomes (Figures 4.5D, 4.5E, and 4.S5).

To investigate whether the accumulation of the autophagic markers is due to a block in autophagy or increased autophagic flux, we checked the expression pattern of a widely-used marker of autophagic flux, P62 (Katsuragi et al., 2015) (Figure 4.5F). We find that P62 is pronouncedly accumulated in S8/Fis1 GCs, suggesting a block in autophagic turnover. Because autophagy utilizes ubiquitin tags, we also probed testis sections with an antibody against multi-ubiquitin (Figure 4.5G). Consistent with previous reports (Baarends et al., 2005; Lu et al., 2010, p. 8), we found ubiquitin signal on the XY body in WT spermatocytes (white arrows), indicating specificity of the antibody. WT round spermatids lacked any ubiquitin signal, whereas S8/Fis1 GCs displayed a pronounced accumulation of ubiquitin aggregates. Taken together, these data indicate that *Fis1* is required for autophagic degradation of spermatid mitochondria.

***Fis1*-null giant cells have aberrant mitochondria and increased respiratory chain activity**

We next examined whether the accumulated mitochondria in *Fis1*-null spermatids have any unique morphological features by performing electron tomography (Figures 4.6 and 4.S6). To visualize mitochondria within entire GCs, we performed montage tomography (Figure 4.S6). In WT round spermatids, mitochondria were generally small and spherical, as described before (Varuzhanyan, n.d.) (Figures 4.6A, 4.6D, and 4.S6). In P24

and P32 S8/Fis1 GCs, mitochondria were elongated, often containing constrictions (Figures 4.6A and 4.6D). In P36 S8/Fis1 GCs, mitochondria had a very distinct and unusual morphology. In single 400 nm sections, mutant mitochondria displayed severe and lengthy constrictions near the center, and a bulbous region at each end (Figures 4.6B, 4.6D, and 4.S6). To visualize morphology of the entire organelle, we performed serial section electron tomography and generated 3D renderings of entire mitochondria (Figures 4.6C and 4.S6 and Video 4.3). This analysis revealed that mutant mitochondria are bowl-like structures in 3D. To check respiratory chain activity of these aberrant mitochondria, we performed COX/SDH enzyme histochemistry in testis sections. S8/Fis1 GCs exhibited increased COX/SDH staining, indicating increased respiratory chain complex IV and II activity (Figures 4.6E and 4.6F).

Relative protein quantification reveals an upregulation of the nuclear DNA damage response in S8/Fis1 germ cells

We next performed relative protein quantification in isolated germ cells using tandem mass tag (TMT) labeling followed by mass spectrometry (Figure 4.7). Because multinucleated GCs are too large to be isolated by FACS, we performed proteomics in P24 mice, which contain fewer and smaller GCs). We therefore expect that the differentially expressed proteins from the proteomics analysis should reveal defects that precede or occur very early during GC formation. The proteomic analysis identified 172 differentially expressed proteins in *Fis1*-null germ cells compared to control ($q<0.05$) (Spreadsheet 1). We verified some of the key phenotypes in S8/Fis1 mice using Gene Set Enrichment

Analysis (GSEA) (Mootha et al., 2003; Subramanian et al., 2005) and DAVID GO analysis (Huang et al., 2009a, 2009b). As described above, *Fis1*-null spermatids have a pronounced increase in mito-Dendra2 fluorescence intensity, indicating mitochondrial accumulation (Figure 4.4A). The autophagy block described in Figure 4.5 suggests that the mitochondrial accumulation is due to decreased turnover, but this could also be due to increased biogenesis. Using GSEA, we checked whether the Reactome Mitochondrial Biogenesis gene set (Jassal et al., 2020) was enriched in our dataset. The GSEA analysis indicates that the proteins that promote mitochondrial biogenesis are significantly downregulated in the mutant compared to control (ES = -0.39; P<0.001) (Figure 4.S7A), supporting our observations that the mitochondrial accumulation is caused by decreased turnover.

We showed above that the mitochondrial accumulation in S8/Fis1 GCs is associated with a block in autophagic flux, which manifests as a buildup of autophagic intermediates (Figure 4.5). To check for enrichment of proteins involved in autophagic flux, we performed GSEA against autophagy-related gene sets from the Gene Ontology (GO) database (Carbon and Mungall, 2018). Consistent with the observations in Figure 4.5, GSEA indicated an upregulation of proteins related phagophore assembly (ES = 0.60; p<0.001), vesicular contents (ES = 0.33; p<0.0001), and mitophagy (ES = 0.37; p<0.0001) (Figure 4.S7B).

Unexpectedly, DAVID GO analysis revealed a significant enrichment in GO terms related to double-strand break (DSB) repair (Table 1). To verify this, we examined all known DNA damage related proteins in our differentially expressed (q<0.05) dataset (Figure 4.7B). Indeed, DNA damage response proteins were among the most significantly

mis-regulated proteins. Because the DNA damage response can be triggered by oxidative stress (Barzilai and Yamamoto, 2004), we used GSEA to look for an upregulation of proteins involved in oxidative stress. We found an enrichment of oxidative stress proteins (ES = 0.56; $p<0.0001$) (Figure 4.S7C), suggesting that the DNA damage response may be triggered by increased oxidative stress. These observations are consistent with the aforementioned mitochondrial accumulation (Figure 4.4A) and increased respiratory chain Complex IV and II activity (Figures 4.6E and 4.6F) in *Fis1*-null GCs.

To look for signs of DNA damage in *Fis1-null* germ cells, we stained testis sections with the well-established marker of DSBs, γH2AX, (Mah et al., 2010) (Figures 4.7C-7F, 4.S7D, and S7E). During normal spermatogenesis, γH2AX is first observed in early prophase I spermatocytes when programmed DSBs are generated to enable homologous recombination. These DSBs are resolved as homologous recombination takes place during Pachytene, but a second wave of γH2AX marks the XY body. In Diplotene, the γH2AX signal is completely resolved and γH2AX signals do not reappear until much later in spermatogenesis, during the histone to protamine transition. Consistent with these observations, we find that WT round spermatids lack γH2AX staining (Figure 4.7C). In contrast, spermatids in S8/Fis1 GCs have robust γH2AX expression (Figures 4.7C and 4.7D). Mutant spermatids which were not part of GCs also occasionally exhibited increased γH2AX expression (Figures 4.7E and 4.7F), indicating that DNA damage may precede GC formation. To check whether spermatids with increased γH2AX are apoptotic, we performed TUNEL staining in testis sections and simultaneously stained with γH2AX.

None of the γH2AX positive cells were associated with TUNEL labeling, indicating that they are not apoptotic (Figures 4.S7D and 4.S7E).

Discussion

A prominent feature of *Fis1* knockout spermatids is formation of multinucleated giant cells (GCs). Germ cell multinucleation occurs in multiple species and in response to various stresses, but how or why they form remains unclear (Elliott et al., 2010; Fawcett et al., 1959, 1959; Holstein and Eckmann, 1986; MacGregor et al., 1990; Morton et al., 2016; Rotter et al., 1993; Singh and Abe, 1987). GC formation is likely not a generic response to dysfunctional germ cells because many severe spermatogenic defects present without multinucleated GCs (Borg et al., 2010). Thus, testicular insults that result in multinucleation may share common molecular and pathological features. Consistent with this idea, a recent study reported spermatid multinucleation in response to germ cell deletion of the peroxisome membrane protein, *Pex13* (Brauns et al., 2019). *Fis1* is primarily located on mitochondria, but it also localizes to the peroxisome, raising the possibility that some common pathological pathway between *Fis1* and *Pex13* deletion contributes to GC formation.

Fis1-null spermatids have a pronounced fragmentation of the acrosome. Acrosomes also fragment in *Atg7*-deficient germ cells (Wang et al., 2014), providing further support for a defect in autophagic flux in S8/Fis1 mice. In the model proposed by Wang and colleagues, the acrosome is a modified lysosome with which autophagosomes can fuse (Wang et al., 2014). We observed that ATG9A localizes to the acrosome. This suggests that the acrosome

is more likely to be a phagophore assembly site because ATG9A normally gets retrieved from phagophores by Dynamin2 mediated vesicle scission and is not normally present on autophagosomes (Riera et al., 2019, p. 2).

Fis1 ablation in *C. elegans* muscle cells and in cultured mammalian cells causes an accumulation of LC3B (Shen et al., 2014), suggesting an evolutionarily conserved role of *Fis1* in autophagy. However, our results indicate species- and cell type-specific differences. In *C. elegans* muscle cells, mitochondria are spared from autophagic aggregates, whereas in mouse spermatids, *Fis1*-null mitochondria can enter the autophagy pathway. It should be noted that autophagic turnover is blocked in *Fis1* mutant spermatids (Figure 4.5). Therefore, even a few *Fis1*-null mitochondria that enter the autophagy pathway will give rise to a persistent mitophagy (red-only) signal. Thus, the increased mitophagy signals in *Fis1*-null spermatids likely reflect the buildup of aberrant mitolysosomes rather than increased mitophagic turnover.

Fis1-null mitochondria elongate before transforming into the unusual bowl-shaped structures at P36. The proteomics analysis at P24 reveals that *Mff* is significantly downregulated in *Fis1* knockouts (Spreadsheet 1). Because *Mff* is known to mediate mitochondrial fission in many cell types, including spermatids (Varuzhanyan, n.d.), reduction of *Mff* likely contributes to the mitochondrial elongation phenotype that precedes mitochondrial bowl formation. Similar structures termed mitochondrial spheroids have previously been observed in cultured cells treated with CCCP (Yin and Ding, 2013), but it is unclear whether these mitochondrial phenotypes are related.

Our proteomics and γH2AX staining revealed a robust increase in the DNA damage response in *Fis1*-null spermatids. Multiple lines of evidence indicate possible mechanisms by which DNA damage can contribute to the spermatogenic arrest in S8/Fis1 mice. Our proteomics analysis indicated that the DNA damage response protein, ESCO2 is the most downregulated protein in S8/Fis1 testes (Figure 4.7B). Similarly to our *Fis1* mutants, germ cell *Esco2* deletion causes spermatogenesis arrest at the round spermatid stage (McNicoll et al., 2020, p. 2). However, this does not result in multinucleation, indicating that the spermatogenic defects in S8/Fis1 mice cannot be explained by ESCO2 reduction alone. Furthermore, a robust mediator of the DNA damage response, P53 (Williams and Schumacher, 2016), is expressed in spermatocytes. Multiple strains of P53 mutant mice present with multinucleated spermatids (Rotter et al., 1993), raising the possibility that nuclear DNA damage caused by *Fis1* deficiency may be driving GC formation.

Materials and methods

Generation of mice

All mouse experiments were approved by the California Institute of Technology (Caltech) Institutional Animal Care and Use Committee. The conditional *Fis1* mouse was generated at the Janelia research campus by floxing exon 2. Cre mediated recombination excises exon two, resulting in a frameshift mutation and a null-allele. S8/Control (Stra8-Cre$^{+/tg}$; *Fis1*$^{+/lox}$; PhAM$^{+/lox}$) and S8/Fis1 (Stra8-Cre$^{+/tg}$; *Fis1*$^{\Delta/lox}$; PhAM$^{+/lox}$) mice were generated by crossing Stra8-Cre; *Fis1*$^{+/\Delta}$; mice to *Fis1*$^{loxP/loxP}$; PhAM$^{loxP/loxP}$ mice. The Stra8-

Cre driver (Jackson Laboratory #017490) (Sadate-Ngatchou, Payne, Dearth, & Braun, 2008) and the mito-Dendra2 allele (Pham, McCaffery, & Chan, 2012) were all described previously. All mice were maintained on a C57B6 genetic background. To generate germ cell-specific mitophagy reporter mice, we crossed Stra8-Cre; *Fis1*$^{+/\Delta}$; mice to *Fis1*$^{loxP/loxP}$; mCherry-EGFP$^{loxP/loxP}$ mice.

Generation of Fis1 KO MEFs

MEFs were isolated from conditional *Fis1* embryos at E14.5 using standard protocol and immortalized at P3 using SV40 large T Antigen (TAg). Briefly, the retroviral TAg vector was cotransfected into 293T cells with pCL-Eco (Adgene #12371) using calcium phosphate precipitation. Virus was collected, filtered, and added to conditional *Fis1* MEFS. Cells were spun at 2,400 rpm for 30 minutes and incubated for 8 hr before replacing with complete medium (DMEM 11995, 10% fetal bovine serum, 1% Pen/Strep). Cells were selected with puromycin for 1 week, then transiently transfected with EGFP-Cre using Lipofectamine 3000 per manufacturer protocol. EGFP-Cre-expressing cells were single-cell sorted in 96 well plates using a benchtop Bio-Rad S3e cell sorter. *Fis1* KO was verified by genotyping, western blotting, and immunostaining.

Epididymal sperm counting

Mice were euthanized at P56, and epididymides were dissected and thoroughly minced in 1.7 ml microcentrifuge tubes containing 1 ml PBS. Samples were incubated at 37°C for 20 minutes to allow sperm to swim out. 900 µl of the supernatant was transferred

into a fresh microcentrifuge tube. For sperm counting and morphology analysis, samples were allowed to settle for several hours for sperm to stop swimming before counting on a hemocytometer. Sperm counts were normalized to the weight of the epididymides of each mouse. For motility quantification, freshly isolated sperm were transferred to a hemocytometer, and the proportion of motile sperm was quantified. For motility movies, freshly isolated sperm were transferred to glass-bottom FluoroDish Cell Culture Plates (FD35-100) and imaged at one frame per second for 10 seconds using a confocal microscope as described below.

Periodic acid-Schiff staining

After dissection, testes were fixed in Bouin's fixative overnight at 4ºC, dehydrated in a 30-90% ethanol gradient, cleared in Xylenes, and embedded in paraffin. Tissue blocks were sectioned at 7 µm, deparaffinized, and rehydrated before staining. Briefly, slides were incubated with 1% periodic acid (Electron Microscopy Sciences (EMS); 19324-10) for 30 minutes at RT, washed in running water for 5 minutes, then rinsed in deionized water. Slides were incubated with Schiff's reagent (EMS; 260582-05) for 30 minutes at RT and washed as described above before counterstaining with Hematoxylin Gill 2 for 30 seconds at RT. Slides were washed in running water for 1 minute, dehydrated with ethanol, cleared with xylene, then mounted using Cytoseal XYL mounting media (Thermo Fisher Scientific; 22-050-262).

Immunofluorescence

For immunostaining of tissue sections, testes were cut at the poles, fixed in 4% PFA for 4 hours at 4°C, incubated with 30% sucrose in PBS overnight at 4°C (or until tissues sank), incubated in a 1:1 solution of 30% sucrose in PBS and optimal cutting temperature (OCT) embedding medium (Thermo Fisher Scientific; NC9636948) for 15-30 minutes, then embedded in OCT medium and frozen in dry ice. Tissue blocks were sectioned at 10 µm onto glass slides, dried overnight, and stored at -80°C until ready for immunostaining. Frozen slides were briefly thawed at room temperature, rehydrated in PBS, permeabilized with 0.15% TX-100 for 15 minutes, and blocked for 1 hour using Blocking Buffer (10% FBS, 3% BSA, 0.05% TX-100 in PBS). Slides were incubated with primary antibodies in a humidified chamber overnight at 4°C, washed three times in PBS for 15 minutes each, then incubated with secondary antibodies in a humidified chamber for 2.5 hours at RT. Slides were counterstained with DAPI, washed as described above, mounted with Fluorogel (EMS; 17985-10), coverslipped, sealed with nail polish, and stored at 4ºC before imaging.

Western blotting

Cells were grown to confluency in 6-well plates and lysed in 200 µL of Lysis Buffer (20 mM Tris-Cl, 150 mM NaCl, 2mM EDTA, 1% Triton X-100, pH 7.5 with Halt Protease Inhibitor added to 1X). Proteins (5 µg) were separated by SDS-PAGE and transferred to Polyvinylidene difluoride membranes using semi-dry electrophoresis. Membranes were blocked with 5% non-fat dry milk for 1 hr at RT, followed by primary antibody incubation overnight at 4°C. HRP-conjugated secondary antibodies were applied for 2 hr at RT.

Immobilon Western chemiluminescent HRP substrate (Millipore 90720) was added according to the manufacturer's instructions and the protein bands were visualized on X-ray film (Amersham Hyperfilm MP). For analysis, densitometry was performed in ImageJ and protein levels were normalized to that of tubulin.

Apoptotic cell labeling

To label apoptotic nuclei, the TUNEL assay was performed in PFA-fixed, OCT-embedded testis sections using the ApopTag® Red In Situ Apoptosis Detection Kit (Millipore; S7165) according to the manufacturer's protocol. Nuclei were counterstained with DAPI.

Electron microscopy and dual-axis tomography

Mouse testes were dissected and immediately fixed with cold 3% glutaraldehyde, 1% paraformaldehyde, 5% sucrose in 0.1 M sodium cacodylate trihydrate. Pre-fixed pieces of tissue were rinsed with fresh cacodylate buffer and placed into brass planchettes (Type A; Ted Pella, Inc., Redding, CA) prefilled with 10% Ficoll in cacodylate buffer. Samples were covered with the flat side of a Type-B brass planchette and rapidly frozen with a HPM-010 high-pressure freezing machine (Leica Microsystems, Vienna Austria). The frozen samples were transferred under liquid nitrogen to cryotubes (Nunc) containing a frozen solution of 2.5% osmium tetroxide, 0.05% uranyl acetate in acetone. Tubes were loaded into an AFS-2 freeze-substitution machine (Leica Microsystems) and processed at -90°C for 72 h, warmed over 12 h to -20°C, held at that temperature for 8 h, then warmed to 4°C

for 2 h. The fixative was removed, and the samples were rinsed 4x with cold acetone, and then were infiltrated with Epon-Araldite resin (Electron Microscopy Sciences, Port Washington PA) over 48 h. Samples were flat-embedded between two Teflon-coated glass microscope slides, and the resin polymerized at 60°C for 24-48 hr.

Flat-embedded testis samples were observed with a stereo dissecting microscope, and appropriate regions were extracted with a microsurgical scalpel and glued to the tips of plastic sectioning stubs. Semi-thick (400 nm) serial sections were cut with a UC6 ultramicrotome (Leica Microsystems) using a diamond knife (Diatome, Ltd. Switzerland). Sections were placed on Formvar-coated copper-rhodium slot grids (Electron Microscopy Sciences) and stained with 3% uranyl acetate and lead citrate. Gold beads (10 nm) were placed on both surfaces of the grid to serve as fiducial markers for subsequent image alignment. Grids were placed in a dual-axis tomography holder (Model 2040, E.A. Fischione Instruments, Export PA) and imaged with a Tecnai TF30ST-FEG transmission electron microscope (300 KeV) equipped with a 2k x 2k CCD camera (XP1000; Gatan, Inc. Pleasanton CA). Tomographic tilt-series and large-area montaged overviews were acquired automatically using the SerialEM software package (Mastronarde, 2005). For tomography, samples were tilted +/- 64° and images collected at 1° intervals. The grid was then rotated 90° and a similar series taken about the orthogonal axis. Tomographic data was calculated, analyzed and modeled using the IMOD software package (Kremer, Mastronarde, & McIntosh, 1996; Mastronarde, 2008) on MacPro computers (Apple, Inc., Cupertino, CA).

Confocal imaging and image processing

Confocal fluorescence images and videos were acquired using an inverted Zeiss LSM 710 confocal microscope with a 60X Plan-Apochromat objective. Epifluorescence and bright-field images were acquired using an upright Nikon Eclipse Ni-E fluorescence microscope equipped with a Ds-Ri2 camera and CFI Plan Apochromat Lambda objectives. For PAS histology images, Z stacks were acquired and all-in-focus images were created using the NIS Elements Extended Depth of Focus plugin. All images were processed using ImageJ. All image modifications were performed on entire images (no masking was used) and were performed identically between genotypes.

Germ cell quantification from testis sections

Germ cells were counted from 10 μm testis sections using the germ cell markers described in the main text. Quantification was restricted to germ cells within round transverse sections of seminiferous tubules and is reported as either the mean number of germ cells per seminiferous tubule cross section or the most differentiated cell type per seminiferous tubule cross section. Only germ cells expressing Dendra2 were included in the quantification to exclude cells without *Stra8-Cre* expression. For each genotype, at least 50 transverse sectioned seminiferous tubules were quantified from at least 4 mice.

Fluorescence-activated cell sorting (FACS)

Testes were dissociated from juvenile males (P24) as described previously (Gaysinskaya et al., 2014; Gaysinskaya and Bortvin, 2015). The cell suspension was passed

through a 100 µm nylon cell strainer, pelleted at 150 *g* for 5 minutes, and suspended in 2 ml to Flow Cytometry Buffer (HBSS with 2.5 mg/ml fraction V BSA, 10 Mm HEPES buffer, 6.6 mM sodium pyruvate, 0.05% sodium lactate, DNase and 1 mM GCl2, pH 7.2). The cells were filtered through a 35 µm Corning™ Falcon™ Test Tube with Cell Strainer Snap Cap (Fischer Scientific; #08-771-23) and sorted using a benchtop Bio-Rad S3e cell sorter. mito-Dendra2 expressing germ cells were collected into 1 mL FACS buffer in a 5 ml glass tube, pre-treated with BS, then pelleted at 500 g for 5 min at 4°C. 800 µl of the supernatant was carefully removed the top of the tube to not disturb the invisible pellet. Cells were washed once with PBS, transferred to 1.7 ml tubes, frozen in liquid nitrogen, and stored at -80°C until proteomics experiments.

Mass spectrometry

Cell pellets were lysed on ice with 40 µL 0.05% SDS/0.5M TEAB lysis buffer by syringe titration with a 23G needle (30x) followed by tip sonication (5 x 5 sec at 20% power). Lysates were then clarified at 16,000 g for 10 min at 4C and protein concentration measured by Bradford assay. Lysates were reduced with 3mM TCEP for 1hr at 50C, alkylated with 10mM iodoacetamide for 15 min at room temperature, digested with 1:100 LysC for 4hr at room temperature, and digested with 1:30 trypsin overnight at 37C.

Digests were stopped by acidifying with 2.5 µL 100% formic acid and desalted on a C4 3mm x 8 mm trap cartridge (Optimize Technologies #10-04818-TM) run on an Agilent 1100 HPLC. Desalted peptides were lyophilized, resuspended in 100 mM TEAB, and peptide quant performed with the Pierce colorimetric peptide quant assay. 22 ug peptides

per sample were diluted to 50 µL total in 100mM TEAB, then labelled with 200 ug TMT reagent in 20 µL anhydrous acetonitrile for 2 hours at room temperature. TMT reactions were quenched with 4 µL 5% hydroxylamine for 15 minutes at room temperature, combined, lyophilized, and desalted on a C18 SPE cartridge. Phosphopeptides were enriched sequentially with the High-Select TiO2 and Fe-NTA phosphopeptide enrichment kits (Thermo Scientific # A32992 and A32993). All native peptides not captured by the phosphopeptide enrichment kits were then separated by offline C4 peptide fractionation (Accucore 150-C4, 2.6 µm pore size, 150mm X 2.1mm, Thermo Scientific).

21 offline C4 fractions were concatenated down to 5 final fractions, and 5 µg of each concatenated fraction was analyzed with 3 hour LC-MS gradients on a 2m C18 monolithic column on an Orbitrap Eclipse, while the phosphopeptide fractions were each analyzed with 3 hour LC-MS gradients on a 25cm C18 Aurora column on a QE HF, as described previously (PNAS paper).

Proteomics data analysis was performed in Proteome Discoverer 2.4 (Thermo Scientific) using the Byonic search algorithm (Protein Metrics) and Uniprot mouse database. All native and phosphopeptide fraction raw files were searched together using the following parameters: fully Tryptic peptides with no more than 2 missed cleavages, precursor mass tolerance of 10 ppm and fragment mass tolerance of 20 ppm, and a maximum of 3 common modifications and 2 rare modifications. Cysteine carbamidomethylation and TMT6 addition to lysine and peptide N-termini were static modifications. Methionine oxidation (up to 2) and phosphorylation of serine, threonine, and tyrosine (up to 3) were common dynamic modifications. Methionine loss on protein N-

termini, methionine loss + acetylation on protein N-termini, protein N-terminal acetylation, and lysine acetylation were rare dynamic modifications (only 1 each). Byonic protein-level FDR was set to 1%. Percolator FDRs were set at 0.01 (strict) and 0.05 (relaxed). Spectrum file retention time calibration was used with TMT6 addition to peptide N-termini and lysines as static modifications. Reporter ion quantification based on s/n ratios used a co-isolation threshold of 50% and average reporter S/N threshold of 10. Normalization was performed on total peptide amount of all identified peptides. Peptide and protein FDRs were set at 0.001 (strict) and 0.01 (relaxed), with peptide confidence at least medium, lower confidence peptides excluded, and minimum peptide length set at 6.

Replicates and statistical reporting

Pairwise comparisons were made using the Student's t-test. When multiple pairwise comparisons were made from the same dataset, *p*-values were adjusted using the Bonferroni correction. For comparisons of more than two means, one-way ANOVA was used, followed by Tukey's post hoc test. Number of mice and replicates are indicated in figure legends. All outliers were included in the analysis. All data are represented as mean ± SEM. **** indicates $p \leq 0.0001$; *** indicates $p \leq 0.001$; ** indicates $p \leq 0.01$; * indicates $p \leq 0.05$.

Antibodies

We used the following antibodies for immunofluorescence. Rabbit anti-γH2AX (ab11174, Abcam); mouse anti-γH2AX (ab26350, Abcam); guinea pig anti-SP-10 (gift

from Prabhakara P. Reddi); Rabbit anti-LC3B (2775S, Cell Signaling), Rabbit anti-LAMP1 (ab24170, Abcam), Rabbit anti-Rab7a (ab137029, EPR7589, Abcam), Rabbit anti-Na/K-ATPase (ab76020, Abcam), Rabbit anti-ATG9A (ab108338, EPR2450(2) Abcam), Mouse anti-multi-Ubiquitin (D058-3, MBL), Rabbit anti-Fis1 (10956-1-AP, Proteintech), Rabbit anti-P62 (PM045, MBL). The following antibodies were used for western blotting Rabbit anti-Fis1 (10956-1-AP, Proteintech).

Acknowledgments

We thank all members of the Chan Lab for helpful discussions. This work was supported by the National Institutes of Health [grant R35 GM127147]. Grigor Varuzhanyan was supported by a National Science Foundation Graduate Research Fellowship (DGE-1144469) and a National Institutes of Health Cell and Molecular Biology Training Grant (GM07616T32). The Proteome Exploration Laboratory was supported by NIH OD010788, NIH OD020013, the Betty and Gordon Moore Foundation through grant GBMF775 and the Beckman Institute at Caltech. Mark Ladinsky was supported by the National Institute of Allergy and Infectious Diseases (NIAID) (2 P50 AI150464) (awarded to Pamela J. Bjorkman, Caltech).

Chapter 4 Figure legends

Figure 4.1: *Fis1* is required for spermatogenesis.

(A) Animal weight measurements from the indicated genotypes.

(B) Longitudinal analysis showing testis weight measurements.

(C) Epididymal sperm count. Spermatozoa from both caudal epididymides were used.

(D) Histological analysis of caudal epididymis sections. Scale bar, 20 μm.

(E) TUNEL staining of testis sections. Scale bar, 20 μm.

(F) Quantification of tubules containing one or more apoptotic germ cell, normalized to control.

(G) Histological analysis of phagocytosis. Notice that phagosomes, marked by Rab7, engulf apoptotic (TUNEL positive) germ cells (white arrows). Scale bar, 20 μm.

(H) Quantification of the number of tubules containing one or more Rab7 phagosome, normalized to control.

All data are from adult (P56) mice. Data are represented as mean ± SEM.

****$p \leq 0.0001$; ***$p \leq 0.001$. For statistical tests used, see the Materials and Methods section. See also Figure S1.

Figure 4.2: Germ cell *Fis1* deletion results in multinucleated giant cells.

(A) Periodic Acid-Schiff (PAS) staining of adult testis sections, counterstained with hematoxylin. Note the large giant cells (GCs) in S8/Fis1 testes. Scale bar, 20 μm.

(B) Immunostaining germ cell boundaries using an antibody against the plasma membrane marker Na/K-ATPase. Scale bar, 20 μm.

(C) Immunohistochemical staining of testis sections with an antibody against the spermatid-specific SP-10 protein. In the mutant, all GCs stain intensely for SP-10, indicating that they are spermatids. Scale bar, 20 μm.

(D) Quantification of GCs with SP-10 reactivity.

(E) Quantification showing the prevalence of spermatid GCs in *Fis1* mutants. Control testes never exhibit GCs.

All data are from adult (P56) mice. Data are represented as mean ± SEM.

Figure 4.3: *Fis1* is required for acrosome maintenance.

(A) Periodic Acid-Schiff (PAS) staining of P28 testis sections. The stage of the seminiferous epithelium is indicated in roman numerals and the spermatid step is indicated in Arabic numerals. Scale bar, 20 μm.

(B) SP-10 immunostaining in P28 testis sections. The spermatid step is indicated in Arabic numerals. The differentiation step in mutant spermatids could not be determined because of aberrant acrosomal structures. Scale bar, 20 μm.

(C) Electron tomography of spermatids in P36 S8/Fis1 giant cells (GCs). The following pseudocoloring is used: spermatid nuclei, pink; acrosomes, blue; Golgi, green; transport vesicles, red; endoplasmic reticula, yellow. ST, spermatid; Acr, acrosome. Scale bar, 500 nm.

(D) Quantification of acrosome morphology from EM micrographs.

(E) Immunostaining against SP-10 in testis sections in P23 mice. The most advanced spermatids in S8/Fis1 testes are shown. The stage of the seminiferous epithelium is

indicated in roman numerals and the spermatid step is indicated in Arabic numerals. Scale bar, 20 μm.

(F) Schematic of the spermatogenic arrest in S8/Fis1 mice. The steps of spermatid differentiation are indicated and correspond to the stage of the cycle of the seminiferous epithelium. In *Fis1* mutants, spermatogenesis arrests between Stage V and VIII. No Step 9 elongating spermatids can be found.

Data are represented as mean ± SEM. ****$p \leq 0.0001$; ***$p \leq 0.001$. For statistical tests used, see the Materials and Methods section.

Figure 4.4: *Fis1*-null giant cells exhibit mitochondrial accumulation and perturbed mitophagy.

(A) Testis sections counterstained with DAPI. Note the accumulation of Dendra2-positive mitochondria in S8/Fis1 giant cells (GCs). Scale bar, 20 μm.

(B) Analysis of mitophagy in PFA-fixed testis sections from S8-mCherry-EGFP mice, counterstained with DAPI. Line scans of the indicated regions are shown to the right. Scale bar, 20 μm.

(C) Quantification of mitophagy in spermatids.

(D) Analysis of transmitophagy/heterophagy in PFA-fixed testis sections from S8-mCherry-EGFP mice, counterstained with DAPI. Note that Sertoli cells contain red-only mitochondria, which are derived from germ cells. Line scans of the indicated regions are shown to the right. Scale bar, 20 μm.

(E) Quantification of red-only signals in Sertoli cells. Scale bar, 20 μm.

All data are from P35 mice. Data are represented as mean ± SEM. ****$p \leq 0.0001$; ***$p \leq 0.001$. For statistical tests used, see the Materials and Methods section. See also Figure S4.

Figure 4.5: S8/Fis1 spermatid giant cells exhibit aberrant autophagy.

(A) Immunostaining of testis sections with the early autophagic marker, ATG9A. Note the localization of ATG9A to the acrosome (white arrows) and the accumulation of ATG9A in mutant spermatids. Scale bar, 20 μm.

(B) Immunostaining of testis sections with autophagosome marker, LC3B. Scale bar, 20 μm.

(C) LAMP1 immunostaining in testis sections. Scale bar, 20 μm.

(D) Electron tomogram of a P36 *Fis1* GC. The following pseudocolors are used: Nucleus, yellow; autophagic structures, blue. Scale bar, 500 nm.

(E) Quantification showing the prevalence of aberrant autophagic structures from EM micrographs.

(F) Immunostaining of testis sections with an antibody against the autophagy marker, P62. Note the accumulation and aggregation of P62 in mutant spermatids. Scale bar, 20 μm.

(G) Immunostaining of testis sections with an antibody against monoubiquitin and multiubiquitin chains (K29-, K48-, and K63-linked). BM, basement membrane; SC, spermatocyte; ST, spermatid. Note that WT spermatids lack ubiquitin signal. Scale bar, 20 μm.

All data are from P35 animals, unless otherwise indicated. Data are represented as mean ± SEM. ****$p \leq 0.0001$. For statistical tests used, see the Materials and Methods section. See also Figure S5.

Figure 4.6: *Fis1*-null giant cells have aberrant mitochondria and increased respiratory chain activity.

(A) EM tomography in P24 testis sections. The control micrograph is from a round spermatid and the mutant micrographs are from spermatid giant cells (GCs). Scale bars, 500 nm.

(B) EM tomogram of a P36 *Fis1* GC from the region indicated in Figure S6. Scale bar, 500 nm.

(C) Serial section EM tomography of a P36 *Fis1* GCs from the region indicated in Figure S6.

(D) Quantification of mitochondrial morphology from EM micrographs.

Data are represented as mean ± SEM. ***$p \leq 0.001$. For statistical tests used, see the Materials and Methods section. See also, Figure S6 and Video 4.2.

Figure 4.7: Relative protein quantification reveals an upregulation of the nuclear DNA damage response in S8/Fis1 germ cells.

(A) Schematic showing the workflow of the proteomics experiment.

(B) Log2-normalized fold change values for the 172 differentially expressed proteins in S8/Fis1 vs S8/Cntrl germ cells. The proteins involved in the DNA damage response are indicated in red.

(C) Immunostaining P35 testis sections with an antibody against the double stranded break repair protein, γH2AX. The XY bodies are indicated by white arrows. Scale bar, 20 μm.

(D) Quantification showing the percent of GC-containing tubules in which at least 1 GC exhibited robust γH2AX staining.

(E) Immunostaining of P24 testis sections with γH2AX. Individual spermatids from a *Fis1* mutant are shown. The XY bodies are indicated by white arrows. Scale bar, 20 μm.

(F) Quantification showing percent of tubules with individual spermatids (not in GCs) that exhibit aberrant γH2AX staining.

Data are represented as mean ± SEM. ***$p \leq 0.001$. ST, spermatid; SC, spermatocyte; GC, giant cell. For statistical tests used, see the Materials and Methods section. See also Figure S7.

Chapter 4 Figures

Figure 4.1

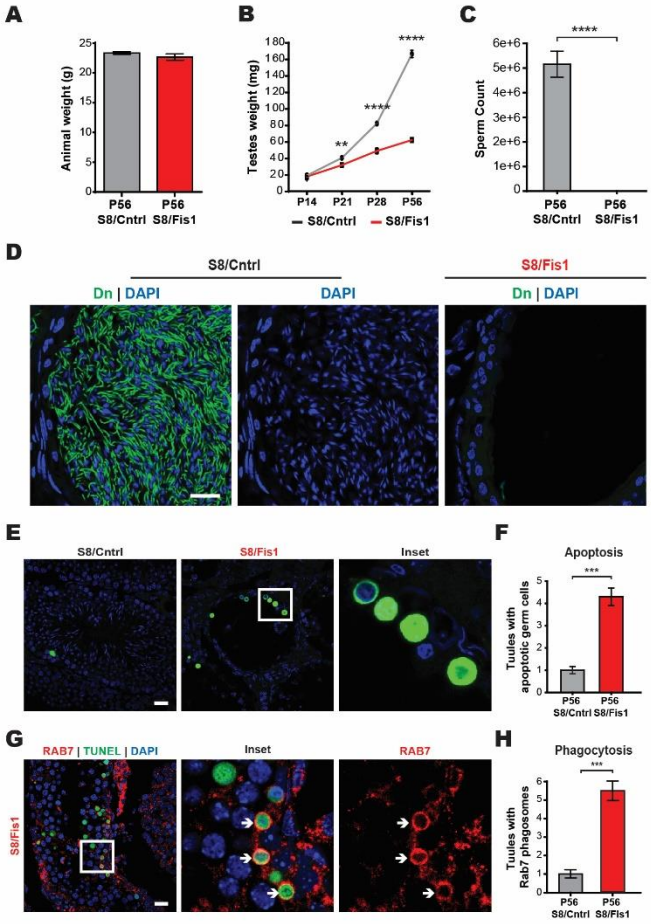

Figure 4.2

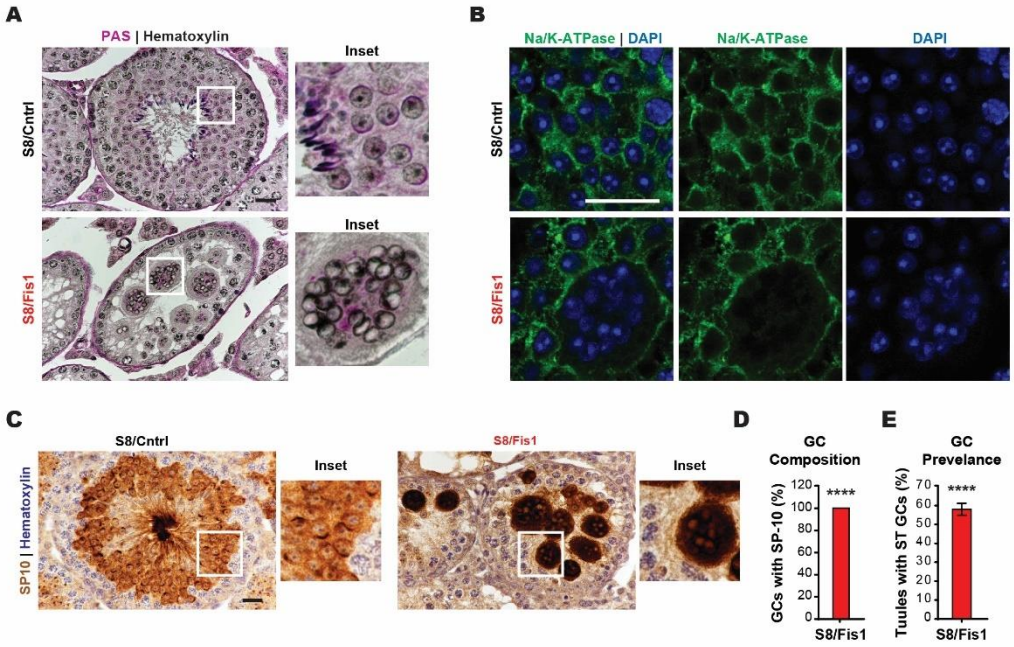
A
PAS | Hematoxylin
Inset
S8/Cntrl
Inset
S8/Fis1
B
Na/K-ATPase | DAPI
Na/K-ATPase
DAPI
S8/Cntrl
S8/Fis1
C
S8/Cntrl
Inset
S8/Fis1
Inset
SP10 | Hematoxylin
D
GC Composition
GCs with SP-10 (%)
120
100
80
60
40
20
0
****
S8/Fis1
E
GC Prevelance
Tuules with ST GCs (%)
70
60
50
40
30
20
10
0
****
S8/Fis1

Figure 4.3

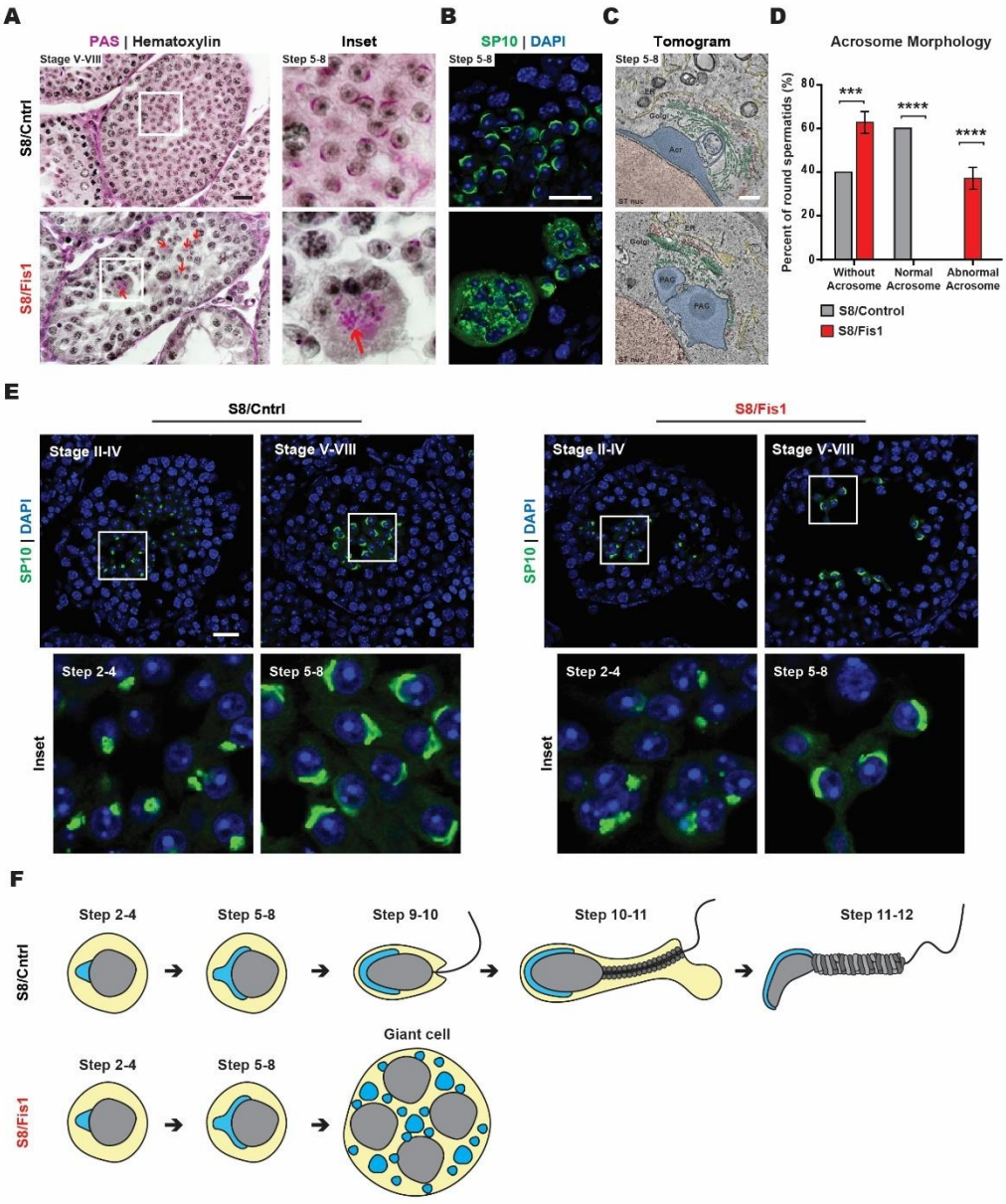
A
PAS | Hematoxylin
Inset
Stage V-VIII
Step 5-8
S8/Cntrl
S8/Fis1
B
SP10 | DAPI
Step 5-8
C
Tomogram
Step 5-8
D
Acrosome Morphology
Percent of round spermatids (%)
***
****
****
Without Acrosome
Normal Acrosome
Abnormal Acrosome
S8/Control
S8/Fis1
E
S8/Cntrl
S8/Fis1
Stage II-IV
Stage V-VIII
SP10 | DAPI
Step 2-4
Step 5-8
Inset
F
S8/Cntrl
S8/Fis1
Step 2-4
Step 5-8
Step 9-10
Step 10-11
Step 11-12
Giant cell

Figure 4.4

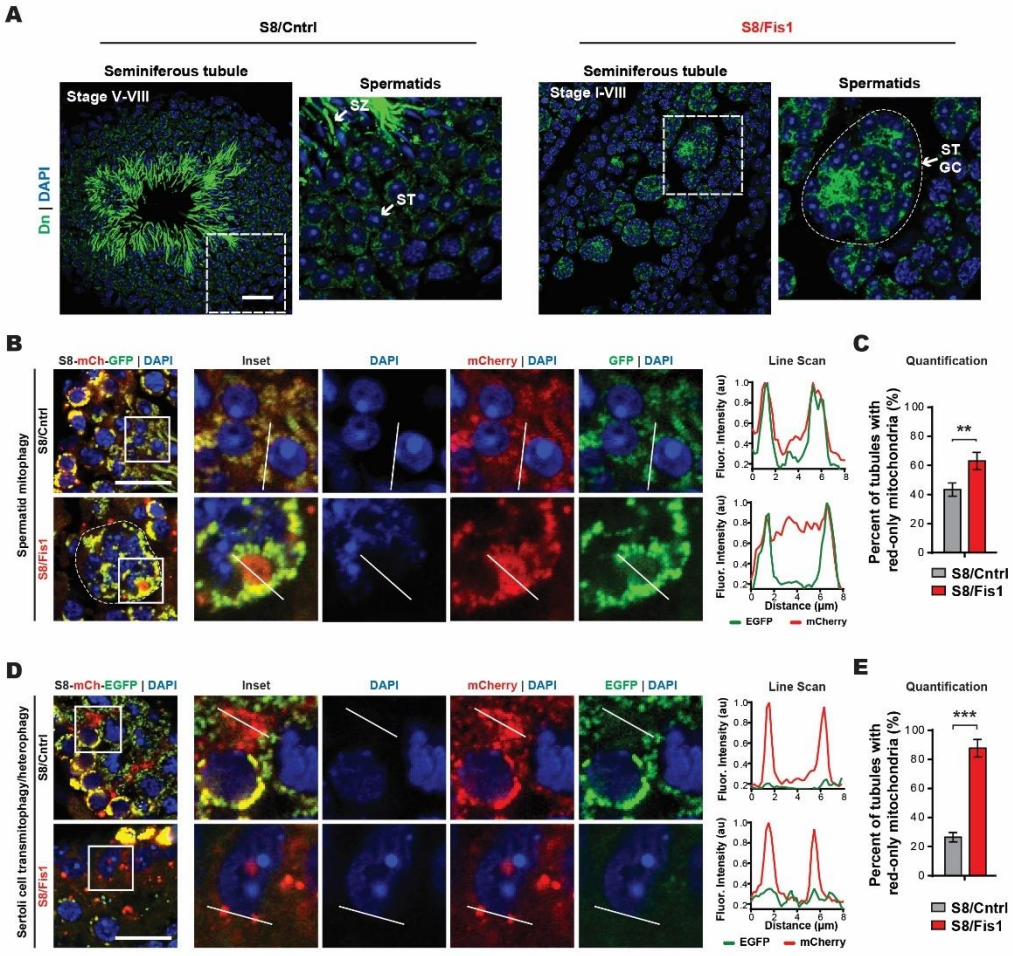
A
S8/Cntrl
S8/Fis1
Seminiferous tubule
Spermatids
Stage V-VIII
Stage I-VIII
SZ
ST
GC
Dn | DAPI
B
S8-mCh-GFP | DAPI
Inset
DAPI
mCherry | DAPI
GFP | DAPI
Line Scan
Spermatid mitophagy
S8/Cntrl
S8/Fis1
Fluor. Intensity (au)
Distance (μm)
EGFP
mCherry
C
Quantification
Percent of tubules with red-only mitochondria (%)
**
S8/Cntrl
S8/Fis1
D
S8-mCh-EGFP | DAPI
EGFP | DAPI
Sertoli cell transmitophagy/heterophagy
E
***

Figure 4.5

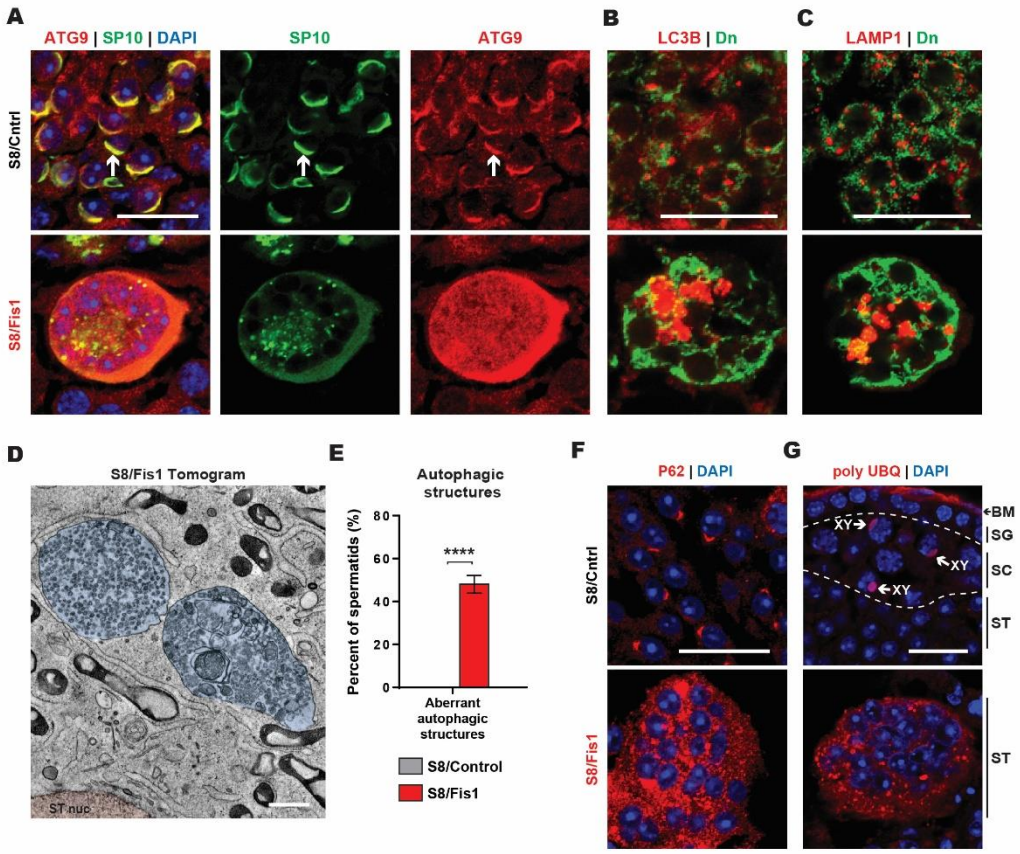
A
ATG9 | SP10 | DAPI
SP10
ATG9
S8/Cntrl
S8/Fis1
B
LC3B | Dn
C
LAMP1 | Dn
D
S8/Fis1 Tomogram
ST nuc
E
Autophagic structures
Percent of spermatids (%)
80
60
40
20
0
****
Aberrant autophagic structures
S8/Control
S8/Fis1
F
P62 | DAPI
G
poly UBQ | DAPI
BM
SG
SC
ST
XY
XY
XY
ST

Figure 4.6

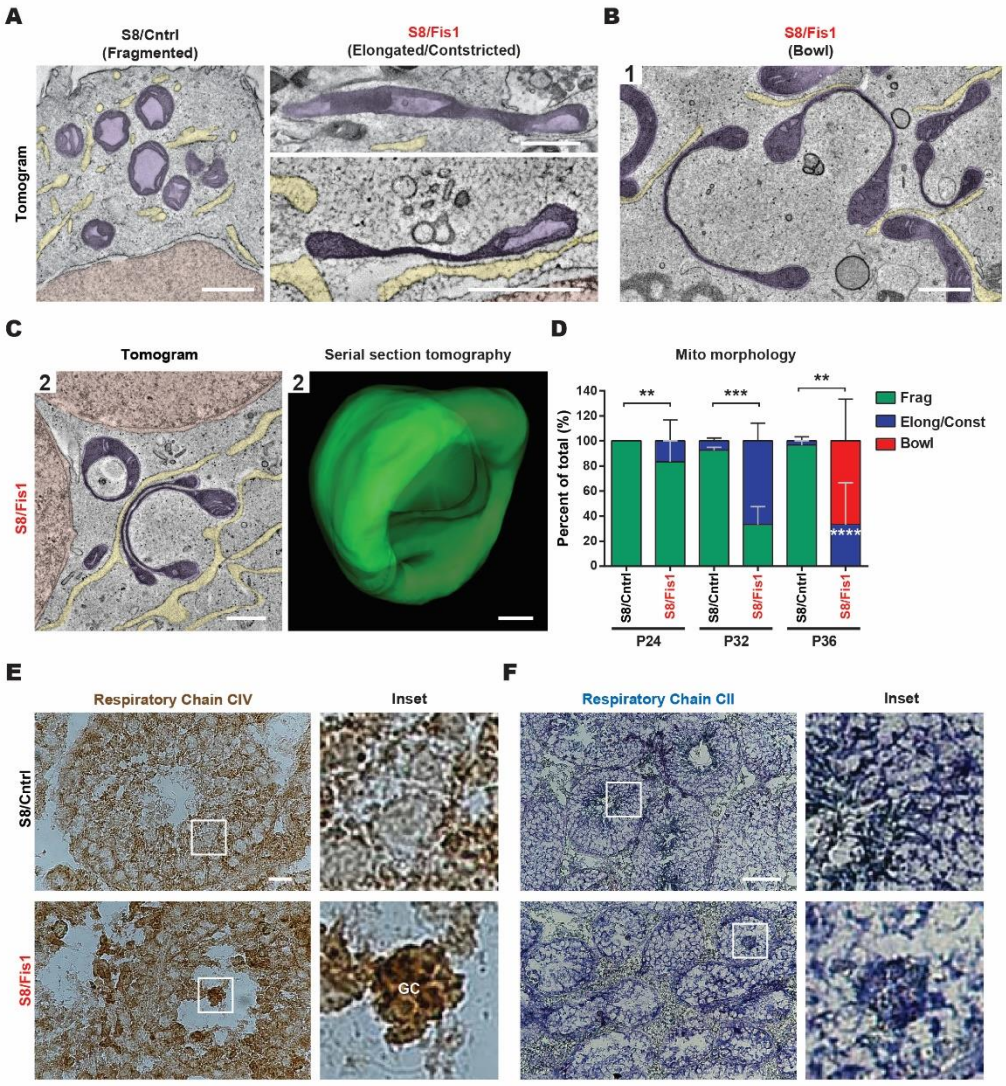
A
S8/Cntrl
(Fragmented)
S8/Fis1
(Elongated/Contstricted)
Tomogram
B
S8/Fis1
(Bowl)
1
C
Tomogram
Serial section tomography
2
2
S8/Fis1
D
Mito morphology
Percent of total (%)
140
120
100
80
60
40
20
0
**
***
**
****
Frag
Elong/Const
Bowl
S8/Cntrl
S8/Fis1
S8/Cntrl
S8/Fis1
S8/Cntrl
S8/Fis1
P24
P32
P36
E
Respiratory Chain CIV
Inset
S8/Cntrl
S8/Fis1
GC
F
Respiratory Chain CII
Inset

Figure 4.7

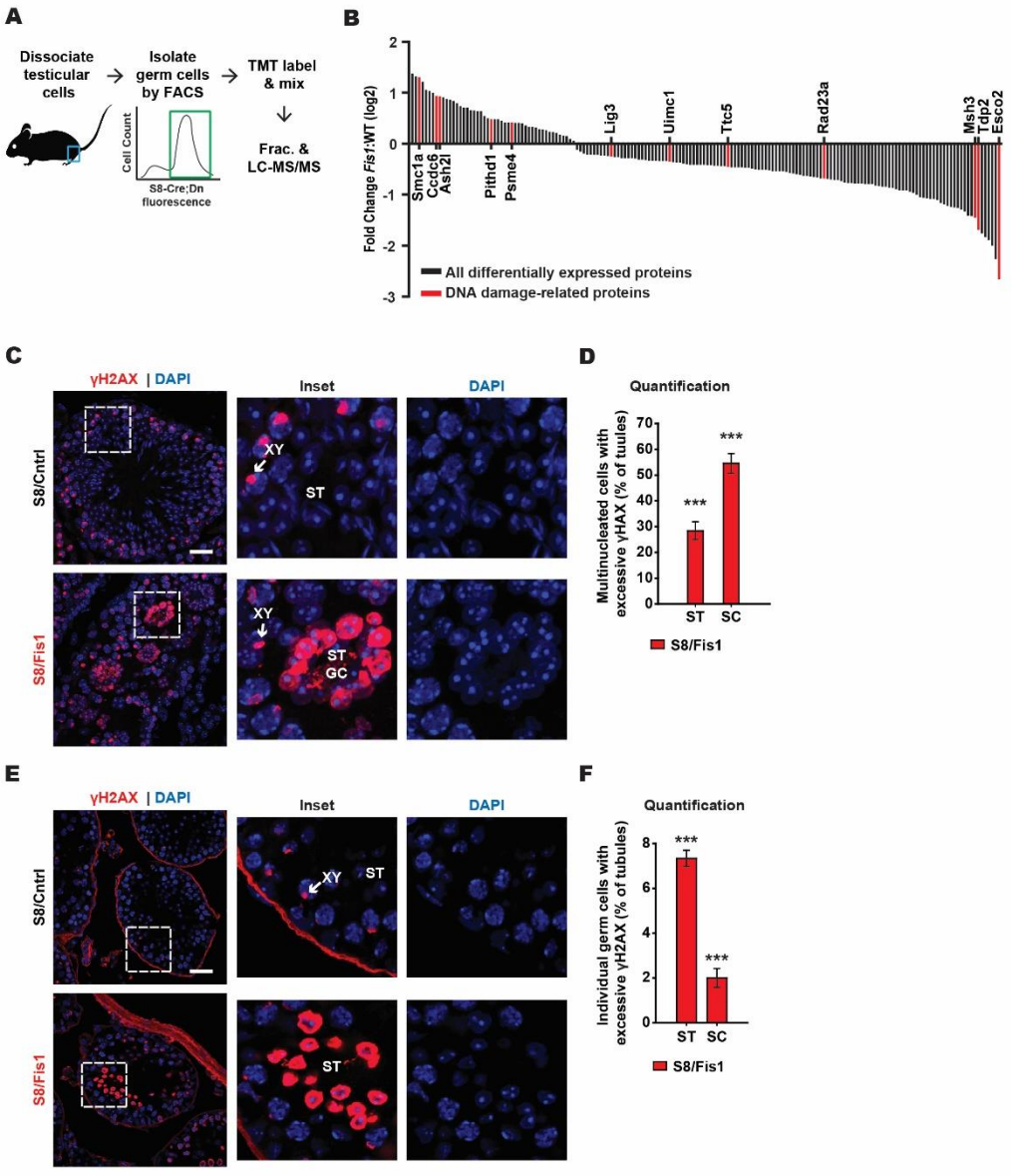
A
Dissociate testicular cells
Isolate germ cells by FACS
TMT label & mix
Frac. & LC-MS/MS
Cell Count
S8-Cre;Dn fluorescence
B
Fold Change Fis1:WT (log2)
Smc1a
Ccdc6
Ash2l
Pithd1
Psme4
Lig3
Uimc1
Ttc5
Rad23a
Msh3
Tdp2
Esco2
All differentially expressed proteins
DNA damage-related proteins
C
γH2AX | DAPI
Inset
DAPI
S8/Cntrl
S8/Fis1
XY
ST
GC
D
Quantification
Multinucleated cells with excessive γHAX (% of tuules)
***
ST
SC
S8/Fis1
E
γH2AX | DAPI
Inset
DAPI
S8/Cntrl
S8/Fis1
XY
ST
F
Quantification
Individual germ cells with excessive γH2AX (% of tubules)
***
ST
SC
S8/Fis1

Chapter 4 Supplementary figure legends

Figure 4.S1: Related to Figure 4.1

(A) Schematic of the conditional (floxed) and excised *Fis1* alleles. *LoxP* sites flank exon 2. After Cre-mediated recombination, deletion of exon 2 causes a frameshift mutation in the *Fis1* open reading frame.

(B) Genotyping of Fis1 KO MEFs and mouse tails. Seven different MEF clones are shown. Clone 4 escaped *Fis1* KO and retained the conditional *Fis1* allele. For more information about the generation of Fis1 KO MEFs, see the Materials and methods section.

(C) Western blots against FIS1 in the seven MEF clones shown above.

(D) Immunostaining against FIS1 in MEF clones 4 and 5. Scale bar, 20 μm.

(E) Immunostaining in testis sections with an antibody against FIS1. Line scans of the indicated regions are shown at the bottom. The regions corresponding to germ and Sertoli cell mitochondria are indicated. Scale bars, 20 μm.

Figure 4.S2: Related to Figure 4.4

(A) Schematic showing the generation of germ-cell specific mitophagy reporter mice.

(B) Genotyping mouse tails of germ-cell specific mitophagy reporter mice.

Figure 4.S3: Related to Figure 4.5.

(B) EM tomograms showing autophagic structures in *Fis1* giant cells (GCs). The following pseudocolors are used. Nuclei, pink; autophagic structures, blue. Scale bar, 500 nm.

Figure 4.S4: Related to Figure 4.6

Montage tomography of testis sections showing round spermatids. The following pseudocoloring is used: spermatid nuclei, pink; acrosomes, blue, Golgi, green; Sertoli cells, purple; spermatogonium, yellow. Ser Nuc, Sertoli nucleus; SG, spermatogonium. Scale bar, 5 μm.

Figure 4.S5: Related to Figure 4.7.

(A) GSEA plot of the Reactome Mitochondrial Biogenesis pathway.

(B) GSEA plots of various autophagy-related Gene Ontology gene sets.

(C) GSEA plot of the Weigel Oxidative Stress Response.

(D) Analysis of apoptosis in *Fis1* GCs. TUNEL assay was performed in P35 testis sections co-stained with an antibody against γH2AX and DAPI. Note that the aberrant *Fis1* GC is not apoptotic. Scale bar, 20 μm.

ES, enrichment score.

Chapter 4 Supplementary figures

Figure 4.S1

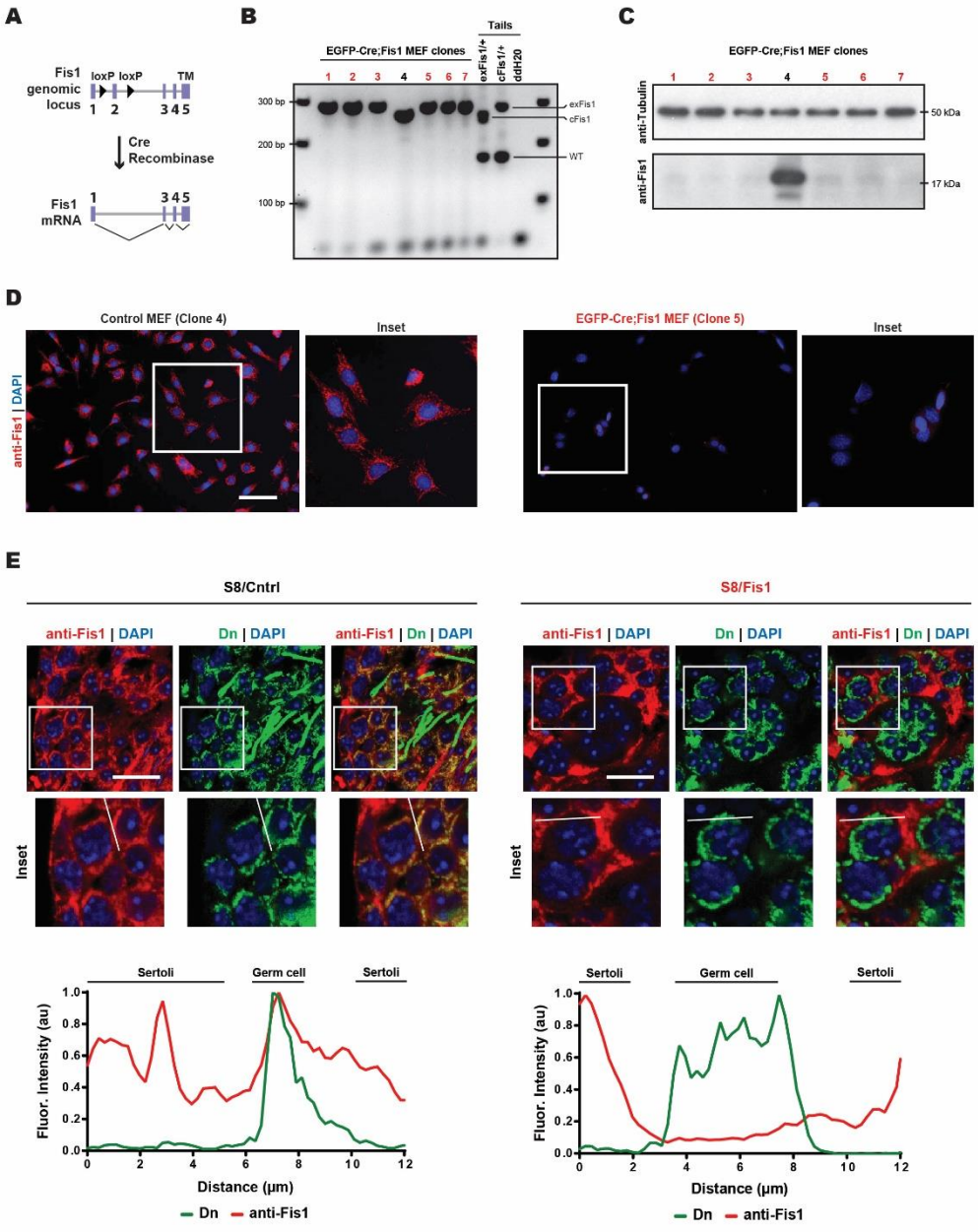

Figure 4.S2

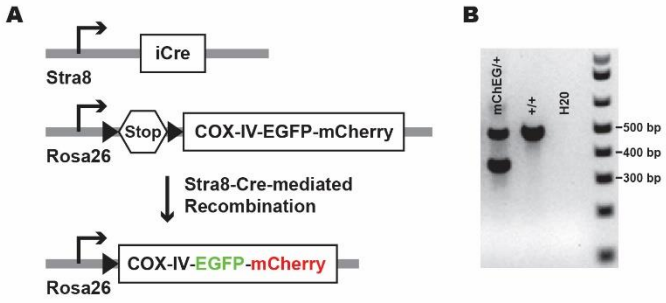
A
iCre
Stra8
Stop
COX-IV-EGFP-mCherry
Rosa26
Stra8-Cre-mediated
Recombination
COX-IV-EGFP-mCherry
Rosa26
B
mChEG/+
+/+
H20
500 bp
400 bp
300 bp

Figure 4.S3

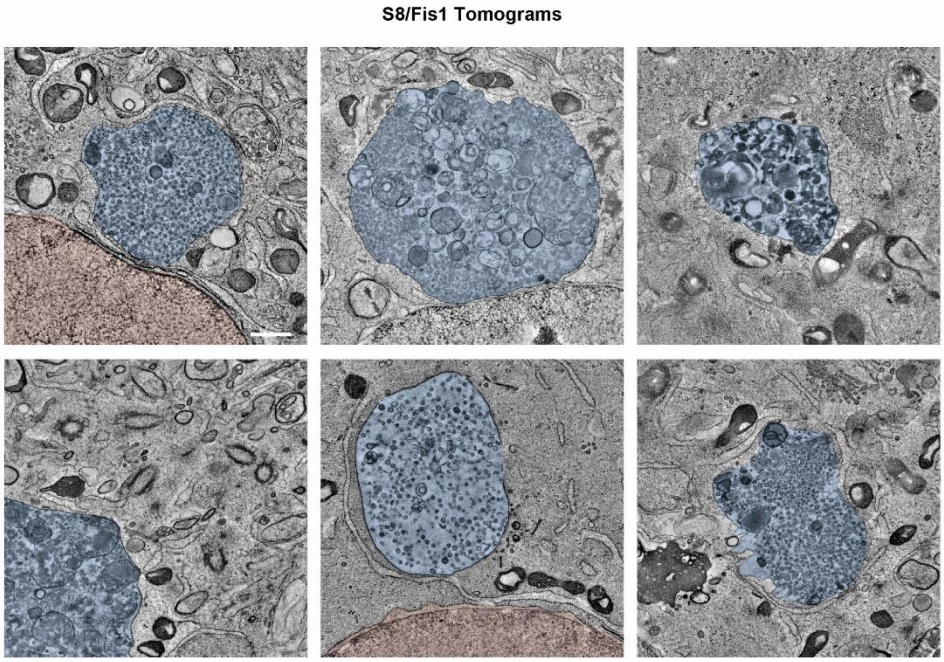

Figure 4.S4

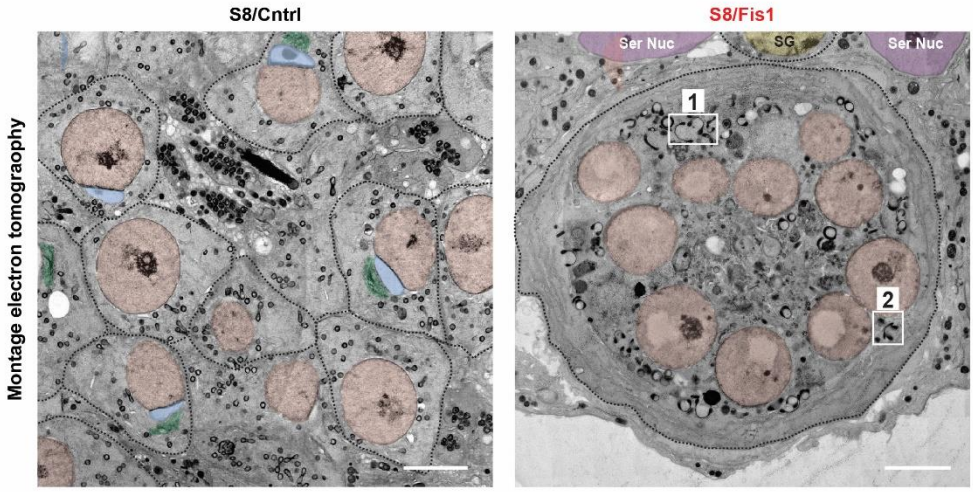
S8/Cntrl
S8/Fis1
Montage electron tomograophy
Ser Nuc
SG
Ser Nuc
1
2

Figure 4.S5

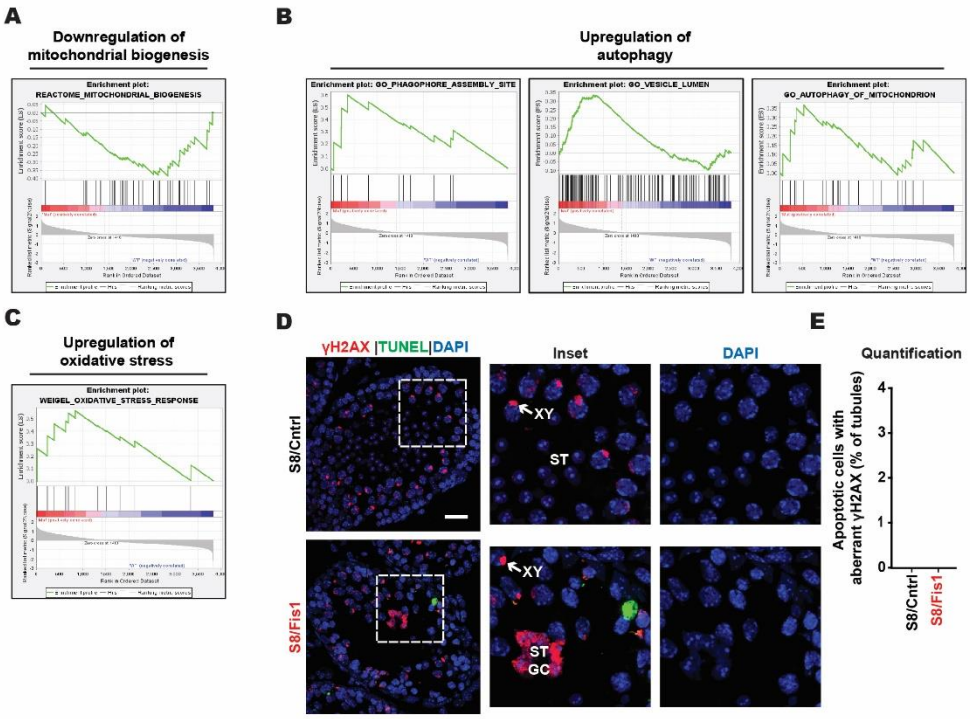
A
Downregulation of mitochondrial biogenesis
Enrichment plot: REACTOME_MITOCHONDRIAL_BIOGENESIS
B
Upregulation of autophagy
Enrichment plot: GO_PHAGOPHORE_ASSEMBLY_SITE
Enrichment plot: GO_VESICLE_LUMEN
Enrichment plot: GO_AUTOPHAGY_OF_MITOCHONDRION
C
Upregulation of oxidative stress
Enrichment plot: WEIGEL_OXIDATIVE_STRESS_RESPONSE
D
γH2AX |TUNEL|DAPI
Inset
DAPI
S8/Cntrl
S8/Fis1
XY
ST
GC
E
Quantification
Apoptotic cells with aberrant γH2AX (% of tubules)
0
1
2
3
4
S8/Cntrl
S8/Fis1

Video Legends

Video 4.1:

Movie from a P36 S8/Cntrl spermatid showing an entire trans Golgi cisterna fused to the acrosome. See also Figure 4.3C.

Video 4.2:

Movie from a P36 S8/Cntrl spermatid showing an entire trans Golgi cisterna fused to the acrosome. See also Figure 4.3C.

Video 4.3:

Movie of a 3D reconstructed mitochondrion using serial section tomography from a P36 S8/Fis1 giant cell. See also Figure 4.6C and 4.S6.

Video Files

Please download video files using the following link: Video Files – Chapter 4

References

Baarends, W.M., Wassenaar, E., Laan, R. van der, Hoogerbrugge, J., Sleddens-Linkels, E., Hoeijmakers, J.H.J., Boer, P. de, Grootegoed, J.A., 2005. Silencing of Unpaired Chromatin and Histone H2A Ubiquitination in Mammalian Meiosis. *Molecular and Cellular Biology* 25, 1041–1053. https://doi.org/10.1128/MCB.25.3.1041-1053.2005

Barzilai, A., Yamamoto, K.-I., 2004. DNA damage responses to oxidative stress. DNA Repair, Bridge Over Break Ends - The Cellular Response to DNA Breaks in H*ealth and Disease* 3, 1109–1115. https://doi.org/10.1016/j.dnarep.2004.03.002

Berruti, G., Paiardi, C., 2011. Acrosome biogenesis. *Spermatogenesis* 1, 95–98. https://doi.org/10.4161/spmg.1.2.16820

Borg, C.L., Wolski, K.M., Gibbs, G.M., O'Bryan, M.K., 2010. Phenotyping male infertility in the mouse: how to get the most out of a 'non-performer.' *Hum Reprod Update* 16, 205–224. https://doi.org/10.1093/humupd/dmp032

Braun, R.E., 1998. Every sperm is sacred—or is it? *Nature Genetics* 18, 202–204. https://doi.org/10.1038/ng0398-202

Brauns, A.-K., Heine, M., Tödter, K., Baumgart-Vogt, E., Lüers, G.H., Schumacher, U., 2019. A defect in the peroxisomal biogenesis in germ cells induces a spermatogenic arrest at the round spermatid stage in mice. *Scientific Reports* 9, 9553. https://doi.org/10.1038/s41598-019-45991-6

Carbon, S., Mungall, C., 2018. Gene Ontology Data Archive. https://doi.org/10.5281/zenodo.3980761

Chan, D.C., 2020. Mitochondrial Dynamics and Its Involvement in Disease. Annual Review of Pathology: *Mechanisms of Disease* 15, null. https://doi.org/10.1146/annurev-pathmechdis-012419-032711

Davis, C.O., Kim, K.-Y., Bushong, E.A., Mills, E.A., Boassa, D., Shih, T., Kinebuchi, M., Phan, S., Zhou, Y., Bihlmeyer, N.A., Nguyen, J.V., Jin, Y., Ellisman, M.H., Marsh-Armstrong, N., 2014. Transcellular degradation of axonal mitochondria. *PNAS* 111, 9633–9638. https://doi.org/10.1073/pnas.1404651111

Elliott, M.R., Zheng, S., Park, D., Woodson, R.I., Reardon, M.A., Juncadella, I.J., Kinchen, J.M., Zhang, J., Lysiak, J.J., Ravichandran, K.S., 2010. Unexpected requirement for ELMO1 in clearance of apoptotic germ cells in vivo. *Nature* 467, 333–337. https://doi.org/10.1038/nature09356

Fawcett, D.W., Ito, S., Slautterback, D., 1959. The Occurrence of Intercellular Bridges in Groups of Cells Exhibiting Synchronous Differentiation. *J Biophys Biochem Cytol* 5, 453–460.

Fekkes, P., Shepard, K.A., Yaffe, M.P., 2000. Gag3p, an Outer Membrane Protein Required for Fission of Mitochondrial Tubules. *J Cell Biol* 151, 333–340. https://doi.org/10.1083/jcb.151.2.333

Gaysinskaya, V., Bortvin, A., 2015. Flow cytometry of murine spermatocytes. *Current protocols in cytometry* 72, 7.44.1-24. https://doi.org/10.1002/0471142956.cy0744s72

Gaysinskaya, V., Soh, I.Y., van der Heijden, G.W., Bortvin, A., 2014. Optimized flow cytometry isolation of murine spermatocytes. Cytometry. Part A : *the journal of the International Society for Analytical Cytology* 85, 556–65. https://doi.org/10.1002/cyto.a.22463

Griswold, M.D., 2016. Spermatogenesis: The Commitment to Meiosis. *Physiological reviews* 96, 1–17. https://doi.org/10.1152/physrev.00013.2015

Hill, B., Enger, J., Harwig, M., Ihenacho, U., Widlansky, M., 2020. Structural studies of human Fis1 reveals a dynamic region important for Drp1 recruitment and mitochondrial fission. *The FASEB Journal* 34, 1–1. https://doi.org/10.1096/fasebj.2020.34.s1.04691

Hobbs, R.M., La, H.M., Mäkelä, J.-A., Kobayashi, T., Noda, T., Pandolfi, P.P., 2015. Distinct germline progenitor subsets defined through Tsc2–mTORC1 signaling. *EMBO reports* 16, 467–480.

Holstein, A.F., Eckmann, C., 1986. Multinucleated Spermatocytes and Spermatids in Human Seminiferous Tubules*. *Andrologia* 18, 5–16. https://doi.org/10.1111/j.1439-0272.1986.tb01729.x

Huang, D.W., Sherman, B.T., Lempicki, R.A., 2009a. Systematic and integrative analysis of large gene lists using DAVID bioinformatics resources. *Nat Protoc* 4, 44–57. https://doi.org/10.1038/nprot.2008.211

Huang, D.W., Sherman, B.T., Lempicki, R.A., 2009b. Bioinformatics enrichment tools: paths toward the comprehensive functional analysis of large gene lists. *Nucleic Acids Res.* 37, 1–13. https://doi.org/10.1093/nar/gkn923

Imai, K., Hao, F., Fujita, N., Tsuji, Y., Oe, Y., Araki, Y., Hamasaki, M., Noda, T., Yoshimori, T., 2016. Atg9A trafficking through the recycling endosomes is required for autophagosome formation. *J Cell Sci* 129, 3781–3791. https://doi.org/10.1242/jcs.196196

Jassal, B., Matthews, L., Viteri, G., Gong, C., Lorente, P., Fabregat, A., Sidiropoulos, K., Cook, J., Gillespie, M., Haw, R., Loney, F., May, B., Milacic, M., Rothfels, K., Sevilla, C., Shamovsky, V., Shorser, S., Varusai, T., Weiser, J., Wu, G., Stein, L., Hermjakob, H., D'Eustachio, P., 2020. The reactome pathway knowledgebase. Nucleic acids research 48, D498–D503. https://doi.org/10.1093/nar/gkz1031

Joshi, A.U., Ebert, A.E., Haileselassie, B., Mochly-Rosen, D., 2019. Drp1/Fis1-mediated mitochondrial fragmentation leads to lysosomal dysfunction in cardiac models of Huntington's disease. *J. Mol. Cell. Cardiol*. 127, 125–133. https://doi.org/10.1016/j.yjmcc.2018.12.004

Katsuragi, Y., Ichimura, Y., Komatsu, M., 2015. p62/SQSTM1 functions as a signaling hub and an autophagy adaptor. *FEBS J.* 282, 4672–4678. https://doi.org/10.1111/febs.13540

Kim, D., Song, J., Kang, Y., Park, S., Kim, Y.-I., Kwak, S., Lim, D., Park, R., Chun, C.-H., Choe, S.-K., Jin, E.-J., 2016. Fis1 depletion in osteoarthritis impairs chondrocyte survival and peroxisomal and lysosomal function. *J. Mol. Med*. 94, 1373–1384. https://doi.org/10.1007/s00109-016-1445-9

Loson, O.C., Song, Z., Chen, H., Chan, D.C., 2013. Fis1, Mff, MiD49, and MiD51 mediate Drp1 recruitment in mitochondrial fission. *Molecular biology of the cell* 24, 659–67. https://doi.org/10.1091/mbc.E12-10-0721

Lu, L.-Y., Wu, J., Ye, L., Gavrilina, G.B., Saunders, T.L., Yu, X., 2010. RNF8-Dependent Histone Modifications Regulate Nucleosome Removal during Spermatogenesis. *Developmental Cell* 18, 371–384. https://doi.org/10.1016/j.devcel.2010.01.010

MacGregor, G.R., Russell, L.D., Beek, M.E.V., Hanten, G.R., Kovac, M.J., Kozak, C.A., Meistrich, M.L., Overbeek, P.A., 1990. Symplastic spermatids (sys): a recessive insertional mutation in mice causing a defect in spermatogenesis. *PNAS* 87, 5016–5020.

Mah, L.-J., El-Osta, A., Karagiannis, T.C., 2010. γH2AX: a sensitive molecular marker of DNA damage and repair. *Leukemia* 24, 679–686. https://doi.org/10.1038/leu.2010.6

McNicoll, F., Kühnel, A., Biswas, U., Hempel, K., Whelan, G., Eichele, G., Jessberger, R., 2020. Meiotic sex chromosome cohesion and autosomal synapsis are supported by Esco2. *Life Sci Alliance 3*. https://doi.org/10.26508/lsa.201900564

Mootha, V.K., Lindgren, C.M., Eriksson, K.-F., Subramanian, A., Sihag, S., Lehar, J., Puigserver, P., Carlsson, E., Ridderstråle, M., Laurila, E., Houstis, N., Daly, M.J., Patterson, N., Mesirov, J.P., Golub, T.R., Tamayo, P., Spiegelman, B., Lander, E.S., Hirschhorn, J.N., Altshuler, D., Groop, L.C., 2003. PGC-1α-responsive genes

involved in oxidative phosphorylation are coordinately downregulated in human diabetes. *Nature Genetics* 34, 267–273. https://doi.org/10.1038/ng1180

Morton, D., Weisbrode, S.E., Wyder, W.E., Maurer, J.K., Capen, C.C., 2016. Spermatid Giant Cells, Tubular Hypospermatogenesis, Spermatogonial Swelling, Cytoplasmic Vacuoles, and Tubular Dilatation in the Testes of Normal Rabbits: *Veterinary Pathology*. https://doi.org/10.1177/030098588602300211

Mozdy, A.D., McCaffery, J.M., Shaw, J.M., 2000. Dnm1p GTPase-mediated mitochondrial fission is a multi-step process requiring the novel integral membrane component Fis1p. *J. Cell Biol.* 151, 367–380. https://doi.org/10.1083/jcb.151.2.367

Navarro-Espíndola, R., Takano-Rojas, H., Suaste-Olmos, F., Peraza-Reyes, L., 2020. Distinct Contributions of the Peroxisome-Mitochondria Fission Machinery During Sexual Development of the Fungus Podospora anserina. *Front. Microbiol.* 11. https://doi.org/10.3389/fmicb.2020.00640

Osuru, H.P., Monroe, J.E., Chebolu, A.P., Akamune, J., Pramoonjago, P., Ranpura, S.A., Reddi, P.P., 2014. The acrosomal protein SP-10 (Acrv1) is an ideal marker for staging of the cycle of seminiferous epithelium in the mouse. *Molecular reproduction and development* 81, 896–907. https://doi.org/10.1002/mrd.22358

Otera, H., Wang, C., Cleland, M.M., Setoguchi, K., Yokota, S., Youle, R.J., Mihara, K., 2010. Mff is an essential factor for mitochondrial recruitment of Drp1 during mitochondrial fission in mammalian cells. *J Cell Biol* 191, 1141–1158. https://doi.org/10.1083/jcb.201007152

Pham, A.H., McCaffery, J.M., Chan, D.C., 2012. Mouse lines with photo-activatable mitochondria to study mitochondrial dynamics. *Genesis* 50, 833–843. https://doi.org/10.1002/dvg.22050

Riera, A.M., Martinez, C.I., Itskanov, S., Steffen, J., Roach, B., Koehler, C.M., Bliek, A.M. van der, 2019. Dynamin-2 controls phagophore maturation. *bioRxiv* 241901. https://doi.org/10.1101/241901

Rojansky, R., Cha, M.-Y., Chan, D.C., 2016. Elimination of paternal mitochondria in mouse embryos occurs through autophagic degradation dependent on PARKIN and MUL1. *eLife* 5, e17896.

Rotter, V., Schwartz, D., Almon, E., Goldfinger, N., Kapon, A., Meshorer, A., Donehower, L.A., Levine, A.J., 1993. Mice with reduced levels of p53 protein exhibit the testicular giant-cell degenerative syndrome. *PNAS* 90, 9075–9079. https://doi.org/10.1073/pnas.90.19.9075

Russell, L.D., Ettlin, R.A., Hikim, A.P.S., Clegg, E.D., 1993. Histological and histopathological evaluation of the testis. *International journal of andrology* 16, 83–83.

Sadate-Ngatchou, P.I., Payne, C.J., Dearth, A.T., Braun, R.E., 2008. Cre recombinase activity specific to postnatal, premeiotic male germ cells in transgenic mice. *Genesis* (New York, N.Y. : 2000) 46, 738–42. https://doi.org/10.1002/dvg.20437

Shang, Y., Wang, H., Jia, P., Zhao, H., Liu, C., Liu, W., Song, Z., Xu, Z., Yang, L., Wang, Y., 2016. Autophagy regulates spermatid differentiation via degradation of PDLIM1. *Autophagy* 12, 1575–1592.

Shen, Q., Yamano, K., Head, B.P., Kawajiri, S., Cheung, J.T.M., Wang, C., Cho, J.-H., Hattori, N., Youle, R.J., van der Bliek, A.M., 2014. Mutations in Fis1 disrupt orderly disposal of defective mitochondria. *Mol. Biol. Cell* 25, 145–159. https://doi.org/10.1091/mbc.E13-09-0525

Singh, S.K., Abe, K., 1987. Light and electron microscopic observations of giant cells in the mouse testis after efferent duct ligation. *Arch Histol Jpn* 50, 579–585. https://doi.org/10.1679/aohc.50.579

Subramanian, A., Tamayo, P., Mootha, V.K., Mukherjee, S., Ebert, B.L., Gillette, M.A., Paulovich, A., Pomeroy, S.L., Golub, T.R., Lander, E.S., 2005. Gene set enrichment analysis: a knowledge-based approach for interpreting genome-wide expression profiles. *Proceedings of the National Academy of Sciences* 102, 15545–15550.

Tieu, Q., Nunnari, J., 2000. Mdv1p Is a Wd Repeat Protein That Interacts with the Dynamin-Related Gtpase, Dnm1p, to Trigger Mitochondrial Division. *J Cell Biol* 151, 353–366. https://doi.org/10.1083/jcb.151.2.353

Varuzhanyan, G., n.d. Mitochondrial fission is required for organization of the mitochondrial sheath in spermatids. *Biochimica et Biophysica Acta - General Subjects* (in press).

Varuzhanyan, G., Chan, D.C., 2020. Mitochondrial dynamics during spermatogenesis. *J Cell Sci* 133. https://doi.org/10.1242/jcs.235937

Varuzhanyan, G., Rojansky, R., Sweredoski, M.J., Graham, R.L., Hess, S., Ladinsky, M.S., Chan, D.C., 2019. Mitochondrial fusion is required for spermatogonial differentiation and meiosis. *eLife* 8, e51601. https://doi.org/10.7554/eLife.51601

Wang, H., Wan, H., Li, X., Liu, W., Chen, Q., Wang, Y., Yang, L., Tang, H., Zhang, X., Duan, E., Zhao, X., Gao, F., Li, W., 2014. Atg7 is required for acrosome biogenesis during spermatogenesis in mice. *Cell Research* 24, 852–869. https://doi.org/10.1038/cr.2014.70

Williams, A.B., Schumacher, B., 2016. p53 in the DNA-Damage-Repair Process. Cold Spring Harb Perspect Med 6. https://doi.org/10.1101/cshperspect.a026070

Wong, Y.C., Ysselstein, D., Krainc, D., 2018. Mitochondria-lysosome contacts regulate mitochondrial fission via RAB7 GTP hydrolysis. *Nature* 554, 382–386. https://doi.org/10.1038/nature25486

Xian, H., Yang, Q., Xiao, L., Shen, H.-M., Liou, Y.-C., 2019. STX17 dynamically regulated by Fis1 induces mitophagy via hierarchical macroautophagic mechanism. *Nature communications* 10, 1–17.

Yamano, K., Fogel, A.I., Wang, C., van der Bliek, A.M., Youle, R.J., 2014. Mitochondrial Rab GAPs govern autophagosome biogenesis during mitophagy. *eLife* 3, e01612. https://doi.org/10.7554/eLife.01612

Yamano, K., Wang, C., Sarraf, S.A., Münch, C., Kikuchi, R., Noda, N.N., Hizukuri, Y., Kanemaki, M.T., Harper, W., Tanaka, K., Matsuda, N., Youle, R.J., 2018. Endosomal Rab cycles regulate Parkin-mediated mitophagy. *eLife* 7. https://doi.org/10.7554/eLife.31326

Yin, X.-M., Ding, W.-X., 2013. The reciprocal roles of PARK2 and mitofusins in mitophagy and mitochondrial spheroid formation. *Autophagy* 9, 1687–1692.

Zhang, M., Chen, L., Wang, S., Wang, T., 2009. Rab7: roles in membrane trafficking and disease. Biosci Rep 29, 193–209. https://doi.org/10.1042/BSR20090032

Zhang, Z., Sliter, D.A., Bleck, C.K.E., Ding, S., 2019. Fis1 deficiencies differentially affect mitochondrial quality in skeletal muscle. *Mitochondrion* 49, 217–226. https://doi.org/10.1016/j.mito.2019.09.005

CHAPTER 5

Mitochondrial dynamics is a distinguishing feature of skeletal muscle fiber types and regulates organellar compartmentalization

Prashant Mishra*, **Grigor Varuzhanyan***, Anh H. Pham and David C. Chan

Division of Biology and Biological Engineering, California Institute of Technology, Pasadena, CA 91125.

***Co-first author**

Abstract

Skeletal muscle fibers differentiate into specific fiber types with distinct metabolic properties determined by their reliance on oxidative phosphorylation (OXPHOS). Using *in vivo* approaches, we find that OXPHOS-dependent fibers, compared to glycolytic fibers, contain elongated mitochondrial networks with higher fusion rates that are dependent on Mfn1 and Mfn2. Switching of a glycolytic fiber to an oxidative IIA type is associated with elongation of mitochondria, suggesting that mitochondrial fusion is linked to metabolic state. Furthermore, we reveal that mitochondrial proteins are compartmentalized to discrete domains centered around their nuclei of origin. The domain dimensions are dependent on fiber type and are regulated by the mitochondrial dynamics proteins Mfn1, Mfn2, and Mff. Our results indicate that mitochondrial dynamics is tailored to fiber type physiology and provides a rationale for the segmental defects characteristic of aged and diseased muscle fibers.

Introduction

Genetic evidence indicates that mitochondrial fusion is important for skeletal muscle function. Deletion of the mitofusins Mfn1 and Mfn2, pro-fusion proteins on the mitochondrial outer membrane, results in severe mitochondrial myopathy, including decreased muscle mass, exercise intolerance and lactic acidosis (Chen et al., 2010). In addition, some patients harboring mutations in Mfn2 or Opa1 (a pro-fusion protein on the mitochondrial inner membrane) manifest late-onset myopathy (Amati-Bonneau et al., 2008; Hudson et al., 2008; Rouzier et al., 2012). Finally, cultured muscle fibers from dissociated *flexor digitorum brevis* muscle show mitochondrial fusion events that are sensitive to Mfn1 but not Mfn2 knockdown (Eisner et al., 2014).

Skeletal muscle has specialized cell biological characteristics that raise important issues concerning the role of mitochondrial dynamics. First, every muscle contains a mixture of distinct fiber types that are specialized according to the work they perform (Pette and Staron, 2000). Oxidative or "slow-twitch" fibers have slow contraction rates, high mitochondrial content, increased reliance on oxidative phosphorylation (OXPHOS), high resistance to fatigue, and high representation in postural muscles. In contrast, glycolytic or "fast-twitch" fibers have rapid contractions, lower mitochondrial content, decreased reliance on OXPHOS, low resistance to fatigue, and high representation in muscle groups used for directional movement. In this study, we refer to four types of muscle fibers that form a continuum in terms of OXPHOS capacity, with I>IIA>IIX>IIB. We wondered whether the dynamics of the mitochondrial network varies according to muscle fiber type.

Second, each individual myofiber is a long, multinucleated cylindrical cell formed by the fusion of numerous myoblasts during development. Due to their extreme size and long, extended shape, intermixing of mitochondria may be constrained compared to cultured mammalian cells, where mitochondrial fusion results in rapid and extensive homogenization of the mitochondrial population (Legros et al., 2002; Mattenberger et al., 2003; Mishra and Chan, 2014). Histological data from aged and diseased fibers hint that regionalization of organelles can occur (Elson et al., 2002; Shoubridge et al., 1990; Wanagat et al., 2001), but there has been no direct demonstration. To address these issues, we developed methods to measure mitochondrial fusion in intact muscle tissues and in specific muscle fiber types. We demonstrate that mitochondrial fusion rates correlate with oxidative capacity at the individual fiber level. We also developed a method to genetically label individual myonuclei in a stochastic manner, allowing us to uncover discrete mitochondrial domains within myofibers. The dimensions of these mitochondrial domains correlate with the oxidative capacity of the muscle fiber and are regulated by mitochondrial fusion and fission. Thus, mitochondrial dynamics is specialized according to fiber type within skeletal muscle and regulates homogenization of the organelle population along the fiber.

Results

Mitochondrial fusion correlates with the metabolic state of muscle fiber types

Using knock-in mice with the fluorescent protein Dendra2 targeted to the mitochondrial matrix (Pham et al., 2012), we first examined mitochondrial morphology in the *extensor digitorum longus* (EDL) and the *tibialis anterior* (TA), both fast-twitch muscles. In approximately 85% of fibers, we observed small block-like mitochondria arranged in rows and columns when viewed along the long axis of the fiber (Figure 5.1A). The architecture of these interfibrillar mitochondria is consistent with previous EM studies (Ogata and Yamasaki, 1997), and we have shown that each block is a mitochondrial dyad, with the z-lines of the sarcomeres running down the middle of the columnar blocks (Pham et al., 2012). In striking contrast, we observed dramatically different mitochondrial morphologies in fibers of the soleus and diaphragm, two slow-twitch muscles with high oxidative capacity. Here, columns of mitochondria are still present, but in addition, there are prominent longitudinal connections that span mitochondria from multiple sarcomeres (Figure 5.1A).

Further analysis revealed that mitochondria in oxidative muscles are indeed interconnected along the longitudinal axis. Photoconversion of Dendra2 in an *ex vivo* preparation was used to probe mitochondrial connectivity. The punctate mitochondria in the predominant EDL fibers show no connections with neighbors along a row (Figure 5.1B). In the soleus, however, the longitudinal rows are partially continuous, as indicated by immediate diffusion of the photoconverted Dendra2 signal (Figure 5.1C). These results suggest a correlation between fiber type and mitochondrial morphology, with fibers of the

more oxidative muscles having elongated and interconnected mitochondria. However, a minority of EDL fibers deviates from the predominant pattern of punctate mitochondria, instead having extended longitudinal mitochondria resembling those in the soleus (Figure 5.1D).

Because each muscle contains a mixture of distinct fiber types, we utilized transgenic mouse models that allow fluorescent labeling of type I, IIA and IIX/IIB fibers (see Experimental Procedures) (Chakkalakal et al., 2012b). As expected, the majority of EDL fibers were identified as glycolytic type IIX/IIB, and these have punctate mitochondria (Figure 5.1D, 5.1E, 5.1F, and 5.S1A). However, ~15% of EDL myofibers were identified as type IIA (labeled by a MyH2-DsRed transgene), and these fibers always contained elongated mitochondria (Figures 5.1D, 5.1E, and 5.1F). This composition of fiber types is consistent with quantitative studies (Agbulut et al., 2003) showing that the mouse EDL consists of predominantly glycolytic type IIB and IIX fibers and a smaller population of oxidative IIA fibers. The mitochondria in the EDL type IIA fibers resemble those of soleus- or diaphragm-derived type I fibers (labeled by a MyH7-CFP transgene), which are also oxidative (Figures 5.1E, 5.1F, 5.S1B, and 5.S1C). These observations indicate that mitochondrial dynamics is specified in a fiber-autonomous manner, as opposed to being determined by the overall muscle type.

To directly monitor fusion rates, we coupled photoconversion of Dendra2-labeled mitochondria with time-lapse imaging of freshly dissected *ex vivo* preparations of muscle tissues. Mitochondrial fusion was sparse or undetectable in glycolytic IIX/IIB fibers (Figure 5.2A). Longitudinal profiles of fluorescence indicated that the organelles are well separated

and did not fuse over a 30 minute period (Figure 5.2B). In contrast, the oxidative IIA fibers in the EDL showed much higher rates of mitochondrial fusion (Figures 5.2A and 5.2B). Fusion could be detected by a decrease in photoconverted signal in activated mitochondria and a simultaneous increase in signal in neighboring organelles (Figure 5.2B). In contrast to fusion events in cultured cells (Chen et al., 2003), these fusion events occurred without apparent mitochondrial movement. We conclude that the glycolytic fiber types (IIX and IIB) have punctate, isolated mitochondria with little fusion, whereas the oxidative fiber types (I and IIA) have elongated, interconnected mitochondria with higher rates of fusion (Figure 5.2C). These differences do not appear to be secondary to changes in the expression of fusion and fission proteins (Figure 5.S1D).

The above results suggest that distinctions in mitochondrial dynamics are a terminal characteristic of differentiated fiber types. This prompted us to examine undifferentiated neonatal myofibers, where establishment of the adult myosin heavy chain expression pattern has not yet occurred (Agbulut et al., 2003). In 10-14 day old animals, all EDL fibers contained highly elongated mitochondria with high rates of mitochondrial fusion (Figure 5.2A-C), even though the majority of them (>85%) (Agbulut et al., 2003) will eventually develop into glycolytic IIX/IIB fibers with low fusion activity. Thus, fusion rates appear to be developmentally regulated and are particularly elevated in undifferentiated fibers prior to growth and specification.

Mfn1 and Mfn2 are required for mitochondrial elongation and fusion in type IIA fibers

Previously, we showed that removal of Mitofusins 1 and 2 (Mfn1 and Mfn2) in skeletal muscle results in smaller muscles with lower mtDNA content (Chen et al., 2010). In that study, only fast-twitch muscles, such as the glycolytic *tibialis anterior*, were studied. The data in our current study suggests that the more oxidative fibers (where fusion rates are elevated) should also have a dependence on mitofusin function. To test this idea, we specifically examined type IIA fibers in *MLC-Cre; mito-Dendra2^{cond}; mfn1$^{-/loxP}$; mfn2$^{-/loxP}$* animals. In the *soleus* of these animals, type IIA fibers are null for *Mfn1* and *Mfn2* and can be identified by expression of mito-Dendra2. Consistent with our previous study (Chen et al., 2010), we found that dual deletion of Mfn1 and Mfn2 caused compensatory proliferation of mitochondria (Figure 5.3A). This resulted in extensive interfibrillar mitochondria that were tightly packed between myofibrils. The mitochondria were aligned longitudinally and spanned the A-band between z-lines of the sarcomere. However, they did not appear interconnected, because the individual organelles were small and punctate (Figure 5.3B). In contrast, the single removal of Mfn1 or Mfn2 did not cause morphological changes in type IIA fibers (Figure 5.3A). Photoconversion experiments to probe mitochondrial connectivity confirmed that the mitochondria in Mfn1/2-deficient IIA fibers were discontinuous (Figure 5.3B) and exhibited no signs of content mixing (Figures 5.3C and 5.3D). Thus, Mfn1 and Mfn2 are together required in oxidative type IIA fibers to generate longitudinally connected mitochondria, and the presence of either protein alone is sufficient to maintain organelle morphology.

Mitochondrial morphology responds to changes in OXPHOS activity

Our results indicate that mitochondrial fusion is enhanced in type I and IIA fibers, which have high oxidative capacity. Neonatal myofibers, which also have high mitochondrial fusion activity, contain uniformly high oxidative activity, regardless of the terminal fiber type (Chen et al., 2010; Redenbach et al., 1988). We therefore wondered whether the distinctions in mitochondrial topology between muscle fibers of different types and developmental stages are a response to their distinct OXPHOS capacities.

To test this hypothesis, we first induced glycolytic fibers to respire more actively in an *in vivo* setting. In mouse, endurance exercise is well known to induce increased respiratory capacity and fiber-type switching in certain hind-limb muscles, such as the plantaris muscle (Allen et al., 2001). We utilized cell lineage tracing to track the fate of IIX/IIB fibers by expression of *Pvalb-Cre*, which permanently activates a mito-Dendra2 expression cassette in these cells. Simultaneously, the type IIA fate was tracked by the expression of DsRed under control of the MyH2 promoter. Thus, using mice with both reporters allows IIA and IIX/IIB fiber types to be simultaneously monitored as a function of a 4-week running regimen. Prior to running, 0% of IIX/IIB fibers (marked by mito-Dendra2) were positive for the IIA DsRed marker (Figures 5.4A-C). This observation indicates that type IIX/IIB and type IIA fibers are non-overlapping cell types under our basal pre-exercise conditions. After 4 weeks of voluntary running, analysis of the plantaris muscle revealed a substantial increase in oxidative myofibers, due to fiber type switching from IIX/IIB to IIA (Figure 5.4A-C). Approximately 30% of the IIX/IIB-marked fibers were now also positive for the type IIA marker, a staining pattern never observed under non-exercise

conditions. In all of these "switched" fibers (expressing both the IIA and IIX/IIB markers), mitochondrial morphology was significantly elongated (Figures 5.4B and 5.4D). Thus, the exercise regimen promoted substantial fiber type switching that is associated with a dramatic change in mitochondrial structure.

To further test the relationship between metabolism and mitochondrial dynamics, we induced EDL muscle to respire more actively *ex vivo*, where fiber type switching does not occur. We isolated individual EDL muscles from animals in which the IIX/IIB fibers were labeled with mito-Dendra2 and measured oxygen consumption in media containing glucose or acetoacetate. Similar to cultured fibroblasts (Mishra et al., 2014), EDL muscle placed in oxidative (acetoacetate-containing) media showed a several-fold higher rate of oxygen consumption and increased mitochondrial membrane potential as compared to muscle in glucose-containing media (Figure 5.4E, 5.S2A-D). With glucose-containing media, the IIX/IIB fibers show largely punctate mitochondria, with half the fibers containing a few tubular mitochondria (Figures 5.4F and 5.4G). Addition of oligomycin, which inhibits complex V activity, resulted in fibers with completely fragmented mitochondria with no interconnections. With oxidative media, the majority of IIX/IIB EDL muscle fibers showed rows of interconnected, highly tubular mitochondria, a phenotype never found in IIX/IIB fibers under the glucose-containing condition or *in vivo* (Figures 5.4F and 5.4G). Photoconversion experiments indicate that the matrices of these rows of mitochondria are partially continuous (Figure 5.S1E). Thus, the data suggest that mitochondrial morphology is not an obligate characteristic of fiber type but instead can dynamically respond to the oxidative activity of each individual fiber.

The length of mitochondrial domains *in vivo* correlates with myofiber type

Muscle fibers are very long, multinucleated cells formed from the fusion of myoblasts. This unusual cell biology raises the issue of whether mitochondria in muscle fibers are well homogenized through extensive mitochondrial fusion, or whether the mitochondria are compartmentalized into discrete domains that are locally controlled by nearby nuclei. To distinguish between these two extreme models, we used mouse genetics to stochastically label a mitochondrial protein encoded and synthesized by a single myonucleus (Figures 5.5A and 5B). During postnatal development, satellite cells (a resident stem cell population of muscular tissue) can differentiate and fuse with existing myofibers, thereby providing new nuclei and organelles to the growing fiber (Keefe et al., 2015). We reasoned that visualization of individual satellite cell fusion events and the extent of mitochondrial spreading should provide an indication of the underlying mitochondrial dynamics.

We crossed the satellite-specific *Pax7-CreERT2* driver (Lepper et al., 2009) to a floxed allele of mito-Dendra2 and cytosolic-YFP (Figure 5.5A). In these animals, activation of Cre leads to mito-Dendra2 expression specifically in pre-fusion satellite cells. The CreERT2 molecule is tamoxifen-dependent, and we expected that low levels of tamoxifen would be needed for stochastic activation in satellite cells. Surprisingly, even in the absence of tamoxifen, we occasionally detected mito-Dendra2 expression in single satellite cells on the fiber periphery, representing pre-fused cells (Figure 5.S3A). In addition, we could also detect post-fusion events, demonstrated by the presence of mito-Dendra2 or cytosolic YFP within an existing myofiber (Figures 5.5C and 5.S3B). Myofibers were uniformly labeled

with cytosolic YFP. In contrast, mito-Dendra2 expression was instead localized to small longitudinal regions, typically less than 100 μm in length (Figures 5.5C and 5.5D). These observations indicate that the CreERT2 is leaky enough to provide stochastic activation of mito-Dendra2 in a small subset of satellite cells. Moreover, mitochondrial proteins show regionalization to their nucleus of origin, in contrast to soluble cytosolic proteins.

The mito-Dendra2 mitochondrial domains were randomly distributed throughout the tissue and were typically shaped as single peaks with a Gaussian distribution of fluorescence intensity along the longitudinal axis (Figures 5.5D and 5.S3C). Such peaks therefore likely represent single fusion events between a satellite cell and a myofiber. By using a conditional nuclear-targeted GFP allele, we could estimate the prevalence of labeled myonuclei within muscle fibers (Figure 5.S3D). Less than 1% of total myonuclei were labeled, and >70% of the time, the GFP expression profile was consistent with the presence of a singly activated myonucleus. Occasionally, we were able to find double and triple peaks, indicating fusion events that had occurred near one another (Figure 5.S3C). Localization of mito-Dendra2 was uniform along the transverse axis, indicating that domains occur only in the longitudinal direction (Figures 5.S3E and 5.S3F).

Multiple lines of evidence indicate that these mitochondrial domains are stable over time, as opposed to being transient phenomena from recent satellite cell fusion events. First, in *ex vivo* culturing experiments, we did not observe significant changes in domain size or dissipation of the mito-Dendra2 signal over the course of 72 hours (Figure 5.S4A and 5.S4B). Thus, mitochondrial domains are stable under standard culturing conditions where myofibers remain healthy and functional (Casas et al., 2010; Eisner et al., 2014; Keire et al.,

2013). Second, we observed a significant increase in the frequency of mitochondrial domains in aged animals, suggesting that domains are stably accumulating over time (Figure 5.S4C and S4D). It is well known that Pax7+ satellite cells decrease in abundance with age (Chakkalakal et al., 2012a; Collins et al., 2007; Fry et al., 2015; Shefer et al., 2006). If the observed mitochondrial domains were transient reflections of recent satellite cell fusion events, we would expect their frequency to decrease in aged animals.

Because interfibrillar mitochondria are localized to the Z-disc with little movement, we hypothesized that domain size would be at least partially dependent on the ability of neighboring organelles to undergo fusion and share protein products. To test this idea, we quantified the size of individual domains (calculated as the full width at half-maximum fluorescence intensity) in a large number of fibers, and classified them by fiber type. To simplify quantification of the peaks, we restricted our analysis to domains with single peaks. In the adult EDL, type IIX/IIB fibers had the smallest domain dimension, approximately 60 μm (Figure 5.5E). In contrast, the more oxidative IIA fibers, which we showed had more fusogenic mitochondria, had larger domains that approached 80 μm. Domain size in neonatal muscle was the largest, approximately twice the size of adult IIX/IIB fibers (Figure 5.5E). Because these results may be complicated by the increased abundance of Pax7+ satellite cells in young animals, we specifically limited our analysis to mito-Dendra2 domains containing a single peak. Indeed, the same fiber types from different muscles showed similar domain size, and aged animals did not show any further decreases in domain size (Figures 5.5E and S4E). The correlation of mitochondrial domain size with the metabolic state of the muscle fibers suggests that mitochondrial fusion is likely an important

regulator of domain size, allowing OXPHOS-dependent fiber types to more efficiently homogenize their organelle population.

Mitofusins and Mff control the length of mitochondrial domains

To definitively implicate mitochondrial dynamics in regulation of domain size, we utilized conditional alleles of Mitofusin 1 and Mitofusin 2. Combining these alleles with the *Pax7-CreERT2* driver allows removal of the mitofusins in the few stochastically activated satellite cells, without affecting overall animal physiology. Domains from these animals showed smaller sizes, particularly in the young and oxidative fiber types (Figure 5.6A). Strikingly, some domains were extremely small in fusion-deficient animals, with limited spread of the Dendra2 signal even along the transverse axis of the fiber (Figures 5.6B and 5.6C). Such transverse gradients were present at much higher frequency in mutant animals, regardless of fiber type (Figure 5.6D). Thus, domain size and shape are dependent on the mitofusins. These changes due to mitofusin disruption are remarkable, given that in this experimental system, the nuclei surrounding the mitochondrial domain have normal mitofusin function. In contrast, deletion of mitochondrial fission factor (Mff) in the whole animal results in much larger domains, especially in the glycolytic IIX/IIB fibers (Figure 5.6A).

Discussion

Our results suggest that mitochondrial fusion rates are a defining characteristic between different muscle fiber types, similar to other mitochondrial properties, such as abundance in the sarcolemmal region and respiratory chain activity. Previous EM studies

have suggested that "red" muscles may have an altered mitochondrial topology, with the mitochondria appearing more "string-like" and stretching across the A-band (Fujioka et al., 2013; Ogata and Yamasaki, 1997). Here, we have extended this analysis by correlating topology, interconnectivity and fusion with specific fiber types as defined by myosin heavy chain expression. The fiber types I and IIA have elongated mitochondria and higher rates of mitochondrial fusion compared to glycolytic muscle fibers. Therefore, the level of mitochondrial fusion correlates with the oxidative capacity of the fiber. We do not think that mitochondrial morphology plays a direct role in the determination of fiber type, as enhanced fusion *ex vivo* is not accompanied with type switching, and deletion of the mitofusins does not prevent formation of oxidative fibers (Chen et al., 2010). Instead, we suspect that mitochondrial morphology adapts to the specific functional needs of the fiber. Elongated mitochondrial networks have been associated with increased metabolic states (Gomes et al., 2011; Mitra et al., 2009; Tondera et al., 2009) and may facilitate maintenance of ATP levels in oxidative muscle fibers that require long-term energy production. One might expect that enhancing mitochondrial fusion (via Mfn1/2 overexpression, for instance) would prove beneficial, particularly for the function of oxidative fibers.

By activating mito-Dendra2 expression in specific myonuclei, we reveal that mitochondrial domains exist in vivo in muscle fibers. The dimensions of these domains are dependent on the fusion and fission processes, with increased fusion correlated with longer domains. In addition, we would also expect a dependence on other biophysical parameters such as protein synthesis and turnover rates, as well as mRNA and protein diffusion constants. Similarly, domains have been visualized previously for Golgi and nuclear

proteins (Hall and Ralston, 1989; Pavlath et al., 1989), as well as structural proteins such as dystrophin (Blaveri et al., 1999; Kinoshita et al., 1998), though the biophysical parameters underlying domain size have not been explored in these cases.

Even though oxidative muscle fibers have higher rates of mitochondrial fusion, we find that all muscle fibers show mitochondrial compartmentalization, which implies that homogenization of mitochondria is relatively limited. We can suggest several reasons why it may be more challenging to homogenize mitochondria in skeletal muscle versus cultured cells. First, myofibers can be extremely long, approaching several centimeters in length. Second, mitochondria in muscle fibers are not known to move, thereby limiting interactions between organelles. And most importantly, the fiber is a syncytial cell in which multiple nuclei are spaced apart longitudinally, providing an intrinsically high degree of heterogeneity as compared with a singly nucleated cell. Our results suggest that mitochondrial proteomes in muscle fibers are determined largely by the nearest nuclei.

The phenomenon of mitochondrial domains, as well as their regulation by OXPHOS capacity, is likely to be relevant to mitochondrial and aging-related disorders, where mutant mtDNA accumulates to high levels in segmental regions along the length of a fiber (Barron et al., 2005; Elson et al., 2002; Wanagat et al., 2001). The dysfunctional region is associated with local, clonal expansion of mutant mtDNA, and appears as "ragged red fibers" on transverse sections of muscle tissue. Our discovery of mitochondrial domains provides a rationale for why these mtDNA defects are limited to discrete longitudinal domains. In particular, the loss of oxidative activity that occurs with clonal expansion of mutated mtDNA should lower local fusion rates, thereby providing a mechanism to promote

regionalization of the defect and prevent it from spreading throughout the fiber (Figure 5.7). We propose that by linking oxidative activity of the mitochondrion to fusion rates, the myofiber can promote health under normal conditions and restrict the spread of defects during disease and aging.

Materials and methods

Mouse breeding

All mouse experiments were approved by the Caltech Institutional Animal Care and Use Committee. Mice with conditional or ubiquitous expression of mito-Dendra2 were described previously (Pham et al., 2012). To label type I fibers and visualize mitochondria, transgenic mice expressing CFP under control of the MyH7 promoter (Chakkalakal et al., 2012b) were crossed to mice with the ubiquitous mito-Dendra2 allele (*MyH7-CFP; mito-Dendra2*). Similarly, type IIA fibers were visualized using transgenic mice expressing DsRed under control of the MyH2 promoter (Chakkalakal et al., 2012b) (*MyH2-DsRed; mito-Dendra2*). To label type IIX/IIB fibers, we utilized the *Pvalb-Cre* allele (Hippenmeyer et al., 2005), which is selectively active in IIX/IIB fibers as well as a subset of central neurons (Berchtold et al., 2000; Chakkalakal et al., 2012b). *Pvalb-Cre; mito-Dendra2*^{cond} mice allowed visualization of mitochondrial morphology specifically in IIX/IIB fibers. To address the role of mitofusins in type IIA fibers, we utilized previously described conditional and excised knockout alleles of Mfn1 and Mfn2, in combination with the *MLC-Cre* allele (Bothe et al., 2000; Chen et al., 2010; Mourkioti et al., 2008).

For voluntary exercise experiments, we generated *MyH2-DsRed; Pvalb-Cre; mito-Dendra2*^{cond} mice, which allows us to label and distinguish IIA and IIX/IIB fibers. At 6 weeks of age, mice were housed in isolation either with (‘exercised’) or without (‘sedentary’) running wheels. Mice were euthanized at 10 weeks of age and muscles were harvested for analysis (see below).

For stochastic labeling of myonuclei, we took advantage of the *Pax7-CreERT2* allele, in which tamoxifen-dependent Cre recombinase is expressed in the Pax7-positive satellite cells (Lepper et al., 2009). In the absence of tamoxifen, leaky activity of the Cre recombinase allows for low-level excision of floxed alleles (Haldar et al., 2009; Kemp et al., 2004; Liu et al., 2010). The *Pax7-CreERT2* allele was combined with conditional expression alleles for mito-Dendra2 (Pham et al., 2012), cytosolic YFP (Srinivas et al., 2001), or nuclear-targeted GFP-βgalactosidase fusion protein (Stoller et al., 2008), allowing visualization of mitochondrial, cytosolic and nuclear domains respectively. All these conditional expression alleles had been integrated into the ROSA26 locus.

To assess the effect of mitochondrial fusion on the size of mitochondrial domains, we utilized previously described (Chen et al., 2003; Chen et al., 2007) conditional and excised knockout alleles of Mitofusin 1 and Mitofusin 2. Complete removal of Mfn1 or Mfn2 is embryonic lethal (Chen et al., 2003), so we instead removed these proteins specifically from stochastically labeled myonuclei using the *Pax7-CreERT2* allele. As the Pax7 and Mfn2 loci are both on chromosome 4, we first isolated animals with a *Pax7-CreERT2 Mfn2*$^{-}$ chromosome by screening for homologous recombination events between the two alleles. Experimental and control littermates were then bred by crossing *Pax7-CreERT2 Mfn2*$^{-/+}$*; Mfn1*$^{-/+}$ mice to *mito-Dendra2*^{cond}*; Mfn1*$^{loxP/loxP}$*; Mfn2*$^{loxP/loxP}$ mice. To assess the effect of mitochondrial fission on the size of mitochondrial domains, we utilized *Mff* mutant mice (unpublished data) carrying a gene-trap allele that abolishes Mff function in mouse embryonic fibroblasts (Loson et al., 2013). Experimental and control littermates were then bred by crossing *Pax7-CreERT2; Mff*$^{-/+}$ mice to *mito-Dendra2*^{cond}*; Mff*$^{-/+}$ mice.

Muscle preparation and imaging

For analysis of mitochondrial morphology or domain measurements, skeletal muscle was dissected and immediately fixed in formalin for 3-4 hours at room temperature, followed by overnight at 4°C. Muscles were then rinsed with PBS and teased apart using fine forceps. Samples were mounted on glass slides with Cytoseal XYL mounting media (Thermo Scientific). Images were acquired on a Zeiss LSM 710 confocal microscope using Plan-Apochromat objectives (63x, 40x or 20x). For mitochondrial morphology measurements, optical slices at 0.7 µm thickness were acquired, and Z-stacks were oversampled at 0.35 µm. For domain measurements, optical slices of 2.0 µm thickness were acquired.

For photoconversion or fusion experiments, acutely dissected whole EDL or soleus muscle was transferred to culturing media [DMEM (Sigma D5030) supplemented with 1x penicillin-streptomycin, 10 mM D-glucose, 2 mM L-glutamine, 10% dialyzed FBS, 25 mM HEPES, pH 7.4] in a coverglass bottom dish. Muscles were stabilized with a slice anchor (Warner Instruments) and imaged on a stage-top heated platform maintained at 37°C. For photoconversion of Dendra2, a small region of interest was irradiated with the 405 nm laser. To follow fusion, Z-stacks were acquired for 30 minutes starting immediately after photoconversion.

Oxygen consumption rates were measured in freshly dissected EDL muscles using a two chamber Clark oxygen electrode system (Oxygraph, Hansatech Instruments), allowing two measurements to be made simultaneously. Chambers were equilibrated to 37°C with the indicated culturing media, and a single EDL muscle was added to each

chamber. After closing the chamber and allowing for equilibration of oxygen levels, basal respiration was measured as the average oxygen consumption rate (OCR) over 3 minutes. For the acetoacetate-containing media, glucose was replaced with acetoacetate (10 mM, Sigma), which was previously shown to increase oxygen consumption in cultured cells (Mishra et al., 2014). Two EDL muscles from the same animal were compared simultaneously in different chambers and the ratio of oxygen consumption rates was calculated. Experiments were performed in triplicate using littermates. Respiratory parameters were measured by the sequential addition of oligomycin (1 µM, Sigma), CCCP (2 µM, Sigma), and antimycin A (1 µM, Sigma). The cellular respiratory control ratio (RCR) was calculated as the ratio of the maximal OCR (CCCP-stimulated) to the oligomycin-inhibited OCR.

Membrane potential measurements were performed by incubating EDL muscles in the above media, supplemented with 200 nM TMRM (Molecular Probes), for 30 min at 37°C. Muscles were then switched to fresh non-TMRM media and imaged immediately. Relative fluorescence was quantified from pixels of mitochondrial signal using ImageJ.

For *ex vivo* analysis of mitochondrial domains, single fibers were isolated by enzymatic digestion. EDL muscles were incubated at 37°C in an orbital shaker (90 rpm for 45 minutes) in 1 mL of DMEM (Invitrogen 11995) supplemented with collagenase type IV (Sigma). Fibers were then manually dissociated in DMEM supplemented with 10% horse serum using mild trituration through decreasing bore sizes of pipet tips pre-coated with 10% horse serum. Individual fibers were then transferred to Matrigel (BD Bioscience) coated dishes,

and cultured for up to 72 hours at 37°C and 5% CO2. Individual mitochondrial domains (mito-Dendra2) were identified and imaged every 12 hours.

For analysis of nuclear GFP expression, single myofibers were isolated as described above. Individual fibers were then transferred to 8-well Permanox slides (Nunc Lab-Tek) pre-coated with Matrigel. After settling, fibers were fixed for 20 minutes at 37°C with formalin, permeabilized for 10min at -20°C with acetone, and then blocked in PBS supplemented with 10% FBS, 1% BSA, 2% Triton X-100. GFP was detected with AlexaFluor555-conjugated αGFP antibody (Molecular Probes) and myonuclei were stained with DAPI (Molecular Probes). The degree of nuclear activation was quantified by comparing the number of GFP-positive nuclei versus total number of nuclei (identified by DAPI staining).

For analysis of protein levels, muscle lysates were prepared via homogenization and clarification in lysis buffer (50 mM Tris, 2% SDS, pH 6.8) supplemented with HALT protease inhibitors, and analyzed by Western blot. The following antibodies were used for detection: Mfn1 (Chen et al., 2003), Mfn2 (Cell Signaling), Mff (gift from A. van der Bliek), Hsp60 (Santa Cruz Biotech), and Tom20 (Santa Cruz Biotech).

Analysis of mitochondrial domains

Mitochondrial domains were imaged as described above. Single optical sections were taken near the center of individual muscle fibers. Curved fibers were digitally straightened, and total fluorescence intensities along the longitudinal axis were calculated in ImageJ. Raw fluorescence intensities were filtered using a moving average, and domain

size was calculated as the peak width at half-maximal intensity. Only single, well-separated peaks were analyzed, and the fluorescent intensity at both tails was required to be below 30% of the maximal intensity.

Acknowledgments

We thank Alexander van der Bliek for providing the α-Mff antibody. We are grateful to Hsiuchen Chen for help with experiments using *Mfn1/2* and *Mff* mutant mice. This work was supported by grants from the NIH (GM062967) and the Muscular Dystrophy Association. P.M. was supported by a Baxter Senior Postdoctoral fellowship. G.V. was supported by grants from the NIH (National Research Service Award T32 GM0076162) and the California Institute for Regenerative Medicine (Stem Cell Bridges Program, TB1-01176). We thank members of the D.C.C. lab for helpful discussions and comments on the manuscript.

Chapter 5 Figure legends

Figure 5.1. Mitochondrial morphology and connectivity correlates with fiber type in mouse skeletal muscle.

(A) Schematic of skeletal muscle showing orientation of images (top), and mitochondrial morphology in glycolytic (EDL, TA) and oxidative (soleus, diaphragm) muscles as visualized by expression of mito-Dendra2. Scale bar, 5 μm.

(B) Photoconversion of mito-Dendra2 in an *ex vivo* EDL muscle. The red box indicates the photoconverted region. Scale bar, 2 μm.

(C) Same as (B), but in soleus muscle.

(D) Co-labeling of mitochondria (mito-Dendra2) and type IIA fibers (MyH2-DsRed transgene) in EDL muscle, with higher magnification images on the far right. Scale bar, 5 μm.

(E) Representative images of mitochondrial morphology in type I, IIA and IIX/IIB fibers, visualized by expression of mito-Dendra2. Scale bar, 5 μm.

(F) Distribution of mitochondrial profiles in Type I, IIA and IIX/IIB fibers. Greater than 30 fibers were scored per fiber type (*$p<0.01$ (z-test)).

Figure 5.2. Mitochondrial fusion is enhanced in oxidative and young muscle fibers.

(A) Time-lapse imaging of photoconverted mito-Dendra2 was used to follow mitochondrial fusion in *ex vivo* EDL muscle preparations from adult (3 mo) and young (p10) animals. At time t = 0 min, a subset of mitochondria were photoconverted. The merged images (left panels) indicate the differences in mitochondrial morphology. The photoconverted signal

(red) was followed over 30 minutes. Longitudinal fusion events (arrowheads) were visualized by spread of signal to neighboring mitochondria. Yellow boxes indicate regions of interest analyzed in (B), and vertical dashed lines indicate the respective longitudinal positions. Scale bars, 5 μm.

(B) Intensity of photoconverted signal at t = 1 and 30 minutes in the regions of interest indicated by yellow boxes in (A). The longitudinal positions indicated by the vertical dashed lines have a counterpart in (A). Fusion events in IIA and young fibers are identified by the decrease in signal in the donating mitochondria on the right, coupled with increasing signal in neighboring mitochondria on the left. IIX/IIB fibers exhibit well-separated organelles with few or no (this case) fusion events.

(C) Percentage of myofibers showing fusion events (over 30 minutes) for adult IIX/IIB, IIA and young myofibers. At least 10 trials were performed per fiber type (*$p<0.05$; **$p<0.01$; n.s., not significant (z-test)).

Figure 5.3. Deletion of Mfn1 and Mfn2 abrogates mitochondrial fusion in oxidative IIA muscle fibers.

(A) Representative images of mitochondrial morphology in type IIA fibers from animals of the indicated genotype. Scale bar, 5 μm.

(B) Photoconversion of mito-Dendra2 in *ex vivo* IIA fibers from animals of the indicated genotype. The red boxes indicate the photoactivated regions. Scale bar, 2 μm.

(C) Photoconversion experiment (as in Figure 5.2A) to follow fusion in an *ex vivo* IIA fiber from an *mfn1 -/-,mfn2 -/-* animal. Scale bar, 10 μm.

(D) Same as Figure 5.2B, but in the IIA fiber shown in (C). The region quantitated is labeled by the yellow box in (C), and the longitudinal position is indicated by the dashed vertical line.

Figure 5.4. Mitochondrial morphology in muscle fibers responds to changes in oxidative activity.

(A) Co-labeling of IIA fibers (MyH2-DsRed transgene; red) and mitochondria from IIX/IIB fibers (mito-Dendra2; green) in plantaris muscle from sedentary and exercised mice. The mito-Dendra2 marker is activated in IIA/IIB fibers by the *Pvalb-Cre* driver. Note that co-expression of these markers is found only in fibers from exercised animals. Scale bar, 10 μm.

(B) Enlarged view of mitochondrial morphology from regions indicated in (A) (boxes). Scale bar, 5 μm.

(C) Percentage of originally IIX/IIB fibers (Dendra2 positive) which are co-labeled with the IIA marker (MyH2-DsRed) in sedentary and exercised mice. At least 30 fibers were scored for 5 animals in each group (*$p<0.05$ (z-test)).

(D) In exercised mice, percentage of originally IIX/IIB fibers (Dendra2 positive) which have elongated or fragmented mitochondria. Fibers were separated into two groups: those having switched to the IIA fiber type (MyH2-DsRed positive) and those that have not switched (MyH2-DsRed negative). *$p<0.01$ (z-test).

(E) Representative oxygen consumption rates (OCR) measured *ex vivo* in paired EDL muscles from the same animal (left). The chamber was closed at the time indicated by the

arrowhead. Respective oxygen consumption rates (nmol/min/mL) are indicated for the time interval between the two arrows. (Right) Oxygen consumption rates, normalized to OCR in glucose-containing media. Experiments were performed in triplicate.

(F) Percentage of IIX/IIB fibers having long tubular, short tubular or fragmented mitochondria, after overnight incubation in the indicated media. At least 30 fibers per muscle were counted, and experiments were performed in triplicate. (*$p<0.01$ (t-test)).

(G) Representative images of mitochondrial morphology from IIX/IIB fibers after overnight incubation in the indicated media. Mitochondria were visualized by expression of mito-Dendra2. Scale bar, 5 μm. Error bars indicate standard errors.

Figure 5.5. Mitochondria form domains in mouse skeletal muscle.

(A) Schematic for stochastic satellite cell labeling experiment. Tamoxifen-dependent Cre-ERT2 (driven by the Pax7 promoter) is expressed in satellite cells. In the absence of tamoxifen, leaky Cre activity excises a poly(A) stop cassette, allowing rare, stochastic expression of mito-Dendra2.

(B) Two extreme models of mitochondrial homogenization in myofibers. Single myonuclei are randomly labeled by leaky activity of Cre-ERT2 recombinase in the absence of tamoxifen. The expressed fluorescent gene products may then be homogenized throughout the fiber (top), or compartmentalized to a “domain” surrounding the labeled myonucleus (bottom).

(C) Low magnification view of cytosolic (cytosolic YFP, shown in red for clarity) and mitochondrial (mito-Dendra2, green) domains in EDL muscle. Scale bar, 50 μm.

(D) Representative single mitochondrial domain (green) from a type IIB fiber. For comparison, note that the cytosolic YFP localization is homogeneous (red). Scale bar, 10 μm. (Bottom) Quantitation of fluorescence intensity of mito-Dendra2 and cytosolic YFP.

(E) (Top) Representative mitochondrial domains from young, IIA and IIX/IIB fibers in wild-type mice. Scale bar, 20 μm. (Bottom) Quantitation of domain size in the indicated fiber types from wild-type mice. At least 30 domains per fiber type were quantified. (*p<0.001 (t-test)). Error bars indicate standard errors.

Figure 5.6. Mitochondrial domain size is regulated by Mfn1, Mfn2 and Mff.

(A) (Left) Representative mitochondrial domains from wild-type and mutant mice with the indicated fiber types and genotypes. Scale bar, 20 μm. (Right) Quantitation of domain lengths. At least 30 domains per group were quantified (*p<0.001 (t-test)).

(B) Representative mitochondrial domains in wildtype and *mfn1/2* IIA fibers. Note that the domain in the *mfn1/2* fiber shows a gradient in the transverse direction (arrow, perpendicular to the long axis of the fiber). Scale bar, 20 μm.

(C) Quantitation of mito-Dendra2 fluorescence intensity in the transverse direction (from B).

(D) Percentage of mitochondrial domains showing transverse gradients, in the indicated fiber type and genotype. At least 30 domains per group were quantified (*p<.001; n.s., not significant (t-test)). Error bars indicate standard errors.

Figure 5.7. Model: the linking of oxidative activity and mitochondrial fusion promotes organellar health and restricts spread of mtDNA defects in myofibers. (Left) In wildtype myofibers, oxidative activity promotes fusion of mitochondria across the sarcomere, thereby promoting some homogenization of the organellar population along the longitudinal axis. Z-lines are depicted in cyan. (Right) In the presence of mutant mtDNA, clonal expansion of the genetic defect (due to unknown mechanisms) results in decreased OXPHOS activity. Decreased OXPHOS at the site of the defect is proposed to lower local fusion rates, thereby promoting compartmentalization and preventing spread of the mutant mtDNA genome throughout the fiber.

Chapter 5 Figures

Figure 5.1

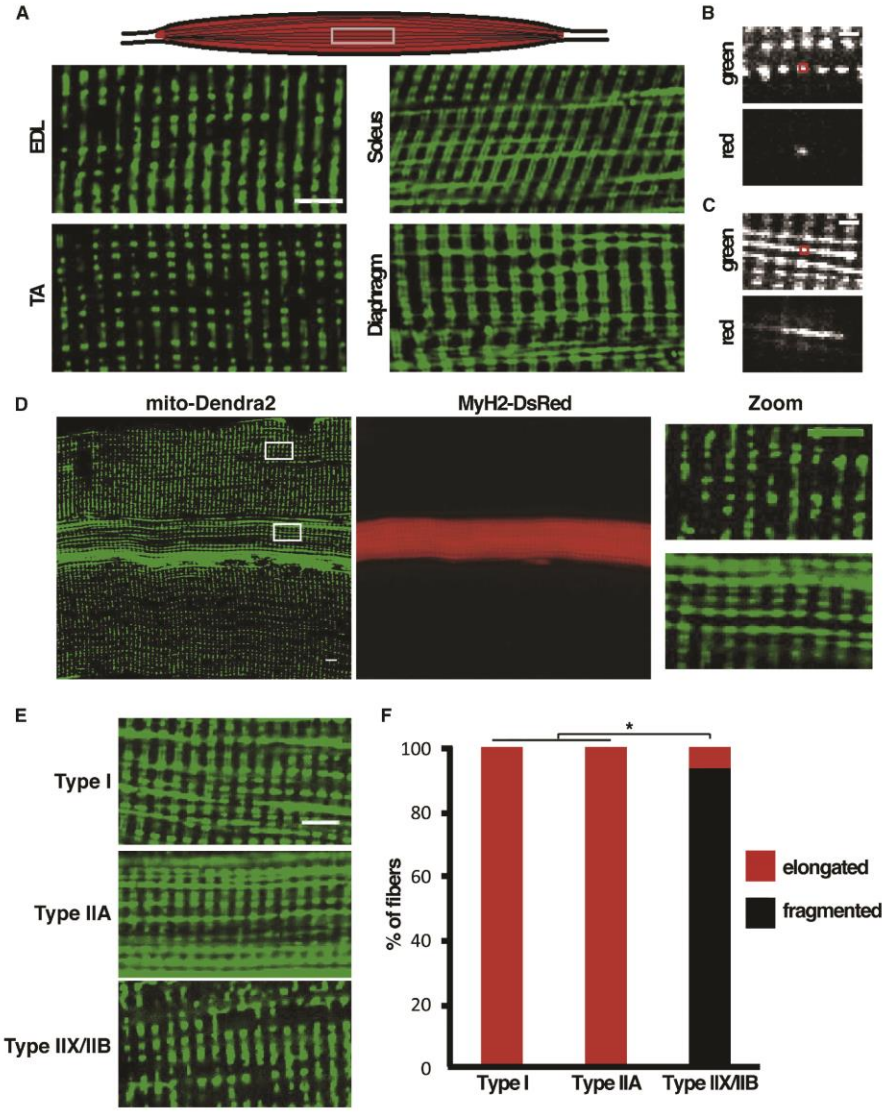

Figure 5.2

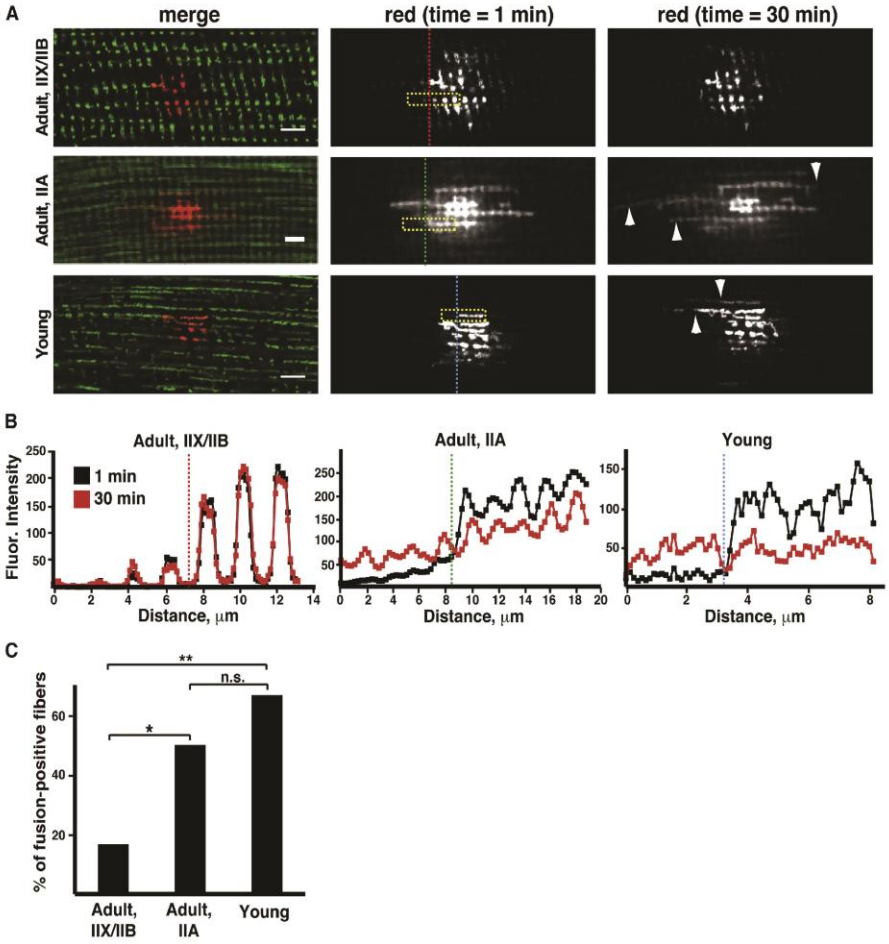
A
merge
red (time = 1 min)
red (time = 30 min)
Adult, IIX/IIB
Adult, IIA
Young
B
Adult, IIX/IIB
Adult, IIA
Young
1 min
30 min
Fluor. Intensity
Distance, μm
C
% of fusion-positive fibers
**
n.s.
*
Adult, IIX/IIB
Adult, IIA
Young

Figure 5.3

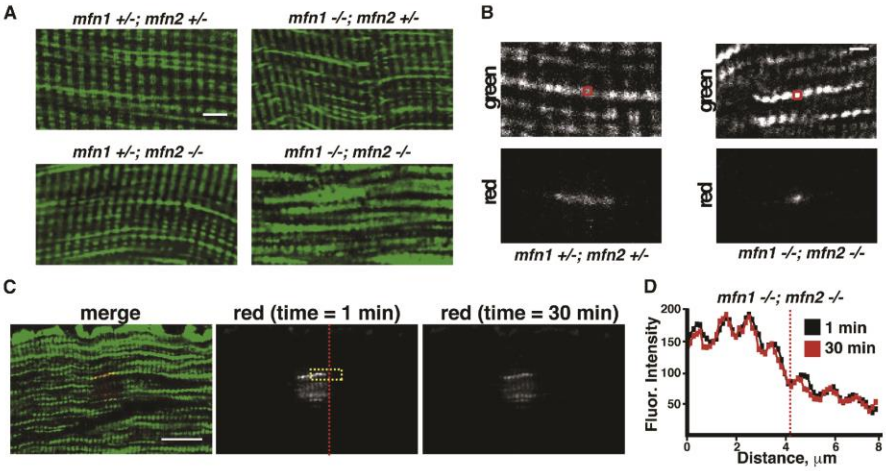
A
mfn1 +/-; mfn2 +/-
mfn1 -/-; mfn2 +/-
mfn1 +/-; mfn2 -/-
mfn1 -/-; mfn2 -/-
B
green
red
mfn1 +/-; mfn2 +/-
mfn1 -/-; mfn2 -/-
C
merge
red (time = 1 min)
red (time = 30 min)
D
mfn1 -/-; mfn2 -/-
1 min
30 min
Fluor. Intensity
200
150
100
50
0
2
4
6
8
Distance, μm

Figure 5.4

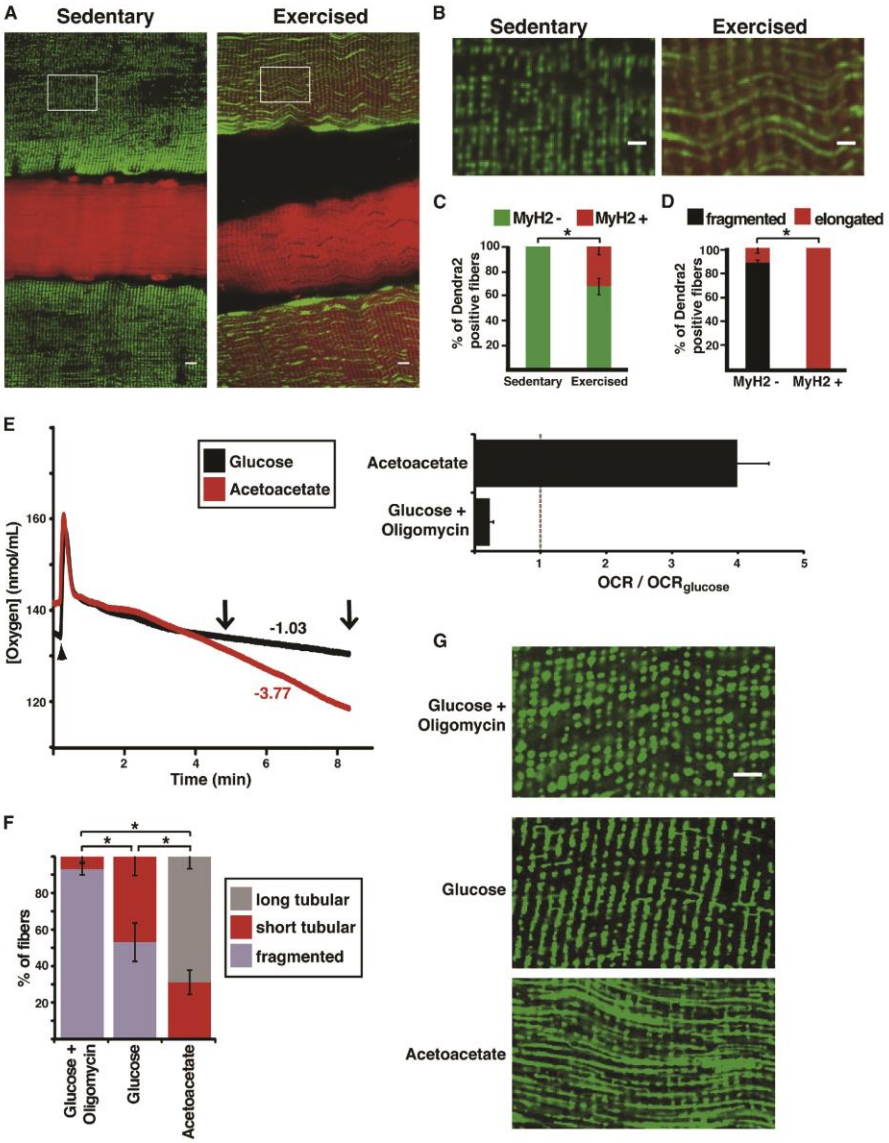
A
Sedentary
Exercised
B
Sedentary
Exercised
C
MyH2 -
MyH2 +
% of Dendra2 positive fibers
Sedentary
Exercised
D
fragmented
elongated
% of Dendra2 positive fibers
MyH2 -
MyH2 +
E
Glucose
Acetoacetate
[Oxygen] (nmol/mL)
-1.03
-3.77
Time (min)
Acetoacetate
Glucose + Oligomycin
OCR / OCR glucose
F
% of fibers
long tubular
short tubular
fragmented
Glucose + Oligomycin
Glucose
Acetoacetate
G
Glucose + Oligomycin
Glucose
Acetoacetate

Figure 5.5

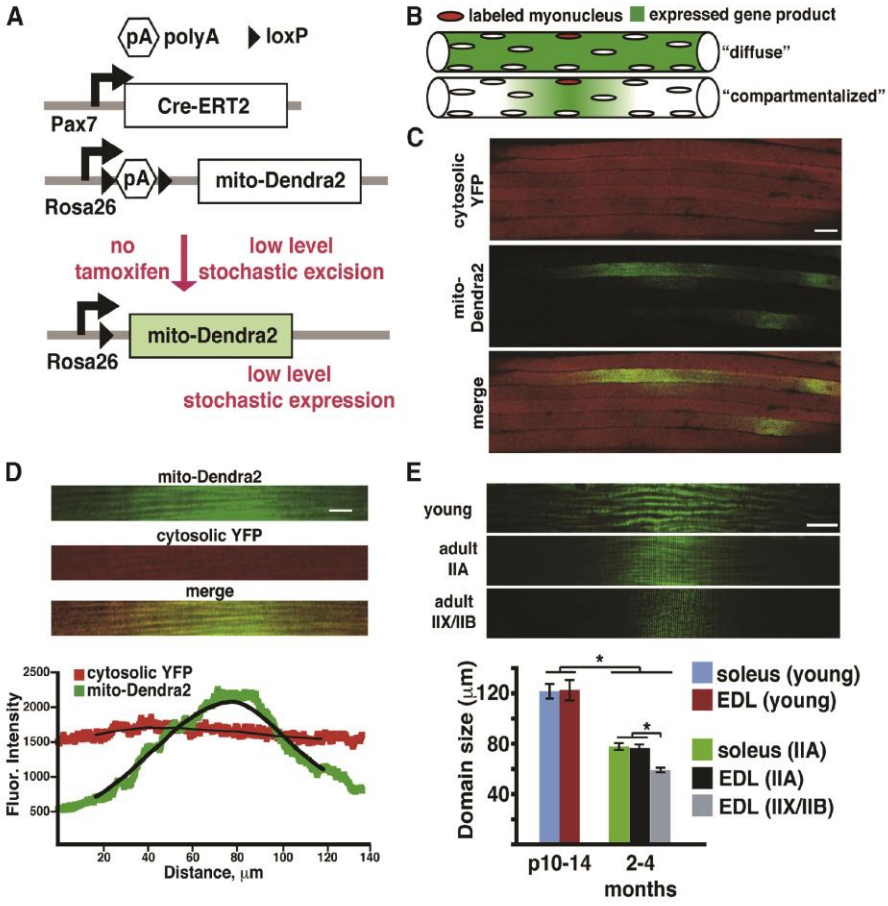
A
pA polyA
loxP
Pax7
Cre-ERT2
Rosa26
pA
mito-Dendra2
no tamoxifen
low level stochastic excision
Rosa26
mito-Dendra2
low level stochastic expression
B
labeled myonucleus
expressed gene product
"diffuse"
"compartmentalized"
C
cytosolic YFP
mito-Dendra2
merge
D
mito-Dendra2
cytosolic YFP
merge
cytosolic YFP
mito-Dendra2
Fluor. Intensity
2500
2000
1500
1000
500
20
40
60
80
100
120
140
Distance, μm
E
young
adult IIA
adult IIX/IIB
Domain size (μm)
120
80
40
*
*
soleus (young)
EDL (young)
soleus (IIA)
EDL (IIA)
EDL (IIX/IIB)
p10-14
2-4 months

Figure 5.6

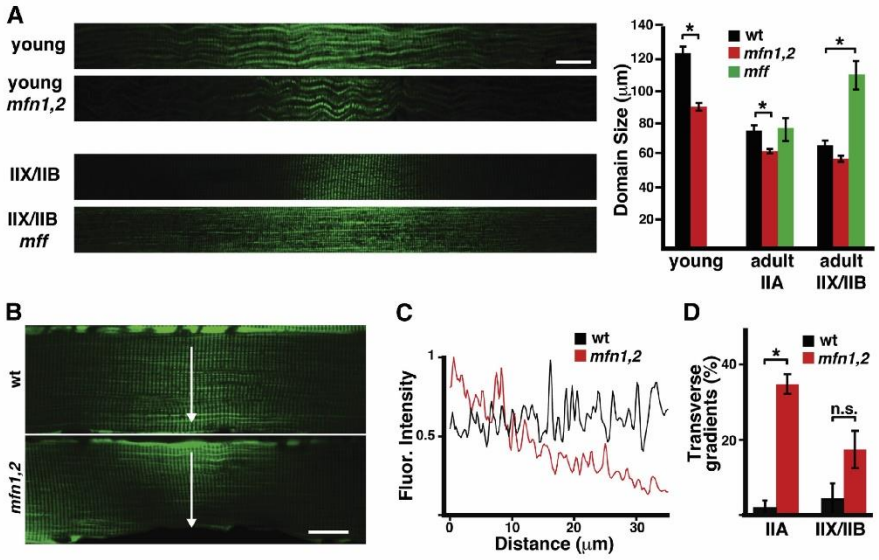
A
young
young
mfn1,2
IIX/IIB
IIX/IIB
mff
Domain Size (μm)
wt
mfn1,2
mff
young
adult IIA
adult IIX/IIB
B
wt
mfn1,2
C
Fluor. Intensity
Distance (μm)
D
Transverse gradients (%)
n.s.
IIA
IIX/IIB

Figure 5.7

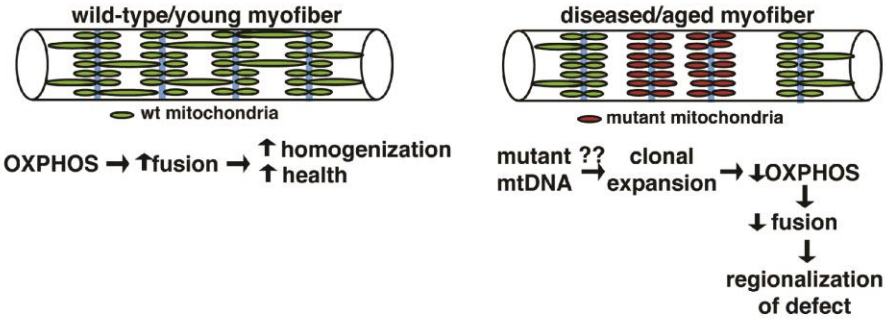
wild-type/young myofiber
wt mitochondria
OXPHOS → ↑fusion → ↑ homogenization
↑ health
diseased/aged myofiber
mutant mitochondria
mutant mtDNA ?? → clonal expansion → ↓OXPHOS
↓ fusion
↓
regionalization of defect

Chapter 5 Supplemental figure legends

Figure S1. Mitochondrial morphology and connectivity in mouse skeletal muscle fibers.

(A) Representative image of mitochondrial morphology in type IIX/IIB fibers from wildtype EDL muscle. Type IIX/IIB fibers were identified by conditional expression of mito-Dendra2 driven by the *Pvalb-Cre* driver. Scale bar, 20 μm. (B) Representative image of mitochondrial morphology in type I fibers (identified by expression of MyH7-CFP) in wildtype diaphragm muscle. Note that the non-CFP expressing fiber does not have elongated mitochondria in the longitudinal direction. Scale bar, 20 μm. (C) Representative image of mitochondrial morphology (visualized by mito-Dendra2 expression) in type I fibers (identified by expression of MyH7-CFP) in wildtype soleus muscle. Scale bar, 10 μm. (D) Levels of the indicated mitochondrial proteins in wild-type adult EDL (a fast twitch muscle) and soleus muscle (a slow twitch muscle), as measured by Western blot.

Figure S2. Mitochondrial function in glucose vs. acetoacetate-media.

(A) Representative images of mitochondrial membrane potential (TMRM staining) in the indicated media condition. Scale bar, 10 μm. (B) Quantification of membrane potential (TMRM staining) in the indicated media condition. Error bars indicate standard deviation. Experiments were performed in triplicate. (C) Representative data of oxygen consumption from intact muscle in glucose-media. Drugs (oligomycin, CCCP, antimycin A) were added at the indicated time points (arrows). Oxygen consumption rates (OCRs) were calculated as the slope of oxygen versus time. (D) Quantification of basal OCR, maximal (CCCP-

stimulated) OCR, and cellular RCR (respiratory control ratio = maximal OCR / oligomycin-inhibited OCR) in the indicated media conditions. Error bars indicate standard deviation. Experiments were performed in triplicate. (E) Photoconversion of mito-Dendra2 in type IIX/IIB fibers from an *ex vivo* EDL muscle, subject to overnight culturing in the indicated media condition. The red box indicates the photoconverted region of interest. Scale bar, 2 μm.

Figure S3. Stochastic labeling of individual myonuclei in mouse skeletal muscle.

(A) Representative image of a mito-Dendra2 expressing satellite cell that has not fused with its adjacent myofiber. Scale bar, 20 μm. (B) Representative image of mito-Dendra2 expression within a myofiber, after fusion of labeled satellite cell. Scale bar, 20 μm. (C) Representative images of a single mitochondrial domain (left) and a dual mitochondrial domain (right). Scale bar, 20 μm. For each myofiber, total vertical fluorescence intensity (green) is plotted as a function of longitudinal axis (below). Moving average of fluorescence intensity is shown in solid black. (D) Nuclear GFP fluorescence in a *Pax7-CreERT2; nuclear-GFP*^{cond} myofiber. GFP immunostaining identifies a single, labeled nucleus within the myofiber. Scale bar, 20 μm. (E) Individual z-slices of a mitochondrial domain taken at the top, middle and bottom of a myofiber. Scale bar, 20 μm. (F) Fluorescence intensity (moving average) is plotted versus distance for the three z-slices shown in (E).

Figure S4. Stability of mitochondrial domains.

(A) Representative images of a mitochondrial domain in an *ex vivo* cultured myofiber at the indicated time points. Scale bar, 20 μm. (B) Quantification of mitochondrial domain size over time during *ex vivo* culturing. Data is normalized to domain size at time t = 0 hr. Error bars indicate standard errors for n>10 fibers. (C) Representative low-magnification tiled images of mitochondrial domains from a young and adult animal. Scale bar, 200 μm. (D) Quantification of domain frequency, calculated as number of domains per 1000 μm of fiber length, for animals of the indicated ages. At least 50 domains per group were quantified (*$p<0.05$, **$p<0.01$ (t-test)). Error bars indicate standard errors. (E) Domain size in the indicated fiber types and tissues from wildtype animals. At least 30 domains per group were quantified (*$p<0.001$ (t-test)). Error bars indicate standard errors.

Chapter 5 Supplementary figures

Figure 5.S1

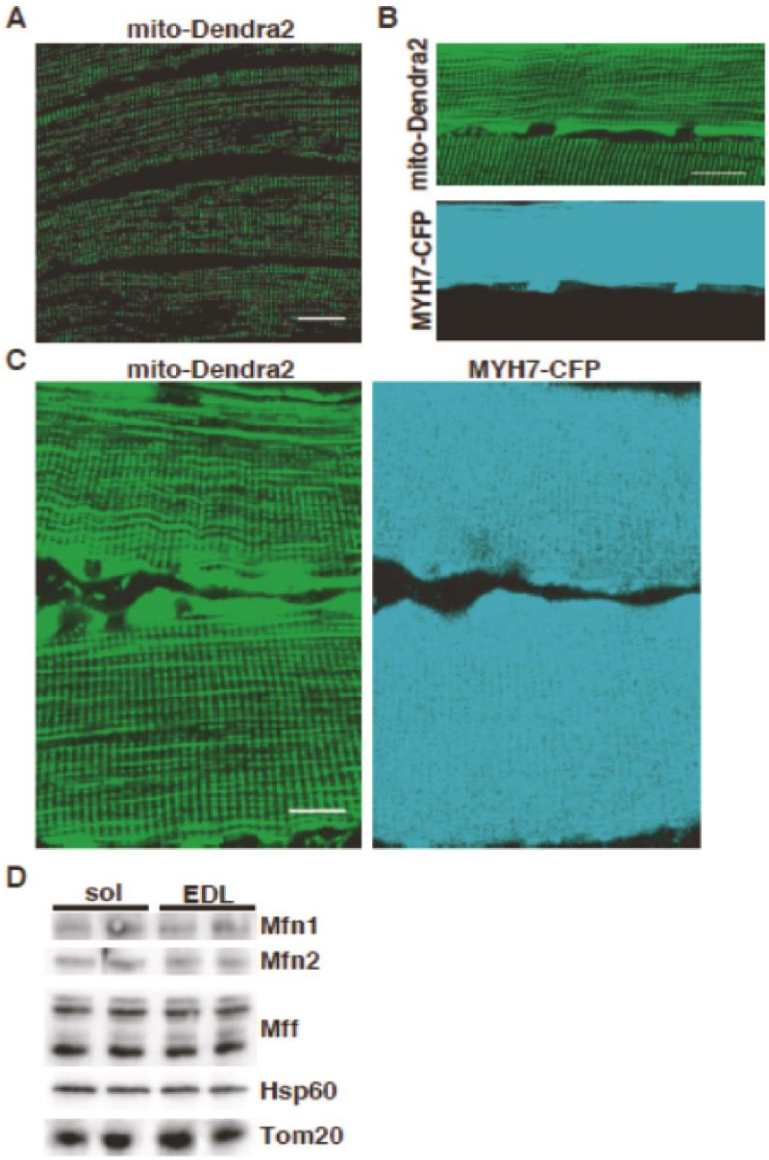

Figure 5.S2

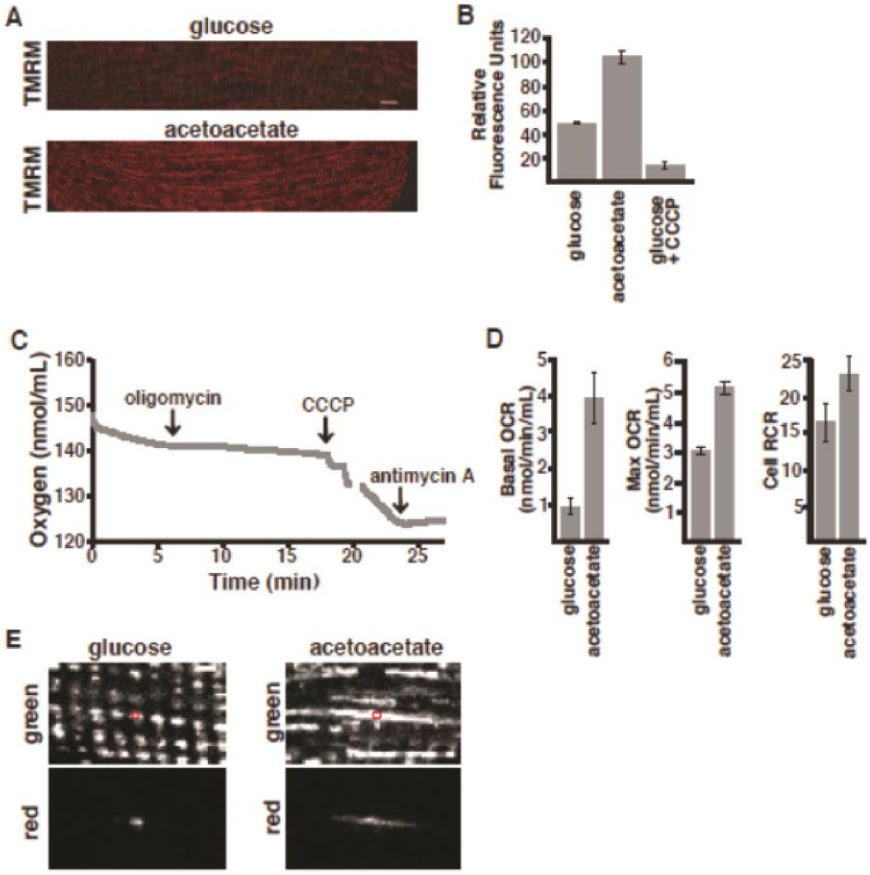
A
glucose
TMRM
acetoacetate
TMRM
B
Relative Fluorescence Units
120
100
80
60
40
20
glucose
acetoacetate
glucose + CCCP
C
Oxygen (nmol/mL)
160
150
140
130
120
oligomycin
CCCP
antimycin A
0
5
10
15
20
25
Time (min)
D
Basal OCR (nmol/min/mL)
Max OCR (nmol/min/mL)
Cell RCR
glucose
acetoacetate
E
glucose
acetoacetate
green
red

Figure 5.S3

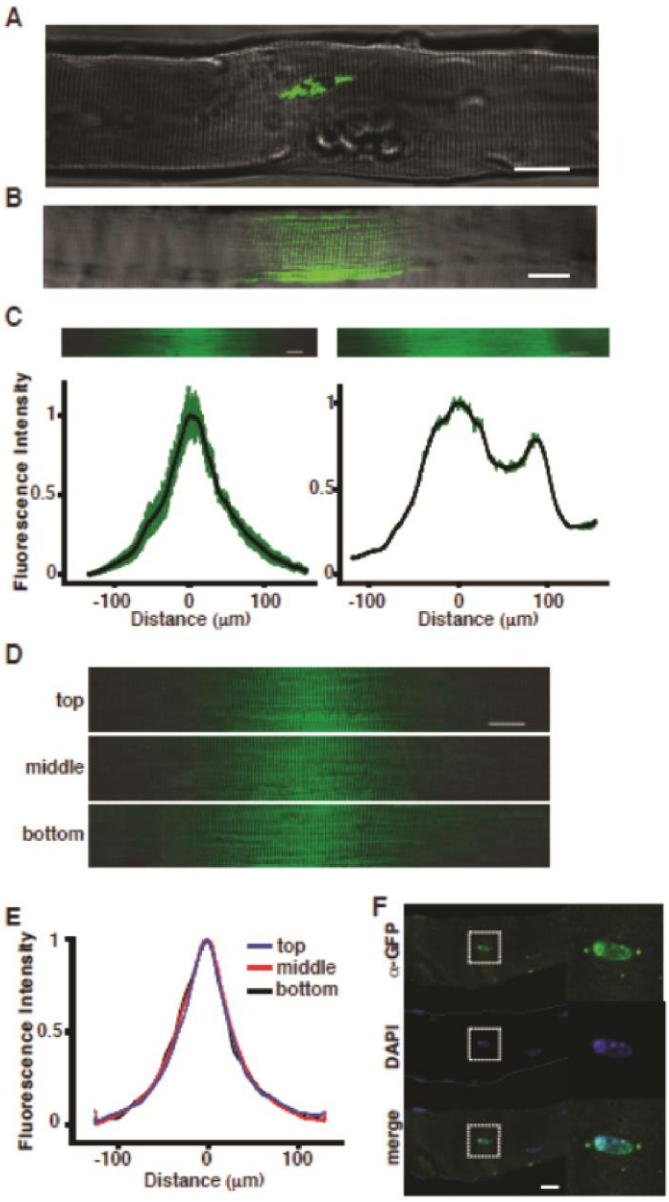
A
B
C
Fluorescence Intensity
1
0.5
0
-100
0
100
Distance (μm)
D
top
middle
bottom
E
Fluorescence Intensity
top
middle
bottom
Distance (μm)
F
α-GFP
DAPI
merge

Figure 5.S4

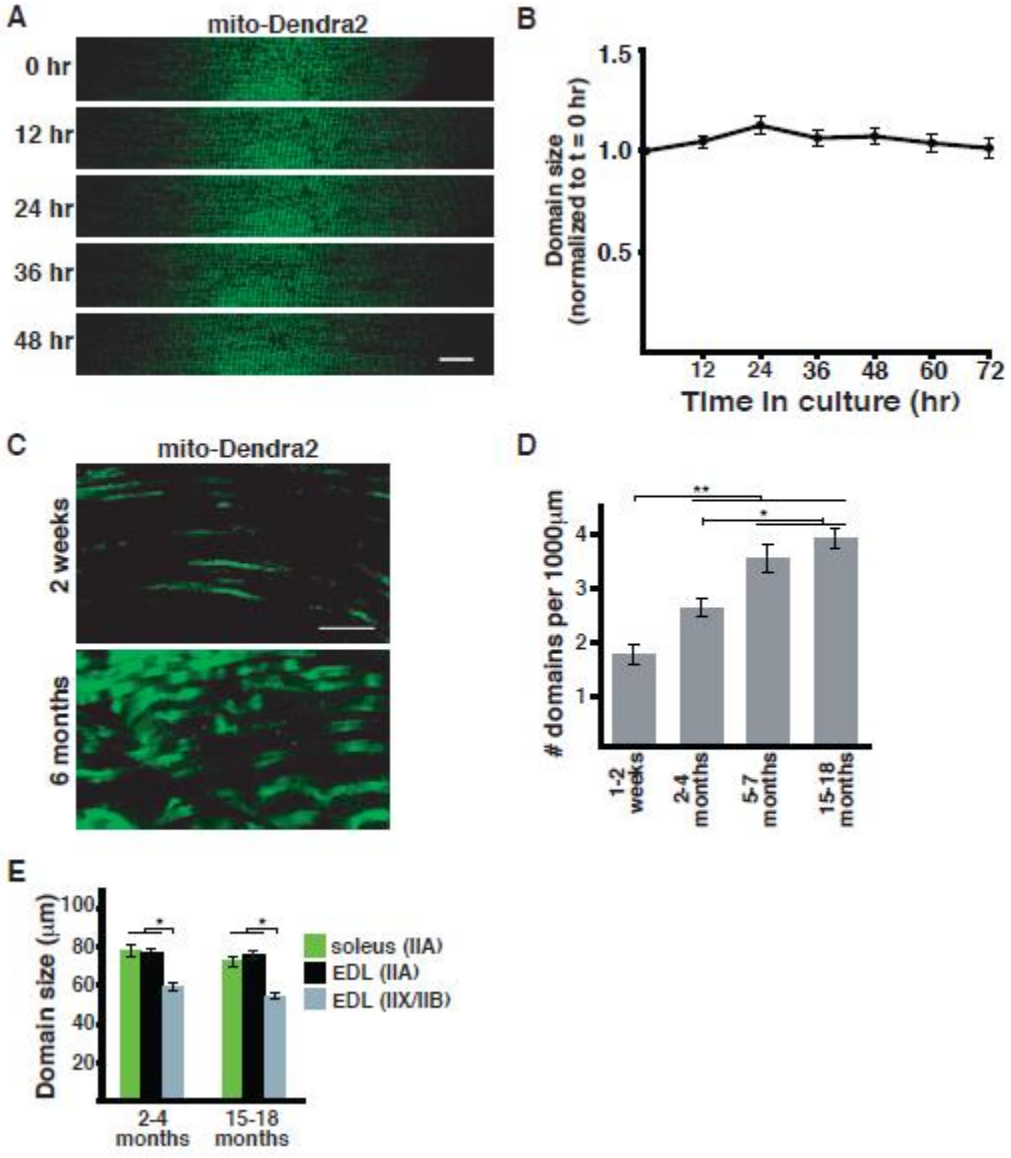
A
mito-Dendra2
0 hr
12 hr
24 hr
36 hr
48 hr
B
Domain size (normalized to t = 0 hr)
1.5
1.0
0.5
12
24
36
48
60
72
Time in culture (hr)
C
mito-Dendra2
2 weeks
6 months
D
domains per 1000μm
1-2 weeks
2-4 months
5-7 months
15-18 months
E
Domain size (μm)
soleus (IIA)
EDL (IIA)
EDL (IIX/IIB)
2-4 months
15-18 months

References

Agbulut, O., Noirez, P., Beaumont, F. and Butler-Browne, G. (2003). Myosin heavy chain isoforms in postnatal muscle development of mice. *Biology of the cell / under the auspices of the European Cell Biology Organization* 95, 399–406.

Allen, D. L., Harrison, B. C., Maass, A., Bell, M. L., Byrnes, W. C. and Leinwand, L. A. (2001). Cardiac and skeletal muscle adaptations to voluntary wheel running in the mouse. *Journal of applied physiology* 90, 1900–8.

Amati-Bonneau, P., Valentino, M. L., Reynier, P., Gallardo, M. E., Bornstein, B., Boissiere, A., Campos, Y., Rivera, H., de la Aleja, J. G., Carroccia, R., et al. (2008). OPA1 mutations induce mitochondrial DNA instability and optic atrophy "plus" phenotypes. *Brain : a journal of neurology* 131, 338–51.

Barron, M. J., Chinnery, P. F., Howel, D., Blakely, E. L., Schaefer, A. M., Taylor, R. W. and Turnbull, D. M. (2005). Cytochrome c oxidase deficient muscle fibres: substantial variation in their proportions within skeletal muscles from patients with mitochondrial myopathy. *Neuromuscular disorders : NMD* 15, 768–74.

Berchtold, M. W., Brinkmeier, H. and Muntener, M. (2000). Calcium ion in skeletal muscle: its crucial role for muscle function, plasticity, and disease. *Physiological reviews* 80, 1215–65.

Blaveri, K., Heslop, L., Yu, D. S., Rosenblatt, J. D., Gross, J. G., Partridge, T. A. and Morgan, J. E. (1999). Patterns of repair of dystrophic mouse muscle: studies on isolated fibers. *Developmental dynamics : an official publication of the American Association of Anatomists* 216, 244–56.

Bothe, G. W., Haspel, J. A., Smith, C. L., Wiener, H. H. and Burden, S. J. (2000). Selective expression of Cre recombinase in skeletal muscle fibers. *Genesis* 26, 165–6.

Casas, M., Figueroa, R., Jorquera, G., Escobar, M., Molgo, J. and Jaimovich, E. (2010). IP(3)-dependent, post-tetanic calcium transients induced by electrostimulation of adult skeletal muscle fibers. *The Journal of general physiology* 136, 455–67.

Chakkalakal, J. V., Kuang, S., Buffelli, M., Lichtman, J. W. and Sanes, J. R. (2012a). Mouse transgenic lines that selectively label Type I, Type IIA, and Types IIX+B skeletal muscle fibers. *Genesis* 50, 50–8.

Chakkalakal, J. V., Jones, K. M., Basson, M. A. and Brack, A. S. (2012b). The aged niche disrupts muscle stem cell quiescence. *Nature* 490, 355–60.

Chen, H., Detmer, S. A., Ewald, A. J., Griffin, E. E., Fraser, S. E. and Chan, D. C. (2003). Mitofusins Mfn1 and Mfn2 coordinately regulate mitochondrial fusion and are essential for embryonic development. *The Journal of cell biology* 160, 189–200.

Chen, H., McCaffery, J. M. and Chan, D. C. (2007). Mitochondrial fusion protects against

neurodegeneration in the cerebellum. *Cell* 130, 548–62.

Chen, H., Vermulst, M., Wang, Y. E., Chomyn, A., Prolla, T. A., McCaffery, J. M. and Chan, D. C. (2010). Mitochondrial fusion is required for mtDNA stability in skeletal muscle and tolerance of mtDNA mutations. *Cell* 141, 280–9.

Collins, C. A., Zammit, P. S., Ruiz, A. P., Morgan, J. E. and Partridge, T. A. (2007). A population of myogenic stem cells that survives skeletal muscle aging. *Stem cells* 25, 885–94.

Eisner, V., Lenaers, G. and Hajnoczky, G. (2014). Mitochondrial fusion is frequent in skeletal muscle and supports excitation-contraction coupling. *The Journal of cell biology* 205, 179–95.

Elson, J. L., Samuels, D. C., Johnson, M. A., Turnbull, D. M. and Chinnery, P. F. (2002). The length of cytochrome c oxidase-negative segments in muscle fibres in patients with mtDNA myopathy. *Neuromuscular disorders : NMD* 12, 858–64.

Fry, C. S., Lee, J. D., Mula, J., Kirby, T. J., Jackson, J. R., Liu, F., Yang, L., Mendias, C. L., Dupont-Versteegden, E. E., McCarthy, J. J., et al. (2015). Inducible depletion of satellite cells in adult, sedentary mice impairs muscle regenerative capacity without affecting sarcopenia. *Nature medicine* 21, 76–80.

Fujioka, H., Tandler, B., Haldar, S. M., Jain, M. K. and Hoppel, C. L. (2013). String mitochondria in mouse soleus muscle. *Microscopy research and technique* 76, 237–41.

Gomes, L. C., Di Benedetto, G. and Scorrano, L. (2011). During autophagy mitochondria elongate, are spared from degradation and sustain cell viability. *Nature cell biology* 13, 589–98.

Haldar, M., Hedberg, M. L., Hockin, M. F. and Capecchi, M. R. (2009). A CreER-based random induction strategy for modeling translocation-associated sarcomas in mice. *Cancer research* 69, 3657–64.

Hall, Z. W. and Ralston, E. (1989). Nuclear domains in muscle cells. *Cell* 59, 771–2.

Hippenmeyer, S., Vrieseling, E., Sigrist, M., Portmann, T., Laengle, C., Ladle, D. R. and Arber, S. (2005). A developmental switch in the response of DRG neurons to ETS transcription factor signaling. *PLoS biology* 3, e159.

Hudson, G., Amati-Bonneau, P., Blakely, E. L., Stewart, J. D., He, L., Schaefer, A. M., Griffiths, P. G., Ahlqvist, K., Suomalainen, A., Reynier, P., et al. (2008). Mutation of OPA1 causes dominant optic atrophy with external ophthalmoplegia, ataxia, deafness and multiple mitochondrial DNA deletions: a novel disorder of mtDNA maintenance. *Brain : a journal of neurology* 131, 329–37.

Keefe, A. C., Lawson, J. A., Flygare, S. D., Fox, Z. D., Colasanto, M. P., Mathew, S. J., Yandell, M. and Kardon, G. (2015). Muscle stem cells contribute to myofibres in

sedentary adult mice. *Nature communications* 6, 7087.

Keire, P., Shearer, A., Shefer, G. and Yablonka-Reuveni, Z. (2013). Isolation and culture of skeletal muscle myofibers as a means to analyze satellite cells. *Methods in molecular biology* 946, 431–68.

Kemp, R., Ireland, H., Clayton, E., Houghton, C., Howard, L. and Winton, D. J. (2004). Elimination of background recombination: somatic induction of Cre by combined transcriptional regulation and hormone binding affinity. *Nucleic acids research* 32, e92.

Kinoshita, I., Vilquin, J. T., Asselin, I., Chamberlain, J. and Tremblay, J. P. (1998). Transplantation of myoblasts from a transgenic mouse overexpressing dystrophin prduced only a relatively small increase of dystrophin-positive membrane. *Muscle & nerve* 21, 91–103.

Legros, F., Lombes, A., Frachon, P. and Rojo, M. (2002). Mitochondrial fusion in human cells is efficient, requires the inner membrane potential, and is mediated by mitofusins. *Molecular biology of the cell* 13, 4343–54.

Lepper, C., Conway, S. J. and Fan, C. M. (2009). Adult satellite cells and embryonic muscle progenitors have distinct genetic requirements. *Nature* 460, 627–31.

Liu, Y., Suckale, J., Masjkur, J., Magro, M. G., Steffen, A., Anastassiadis, K. and Solimena, M. (2010). Tamoxifen-independent recombination in the RIP-CreER mouse. *PloS one* 5, e13533.

Loson, O. C., Song, Z., Chen, H. and Chan, D. C. (2013). Fis1, Mff, MiD49, and MiD51 mediate Drp1 recruitment in mitochondrial fission. *Molecular biology of the cell* 24, 659–67.

Mattenberger, Y., James, D. I. and Martinou, J. C. (2003). Fusion of mitochondria in mammalian cells is dependent on the mitochondrial inner membrane potential and independent of microtubules or actin. *FEBS letters* 538, 53–9.

Mishra, P. and Chan, D. C. (2014). Mitochondrial dynamics and inheritance during cell division, development and disease. *Nature reviews. Molecular cell biology* 15, 634–46.

Mishra, P., Carelli, V., Manfredi, G. and Chan, D. C. (2014). Proteolytic cleavage of Opa1 stimulates mitochondrial inner membrane fusion and couples fusion to oxidative phosphorylation. *Cell metabolism* 19, 630–41.

Mitra, K., Wunder, C., Roysam, B., Lin, G. and Lippincott-Schwartz, J. (2009). A hyperfused mitochondrial state achieved at G1-S regulates cyclin E buildup and entry into S phase. *Proceedings of the National Academy of Sciences of the United States of America* 106, 11960–5.

Mourkioti, F., Slonimsky, E., Huth, M., Berno, V. and Rosenthal, N. (2008). Analysis of

CRE-mediated recombination driven by myosin light chain 1/3 regulatory elements in embryonic and adult skeletal muscle: a tool to study fiber specification. *Genesis* 46, 424–30.

Ogata, T. and Yamasaki, Y. (1997). Ultra-high-resolution scanning electron microscopy of mitochondria and sarcoplasmic reticulum arrangement in human red, white, and intermediate muscle fibers. *The Anatomical record* 248, 214–23.

Pavlath, G. K., Rich, K., Webster, S. G. and Blau, H. M. (1989). Localization of muscle gene products in nuclear domains. *Nature* 337, 570–3.

Pette, D. and Staron, R. S. (2000). Myosin isoforms, muscle fiber types, and transitions. *Microscopy research and technique* 50, 500–9.

Pham, A. H., McCaffery, J. M. and Chan, D. C. (2012). Mouse lines with photo-activatable mitochondria to study mitochondrial dynamics. *Genesis* 50, 833–43.

Redenbach, D. M., Ovalle, W. K. and Bressler, B. H. (1988). Effect of neonatal denervation on the distribution of fiber types in a mouse fast-twitch skeletal muscle. *Histochemistry* 89, 333–42.

Rouzier, C., Bannwarth, S., Chaussenot, A., Chevrollier, A., Verschueren, A., Bonello-Palot, N., Fragaki, K., Cano, A., Pouget, J., Pellissier, J. F., et al. (2012). The MFN2 gene is responsible for mitochondrial DNA instability and optic atrophy "plus" phenotype. *Brain : a journal of neurology* 135, 23–34.

Shefer, G., Van de Mark, D. P., Richardson, J. B. and Yablonka-Reuveni, Z. (2006). Satellite-cell pool size does matter: defining the myogenic potency of aging skeletal muscle. *Developmental biology* 294, 50–66.

Shoubridge, E. A., Karpati, G. and Hastings, K. E. (1990). Deletion mutants are functionally dominant over wild-type mitochondrial genomes in skeletal muscle fiber segments in mitochondrial disease. *Cell* 62, 43–9.

Srinivas, S., Watanabe, T., Lin, C. S., William, C. M., Tanabe, Y., Jessell, T. M. and Costantini, F. (2001). Cre reporter strains produced by targeted insertion of EYFP and ECFP into the ROSA26 locus. *BMC developmental biology* 1, 4.

Stoller, J. Z., Degenhardt, K. R., Huang, L., Zhou, D. D., Lu, M. M. and Epstein, J. A. (2008). Cre reporter mouse expressing a nuclear localized fusion of GFP and beta-galactosidase reveals new derivatives of Pax3-expressing precursors. *Genesis* 46, 200–4.

Tondera, D., Grandemange, S., Jourdain, A., Karbowski, M., Mattenberger, Y., Herzig, S., Da Cruz, S., Clerc, P., Raschke, I., Merkwirth, C., et al. (2009). SLP-2 is required for stress-induced mitochondrial hyperfusion. *The EMBO journal* 28, 1589–600.

Wanagat, J., Cao, Z., Pathare, P. and Aiken, J. M. (2001). Mitochondrial DNA deletion mutations colocalize with segmental electron transport system abnormalities,

muscle fiber atrophy, fiber splitting, and oxidative damage in sarcopenia. *FASEB journal : official publication of the Federation of American Societies for Experimental Biology* 15, 322–32.

CHAPTER 6

Conclusions and perspectives

Grigor Varuzhanyan and David C. Chan

Division of Biology and Biological Engineering, California Institute of Technology, Pasadena, CA 91125, USA.

Summary

Mitochondrial dynamics and mitophagy are well-established quality control mechanisms that maintain basal cellular homeostasis (Chan, 2020). However, their role during development has remained poorly characterized. We addressed this gap in knowledge by characterizing mitochondrial dynamics and mitophagy during the development of the male germline (Figure 6). In Chapter 2, we showed that the mitofusins *Mfn1* and *Mfn2* promote OXPHOS to enable spermatogonial differentiation and meiosis. In Chapter 3, we found that *Mff* mediates acute mitochondrial fragmentation to facilitate the wrapping of the mitochondria around the sperm midpiece. Our analyses in Chapter 4 revealed that the putative mitophagy-related gene, *Fis1* regulates mitochondrial degradation during post-meiotic spermatid development. Thus, mitochondria undergo fusion during the early stages of spermatogenesis before undergoing fragmentation and degradation during post-meiotic spermatid development (Figure 6).

Future directions

Mitochondrial fusion and OXPHOS during spermatogenesis

In Chapters 1 and 2, we described the mitochondrial transitions that occur during spermatogenesis and showed that mitochondria undergo fusion during spermatogonial differentiation and meiosis. Because mitochondrial dynamics is intricately linked to cellular metabolism (Mishra and Chan, 2016), these mitochondrial transitions likely reflect the changing metabolic requirements of germ cells as they traverse the compartmentalized seminiferous epithelium. Indeed, OXPHOS is known to fuel mammalian spermatogenesis

and, in particular, meiosis (Varuzhanyan and Chan, 2020). *Opa1*, which plays a central role in mitochondrial fusion and regulates OXPHOS, would be expected to play a similar role during male germ cell development, but this should be tested experimentally.

In elongating spermatids, mitochondria elongate as they wrap around the developing midpiece, raising the possibility that these mitochondria undergo fusion. Analysis of static EM images seems to suggest that mitochondria elongate without undergoing fusion (Ho and Wey, 2007). However, future studies should address this genetically by removing mitofusins or *Opa1* from post-meiotic spermatids.

The product of spermatogenesis is a highly motile sperm cell capable of a long journey to fertilization. Flagellar motility depends on cellular ATP, which is converted into mechanical work by dynein motors (Serohijos et al., 2006). The source of this ATP has been studied extensively in various species (Storey, 2004). Both glycolysis and OXPHOS are active in spermatozoa, but the primary source of ATP for sperm motility remains unclear (du Plessis et al., 2015). Given the prominence of mitochondria at the sperm midpiece and their relatively high efficiency of generating ATP, it is likely that OXPHOS plays the major role in fueling flagellar locomotion. Indeed, in mice, species that exhibit higher sperm motility and ATP production are associated with higher OXPHOS utilization (Tourmente et al., 2015). Thus, it would be interesting to determine whether mitochondrial morphology and ultrastructure correlate with the high OXPHOS utilization in these species.

Mitochondrial fission during spermatogenesis

Our data in Chapter 3 showed that *Mff* is required in post-meiotic spermatids for developmentally regulated mitochondrial fission and formation of the mitochondrial sheath (Varuzhanyan et al., 2020, in press). Thus, spermiogenesis may be a promising system for studying the regulatory networks that drive mitochondrial fission *in vivo*. Future studies could usefully explore whether other mitochondrial fission factors, such as *Mid49*, *MiD50*, and *Drp1*, are also required for mitochondrial sheath formation. Removal of *Mfn1* does not rescue the spermatogenesis defect of Mff^{gt} mice (Chen et al., 2015), suggesting a specific requirement for mitochondrial fission in spermatids. Taken together, these data suggest that round spermatids acutely downregulate fusion and upregulate fission to ensure robust mitochondrial fragmentation, which may help reorganize mitochondria during spermatid polarization and recruit them to the developing midpiece for formation of the mitochondrial sheath.

Near the end of spermiogenesis, spermatid mitochondria face two distinct fates. A small group of about 50 mitochondria lines the midpiece to form the mitochondrial sheath, while the remaining mitochondria, along with other cytosolic components, are transferred into residual bodies destined for phagocytic degradation in Sertoli cells (Figure 1.5). It remains unknown whether this mitochondrial segregation happens at random or involves an active selection process. Thus, it would be interesting for future research to examine whether mitophagy or mitochondrial motor proteins such as Miro and Milton (Schwarz, 2013) contribute to this mitochondrial segregation during mitochondrial sheath formation.

Mitophagy during spermatogenesis

Meiosis produces haploid round spermatids, which undergo dramatic cellular remodeling to become the highly specialized sperm cells capable of fertilization. During this process, spermatids generate a lysosome related organelle called the acrosome, which releases digestive enzymes to penetrate the zona pellucida during fertilization. Notably, spermatids undergo a morphological transformation and culling of excess cellular components to become highly slender and compacted cells. These cellular remodeling processes require the autophagy gene *Atg7a* (Shang et al., 2016; Wang et al., 2014), but the role of mitophagy during mammalian spermatogenesis remained largely unknown due to technical challenges associated with studying mitophagy *in vivo*.

Some evidence implicates mitophagy in *D. melanogaster* spermatid development. In *Pink1* mutant flies, spermatids have aberrant mitochondria and defects in individualization (Clark et al., 2006). The ubiquitin proteasome system (UPS), which drives Parkin-mediated mitophagy (Chan et al., 2011; Chan and Chan, 2011; Rakovic et al., 2019), is highly active during mammalian spermiogenesis (Bose et al., 2014; Hermo et al., 2010), suggesting an evolutionarily conserved role for mitophagy in spermatogenesis.

Towards the end of spermatid development in mammals, excess mitochondria and other cellular components agglomerate into residual bodies for phagocytic degradation by Sertoli cells (Dietert, 1966). The work presented in Chapter 4 indicates that *Fis1* mediates the autophagic degradation of mitochondria during spermatid development. However, it should be noted that since *Fis1* deletion arrests spermatogenesis during early spermatid development, the role of mitophagy in later stages remains unknown. A natural progression

of this work is to address whether other mitophagy-related genes are also required for spermatid development. Because mitochondrial fission has been linked to mitophagy (Burman et al., 2017; Tanaka et al., 2010), it would be interesting to explore whether mitochondrial fission facilitates mitochondrial degradation during spermatid development. In cultured cells, mitophagy can also occur independently of mitochondrial fission (Yamashita et al., 2016). In this model, small regions of mitochondria bud directly into autophagosomes in a *Drp1*-independent manner.

Finally, recent studies have implicated *Fis1* in regulating mitochondrion-lysosome contact sites via the *Tbc1d15-Rab7a* pathway (Peng et al., 2020; Wong et al., 2018). Thus, a potentially fruitful area for future research would be to explore whether such interorganellar contacts are required for spermatid development. To this end, we developed a split GFP system to monitor contacts between mitochondria and lysosomes. In this system, mitochondria and lysosomes are tagged with two halves of a split GFP protein. Upon organellar contact, the two split GFPs connect, forming a full GFP protein that fluoresces and serves as a readout for mitochondria and lysosome contact sites. This system can be used to explore the kinetics of mitochondrion-lysosome contacts and investigate how *Fis1* regulates this process.

Chapter 6 figure legend

Figure 6. Summary schematic showing the stages of spermatogenic arrest upon deletion of *Mfn1*, *Mfn2*, *Mff*, or *Fis1*.

Loss of either *Mfn1* or *Mfn2* blocks spermatogonial differentiation, whereas ablation of *Mfn1* alone blocks meiosis before the first meiotic division (MI). *Fis1*-ablation prevents maturation of the round spermatids. *Mff*-deficient mice exhibit a mitochondrial fission defect during the round spermatid stage (dashed arrow), which prevents proper formation of the mitochondrial sheath in mature spermatozoa. MI, meiosis I; MII, meiosis II; 1º, primary spermatocyte; 2º, secondary spermatocyte.

Chapter 6 Figure

Figure 6

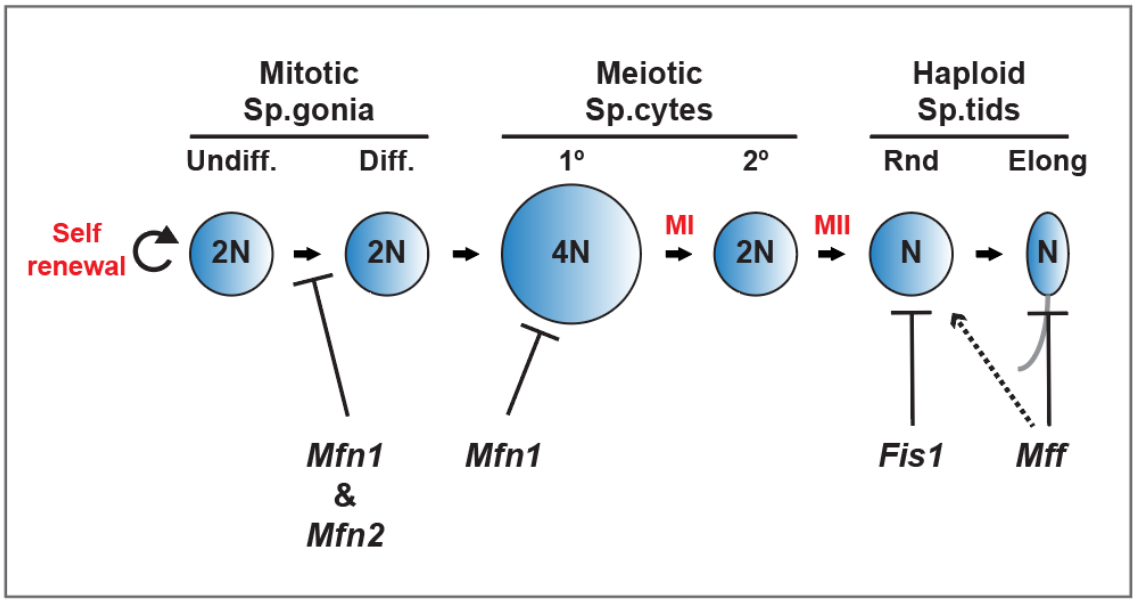

References

Bose, R., Manku, G., Culty, M., Wing, S.S., 2014. Ubiquitin–Proteasome System in Spermatogenesis, in: Sutovsky, P. (Ed.), Posttranslational Protein Modifications in the Reproductive System, *Advances in Experimental Medicine and Biology*. Springer, New York, NY, pp. 181–213. https://doi.org/10.1007/978-1-4939-0817-2_9

Burman, J.L., Pickles, S., Wang, C., Sekine, S., Vargas, J.N.S., Zhang, Z., Youle, A.M., Nezich, C.L., Wu, X., Hammer, J.A., Youle, R.J., 2017. Mitochondrial fission facilitates the selective mitophagy of protein aggregates. *J. Cell Biol.* 216, 3231–3247. https://doi.org/10.1083/jcb.201612106

Chan, D.C., 2020. Mitochondrial Dynamics and Its Involvement in Disease. *Annual Review of Pathology: Mechanisms of Disease* 15, null. https://doi.org/10.1146/annurev-pathmechdis-012419-032711

Chan, N.C., Chan, D.C., 2011. Parkin uses the UPS to ship off dysfunctional mitochondria. *Autophagy* 7, 771–772. https://doi.org/10.4161/auto.7.7.15453

Chan, N.C., Salazar, A.M., Pham, A.H., Sweredoski, M.J., Kolawa, N.J., Graham, R.L.J., Hess, S., Chan, D.C., 2011. Broad activation of the ubiquitin–proteasome system by Parkin is critical for mitophagy. *Hum Mol Genet* 20, 1726–1737. https://doi.org/10.1093/hmg/ddr048

Chen, H., Ren, S., Clish, C., Jain, M., Mootha, V., McCaffery, J.M., Chan, D.C., 2015. Titration of mitochondrial fusion rescues Mff-deficient cardiomyopathyCardiac physiology restored in Mff/Mfn1 mutants. *J Cell Biol* 211, 795–805. https://doi.org/10.1083/jcb.201507035

Clark, I.E., Dodson, M.W., Jiang, C., Cao, J.H., Huh, J.R., Seol, J.H., Yoo, S.J., Hay, B.A., Guo, M., 2006. Drosophila pink1 is required for mitochondrial function and interacts genetically with parkin. *Nature* 441, 1162.

Dietert, S.E., 1966. Fine structure of the formation and fate of the residual bodies of mouse spermatozoa with evidence for the participation of lysosomes. *Journal of Morphology* 120, 317–346. https://doi.org/10.1002/jmor.1051200402

du Plessis, S.S., Agarwal, A., Mohanty, G., Van der Linde, M., 2015. Oxidative phosphorylation versus glycolysis: what fuel do spermatozoa use? *Asian journal of andrology* 17, 230.

Hermo, L., Pelletier, R.-M., Cyr, D.G., Smith, C.E., 2010. Surfing the wave, cycle, life history, and genes/proteins expressed by testicular germ cells. Part 4: intercellular bridges, mitochondria, nuclear envelope, apoptosis, ubiquitination,

membrane/voltage-gated channels, methylation/acetylation, and transcription factors. *Microsc. Res. Tech.* 73, 364–408. https://doi.org/10.1002/jemt.20785

Ho, H.-C., Wey, S., 2007. Three dimensional rendering of the mitochondrial sheath morphogenesis during mouse spermiogenesis. *Microscopy research and technique* 70, 719–723.

Hoppins, S., 2014. The regulation of mitochondrial dynamics. Current Opinion in Cell Biology, *Cell organelles* 29, 46–52. https://doi.org/10.1016/j.ceb.2014.03.005

Mishra, P., Chan, D.C., 2016. Metabolic regulation of mitochondrial dynamics. *J. Cell Biol.* 212, 379–387. https://doi.org/10.1083/jcb.201511036

Peng, W., Wong, Y.C., Krainc, D., 2020. Mitochondria-lysosome contacts regulate mitochondrial Ca2+ dynamics via lysosomal TRPML1. *PNAS* 117, 19266–19275. https://doi.org/10.1073/pnas.2003236117

Rakovic, A., Ziegler, J., Mårtensson, C.U., Prasuhn, J., Shurkewitsch, K., König, P., Paulson, H.L., Klein, C., 2019. PINK1-dependent mitophagy is driven by the UPS and can occur independently of LC3 conversion. *Cell Death Differ* 26, 1428–1441. https://doi.org/10.1038/s41418-018-0219-z

Schwarz, T.L., 2013. Mitochondrial trafficking in neurons. Cold Spring Harb Perspect Biol 5. https://doi.org/10.1101/cshperspect.a011304

Serohijos, A.W.R., Chen, Y., Ding, F., Elston, T.C., Dokholyan, N.V., 2006. A structural model reveals energy transduction in dynein. *PNAS* 103, 18540–18545. https://doi.org/10.1073/pnas.0602867103

Shang, Y., Wang, H., Jia, P., Zhao, H., Liu, C., Liu, W., Song, Z., Xu, Z., Yang, L., Wang, Y., 2016. Autophagy regulates spermatid differentiation via degradation of PDLIM1. *Autophagy* 12, 1575–1592.

Storey, B.T., 2004. Mammalian sperm metabolism: oxygen and sugar, friend and foe. Int. *J. Dev. Biol.* 52, 427–437. https://doi.org/10.1387/ijdb.072522bs

Tanaka, A., Cleland, M.M., Xu, S., Narendra, D.P., Suen, D.-F., Karbowski, M., Youle, R.J., 2010. Proteasome and p97 mediate mitophagy and degradation of mitofusins induced by Parkin. *J. Cell Biol.* 191, 1367–1380. https://doi.org/10.1083/jcb.201007013

Tourmente, M., Villar-Moya, P., Rial, E., Roldan, E.R.S., 2015. Differences in ATP Generation Via Glycolysis and Oxidative Phosphorylation and Relationships with Sperm Motility in Mouse Species. *J Biol Chem* 290, 20613–20626. https://doi.org/10.1074/jbc.M115.664813

Varuzhanyan, G., Chan, D.C., 2020. Mitochondrial dynamics during spermatogenesis. *J Cell Sci* 133. https://doi.org/10.1242/jcs.235937

Varuzhanyan, G., Chen, H., Rojansky, R., Ladinsky, M., S., McCaffery, M., Chan, D., 2020. Mitochondrial fission is required for organization of the mitochondrial sheath in spermatids. *Biochimica et Biophysica Acta (BBA) - General Subjects* (in press).

Varuzhanyan, G., Rojansky, R., Sweredoski, M.J., Graham, R.L., Hess, S., Ladinsky, M.S., Chan, D.C., 2019. Mitochondrial fusion is required for spermatogonial differentiation and meiosis. *eLife* 8.

Wang, H., Wan, H., Li, X., Liu, W., Chen, Q., Wang, Y., Yang, L., Tang, H., Zhang, X., Duan, E., 2014. Atg7 is required for acrosome biogenesis during spermatogenesis in mice. *Cell research* 24, 852.

Wong, Y.C., Ysselstein, D., Krainc, D., 2018. Mitochondria–lysosome contacts regulate mitochondrial fission via RAB7 GTP hydrolysis. *Nature* 554, 382–386. https://doi.org/10.1038/nature25486

Yamashita, S., Jin, X., Furukawa, K., Hamasaki, M., Nezu, A., Otera, H., Saigusa, T., Yoshimori, T., Sakai, Y., Mihara, K., Kanki, T., 2016. Mitochondrial division occurs concurrently with autophagosome formation but independently of Drp1 during mitophagy. *J Cell Biol* 215, 649–665. https://doi.org/10.1083/jcb.201605093

Zhang, J., Wang, Q., Wang, M., Jiang, M., Wang, Y., Sun, Y., Wang, J., Xie, T., Tang, C., Tang, N., Song, H., Cui, D., Chao, R., Ding, S., Ni, B., Chen, X., Wang, Y., 2016. GASZ and mitofusin-mediated mitochondrial functions are crucial for spermatogenesis. *EMBO reports* 17, 220–34. https://doi.org/10.15252/embr.201540846